Structure and energy relationships in ice and crystalline hydrates

Gareth Aneurin Tribello

Davy-Faraday Research Laboratory, The Royal Institution of Great Britain

Department of Chemistry, University College London

Thesis submitted for the degree of Doctor of Philosophy

to the

University of London

2007

ProQuest LLC
789 East Eisenhower Parkway
P.O. Box 1346
Ann Arbor, MI 48106-1346

I, Gareth Aneurin Tribello, confirm that the work presented in this thesis is my own. Where information has been derived from other sources, I confirm that this has been indicated in the thesis.

Abstract

Computer simulations of the various phases of ice have been carried out using potential methods and density functional theory. Plane wave DFT and subsequent Wannier transformations of the Kohn-Sham orbitals were used to obtain highly localised orbitals, which were treated as molecular orbitals in the calculation of molecular multipoles. Using these multipoles it has been shown that the energy differences, calculated using DFT, between different proton topologies of ice VII and Ih are reproduced when the interaction electrostatic potential energy is calculated up to terms in $(1/r^6)$ and thus that the driving force for proton ordering is electrostatic. Armed with this knowledge, successful blind predictions, which have been experimentally verified, of the proton ordered forms of ice V and XII (ices XIII and XIV respectively) have been made using plane wave DFT.

The recently developed TIP6P potential has been modified so as to reproduce the correct structure for ice XI, the proton ordered form of ice Ih, and to reproduce the DFT energy differences between different hydrogen bonding topologies. Total energy calculations, using this potential, show that the surface energy depends strongly on the hydrogen bond topology exposed at the surface. In particular surfaces on which under-coordinated protons are clustered have high energies. Monte Carlo calculations have shown that the hydrogen bond topology adopted by ice, both at the surface and in the bulk, depends on the temperature.

A comparison of the structures that are possible to make out of silica and ice has been undertaken in the hope that new ice and silica phases can be identified. This comparison is possible because both silica and water form the backbones of 4-connected nets. DFT calculations have shown that the energy maps of the various four connected nets are very similar for both structures, with any differences arising because of the greater flexibility of the O-Si-O angle in silica. Furthermore, this analysis has highlighted a number of potential new ice phases and led to the proposal of a synthetic route to a new clathrate based on the zeolite framework SGT.

Acknowledgments

I have been lucky enough, over the past three years, to work with and meet with an amazing group of people and it would be churlish of me not to acknowledge the roles they have played in helping me produce this thesis. Foremost amongst them is my supervisor, Dr Ben Slater, who has given me support, encouragement and a great deal of flexibility to dictate the direction of my own research.

In addition, I must also acknowledge hours of useful discussions with Dr Alexei Sokol, who has been like a walking textbook, and productive collaborations with Prof PA Madden, Miss L Foy, Dr MA Zwinjenburg, Dr C Salzmann, Prof J Finney and Dr DA Fortes. I would like to also thank Prof Catlow for the opportunity to do this PhD and for the chance to supervise a very talented A-level student, Miss S Renner, through her summer project.

The research would not have been possible without the funding from the Engineering and Physical Sciences Research Council and computer time on HPCx, the UK Capability Computing resource.

Finally, I wish to acknowledge all my friends in London, my housemates James and Edmund, my office-mates Paul, Hong, Tariq, Malek, Mike, Wing, Iza, Mark and Kim and my family, especially my mum - I hope when this is being read she hasn't finished building her house because if she hasn't it means I've won!

Contents

List of Figures

List of Tables

Chapter 1

Introduction - Ice in nature

Water is a fascinating material, the study of which dates back to the ancient Greeks. Its abundance on the planet is the reason that there is life and the Earth's weather is largely a consequence of the coexistence of gaseous, liquid and solid water in the atmosphere. Water is also the most common solvent in chemistry and the hydrogen bonds that hold the molecules in this liquid together have the same physical origin as the forces that hold together the strands in the DNA double helix.

Solid water, ice, is arguably as interesting as the liquid and is unique amongst crystalline materials as it is of interest to a community of scientists which includes physicists, chemists, geologists, astronomers, engineers and meteorologists [1]. In the sections that follow, a brief survey of the importance of ice in the universe is undertaken and a description of the contribution that theory can make to an understanding of the role of ice in these disparate roles is provided.

1.1 Ice in rivers and lakes

In winter, the surfaces of many rivers and lakes become frozen, while the water underneath the ice remains in the liquid state. This occurs because water with its free surface at 0 °C is stable against convection, because of its maximum in density at 4 °C, and because ice is less dense than water. The polycrystalline nature

of the ice that forms has been classified by Michel and Ramseier [2]. They first distinguish between the primary layer that forms first, the secondary layer which grows underneath the primary layer and the superimposed ice that forms from water that floods over the top of the frozen lake or from snow that falls on the surface. The three types of primary ice are

- *P1 ice* - The surface formed by this ice is composed of large platelike grains which all have their c-axis oriented perpendicular to the surface but their a-axis randomly oriented within the plane. This is the the type of ice that forms slowly on still water

- *P2 ice* - This ice has a more complex granular structure with needle shaped crystals as well as platelets. It is formed when the temperature gradients are larger because more crystals are nucleated.

- *P3 ice* - This ice forms when the surface is agitated by wind or flow. The crystals that form may be needles or platelets and once they form they remain in suspension and form a thick layer of slush. This slush can freeze solid forming an ice which has random orientations for all its constituent grains.

- *P4 ice* - Snow falling on a lake can trigger nucleation and produce an ice sheet that is composed of small randomly oriented grains.

Secondary ice grows downwards from the primary ice in long columnar crystals, which get larger in width and fewer in number as they grow downwards. The structure of the secondary ice is strongly dependent on the nature of the primary ice which it grows from and can be classified as one of three types:

- *SI ice* - This has the c-axis of all the crystals approximately vertical and forms naturally under P1 ice.

- *S2 ice* - This has the c-axis all lying in the horizontal plane with random orientations and forms from P2, P3 or P4 ice.

- *S3 ice* - This is like C2 but the *c*-axis have a preferred direction in the horizontal plane.

It is well established in the theory of crystal growth [3] that crystals grown over short timescales adopt morphologies which maximise the surface area of the slowest growing faces. Over longer timescales however the crystal converts to a morphology which minimises the total surface energy. The morphology which minimises the surface energy can now be calculated with relative ease [3]. Furthermore, recent work [4] has shown that kinetic Monte Carlo approaches can be used to calculate the morphology of crystals grown under kinetic control. Similar simulations for ice could help in the understanding of under what conditions P1 and P2 ice form.

1.2 Snow and Glaciers

Snowfalls that cover landscapes are composed of ice crystals, air and sometimes water and, when it first falls, is typically not very dense. As it lies on the surface of the earth however it densifies, eventually forming firn, which is solid ice with pores. This increase in density occurs through complex chemical processes akin to the sintering of ceramic materials. These processes are driven by the desire to reduce the combined ice-vapour and grain-boundary surface energy and may occur through mass transfer by diffusion in the surface layer, through the vapour or along the grain-boundary. Although early parts of this densification take place in snow just lying on the surface, later processes require pressure to occur and take place because of the weight of snow cover above. This stage of densification is interesting because if the stresses are kept low it can be treated like a normal solid, but if the compressive stress exceeds a certain limit the snow undergoes a large irreversible change in volume and transforms into a much more compact state with different properties.

Once snow has accumulated over a large number of years it forms glaciers which can sculpt landscapes through erosive processes. The ice in these glaciers flows over

the landscapes through complex mechanisms which involve both the plastic deformation of single crystals and deformation along grain boundaries in the polycrystalline glacier. The plastic deformation of single crystals is a potential area where simulation could provide understanding as it occurs through the motion of line defects within the bulk, which have been studied in MgO and zeolite A using computer simulation [5]. In ice the motion of these line defects is affected by the local proton topology about the defect as the proton topology [6, 7] must re-order in order for the defect to be able to move through the crystal without the formation of further defects.

1.3 Ice in the atmosphere

Ice, present in the atmosphere in clouds and in the boundary layer in ice sheets and glaciers can provide surfaces for heterogenous catalysis [8] and also has a critical role in the physics of clouds and thus the production of weather [9]. A cloud is formed when moist air rises in the atmosphere and cools adiabatically, resulting in supersaturated water vapour and condensation of water droplets, typically 10 μm in diameter. These droplets are so stable that they do not coalesce, fall out of the cloud or freeze above about $-40\,^{\circ}\mathrm{C}$. However, freezing is commonly triggered by other nuclei present in the air and may occur either by the freezing of a droplet or by the formation of ice from water vapour. Once frozen the fact that ice has a lower vapour pressure than water means that the ice crystals grow by vapour transfer from the droplets, eventually becoming heavy enough to precipitate from the cloud and fall to the earth as snow or rain. The ice crystals grown from vapour in these clouds have a wide variety of different shapes ranging from plate like crystals to prisms, needles and beautiful six pointed snow flakes, and again their growth could be studied using computer simulations. Furthermore, an important question to meteorologists is the nature of ice forming nuclei in clouds and whether the concentrations of these may be affected by pollution or controlled by scattering nuclei from aircrafts, which is

also something that could potentially be investigated with the aid of simulation.

Higher in the atmosphere, in the upper troposphere and tropopause, clouds can be formed by the direct condensation of ice crystals from water vapour. Interaction of gas-phase species with these clouds has the potential to both promote heterogenous chemistry and to scavenge semi-volatile gas-phase species. Furthermore, over the poles, during the winter, polar stratospheric clouds (PSCs) can form which have highly complex compositions but have been shown to contain a large quantities of ice. These clouds can act as catalysts for the processes which are involved of the depletion of the ozone layer [10]. The importance of these processes was highlighted by the award of the 1995 Nobel Prize for chemistry to P. J. Crutzen, M. J. Molina and F. Sherwood Rowland.

1.4 Ice in space

When astronomers refer to ice they are referring not just to solid water but to complex mixtures of volatile compounds such as ammonia, carbon monoxide, carbon dioxide, methane and nitrogen, which are common in the low-temperature regions of the Solar System and are also believed to be constituents of the interstellar dust [1]. The largest quantities of ice in the Solar System are found in the moons of the planets from Jupiter outwards, which have densities that are far smaller than the Earth's moon and are as such believed to be composed of ice together with a small amount of silicate rock [11]. It is believed these planets formed by the aggregation of material in the nebula that initially surrounded each of the planets and that the volatile materials, which make up these planets would only condense in the cooler parts of the Solar System - i.e. those parts at a large distance from the sun. The moons formed in this way would initially consist of a homogenous mixture of ice and rock, which for the larger of these planets, slowly evolved into a planet with a rocky core surrounded by ice - the temperature required to undergo this process being provided through tidal friction as the rotation of the satellite is brought into

synchronism with its orbital motion so that the same face is presented to the planet at all times.

Modelling the internal structure and temperature distribution of moons composed of ice and rock is fundamentally dependent on the the properties of ice, ice mixtures or clathrates which are present in the unusual conditions present in these bodies [1]. It is possible to establish the pressure in the interior of these planets by modelling them as uniform spherical bodies and thus to use lab based experiments on ice and clathrates to obtain information on what will be present at the deep parts of these planets. For large bodies an analysis of this sort [1] shows that at the centre of the planet one is well into the pressure regime when ice VII becomes the most stable ice phase. Thus one would expect the core of the planet to be composed of ice VII, while at the surface ice Ih would be dominant. In between these two extremes all the lower pressure ice phases would be expected to be observed and the coexistence of all these phases would be expected to have interesting geophysical effects, which may cause the fracturing of the surface.

In the initial condensation of these ice planets the temperature would have been so low that amorphous ice would have grown [1]. This would have subsequently converted to ice Ic with the release of considerable heat. Ice Ic is metastable so would it eventually undergo further phase transitions which would also release heat, all of which would greatly effect the heat balance of the evolving moon. It is thus important to understand the enthalpy of transition between the various ice phases in order to understand the evolution of these planets. It is also important to understand the mechanical properties of the various ice phases as the heat generated by the phase transitions may cause internal convection and the extrusion of ice from the interior of the planet to the exterior in volcanic-type processes. The likelihood of these processes and their rate is going to be controlled by the rate at which the ice can flow and convert from one phase to another.

Finally, comets are believed to be composed of an aggregate of frozen gasses

and stony material [1]. These entities have a highly eccentric orbit about the sun, spending the majority of their time at great distances from it. For short periods of time however they become visible as they come near to the sun and get heated by solar radiation, which causes then to emit vapours and dust. Comets form at low temperatures and as such the ice within them, when they are initially formed, is expected to be amorphous. An interesting question is thus: how much does their interior become consolidated or transformed to ice Ic, ice Ih or clathrate hydrates?

1.5 Clathrates Hydrates

Clathrate hydrate materials consist of a three dimensional framework of hydrogen bonded water molecules within which are incorporated small numbers of relatively inert "guest" molecules, like O_2, H_2, N_2, CO_2, CH_4, H_2S, Ar, Kr, Xe and some hydrocarbons [12]. These "compounds" are not formed by chemical reactions, because there is no chemical interaction between the framework and guest, but instead are formed during first order phase transitions. As already mentioned clathrate hydrates occur in the universe, where there are mixtures of volatile gasses and water. In particular clathrate hydrates are believed to be present in the outer parts of proto-planetary nebulae and it has been suggested that they are responsible for the volatile enrichment, with respect to the Solar abundances, observed in the four giant planets of the Solar System [13]. It is believed that near where these planets were later formed volatiles were trapped in the form of hydrates and incorporated into planetesimals, which are the smallest bodies that can be attracted into a protoplanet's feeding zone by the force of gravity. Clathrate hydrates are still present in the modern day Solar System, one of the most striking examples being, in the southern parts of Saturn's moon Enceladus where there is geyser activity which is believed to occur as a result of carbon dioxide, methane and nitrogen being released from clathrate hydrates, which have been exposed to the vacuum of space by fractures in the surface of the planet [14].

Hydrocarbon clathrate hydrates are also found on Earth in the permafrost regions and on the seafloor. These structures are believed contain significant amounts of methane and as such may be a future energy source. Of greater concern is the fact that, if these compounds were to decompose they would release vast quantities of methane into the atmosphere with atmospherically devastating consequences, as CH_4 is a greenhouse gas. However, CO_2, another greenhouse gas, forms a hydrate that is potentially more stable than methane hydrate, which suggests that clathrates could be used to capture CO_2 and store it in a solid form that could be disposed of in a landfill site [15].

Ice's importance in the universe is unquestionable and, as the previous sections have highlighted, there is a need for a better understanding of the surface structure of ice, the mechanisms by which ice undergoes its phase transitions and the processes by which ice deforms and flows. Computer simulation provides tools that will aid in the understanding of all these phenomena and can thus greatly enrich our understanding of phenomena ranging from critical reactions in Earth's atmosphere to the processes which took place in the birth of the Solar System.

Bibliography

[1] V. F. Petrenko and R. W. Whitworth. *Physics of ice.* OUP, (1999).

[2] B. Michel and R. Ramseier. *Canadian Geotechnical Journal*, **8**, 36 (1971).

[3] I. Sunagawa. *Crystals, Growth, Morphology and Perfection.* Cambridge University Press, (2005).

[4] S. Piana and J. D. Gale. *J. Am. Chem. Soc.*, **127**, 1975 (2005).

[5] A. M. Walker. *Computational studies of point defects and dislocations in forsterite and some implications for the rheology of mantle olivine.* PhD thesis, Univeristy College London, (2004).

[6] N. Bjerrum. *Science*, **115**, 386 (1952).

[7] J. W. Glen. *Physik der Kondensierten Materie*, **7**, 43 (1968).

[8] J. P. D. Abbatt. *Chem. Rev.*, **103**, 4783 (2003).

[9] P. Hobbs. *Ice Physics.* Clarendon Press, Oxford, (1974).

[10] M. J. Molina. *Angewandte Chemie International Edition*, **35**, 1778 (1996).

[11] D. Rothery. *Satellites of the outer planets.* Clarendon Press, Oxford, (1992).

[12] G. A. Jeffrey. *Inclustion Compounds volume 1*, chapter Hydrate Inclusion Compounds. Academic Press, (1984).

[13] F. Hersant, D. Gautier and J. Lunine. *Planetary and Space Science*, **52**, 623 (2004).

[14] S. W. Kieffer, X. L. Lu, C. M. Bethke, J. R. Spencer, S. Marshak and A. Navrotsky. *Science*, **314**, 1764 (2006).

[15] P. M. Rodger. *Issues underlying the feasibility of storing CO_2 as hydrate deposits.* PH3/25, International Energy Agency, GreenHouse Gas programme, (2000).

Chapter 2

The Phases of Ice

Water and ice have countless anomalous properties, which include: its expansion on freezing, its maximum in its density at $\sim 3.5\,^{\circ}\mathrm{C}$ and its very high dielectric constant. Furthermore, ice has a complex phase diagram with at least 15 solid crystalline phases. What is most remarkable about water though is that all this complexity arises from molecules that consist of only two hydrogen atoms and one oxygen. Although these remarkable properties may be attributed to the fact that water molecules form hydrogen bonds this observation does not do justice to the quantity of research [1, 2, 3, 4] into water and ice's structure and properties. What it does though is give a starting point from which a more profound understanding can be obtained.

2.1 Hydrogen bonds and the structure of ice

In all known ice phases, every oxygen atom sits at the centre of a tetrahedron of hydrogen bonds. Furthermore, in all but ice X (the phase formed at the highest experimentally attainable pressures) the molecular nature of the water molecules is retained - meaning that on the hydrogen bonds the hydrogen atom does not lie on the centre of the bond and that about one oxygen two of the hydrogen atoms are displaced towards the central oxygen and two displaced away. This arrangement is

shown schematically in figure 2.1:

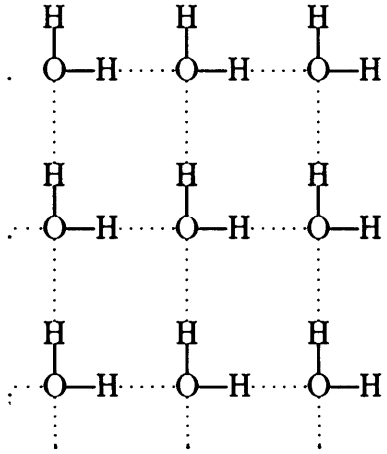

Figure 2.1: Diagram showing schematically one of the Bernal-Fowler allowed hydrogen bonding topologies. Each oxygen atom donates and accepts two hydrogen bonds.

Any structure of ice may be thought of as a 4 connected net with the oxygen atoms lying on the vertices of the net and the hydrogen atoms lying on the edges. This is much like SiO_2 [5] which can be thought of as a net of four connected silicon atoms. Unlike silica however the bonds holding together oxygen atoms in ice are hydrogen bonds, which are far weaker than the covalent Si-O-Si bonds that hold silica together.

Another important difference between the structure of ice and that of silica is the fact that the hydrogen atoms do not lie on the centre of the hydrogen bonds (the oxygen atoms lie equidistant from the two silicas that make up the Si-O-Si bond). Thus in x-ray and neutron diffraction studies of certain ice phases one observes 4 possible hydrogen positions for each oxygen atom within the structure. Each of these hydrogen positions is assigned an occupancy of one half so that the correct overall stoichiometry is retained but the hydrogen bonding disorder is described. Bernal and Fowler [1] argued that there were only two constraints on the hydrogen positions and these constraints have been dubbed the ice rules:

1. There is only one hydrogen atom per bond.

2. There are only two hydrogen atoms adjacent to each oxygen.

Pauling [6] hypothesized that "under ordinary conditions the interaction of non-adjacent molecules is not such as to stabilize any one of the many configurations satisfying the above ice rules with reference to the others." From this approximation he then estimated the residual entropy of any ice phase by noting that there are 6^N possible arrangements for all the water molecules (if Bernal-Fowler rule 1 is ignored). Each bond within these possible arrangements will then have one of four possible arrangements, two hydrogen atoms on it, no hydrogen atoms on it and two arrangements with one hydrogen atom on it. As such there is a probability of $\frac{1}{2}$ that each bond is correctly formed. Thus the total number of Bernal-Fowler rule obeying allowed ice configurations, and hence the residual entropy, are given by:

$$W = 6^N \times \left(\frac{1}{2}\right)^{2N} = \left(\frac{3}{2}\right)^N \qquad \Rightarrow S_0 = Nk_B \ln\left(\frac{3}{2}\right) \tag{2.1}$$

2.2 The phase diagram of ice

As already mentioned ice exists in 15 known crystalline forms. Furthermore, it may also have one of a number of different solid amorphous forms [2] and can form solid hydrates when crystallised in the presence of small gas molecules [7]. The phase diagram is shown in figure 2.2. Several metastable phases of ice are known that are not included on this phase diagram (Ic, IV, IX, XII, XIII and XIV) [2].

One of the most important features in the phase diagram is the slope $\mathrm{d}T/\mathrm{d}p$ of the line representing the equilibrium between two phases, which in classical thermodynamics is given by the Clausius-Clapeyron equation [8]:

$$\frac{\mathrm{d}p}{\mathrm{d}T} = \frac{\Delta S}{\Delta V} \tag{2.2}$$

Where ΔS is the difference in the entropies of the two phases and ΔV is the differences between the volumes. On the phase diagram for some of the phase

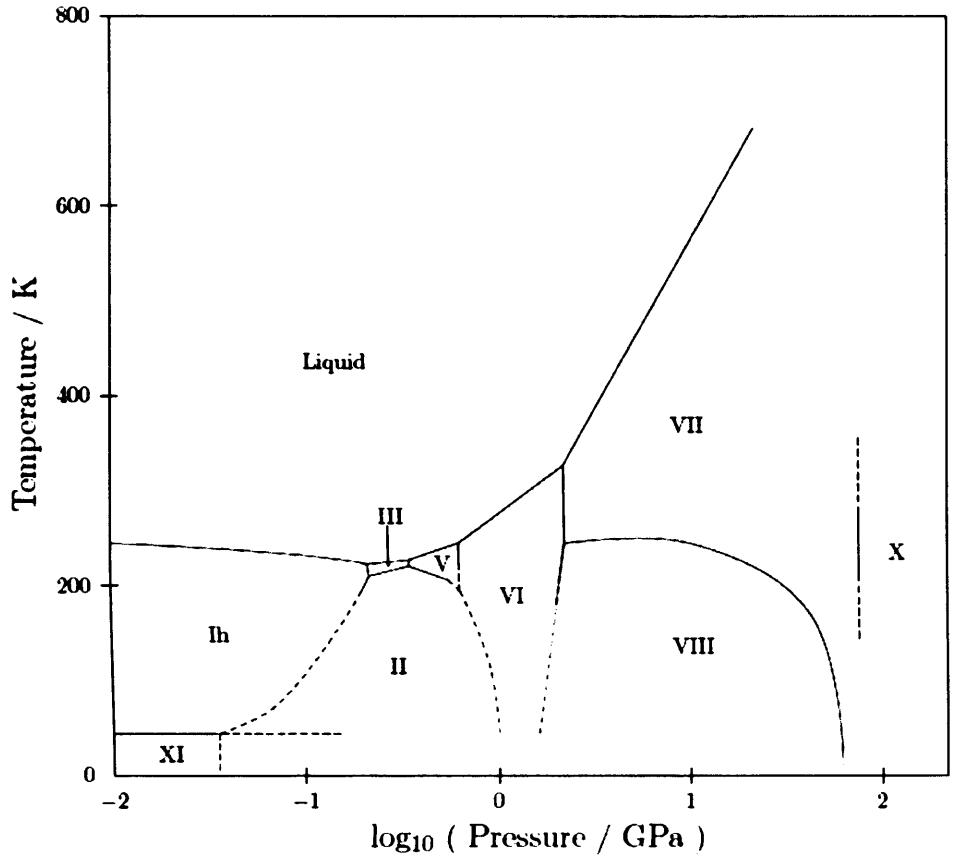

Figure 2.2: The phase diagram of water ice (copied from [2]). Dotted lines show phase boundaries that have been extrapolated

boundaries the boundary line is almost vertical (eg. Ice V $\rightarrow$ VI), suggesting that ΔS is zero for these transitions. Given that the entropy of any given ice phase can be thought of as consisting of two components, the vibrational entropy (which is the smaller of the two contributions) and the contribution due to proton disorder, these vertical phase boundaries can be understood to result from transitions in which there has been no loss of proton disorder. For any sloped boundaries meanwhile, there is either a reversion to a proton disordered solid as one crosses the phase boundary or a loss of proton disorder.

Whether a phase is proton ordered or disordered provides a very useful way of classifying the known ice phases. In fact, the majority of proton ordered phases have a corresponding proton disordered phase as is shown in table 2.1. These ordered and disordered phases have the same underlying oxygen network but different arrangements of hydrogen atoms - in the ordered form the arrangement of hydrogen

Proton disordered form	Proton ordered form
Ice Ih	Ice XI
-	Ice II
Ice III	Ice IX
Ice IV	-
Ice V	Ice XIII
Ice VI	-
Ice VII	Ice VIII
Ice VII	Ice XIV

Table 2.1: The known ice disordered ice phases and their corresponding ordered phases.

atoms is periodically repeated throughout the structure.

Phase transitions in ice can be classified as either those that change the oxygen network or those that do not change the oxygen network but result in the hydrogen positions becoming ordered. These two types of transition are dealt with in more depth in the next few sections.

2.3 Order-disorder phase transitions

When one applies an electric field to a disordered phase of ice 3 distinct processes occur [2]:

1. The individual molecules are polarised by the field.

2. The ice is polarised by the reorientation of molecules or bonds.

3. If suitable electrodes are present a current flows through the ice.

The first of these phenomena involves displacement of electrons and small distortions of the nuclear positions. All materials exhibit this sort of response to an electric field. These second two effects are more interesting however and are due to structural features that are unique to ice. Any current one observes in ice is not due to the motion of electrons through the system, but is instead due to the motion of protons. It is difficult to comprehend how this may occur in ice because the protons

are bound by relatively strong hydrogen bonds to their lattice sites. Furthermore, the only way to change the proton topology and maintain a structure that obeys the Bernal-Fowler rules is to reverse the directions of all the hydrogen bonds in a 6-membered ring [2]. This process would have a huge activation barrier however and would also not change the polarisation of the ice sample and thus not explain the observed polarisation of the lattice that occurs when one applies an electric field.

The protonic conductivity of ice is thus attributed to the motion of hydrogenic defects through the lattice [2]. There are four types of hydrogenic defect - the two protonic defects OH^- and H_3O^+, the Bjerrum D-defect, which consists of two hydrogen atoms on a hydrogen bond, and the Bjerrum L-defect, no hydrogen atoms on a hydrogen bond. These defects can move through the lattice and thus give rise to the observed conductivity. Furthermore, as they move about the hydrogen bonding topology will change, which explains how the ice can be polarised by the reorientation of molecules.

Ice not in an electric field will also contain these defects but now rather than moving about in a correlated way they move randomly about the lattice changing the hydrogen bonding topology as they go. The hydrogen bonding topology of a disordered ice phase is thus not a constant

At low temperatures some ice phases (eg. ice VII) will no longer show polarisation by the reorientation of molecules or bonds on application of an electric field. This suggests that at these low temperatures the hydrogen bond topology becomes locked in. Part of the reason for this is that at low temperatures there is not the energy to sustain the Bjerrum defects but there is also a thermodynamic reason for this phenomenon. The third law of thermodynamics states that for any material with a non degenerate lowest energy structure the entropy at 0 K is 0. Furthermore, statistical mechanics shows that, in the microcanonical ensemble, the entropy is equal to the logarithm of the weight function - i.e. it is related to the number of states the system may occupy. As already discussed in section 2.1, Pauling [6]

showed that because there are a large number of hydrogen bonding configurations which satisfy the Bernal-Fowler ice rules ice has a residual entropy. By the third law though the system must not be able to access all these different hydrogen bonding topologies at low temperatures unless they all have the same energy - in other words at low temperatures there must be some phase transition which removes the entropy due to proton disorder.

Computer simulations [9, 10] have shown that different proton topologies, of a given oxygen network, are not degenerate and hence that proton disorder arises because there is a Boltzmann distribution of hydrogen bonding topologies. At low temperatures one would expect only the lowest energy hydrogen bonding topology will be energetically accessible, which will result in the required loss of proton disorder. This is precisely what is observed in the proton ordering phase transitions highlighted in table 2.1. So for instance for ice VII the structure of ice VIII has the same oxygen network as ice VII but now the hydrogen atoms are all locked into one topology. Currently there are 5 known proton ordering phase transitions and based on the structure of the phase diagram it is believed that it should be possible to isolate a proton ordered form of ice VI.

2.3.1 Graph Invariants

A unique, and somewhat overlooked, method for testing any water potential or quantum mechanical recipe is to see if it correctly predicts the structure of the proton ordered forms of ice phases. One could simulate these transitions directly using low temperature Monte Carlo simulations, which exploit some proton topology changing move (like the method advocated by Rick [11]), and start from a disordered proton topology. This disordered topology would then change to an ordered one over the course of the simulation. A simulation like this would be computationally expensive however and is, as such, not commonly advocated in the literature [9, 10]. Instead theorists assume that it will be possible to describe the structure of the ordered form

using the unit cell of the disordered form. Using this assumption, the problem then becomes one of enumerating all symmetry distinct structures of this small cell and calculating their energies. The hydrogen bond topology with the lowest energy will, most likely, correspond to the structure of the ordered form.

This enumeration of all symmetry distinct topologies for a given unit cell is a far from simple problem. Until recently it was undertaken by determining all hydrogen bonding topologies allowed by the Bernal-Fowler rules and examining the resulting structures by eye to identify identical topologies [12]. Recently a new methodology for enumerating hydrogen bonding topologies has been developed by Kuo *et al.* [9, 13, 14]. This method starts by recognising that any hydrogen topology can be represented by a diagraph, *i.e.* a graph in which all the vertices of the graph (oxygen atoms) are linked by "bonds" which have a direction (in the case of ice from hydrogen bond donor to acceptor). If one numbers the oxygen atoms in the unit cell, one can then describe the hydrogen bonding topology using a list of pairs of ordered "oxygen numbers" (the order representing the direction).

The difference between a graph and a diagraph is simply that in a diagraph the bonds have a direction. Thus for any graph with N bonds there are 2^N possible diagraphs that would exist if the direction of bonds did matter (as each bond can point in two possible ways). Rather than specify all these diagraphs manually it is useful, for both enumeration and storage purposes, to define one particular diagraph as the canonical orientation. Other diagraphs are then represented by binary strings in which each bit, or bond variable in the notation of Kuo *et al.*, refers to whether or not a particular bond points in the same direction in the diagraph of interest and the canonical orientation. Enumerating all the possible diagraphs of an underlying graph in this way will always give hydrogen bonding topologies that obey Bernal and Fowler's requirement that every hydrogen bond have one hydrogen. However, it neglects Bernal and Fowler's requirement that each oxygen donates and accepts two hydrogen atoms. Nevertheless this method of specifying hydrogen bonding

topologies is invaluable.

Kuo *et al.* [9, 13, 14] have exploited the representation of hydrogen bond topologies as diagraphs further in order to distinguish symmetry distinct hydrogen bonding topologies. They showed that if one generated the canonical orientation in such a way that it belonged to a very high symmetry space group one could apply a projection operator, of the totally symmetric representation of the group, to the bond variables and generate an even more compact representation of the hydrogen bonding topologies. These "graph invariants" are given by:

$$I_{ij..l} = C_{rs...u} \sum_{\alpha} g_{\alpha}(b_r b_s ... b_u) \tag{2.3}$$

The order of these invariants is the number of bond variables used in their generation and this goes from 1 to the number of bonds in the unit cell. The great advantage of this representation is the ease with which structures can be compared - if any structures have the same values for the invariants then they are symmetrically identical. There are as many invariants for a structure as there are hydrogen bonds but one need not generate all the possible invariants because two symmetrically distinct structures will have different values for their second order invariants, which renders the third and higher order invariants redundant.

Kuo *et al.* [9], based on earlier work which suggested that the energy of an oxygen topology can be fitted to a quantity that describes the local geometry, showed that the total energy can be fitted to a linear combination of the graph invariants. Unlike prior work though, this sum can be tuned so that longer ranged structural features can be described. However, in all the phase transitions they have studied (ice Ih[9], ice VII [9, 15] and ice III [16]) the variation of total energy with proton topology is adequately described by invariants that describe the relative orientations of bonds separated by, at most, a single hydrogen bond.

2.4 Classifying Oxygen Nets

As already discussed, the oxygen atoms in an ice structure sit on tetrahedral sites connected to four other oxygen atoms via hydrogen bonds. This is analogous to the situation in siliceous and zeolitic structures but oxygen atoms replace the silicon and aluminium atoms, so that the Si-O-Si, Al-O-Si and Al-O-Al bonds are replaced by hydrogen bonds. There are many more zeolitic structures than there are ice phases and it has proved useful to classify the various silica structures using language from the theory of 4-connected nets [17]. A 3-dimensional net can be represented by a graph which lists what vertices (oxygen atoms in the case of ice) are linked together by edges (hydrogen bonds). However, there are multiple ways one can number the vertices and edges and as such multiple ways that the topology of the net can be described. To get round this problem, it is useful to introduce the Schläfli symbol and coordination sequence which provide a partial characterisation of the topology of a net [5]. These are discussed in more detail in the sections that follow.

More important than the Schläfli symbol and coordination sequence though is the overall symmetry of the net. From crystallography it is known that any 3D periodic structure must belong to one of the 230 space groups. Furthermore, if one knows the symmetry of the net it is possible to show that vertices and edges lie on points that are symmetrically non-distinct. As such it is possible to specify the network by specifying the coordinates of a small number of the vertices and generating the remaining vertex positions using the symmetry of the unit cell. Obviously, what vertices the edges connect drop out of this treatment and symmetrically equivalent vertices will have the same Schläfli symbol and coordination sequence due to the symmetry of the cell. This allows networks to be specified simply - for the clathrate structure sII (see section 2.6) it is possible to show that there are only 3 symmetry distinct vertices amongst the 136 vertices in the unit cell.

2.4.1 Schläfli Symbols

As already mentioned a 3-dimensional infinite net can be considered as a infinite periodic graph [5]. In graph theory a *path* is defined as continuous sequences of edges and a *circuit* is defined as a closed path. It proves useful, in the context of discussing nets, to introduce the notion of a *ring*. In any 4-connected net the 4 edges that meet at a vertex define six angles and for an angle at vertex, A, defined by edges 1 and 2 there are an infinite number of circuits starting at A that begin by traversing edge 1 and finish by traversing edge 2. The shortest such circuit associated with each angle is termed a *ring* and so at each vertex there are 6 such rings, corresponding to each of the six angles at the vertex. The size of each of these rings, specified by the number of edges in them, is termed the Schläfli symbol of the vertex. Where there are multiple paths of the same length that one can take though the structure the number of equivalent length paths is specified by a subscript in the Schläfli symbol.

A net in which all the symmetry non-distinct vertexes have Schläfli symbols for which all the subscripts of the ring sizes are 1 is termed a simple tiling. The structures of these simple tilings can be decomposed into a space-filling set of face-sharing polyhedral cages, so called polyhedral tiles. The shapes of these polyhedral tiles can then be described using a symbol that describes the number of faces with a particular number of edges, so for instance a tetrahedron is a 3^4 polyhedron as all 4 faces have 3 edges. This description of the net as a number of linked polyhedra has proved extremely useful - Zwijnenburg *et al.* [18] has shown that, for simple tilings, the energy of a silica phase is a function of the average and standard deviation of the sizes of the faces of the constituent polyhedra. Furthermore, thinking of nets as linked polyhedra proves useful in visualising the nets and determining the relationships between similar nets.

2.4.2 Coordination Sequences

The second way to describe the topology of the net is to use the coordination sequence of each symmetry distinct vertex. The first number in the coordination sequence is the number of vertices attached to the central vertex. The second is then the number of vertices for which the shortest path back to the central vertex consists of 2 edges, third is the number of vertices for which the shortest path back to the central vertex consists of 3 edges and so on. In general the k^{th} number in this sequence is the number of vertices for which the shortest path back to the central vertex consists of k edges and the coordination sequence is usually given up to k=10. The coordination sequence is useful as, for some nets (eg diamond and lonsdaleite), the Schläfli symbols are identical even though the two nets are not the same.

2.5 The Phases of ice

Re-examining the phase diagram in figure 2.2 it is possible to see that structure of the oxygen network is chiefly controlled by the pressure applied to the system. Ice Ih, the form of ice observed at atmospheric pressure, is a very open structure, while all other ice phases have denser packings of the water molecules. When ice is compressed the hydrogen bonds within it are shortened, which results in an increase in density. However, this shortening of the hydrogen bonds has an energetic cost and when this gets too large a phase transition to a structure of higher density occurs. In these higher pressure phases the water molecules are packed more densely but the hydrogen bond lengths have similar values to the hydrogen bond lengths in ice Ih. This is achieved, for those phases that lie in the centre of the phase diagram (II,III,IV,V,XII), by forming a structure in which the oxygen tetrahedra are distorted and the hydrogen bonds are non-linear. The high pressure phases (VI,VII) meanwhile, have structures consisting of interpenetrating nets of water molecules and, in the case of ice VII, close contact between non-hydrogen bonded

oxygen atoms.

In the following sections the structures of the various proton disordered phases of ice are discussed. In all cases, except for ice II, the nature of the proton ordered form, if known, is discussed in a subsection.

2.5.1 Ice Ih

Ice Ih is isostructural to the rare form of diamond, Lonsdaleite and the dense silica phase tridymite [5]. The oxygen network in this structure is shown in figure 2.3(a) and its unit cell parameters, oxygen coordinates, Schläfli symbol and coordination sequence are given in table 2.2.

Ice Ih	Hexagonal $P6_3/mmc$ a = 4.518 Å c = 7.356
Vertices in 4 f	±(1/3,2/3,z ; 2/3,1/3,1/2+z), z=1/16
Schläfli symbol	6_2 6_2 6_2 6_2 6_2 6_2
Coordination sequence	4 12 25 44 67 96 130 170 214 264

Table 2.2: Structural details for the lonsdaleite net, which is isostructural to the ice Ih structure.

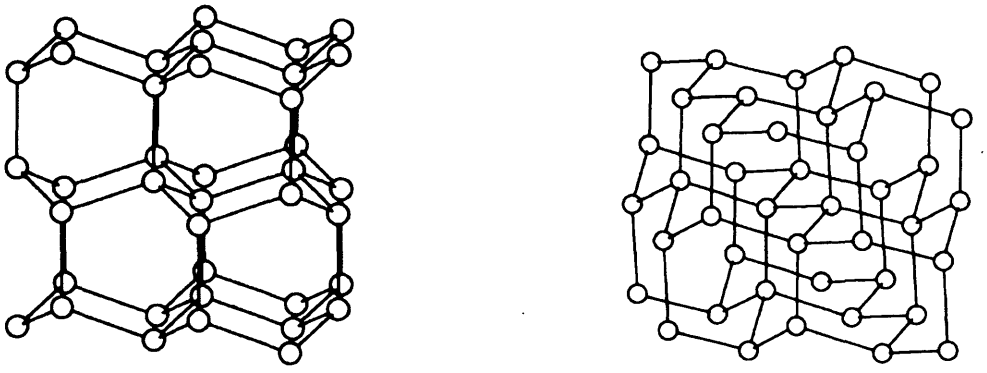

(a) Ice Ih (Lonsdaleite Net)

(b) Ice Ic (Diamond Net)

Figure 2.3: The structures of ice Ih and ice Ic.

Ice Ih is the most stable phase of ice at atmospheric pressure and as such is the most prevalent phase of ice in the atmosphere. Its structure was first studied with x-ray diffraction experiments by Dennison [19] and later a structure was proposed by Bragg [20]. Barnes [21] later confirmed Bragg's suggested oxygen positions by performing single crystal x-ray diffraction. The locations of the hydrogen atoms

(namely that they do not lie on the centres of the hydrogen bonds) was only fully solved with the advent of neutron diffraction and the experiments of Wollan *et al.* in 1949 [22]. Although Raman spectroscopy [2], prior to this date, had shown that the molecules must still be intact in the ice structure.

2.5.1.1 Ice XI

Ice XI has an orthorhombic $Cmc2_1$ structure and is the proton ordered form of ice Ih. The transition from ice Ih to ice XI occurs in doped ice Ih, and has never been observed in pure ice. Ice XI was first discovered by Kawada [23], who noticed that the dielectric permittivity of KOH doped ice became very small below about 70 K and that there was evidence of a latent heat, seen as a plateau in the temperature-time graph as the doped ice was warmed through this temperature. More precise calorimetric experiments [24, 25] were performed later and it was shown that the entropy change associated with the transition was dependent on the level of doping and the time taken to anneal the sample below the transition temperature. This all suggested that full conversion to ordered ice Ih never occurs and as such the entropy change is a function of the degree of conversion achieved. The structure of ice XI proved difficult to determine as the experimentally observed structure is a mixture of the ice Ih structure and the ice XI structure. The structure was finally determined by Line, Whitworth and Jackson *et al.* [26, 27] and is shown in figure 2.4.

As shown in figure 2.4 all bonds parallel to the c-axis are oriented in the same direction, which means that the ordering is ferroelectric along this axis. In the (001) layers that lie perpendicular to the c-direction the water molecules are all aligned ferroelectrically however adjacent layers are aligned anti-ferroelectrically, so that there is no overall dipole along the a and b directions. Adjacent (001) layers are displaced in opposite directions in a distortion of the lattice that is allowed by symmetry.

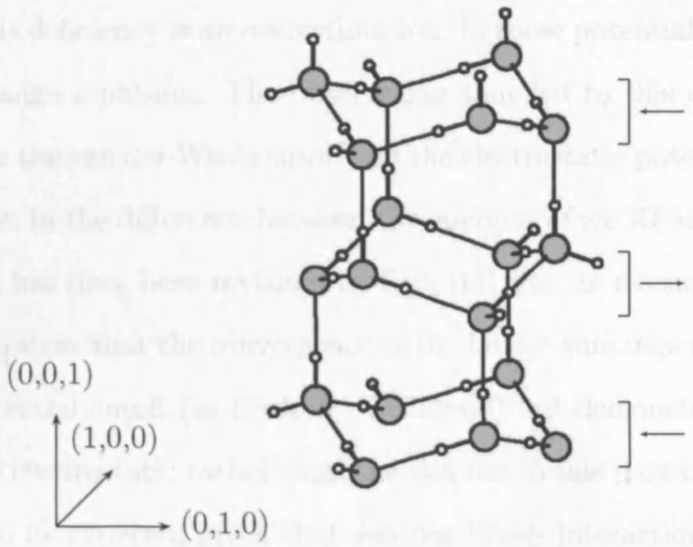

Figure 2.4: The orthorhombic $Cmc2_1$ crystal structure of ice XI. The arrows on the right indicate the directions of small displacements of the layers.

It has proved very difficult to determine the structure of the ordered form of ice XI using theoretical methods. Bjerrum [28, 29] was the first to take on this problem; he noted that, within the structure of ice, neighbouring water molecules may take one of the four possible orientations shown in figure 2.5. He then suggested that the ordered form will have the molecules arranged in such a way that the structure has only trans configurations of neighbouring water molecules. In this structure he proposed suprafacial repulsions between hydrogen atoms will be minimised.

(a) h-cis (b) h-trans (c) c-cis (d) c-trans

Figure 2.5: Possible hydrogen bonded dimer configuration in ice Ih

The Bjerrum structure however is not the structure of ice XI - ice XI has only h-cis and c-trans configurations of neighbouring water molecules. Furthermore, Buch *et al.* [30] and Hirsch and Ojamäe[10] have shown that many of the common interatomic potentials predict that Bjerrum's structure will be lower in energy than the true structure of ice XI. This highlights a major deficiency in the ability of these methods to predict structure versus energy relationship with any precision. Buch *et al.* [30]

believe this deficiency is an overestimation, in these potential models, of the amount of short-range repulsion. The observation that led to this conclusion was that an increase in the van der Waals cutoff and the electrostatic potential cutoff gives rise to a reduction in the difference between the energies of ice XI and Bjerrum's structure. This work has since been revisited by Rick [11] who, in essence, refined the approach of Buch to show that the convergence of the lattice sum depends strongly on the size of the potential cutoff (as Buch *et al.* showed) but demonstrated that the problem lies in the electrostatic rather than the van der Waals part of the potential. This is perhaps to be expected given that van der Waals interactions have a much steeper distance dependence than electrostatic forces.

Kuo *et al.* [9, 14] have used graph invariants to enumerate all possible proton topologies for a 8 molecule unit cell of ice XI. They then used these invariants to fit an expression for the dependence of the total energy on the hydrogen bonding topology. The total energies were calculated using DFT, which correctly predicts the ice XI structure as the lowest energy hydrogen bonding topology. Hirsch and Ojamäe [10] performed calculations on the 16 hypothetical unit cells, obtained by Kuo *et al.* [9, 14], using the local orbital based code, $DMol^3$ with the BLYP functional and plane-wave based CASTEP [31] program with the PW91 functional. Again the structure of ice XI was found to be lowest energy structure. Finally, Cassasa [32] have performed periodic Hartree-Fock theory calculations on Bjerrum's structure and found that the true ice XI structure lies lower in energy.

2.5.2 Ice Ic

Ice Ic, also designated cubic ice, is a metastable variant of ice Ih in which the oxygen atoms are arranged in the diamond net and is isostructural with the dense silica phase cristobalite. The oxygen network in this structure is shown in figure 2.3(b) and its unit cell parameters, oxygen coordinates, Schläfli symbol and coordination sequence are given in table 2.3.

Ice Ic	Cubic Fd3m a = 6.358 Å
Vertices in 8 a	±(1/8,1/8,1/8)
Schläfli symbol	6_2 6_2 6_2 6_2 6_2 6_2
Coordination sequence	4 12 24 42 64 92 124 162 204 252

Table 2.3: Structural details for the diamond net, which is isostructural to the ice Ic structure.

As can be seen from tables 2.3 and 2.2 the Schläfli symbols for lonsdaleite and diamond are the same. In fact the difference between these two nets is only visualisable when one takes the 3rd value in the coordination sequence into account.

Cubic ice was first identified by König [33], in experiments on vapour deposited ice layers. Later experiments have shown that ice Ih is formed above 150 K, cubic ice between about 130 K and 150 K and below 130 K the deposited layer is amorphous [34]. Furthermore, if ice II and IX are recovered in liquid nitrogen and subsequently warmed they converted to cubic ice at 120-170 K before reverting to ice Ih at about 200 K [35]. On conversion of ice Ic to ice Ih 13 - 50 J mol^{-1} is released [36], there is no sharp transition though and ice Ih never converts to ice Ic on cooling, suggesting that ice Ic is always metastable. Neutron diffraction has confirmed that cubic ice is hydrogen disordered [37] and also that ice Ic is highly defective [38], with numerous glide type stacking faults. There is some theoretical evidence that in small clusters of ice the structure is that of ice Ic [39] and that ice Ih may nucleate via ice Ic [40] and hence that ice Ic may be present in the atmosphere.

2.5.3 Ice II

Ice II is a phase of ice that forms at intermediate pressures - it is unique amongst ice phases because it is the only one which is proton ordered at all temperatures. It is prepared by compressing ice Ih at -60 to −80 °C or by decompression of ice V at −30 °C. The structure is shown in figure 2.6 and has the unit cell parameters, oxygen coordinates, Schläfli symbol and coordination sequence given in table 2.4:

This structure was determined using neutron diffraction by Kamb *et al.* [41] and

Ice II	Rhombohedral R3 a = 7.78 Å $\alpha = 113.1°$
6 at f	±(x,y,z ; z,x,y, ; y,z,x) x=0.5225 y=0.2516 z=0.6707
6 at f'	±(x,y,z ; z,x,y, ; y,z,x) x=0.0204 y=0.8513 z=0.2681
Schläfli symbol	6 6_2 6 6_2 6 8_4
Coordination sequence	4 12 29 58 88 124 169 222 280 346 419 500 586

Table 2.4: Structural details for ice II.

Figure 2.6: The ice II structure in [001] projection. Large grey spheres show oxygen positions, while the smaller white ones are the hydrogen positions.

is consistent with the structure inferred from x-ray diffraction [42]. It consists of roughly co-planar 6 membered rings connected by a more complex arrangement of smaller rings, which no longer allows rings in adjacent layers to be aligned to form hexagonal channels like in ice Ih. In the net there are two distinct vertex types and hence two different environments for water molecules, in which the water molecules have HOH angles of 103.2° and 107.6°. Because there are two non-equivalent water molecules there are four non-equivalent hydrogen bonds, which is reflected in the infrared spectrum, which shows the OH stretch is split into four [43].

The structure of ice II is similar to that of helium hydrate [44], which contains up to two helium atoms per unit cell. These helium atoms are incorporated at sites between the hexagonal rings of water molecules and act to stabilise ice II.

2.5.4 Ice III

Ice III is one of a number of phases of similar density, in the central region of the phase diagram, that are stable over only a narrow range of conditions or which exist only as metastable phases. All the phases known in this region of the phase

diagram have very complex packings of similar densities. This is perhaps the most likely part of the phase diagram in which new phases of ice will be discovered as where structures are simple, as in ice Ih or ice VII, there are considerably fewer possible packings with similar densities [2, 5].

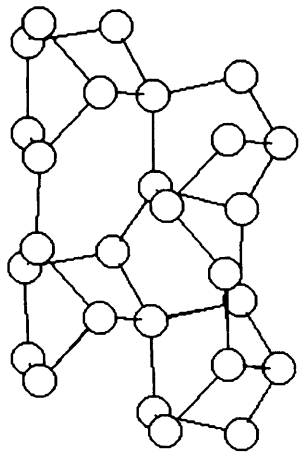

Figure 2.7: The positions of the oxygen atoms, white circles, in the ice III structure shown in the [100] projection.

Ice III itself is the least dense of the high pressure phases of ice. Its structure, which is shown in figure 2.7, was determined by Kamb and Prakash [45], and is isostructural with the dense silica phase keatite [5]. The unit cell parameters, oxygen coordinates, Schläfli symbol and coordination sequence are given in table 2.5.

Ice IIII	Tetragonal $P4_12_12$ a = 6.666 Å c = 6.936 Å
Vertices in 4 a	(0.3926,0.3926,0.0)
Schläfli symbol	$5\ 5\ 5_2\ 7_2\ 8_2\ 8_2$
Coordination sequence	4 12 26 48 76 114 152 206 252 318 382 458 544
Vertices in 8 b	(0.1092,0.3015,0.2858)
Schläfli symbol	$5\ 7\ 5\ 7\ 5\ 7_2$
Coordination sequence	4 12 29 50 82 116 156 202 262 320 395 465 543

Table 2.5: Structural details for ice III.

Dielectric measurements [46] have shown that ice III has a high permittivity which is characteristic of proton disorder and that this falls off between -65 and $-108\,^{\circ}\mathrm{C}$ which suggests that there is a proton ordering transition. However, unlike the ordering transitions in other ice phases, the transition in ice III is gradual. This gradual ordering is possible because the space group symmetry of the disordered

form does not require any the hydrogen bonds to have two symmetrically equivalent hydrogen positions. As such both the ordered form, ice IX, and the disordered form, ice III, have the same space group [47] and all possibilities between full order and full disorder are allowed. What is more, neutron diffraction on ice III suggests that there is some residual order at high temperatures [48].

Kuo and Singer have performed graph invariant calculations on the ice III / IX transitions and have shown that DFT correctly reproduces the structure of the proton ordered form [16].

2.5.5 Ice IV

Ice IV is a metastable form of ice that can be formed from the liquid over most of the pressure range where ice III, V or VI would be prevalent, so long as appropriate conditions are met or a nucleating agent is present [49, 50].

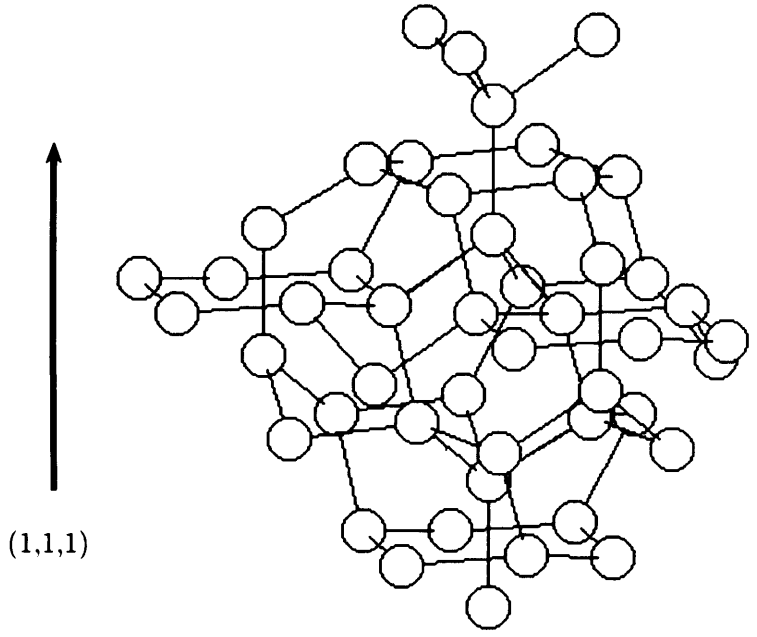

Figure 2.8: The oxygen positions, white circles, in ice IV.

The structure of ice IV, as determined by Endgelhardt and Kamb [51], consists of one continuous oxygen network but some of the hydrogen bonds pass through rings in the network, as shown in figure 2.8. The unit cell parameters, oxygen coordinates, Schläfli symbol and coordination sequence are given in table 2.6:

Ice IV Rhombohedral $R\bar{3}c$ a = 7.60 Å $\alpha = 70.1°$	
Vertices in 4 c	(0.53000,0.53000,0.53000)
Schläfli symbol	$6_2\ 8_2\ 6_2\ 8_2\ 6_2\ 8_2$
Coordination sequence	4 12 31 65 100 141 193 251 319 402 493 584 679
Vertices in 12 f	(0.11960,0.73960,0.61090)
Schläfli symbol	$6\ 6_2\ 6\ 8_3\ 6\ 8_8$
Coordination sequence	4 12 31 65 99 139 191 253 324 402 486 582 683

Table 2.6: Structural details for ice IV.

Ice IV appears to be fully proton disordered [2] and no evidence for a proton ordering transition has been observed.

2.5.6 Ice V

Ice V has a very complex structure that contains four membered rings. Structural data, as determined by Kamb *et al.* [52], are given in table 2.7 and the oxygen positions are shown in figure 2.9:

Monoclinic A2/a a = 9.22 Å b = 7.54 Å c = 10.35 Å $\beta = 109.2°$	
Vertices in 4 e	(0.25,-0.1847,0)
Schläfli symbol	$5_3\ 8_2\ 6\ 6\ 9\ 9$
Coordination sequence	4 12 26 54 92 128 196 236 302 374 466 542 654
Vertices in 8 f	(0.4629,0.0565,0.1544)
Schläfli symbol	$4\ 6\ 5\ 6\ 5_2\ 8_2$
Coordination sequence	4 11 25 56 92 129 189 235 304 384 452 546 651
Vertices in 8 f'	(0.2751,-0.3475,0.2477)
Schläfli symbol	4 6 6 8 8 9
Coordination sequence	4 11 26 53 93 134 180 245 299 378 460 549 642
Vertices in 8 f"	(0.3993,0.3596,-0.0146)
Schläfli symbol	$4\ 8\ 4\ 8\ 5\ 8_2$
Coordination sequence	4 10 23 50 90 131 177 240 305 379 459 538 636

Table 2.7: Structural details for ice V.

Dielectric measurements indicate that ice V is proton disordered [53].

2.5.6.1 Ice XIII

There was evidence from neutron diffraction [54, 48], Raman spectroscopy [55] and calorimetry [56] that partial ordering of ice V occurs at low temperatures. Further-

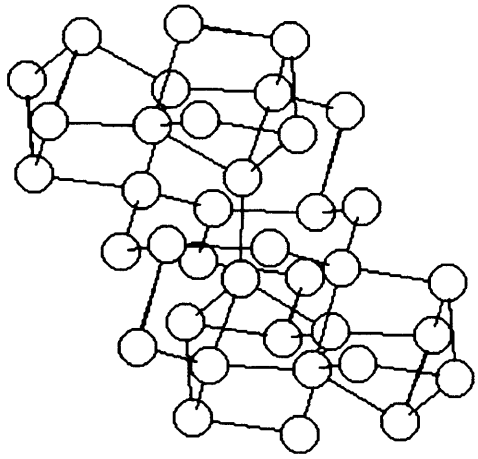

Figure 2.9: The oxygen positions, white circles, in ice V. The structure is shown in the [010] projection.

more, the rate of ordering is enhanced by doping with KOH but until recently it was thought that the third law of thermodynamics could be satisfied by transformation of ice V to ice II at low temperatures. Finney and Salzmann [57] however, have performed experiments with HCl doped ice V and shown that at low temperatures it undergoes a phase transition to a proton ordered form, ice XIII.

2.5.7 Ice XII

Ice XII is a metastable phase of ice that exists within the region of stability of ice V. It was first identified by Lobban *et al.* [58] who also determined its structure using neutron powder diffraction of D_2O. This structure is shown in figure 2.10 with the details given in table 2.8.

Ice XII Tetragonal $I\bar{4}2d$ a = 8.304 Å c = 4.024 Å	
Vertices in 4 a	(0.0,0.0,0.0)
Schläfli symbol	$7_2\ 7_2\ 7_2\ 7_2\ 8_4\ 8_4$
Coordination sequence	4 12 36 66 106 148 202 268 338 420 510 600 714
Vertices in 8 d	(0.3643,0.25,0.125)
Schläfli symbol	$7\ 7_3\ 7_3\ 7_3\ 8\ _4\ 8_4$
Coordination sequence	4 12 36 60 102 150 206 262 340 416 508 604 712

Table 2.8: Structural details for ice XII.

Ice XII also forms as an impurity phase in high-density amorphous ice [59]. It has a simpler structure than ice V but also slightly higher density. This increased

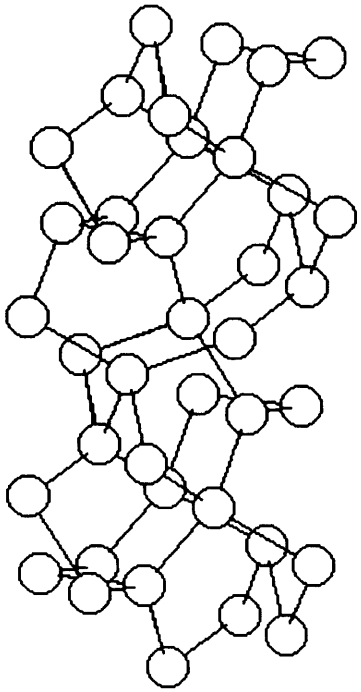

Figure 2.10: The oxygen positions, white circles, in ice XII. The structure is shown in the [001] projection.

density is achieved by distorting the O-O-O angles more than they are distorted in ice V rather than forming interpenetrating lattices. The structure appears to be fully proton disordered.

2.5.7.1 Ice XIV

Finney and Salzmann [57] have synthesised HCl doped ice XII and shown that this undergoes a phase transition to a proton ordered form at low temperatures. This structure however retains some proton disorder as there are partial occupancies on particular hydrogen positions.

2.5.8 Ice VII

Ice VII has a structure that consists of two independent interpenetrating ice Ic sublattices as shown in figure 2.11. The structural details are given in table 2.9, Schläfli symbols will be as for ice Ic because the structure is composed of two interpenetrating ice Ic lattices.

Ice VII	Cubic Pn3m	a = 3.344 Å
vertices in 2a	(1/4,1/4,1/4)	

Table 2.9: Structural details for ice VII.

The structure of ice VII was determined using x-rays by Walrafen *et al.* [60] and using neutrons by Kuhs *et al.* [61]. In it each oxygen has 8 nearest neighbours but is only hydrogen bonded to 4 of these. The hydrogen bonds are longer than they are in ice Ih as the presence of the non-bonded neighbours pushes the structure apart. The neutron data shows that in ice VII the protons are fully disordered and that there is some displacement of oxygen atoms off their sites which seems to be dependent on the local hydrogen bonding topology. There are 2 models for this distortion [61, 62] but both give rise to unphysical features. Kuo and Klein [15] have used DFT to try to understand the structure and have shown that perhaps the best model for understanding the lattice distortions is to allow the two sub-lattices to displace relative to each other in local regions of the structure.

2.5.8.1 Ice VIII

Walley *et al.* [63] showed that the Debye relaxation for ice VII disappeared at low temperature and so discovered the ordered form of ice VII, which they named ice VIII. The transformation from ice VII to ice VIII is easily achieved unlike the transformation from ice Ih to XI and the structure of ice VIII has been determined using neutron diffraction [61]. The structure is shown in figure 2.11 which shows that the hydrogen on the two sub-lattices are ferroelectrically ordered in opposite senses along the (001) direction. As such the structure is overall antiferroelectric.

The reduction in symmetry in going from ice VII to ice VIII allows a small relative displacement of the two sub-lattices in the c-direction, which neutron diffraction has shown is of the order of 0.2 Å. It is distortions like this that Kuo and Klein [15] believe are responsible for the movement of the oxygen atoms off their sites in ice VII.

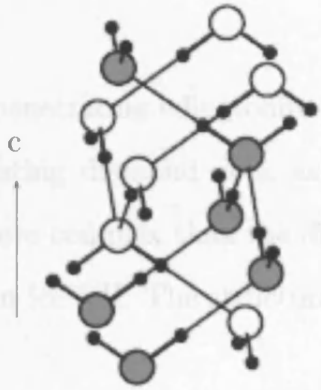

Figure 2.11: The structure of ice VIII, the oxygen atoms of the two interpenetrating ice Ic sub-lattices are shown open and shaded. Unlike in ice VII these two sub-lattices are slightly displaced, the shaded is displaced in the negative c-direction whilst the open one is displaced in the positive c-direction.

Kuo *et al.* [9] have used graph theory to investigate the transition of ice VII to ice VIII. They have shown that DFT correctly predicts the structure of the proton ordered form.

2.5.8.2 Ice X

Hemley *et al.* [64] have shown that the O-O bond length in ice VII falls off roughly exponentially with increasing pressure and that at 8 GPa the O-O bond length in ice VII is the same as that in ice Ih. Similar observations have been made for the O-O bond length in ice VIII, in this structure it is also possible to investigate the O-H bond length, which in contrast to O-O remains stable at 0.972 Å [65, 66]. This observation shows that as the pressure increases the two distinct sites on which a hydrogen atom sits in ice VII get closer and closer together. This begs the question - at very high pressure do the two sites merge and thus does the hydrogen bond become symmetric?

Modelling [67, 68] suggests that at high pressures this phase transition will occur. Furthermore, Raman scattering [69] and Brillouin scattering [70] experiments suggest features which may indicate the presence of a symmetrical ice phase. However, no structural data has yet been attained as it is currently not technically possible to do neutron diffraction experiments at such high pressures [2].

2.5.9 Ice VI

Ice VI consists of two interpenetrating edingtonite (EDI) nets [5], much like ice VII consists of two interpenetrating diamond nets, as shown in figure 2.12. The two EDI nets however, being more complex than the diamond net, avoid the close non-bonded contacts observed in ice VII. The structural details are given in table 2.10 [71]:

Ice VI	Tetragonal $P4_2/nmc$ a = 6.181 Å c = 5.698 Å
Vertices in 2 a	(0.75,0.25,0.75)
Schläfli symbol	$4_2\ 4_2\ 8_4\ 8_4\ 8_4\ 8_4$
Coordination sequence	4 8 18 32 52 74 100 128 162 204 244 286 340
Vertices in 8 g	(0.75,0.5295,0.1339)
Schläfli symbol	$4\ 8_3\ 4\ 8_3\ 4_2\ 8_4$
Coordination sequence	4 9 19 35 52 72 100 131 163 201 244 290 340

Table 2.10: Structural details for ice VI.

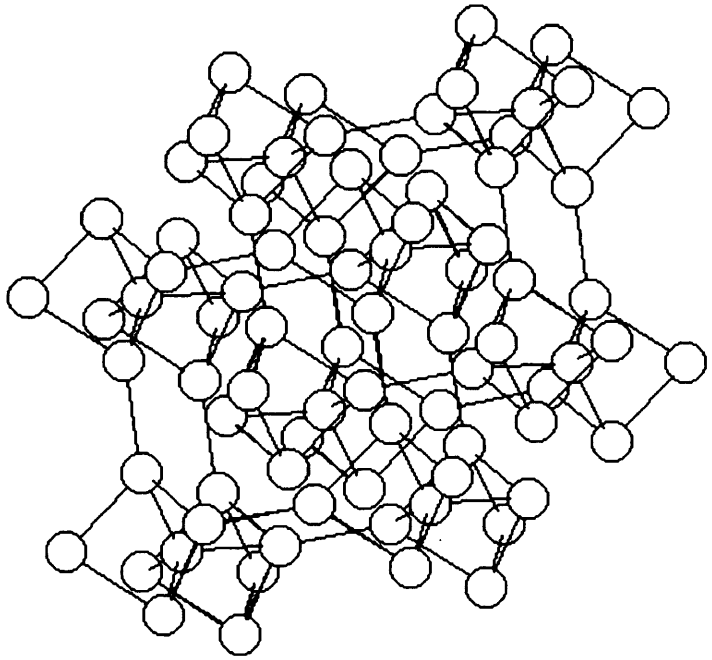

Figure 2.12: The positions of the oxygen atoms, white circles, in the ice VI structure. This structure is shown in the [001] projection.

The structure is disordered but unless the extrapolated phase boundaries with ice II and ice VIII meet above 0K, there should be a proton ordered form of ice VI [2] but the transition is at a temperature where it is difficult for ordering to occur.

Both Singer *et al.* [72] and Kuo and Kuhs [73] have used graph invariants to attempt to predict the structure of the ordered form of ice VI. Their DFT calculations show that there are two low energy hydrogen bonding topologies that lie very close in energy. However, Salzmann has attempted to determine the structure of the proton ordered form of ice VI by doping it with HCl and has found it to be neither of Singer's low energy structures [74].

2.6 Clathrate and Hydrate Materials

Clathrate hydrate materials have a structure which consists of a network of water molecules that contains voids. These voids are then filled with gas phase guest molecules like noble gases, diatomics of elements from the first row of the p-block and small hydrocarbon molecules and their derivatives [7]. These structures have a long scientific history - they were first studied by Davy [75] and Faraday [76] and later presented a problem to the Lewis-Sidgwick theory of valence because octet theory, which neglects the fact that dispersive forces can bind molecules together in a solid, cannot predict or explain why stable molecules would combine to form these "molecular compounds."

The structures of the two basic types of gas hydrates were proposed in 1950 [77, 78, 79]. These two structures are analogous to the silica clathrasils MEP and MTN [5] and their structural data is given in table 2.11.

As can be seen from the Schläfli symbols, both these structures are simple tilings - MEP is a tiling of 5^{12} and $5^{12}6^2$ polyhedra, while MTN is a tiling of 5^{12} and $5^{12}6^4$ polyhedra. The way these polyhedra pack together in these two structures is shown in figure 2.13.

Three further gas hydrates have been discovered - one has a hexagonal structure [80] and is termed sH; it is isostructural to the clathrasil DOH and is a simple tiling of $5^{12}6^8$, $4^3 5^6 6^3$ and 5^{12} polyhedra. The second is called sT [81], is tetragonal and is a simple tiling of $4^2 5^8 6^4$ polyhedra. The way the polyhedra pack in these two

Clathrate sI (MEP) Cubic Pm3n a = 11.87 - 12.03 Å	
Vertices at 6 c	(0,1/2,1/4)
Schläfli symbol	5 5 5 5 6 6
Coordination sequence	4 12 26 44 64 98 144 172 222 272
Vertices at 16 i	(0.1826,0.1826,0.1826)
Schläfli symbol	5 5 5 5 5 5
Coordination sequence	4 12 24 42 67 95 133 177 219 277
Vertices at 24 k	(0.3098,0.1142,0.0)
Schläfli symbol	5 5 5 5 5 6
Coordination sequence	4 12 25 42 69 100 129 176 229 277
Clathrate sII (MTN) Cubic Fd3m a = 17.175 - 17.31 Å	
Vertices at 8 a	(1/8,1/8,1/8)
Schläfli symbol	5 5 5 5 5 5
Coordination sequence	4 12 24 36 64 112 132 156 222 264
Vertices at 32 e	(0.2181,0.2181,0.2181)
Schläfli symbol	5 5 5 5 5 5
Coordination sequence	4 12 24 39 66 103 130 168 216 274
Vertices at 96 g	(0.0680,0.0680,0.3712)
Schläfli symbol	5 5 5 5 5 6
Coordination sequence	4 12 25 43 68 95 133 177 223 274

Table 2.11: Structural details of the sI and sII clathrate structures.

structures is shown in figures 2.14(a) and 2.14(c). The final true clathrate only forms when *tert*-butylamine is used as the guest [82]. It has a unit cell with 156 water molecules in it and is a simple tiling of $4^4 5^4$ and $4^3 5^9 6^2 7^3$ polyhedra.

The final structure shown in figure 2.14(b) is the way that $4^6 6^8$ polyhedra pack together to form the silica structure sodalite. The oxygen positions of $HPF_6.6H_2O$ lie on the vertices of the sodalite net [83] but the hydrogen positions are not known, so it cannot be stated whether or not this is a true clathrate - it is likely that the structure is an anionic guest in a cationic host structure [7].

The 5^{12} polyhedra, is common to both the sI and sII structure. It is believed to be a favourable structural feature because the O-O-O angles within it are between 108° and 110°. As a result the hydrogen bond network in this cluster does not have any large distortions of HOH angles, which would be energetically unfavourable [7]. Although it is not possible to form a structure consisting of only 5^{12} polyhedra [5]

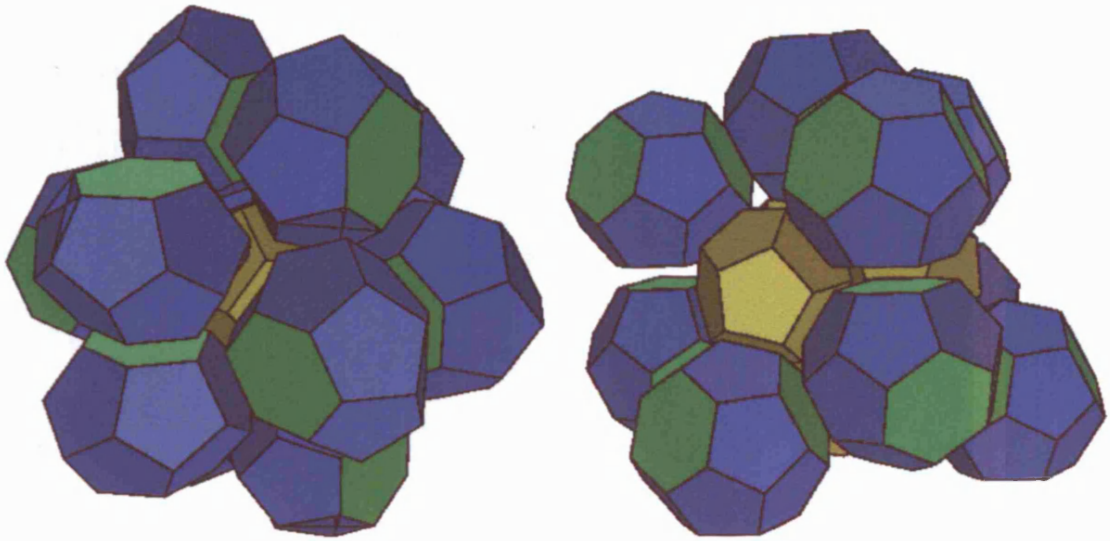

(a) sI Clathrate (MEP) (b) sII Clathrate (MTN)

Figure 2.13: Structures of the two most common water clathrates. For clarity all 5 sided faces are shown in blue, 6 sided faces are shown in green and yellow is used to colour the 5^{12} polyhedra.

it is possible to form countless other structures that contain this cage. Jeffrey [7] has highlighted 3 such structures, which have been inferred from polyhedral packing, but none of these structures has yet been observed. This approach has been justified however as recently a new clathrate has been discovered, which is an intergrowth of the sH and sII structures [84]. This structure was formed when choline hydroxide was co-crystallised with tetra-*n*-propylammonium fluoride from aqueous solution.

When put under pressure water clathrates can undergo phase transitions to other clathrate structures. In general it would seem that clathrates that crystallise in sI transform as follows [85]:

$$\text{sI} \rightarrow \text{sII} \rightarrow \text{sH} \rightarrow \text{sO} \rightarrow \text{sO'}$$

Whilst those that crystallise in the sII structure transform as follows [85]:

$$\text{sII} \rightarrow \text{sH} \rightarrow \text{sT} \rightarrow \text{sO}$$

In these sequences sO and sO' refer to, so-called, stuffed ice Ih structures. In

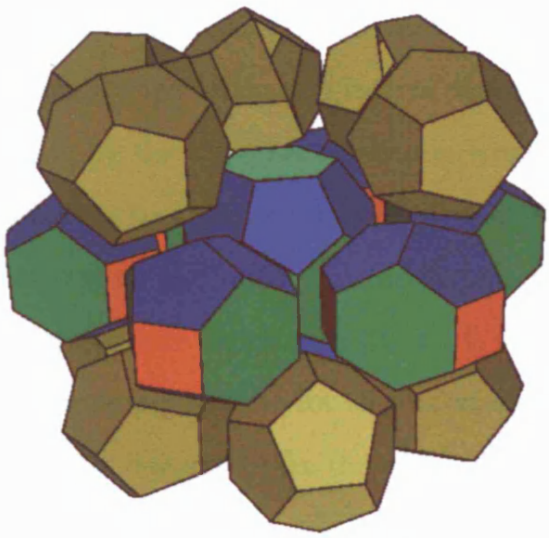

(a) sH Clathrate (DOH)

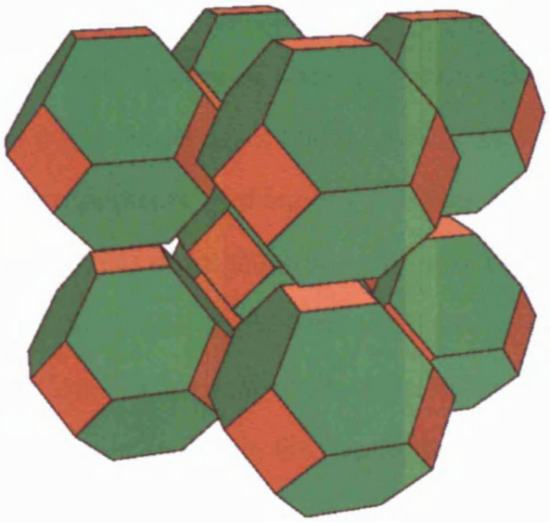

(b) HPF_6 hydrate (SOD)

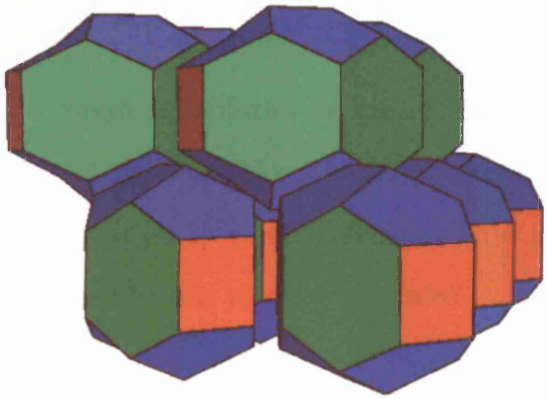

(c) sT Clathrate

Figure 2.14: Structures of the other known water clathrates and hydrates. For clarity all 4 sided faces are shown in red, 5 sided faces are shown in blue, 6 sided faces are shown in green and yellow is used to colour the 5^{12} polyhedra. *n.b.* in the figure of sH one 5^{12} polyhedra has been excluded to make it clearer.

these structures the guest molecule fills the channels in the ice Ih structure. Other stuffed ices have also been observed; in particular helium hydrate and low pressure hydrogen hydrate are known to have the water molecules arranged as they would be in ice II [86], while at high pressure hydrogen hydrate forms a stuffed ice Ic structure, which is much like the ice VII structure with the water molecules in one sub-lattice replaced by hydrogen molecules [87].

In clathrate materials the hydrogen atoms are disordered subject to the Bernal-Fowler rules. As such, non-integer occupancies of hydrogen sites are observed in

neutron diffraction [88] and there is a dielectric relaxation [89, 90], although interestingly the relaxation rate is dependent on the nature of the guest molecules. Again, by the third law of thermodynamics one would expect there to be a phase transition to a proton ordered form at low temperature and indeed this has been observed for clathrates of acetone, trimethyl oxide and tetrahydrofuran when these compounds are doped with KOH [91, 92]. However, these transitions are believed to be more complex than for the ordering transitions for ice as for non-spherical guest molecules one must take the orientation of the guest molecule into account [93].

2.7 Modelling Water

From the early days of computer simulation to recent times the study of the static and dynamic properties of water molecules in small clusters and condensed phases has been a huge area of interest [1, 3]. In the following three sections a justification of the particular methods used in this thesis is provided.

2.7.1 Quantum Mechanical Methods

Hartree-Fock calculations on the proton ordering phase transition in ice Ih have been carried out by Cassasa [32]. They have calculated the energies of ice XI and Bjerrum's structure and have found that it the ice XI structure lies lower in energy. Density functional methods have also been used and Hirsch and Ojamäe[10], who have performed calculations on 16 hypothetical 8 molecule ice Ih unit cells, using the local orbital based code DMol^3 (BLYP functional) and the plane-wave based code CASTEP [31] (PW91 functional) have shown that both these methods correctly predict the structure of ice XI and that both techniques give similar relative energies. Kuo *et al.* [9, 16, 15] have also used plane wave DFT in all their graph invariant work and again found that these techniques predict the correct ordered forms.

Established work in the literature has shown that, although using the LDA functional gives a poor description of the water dimer and liquid water, the GGA

functionals BLYP and PW91 both reproduce most of the properties of liquid water equally well [94]. The best description of the properties of liquid water is obtained when the RPBE functional (a re-parameterization of PBE [95]) is used [96]. Furthermore, both PBE and PW91 give good agreement with experiment for the sublimation energy and the volume of ice Ih [97]. Recent work [98], on clusters of water molecules ranging in size from dimer to pentamer have shown that many of the commonly used density functionals reproduce the MP2 energies of these clusters to within 1 kcal mol^{-1}.

2.7.2 Potential Models

There are well over 100 potentials that have been proposed for water [3], the earliest was proposed by Bernal and Fowler [1]. It described the water molecule as a rigid unit with point charges on the hydrogen atoms and the HOH bisector to describe the charge distribution in the gas phase molecule. The van der Waals attraction was given by $(3/4)I\alpha^2 r^{-6}$, where α is the polarizability and I is the ionisation potential, and the short range repulsion was empirically fitted by requiring that all forces be equal to zero a when the structure is in its equilibrium geometry. This potential was not fitted with computer simulation in mind though and more recent attempts to fit water potentials that treat the molecules as rigid bodies were done so that the properties of liquid water would be reproduced in computer simulations [99, 100]. With the advent of faster computers attempts have been made to fit more transferable water potentials in which polarisation and flexibility are described explicitly [101, 102, 103]. These potentials are generally fitted to gas phase properties and for all their extra expense provide no better description of the condensed phases than the rigid potentials [3].

The most commonly used water potentials are the SPC/E [99] and TIP4P [100] models, Buch *et al.* [30] have used both these potentials, and a number of others, to study the proton ordering phase transition from ice Ih to ice XI. They have

found that all these predict the wrong structure for the ordered form. Worse still Hirsch and Ojamäe have performed a comparison of the relative energies, for the 16 hypothetical ice Ih 8 molecule unit cells, calculated using the COMPASS[104, 105] and the flexible SPC [102] potentials with the total energy computed from the first principles CASTEP/DMol^3 results and shown that the DFT and potential results are inversely-correlated.

On the simulation of ice Ih itself, free energy calculations using the SPC model [106, 107] predict the melting point of water to be 191 $\pm$ 7 K. To resolve this issue Nada and van der Eerden [107] have created a new rigid, point charge model (hereafter referred to as TIP6P) that was explicitly fitted to ensure that it reproduced:

- The correct densities of ice and water at 273 K
- The correct density of water at 298 K
- The experimental melting point of ice, by ensuring that at 273 K ice and water have the same free energies.

Abascal *et al.* [108] have taken this even further and used free energy calculations to refit the TIP4P potential so that it reproduces, as closely as possible, the phase diagram of ice.

Studies of the ice surface with molecular dynamics using TIP4P have shown unambiguous evidence of the formation of a liquid layer at the ice surface at temperatures between 190 and 250 K [109]. Above 230 K it was found that the order parameters and nobilities of the molecules in the top few layers increased dramatically suggesting that these layers had become liquid-like. Furthermore, between 190 and 210 K there was increased hydrogen bonding in the surface layers because water molecules moved closer together. In the terminating layer, pentagon, heptagon and other polygons began to form and dipoles pointed downwards on the surface validating the suggestions of the surface charge work [110, 111]. These results are questionable because of the low melting temperature of the TIP4P potential. Wake

[112] has performed similar calculations using the TIP6P potential and shown that on the {0001} surface of ice there are defects in the top bilayer at temperatures from 240 K upwards and that the number of these defects increases with temperature. These defects give rise to surface disorder which was found to take three forms:

- Water molecules were ejected out of the terminal layer and readsorbed to form a new layer atop the existing layer.
- Interstitials were created.
- Surface reconstruction was observed with in plane water molecules forming polygons other than hexagons.

Furthermore, increased mobility was observed for water molecules on the surface and there was a build up of areas of high and low densities of water molecules.

One question Wake's work didn't address however was how the surface energy of the initial ideal ice configuration depended on the arrangement of the water molecules on the surface as one might suspect that if there are lots of dangling hydrogen bonds near to each other on the surface the surface energy will be high due to suprafacial repulsions.

2.7.3 Unit cell choice

An issue which must be addressed in performing simulations on disordered ice Ih, or any other disordered ice phase, is how to represent an infinitely disordered hydrogen bonding arrangement in a finite simulation cell. Hayward and Reimers [113] have addressed this problem by deriving an energy independent protocol of generating bulk configurations. This essentially depends on maximising disorder whilst minimising net polarity within the cell. These cells have been used extensively in the literature to simulate both the bulk and surface of ice, where the constraint of apolarity is essential. Where these cells have been used, the energy independent generation protocol and the zero dipole constraint have not been questioned. In this

thesis these issues are broached and a new recipe for generating reasonable unit cells is proposed.

Bibliography

[1] J. D. Bernal and R. H. Fowler. *J. Chem. Phys.*, **1**, 515 (1933).

[2] V. F. Petrenko and R. W. Whitworth. *Physics of ice.* OUP, (1999).

[3] B. Guillot. *Journal of Molecular Liquids*, **101**, 219 (2002).

[4] M. Chaplin. www.lsbu.ac.uk, (2007).

[5] M. O'Keeffe and B. G. Hyde. *Crystal structures I. Patterns and Symmetry.* Mineralogical Society of America, (1996).

[6] L. Pauling. *J. Amer. Chem. Soc.*, **57**, 2680 (1935).

[7] G. A. Jeffrey. *Inclustion Compounds volume 1*, chapter Hydrate Inclusion Compounds. Academic Press, (1984).

[8] P. W. Atkins. *Physical Chemistry.* OUP, (2001).

[9] S. J. Singer, J.-L. Kuo, T. K. Hirsch, C. Knight, L. Ojamae and M. L. Klein. *Phys. Rev. Lett.*, **94**, 135701 (2005).

[10] T. K. Hirsch and L. Ojamäe. *J. Phys. Chem. B*, **108**, 15856–15864 (2004).

[11] S. W. Rick. *J. Chem. Phys.*, **122**, 094504 (2005).

[12] R. Howe. *Journal de Physique*, **48**, 599 (1987).

[13] J.-L. Kuo and S. J. Singer. *Physcial Review E*, **67**, 016114 (2003).

[14] J.-L. Kuo, J. V. Coe, S. J. Singer, Y. B. Band and L. Ojamae. *J. Chem. Phys.*, **114**, 2527–2540 (2001).

[15] J.-L. Kuo and M. L. Klein. *J. Phys. Chem. B*, **108**, 19634 (2004).

[16] C. Knight and S. J. Singer. *J. Chem. Phys.*, **125**, 064506 (2006).

[17] C. B. ad W. M. Meier and D. H. Olson. *Atlas of Zeolite Framework Types.* Elsevier, (2001).

[18] M. Zwijnenburg, S. Bromley, M. Foster, R. Bell, O. Delgado-Friedrichs, J. Jansen and T. Maschmeyer. *Chemistry of materials*, **16**, 3809 (2004).

[19] D. Dennison. *Phys. Rev.*, **17**, 20 (1921).

[20] W. H. Bragg. *Proceedings of the Physical Society*, **34**, 98 (1922).

[21] W. H. Barnes. *Proceedings of the Royal Society of London*, **A125**, 127 (1929).

[22] E. Wollan, W. Davidson and C. Shull. *Physical Review*, **75**, 1348 (1949).

[23] S. Kawada. *J. Phys. Soc. Japan*, **32**, 1442 (1972).

[24] Y. Tajima, T. Matsuo and H. Suga. *Journal of Physics and Chemistry of Solids*, **45**, 1135 (1984).

[25] T. Matsuo, Y. Tajima and H. Suga. *Journal of Physics and Chemistry of Solids*, **47**, 165 (1986).

[26] C. M. B. Line and R. W. Whitworth. *J. Chem. Phys.*, **104**, 10008 (1996).

[27] S. M. Jackson, V. M. Nield, R. W. Whitworth, M. Oguro and C. C. Wilson. *J. Phys. Chem. B*, **101**, 6142 (1997).

[28] N. Bjerrum. *Science*, **115**, 386 (1952).

[29] K. S. Pitzer and J. Polissar. *J. Am. Chem. Soc.*, **60**, 1140 (1956).

[30] P. S. V. Buch and J. Sadlej. *Phys. Chem. B*, **102**, 8641 (1998).

[31] M. D. Segall, P. L. D. Lindan, M. J. Probert, C. J. Pickard, P. J. Hasnip, S. J. Clark and M. C. Payne. *J. Phys.: Cond. Matt.*, **14**, 2712 (2002).

[32] S. Casassa, M. Calatayud, K. Doll, C. Minot and C. Pisani. *Chem. Phys. Lett.*, **409**, 110 (2005).

[33] H. Konig. *Zeitschift fur Kristallographie*, **105**, 279 (1943).

[34] M. Blackman and N. Lisgarten. *Advances in Physics*, **7**, 189 (1958).

[35] J. Bertie, L. Calvert and E. Whalley. *J. Chem. Phys.*, **38**, 840 (1963).

[36] Y. Handa, D. Klug and E. Walley. *Canadian Journal of Chemistry*, **66**, 919 (1988).

[37] G. Arnold, E. Finch, S. Rabideau and R. Wensel. *J. Chem. Phys.*, **49**, 4365 (1968).

[38] W. Kuhs, D. Bliss and J. Finney. *Journal de Physique*, **48**, 631 (1987).

[39] H. Kiefte, M. Clouter and E. Walley. *J. Chem. Phys.*, **81**, 1419 (1984).

[40] M. A. Carignano. *J. Phys. Chem. C*, **111**, 501 (2007).

[41] B. Kamb, W. Hamilton, S. LaPlaca and A. Prakash. *J. Chem. Phys.*, **55**, 1934 (1971).

[42] B. Kamb. *Acta. Cryst.*, **17**, 1437 (1964).

[43] J. E. Bertie and E. Walley. *J. Chem. Phys.*, **40**, 1646 (1964).

[44] D. Londono, J. Finney and W. Kuhs. *J. Chem. Phys.*, **97**, 547 (1992).

[45] B. Kamb and A. Prakash. *Acta. Cryst.*, **B24**, 1317 (1968).

[46] E. Whalley, J. Heath and D. Davidson. *J. Chem. Phys.*, **48**, 2362 (1968).

[47] J. Londono, W. Kuhs and J. Finney. *J. Chem. Phys.*, **48**, 4878 (1993).

[48] W. Kuhs, C. Lobban and J. Finney. *The Review of High Pressure Science and Technology*, **7**, 1141 (1998).

[49] L. Evans. *J. Applied Phys.*, **38**, 4930 (1967).

[50] H. Engelhardt and E. Whalley. *J. Chem. Phys.*, **56**, 2678 (1972).

[51] H. Engelhardt and B. Kamb. *J. Chem. Phys.*, **75**, 5887 (1981).

[52] B. Kamb, A. Prakash and C. Knobler. *Acta. Cryst.*, **22**, 706 (1967).

[53] G. Wilson, R. Chan, D. Davidson and E. Whalley. *J. Chem. Phys.*, **2384**, 43 (1965).

[54] W. Hamilton, B. Kamb, S. LaPlaca and A. Prakash. *Physics of ice.* Plenum Press, New York, (1969).

[55] B. Minceva-Sukarova, W. Sherman and G. Wilkinson. *J. Phys. C*, **17**, 5833 (1984).

[56] Y. Handa, D. Klug and E. Whalley. *Journal de Physique*, **48**, 435 (1987).

[57] C. Salzmann, P. Radaelli, A. Hallbrucker, E. Mayer and J. Finney. *Science*, **311**, 1758 (2006).

[58] C. Lobban, J. Finney and W. Kuhs. *Nature*, **391**, 268 (1998).

[59] M. Koza, H. Schober, A. Tolle, F. Fujara and T. Hansen. *Nature*, **397**, 660 (1999).

[60] G. Walfaren, M. Abbe, F. Mauer, S. Block, G. Piermarini and R. Munro. *J. Chem. Phys.*, **77**, 2166 (1982).

[61] W. Kuhs, J. Finney, C. Vetteir and D. Bliss. *Journal de Physique*, **48**, 3 8 (1984).

[62] R. Nelmes, J. Loveday, W. Marshall, G. Hamel, J. Besson and S. Klotz. *PRL*, **81**, 2719 (1998).

[63] E. Whalley, D. Davidson and J. Heath. *J. Chem. Phys.*, **45**, 3976 (1966).

[64] R. Hemley, A. Jephcoat, H. Mao, C. Zha, L. Finger and D. Cox. *Nature*, **330**, 737 (1987).

[65] J. Besson, P. Pruzan, S. Klotz, G. Hamel, B. Silvi and R. Nelmes. *Phys. Rev.*, **B49**, 12540 (1994).

[66] R. Nelmes, J. Loveday, W. Marshall, J. Besson and S. Klotz. *The Review of High Pressure Science and Technology*, **7**, 1138 (1998).

[67] W. Holzapfel. *J. Chem. Phys.*, **56**, 712 (1972).

[68] F. H. Stilinger and K. Schweizer. *J. Phys. Chem.*, **87**, 4281 (1983).

[69] K. Hirsch and W. Holzapfel. *Phys. Lett.*, **A101**, 142 (1984).

[70] A. Polian and M. Grimsditch. *PRL*, **52**, 1312 (1984).

[71] B. Kamb. *Science*, **150**. 205 (1965).

[72] C. Knight and S. Singer. *J. Phys. Chem. B*, **109**, 21040 (2005).

[73] J. L. Kuo and W. F. Kuhs. *J. Phys. Chem. B*, **110**, 3697 (2006).

[74] C. G. Salzmann. Personal communication, (2007).

[75] H. Davy. *Philos. Trans. R. Soc. (London)*, **101**, 155 (1811).

[76] M. Faraday. *Quant. J. Sci. Lit. Arts*. **15**, 71 (1823).

[77] M. von Stackelberg and H. Muller. *Naturwiss*, **38**, 456 (1949).

[78] W. Claussen. *J. Chem. Phys.*, **19**, 259 (1951).

[79] L. Pauling and R. Marsh. *Proc. Natl. Acad. Sci. USA*, **38**, 112 (1952).

[80] J. Ripmeester, J. Tse, C. Ratcliffe and B. Powell. *Nature*, **325**, 135 (1987).

[81] A. Kurnosov, A. Manakov, V. Komarov, V. Voronin, A. Teplykh and Y. Dyadin. *Doklady Physical Chemistry*, **381**, 303 (2001).

[82] R. McMulland, G. Jeffrey and D. Panke. *J. Chem. Phys.*, **47**, 1229 (1967).

[83] H. Bode and G. Teufer. *Acta Cryst.*, **8**, 611 (1955).

[84] K. Udachin and J. Ripmeester. *Nature*, **397**, 420 (1999).

[85] H. Hirai, T. Tanaka, T. Kawamura, Y. Yamamoto and T. Yagi. *J. Phys. Chem. Solid*, **65**, 1555 (2004).

[86] D. Londono, J. Finney and W. F. Kuhs. *J. Chem. Phys.*, **98**, 4878 (1993).

[87] W. Vos, L. Finger, R. Hemley and H. Mao. *PRL*, **71**, 3150 (1993).

[88] F. Hollander and G. Jeffrey. *J. Chem. Phys.*, **66**, 4699 (1977).

[89] S. Gough, E. Whalley and D. Davidson. *Canadian Journal of Chemistry*, **46**, 1673 (1968).

[90] D. Davidson, Y. Handa, C. Ratcliffe, J. Tse and B. Powell. *Canadian Journal of Chemistry*, **55**, 3641 (1977).

[91] H. Suga, T. Matsuo and O. Yamamuro. *Physics and Chemistry of Ice*. Hokkaido University Press, Sapporo, (1992).

[92] H. Suga. *Cryo. Lett.*, **18**, 55 (1997).

[93] D. Davidson and J. Ripmeester. *Inclusion Compounds volume 3*. Academic Press London, (1984).

[94] P. Vassilev, C. Hartnig, M. T. M. Koper and F. Frechard. *J. Chem. Phys.*, **115**, 9815 (2001).

[95] B. Hammer, L. B. Hansen and J. K. Norskov. *Phys. Rev. B*, **59**, 7413 (1999).

[96] M. V. Fernandez-Serra, G. Ferlat and E. Artacho. *Molecular Simulation*, **31**, 361 (2005).

[97] D. R. Hamman. *Phys, Rev. B*, **55**, R10157 (1997).

[98] B. Santra, A. Michaelides and M. Scheffler. *In Prepaparation*, (2007).

[99] H. J. C. Berendsen, J. P. M. Postma, W. F. van Gunsteren and J. Hermans. *Intermolecular Forces, ed B.* Pullman, Reidel, Dordrecht, (1981).

[100] W. L. Jorgenson, J. Chandrasekhar, J. D. Madura, W. R. Impey and M. L. Klein. *J. Chem. Phys.*, **79**, 926 (1983).

[101] S. Kuwajima and A. Warshel. *J. Phys. Chem.*, **94**, 460 (1990).

[102] K. Toukan and A. Rahman. *Phys. Rev. B*, **31**, 2643 (1985).

[103] J. Jeon, A. E. Lefohn and G. A. Voth. *J. Chem. Phys.*, **118**, 7504 (2003).

[104] H. Sun. *J. Phys. Chem. B*, **102**, 7338 (1998).

[105] Z. Peng, C. S. Ewig, M.-J. Hwang, M. Waldman and A. T. Hagler. *J. Phys. Chem. A*, **101**, 7243 (1997).

[106] G. T. Gao, X. C. Zeng and H. Tanaka. *J. Chem. Phys.*, **110**, 55 (1999).

[107] H. Nada and J. P. J. M. van der Eerden. *J. Chem. Phys.*, **118**, 7401–7413 (2003).

[108] J. Abascal, E. Sanz, G. G. Fenandez and C. Vega. *J. Chem. Phys.*, **122**, 234511 (2005).

[109] G. J. Kroes. *Surface Science*, **275**, 365 (1992).

[110] N. H. Fletcher. *Philosophical Magazine*, **7**, 255 (1962).

[111] V. F. Petrenko and I. A. Ryzhkin. *J. Phys. Chem. B*, **101**, 6285 (1997).

[112] C. L. Wake, G. Tribello and B. Slater. *In Preparation*, (2007).

[113] J. A. Hayward and J. R. Reimers. *J. Chem. Phys.*, **106**, 1518 (1996).

Chapter 3

Theoretical Methods

The foundation of much of theoretical chemistry is statistical mechanical, so rather than describe the state of the system using the values of state functions (eg. entropy, internal energy, temperature) the state is described using the full set of positions and velocities for all its constituents (the position in phase space). The instantaneous values of any thermodynamical state function, or quantity of interest, can then be calculated from the coordinates and momenta of the particles in the system [1]. If one can calculate a phase space probability density (or distribution function) $f^N(\boldsymbol{r}, \boldsymbol{p})$ which gives the probability of being at any point in phase space it is possible to calculate the average of any function of the coordinates and momenta using [1]:

$$< F >= \int \int F(\boldsymbol{r^N}, \boldsymbol{p^N}) f^N(\boldsymbol{r^N}, \boldsymbol{p^N}) d\boldsymbol{r^N} d\boldsymbol{p^N} \tag{3.1}$$

Where F is the observable of interest and the distribution function is normalised. It is possible to write out the explicit form of f^N if one keeps a subset of the macroscopic thermodynamic state functions constant, so for instance if one keeps the energy, volume and number of molecules constant then the distribution function is given by:

$$f^N(\boldsymbol{r}, \boldsymbol{p}) = \frac{\delta(H(\boldsymbol{r}, \boldsymbol{p}) - E)}{\Omega} \tag{3.2}$$

Where δ is a Dirac delta function, H is the Hamiltonian for the system and Ω

is the number of microstates that have an energy E. Alternatively, if one keeps temperature, volume and number of molecules fixed the distribution function is [1]:

$$f_{NVT}^{(N)}(\boldsymbol{r^N}, \boldsymbol{p^N}) = \frac{e^{-H(r,p)/k_BT}}{Q_N(V,T)} \tag{3.3}$$

Here Q is the canonical partition function which is given by [1]:

$$Q_N = \int \dots \int e^{-H(q,p)/k_BT} d\boldsymbol{r^N} d\boldsymbol{p^N} \tag{3.4}$$

The Hamiltonian is the sum of the potential and kinetic energies of the particles in the system. Furthermore, in Cartesian coordinates it separates into a momentum dependent kinetic part and a coordinate dependent potential part (*n.b.* this is only valid for classical Hamiltonians).

$$\begin{aligned} H(\boldsymbol{p},\boldsymbol{q}) &= K(\boldsymbol{p}) + V(\boldsymbol{q}) \\ \Rightarrow e^{-H(p,q)/k_BT} &= e^{-K(p)/k_BT} e^{-V(q)/K_BT} \end{aligned} \tag{3.5}$$

Thus equation 3.4 becomes:

$$Q_N = \int e^{-K(p)/k_BT} d\boldsymbol{p} \int e^{-V(q)/k_BT} d\boldsymbol{q} \tag{3.6}$$

The first of the two integrals in the above equation is solvable; however, the second is not. It is called the configurational integral, Z_N, and most of the effort in computer simulation is directed towards calculating approximate values for this integral. This is usually done by replacing the integral with a sum over a number of states and averaging over them. In later parts (section 3.4) there is a discussion of how one goes about selecting a sensible set of points, but the first problem to be addressed is how one calculates the potential energy from the particle coordinates.

3.1 Calculating the potential energy

In quantum mechanics the wavefunction for the system contains all the physical information about the system. Sadly however, the wavefunction is not measurable and can only be obtained by solving the time dependent Schrödinger equation. It is trivial to show that for time independent potentials the space and time dependent parts of the Schrödinger equation can be separated. Solution of the time dependent partial differential equation gives rise to a time dependent phase factor, which is multiplied by the solution of the differential equation given below:

$$\begin{aligned} \widehat{H}\Psi &= E\Psi \\ \text{where} \quad \widehat{H} &= -\frac{\hbar^2}{2m}\nabla^2 + V(x) \end{aligned} \tag{3.7}$$

Where Ψ is the wavefunction, $\widehat{H}$ is the Hamiltonian and E is the total energy. Multiplying both sides of equation 3.7 by the complex conjugate of Ψ and integrating over all space (assuming the wavefunction is normalised) gives:

$$\begin{aligned} H[\Psi] =< \Psi|\widehat{H}|\Psi > &= E < \Psi|\Psi > \\ H[\Psi] =< \Psi|\widehat{H}|\Psi > &= E \end{aligned} \tag{3.8}$$

The energy calculated using this functional is called the expectation value. The Variational Theorem states that any estimate of the ground state energy will always lie above the actual energy of the ground state. This means that the most accurate ground state wavefunction will be the one that minimises the value of the expectation value of the energy. To minimise the expectation value it is useful to express the wavefunction, Ψ, as a linear combination of of a complete set of orthonormal basis functions because these basis functions and any linear combination of them will belong to a vector space. This is to say because the set of functions share certain properties with a complete set of position vectors they can be treated in an analogous

fashion. Using this analogy the Variational Theorum can be re-expressed in terms of the functional derivative below:

$$\lim_{\epsilon \to 0} \frac{H[\Psi + \epsilon \mathbf{u}] - H[\Psi]}{\epsilon} = 0 \tag{3.9}$$

In the above equation $\mathbf{u}$ is a function that is analogous to a unit vector. If one is at a true minimum of the functional then this equation will hold regardless of the direction in which $\mathbf{u}$ points. Using Lagrange multipliers to constrain the solutions of equation 3.9 to be orthonormal recaptures equation 3.7 but, more importantly, the Variational Principle can be used to derive approximate wavefunctions.

For an atom containing one electron, equation 3.7 is solvable as the potential is simply proportional to $(1/r)$, where r is the distance between the electron and the nucleus. For any system containing more than 2 bodies though this equation becomes impossible to solve analytically and for this reason it is necessary to make approximations. Typically the first approximation to be made is the Born-Oppenheimer approximation [2], which assumes that the positions of nuclei are fixed. So the wavefunction for the electrons is calculated in the static electric potential arising from the nuclei in their fixed arrangement.

3.1.1 Hartree-Fock Theory

Hartree-Fock theory [3, 4, 5, 6, 7] begins by assuming that the true wavefunction, Ψ, of a multi electron system is similar in form to the electronic wavefunction that would be obtained if electron-electron interactions were neglected,Ψ_0. That is to say that Ψ_0 is a solution of:

$$\begin{aligned} H^0\Psi^0 &= E^0\Psi^0 \\ \text{where} \quad H^0 &= -\frac{\hbar^2}{2m_e}\sum_i^n \nabla_i^2 - \sum_i^n \sum_I^N \frac{Z_I e^2}{4\pi\epsilon_0 r_{Ii}} \end{aligned} \tag{3.10}$$

This equation separates into a set of n one electron equations, with solutions

$\phi_N(\boldsymbol{x_N})$. Ψ can then be expressed as a product of of all these one-electron wavefunctions but this treatment leads to a wavefunction that is symmetric with respect to exchange of particle labels, which violates the Pauli principle. To resolve this spin is introduced, the 1 electron wavefunctions are replaced by spin-orbitals and the products of the wavefunctions are replaced by Slater determinants. Now Ψ_0 is given by:

$$\Psi_0 = \frac{1}{\sqrt{N!}} \begin{vmatrix} \phi_1(\boldsymbol{x_1}) & \phi_2(\boldsymbol{x_1}) & \dots & \phi_N(\boldsymbol{x_1}) \\ \phi_1(\boldsymbol{x_2}) & \phi_2(\boldsymbol{x_2}) & \dots & \phi_N(\boldsymbol{x_2}) \\ \vdots & \vdots & \ddots & \vdots \\ \phi_1(\boldsymbol{x_N}) & \phi_2(\boldsymbol{x_N}) & \dots & \phi_N(\boldsymbol{x_N}) \end{vmatrix}$$

An N electron wavefunction can be expanded in a series of N-particle Slater determinants and there are multideterminant methods that give a wavefunction as a sum of Slater determinants. Hartree-Fock however is not one of these; instead it assumes that the wavefunction is given by only one Slater Determinant. Physically this approximation means that the theory does not account for electronic correlation effects like dispersion, which leads to underbinding in solids and molecules.

An expectation value for the energy, including electron-electron terms, for any given Slater Determinant can be obtained by calculating the expectation value of the multi-electron Hamiltonian. Thus the variational theorem (equation 3.9) can be applied and the conditions for a minimum in the functional established. This treatment gives N equations in terms of N one electron wavefunctions which are given by:

$$\begin{aligned} h(\boldsymbol{r_1})\phi_n(\boldsymbol{r_1}) \;+\; & \sum_{k=1}^{N} \left[\int d\boldsymbol{r_2} \frac{|\phi_k(\boldsymbol{r_2})|^2}{r_{12}} \phi_n(\boldsymbol{r_1}) - \int d\boldsymbol{r_2} \frac{\phi_k(\boldsymbol{r_2}) * \phi_n(\boldsymbol{r_2})}{r_{12}} \phi_k(\boldsymbol{r_1}) \right] \\ &= \lambda_n \phi_n(\boldsymbol{r_1}) \\ \text{where} \qquad h(\boldsymbol{r}) &= -\frac{1}{2}\nabla + V(\boldsymbol{r}) \end{aligned} \tag{3.11}$$

Where $r_{12} = |\boldsymbol{r_1} - \boldsymbol{r_2}|$ and $V(\boldsymbol{r})$ is the value of the external potential at $\boldsymbol{r}$. These

equations must be solved self consistently as the energy depends on the values of the wavefunctions and assume that the space part of the electronic wavefunction is independent of the spin part. The first integral in this equation is the electrostatic repulsion between electrons and the second is the, so-called, exchange interaction.

3.1.2 Density Functional Theory

A wavefunction is a 3N dimensional function, thus storage of the function in the memory of a computer is a considerable problem. One resolution to this problem is the Hohenberg-Kohn theorem [8] which states that there is a one to one mapping between the ground state energy of a system and the electron density. In other words it is possible to write a functional for the energy in terms of the electronic density of the system. To prove this statement one must prove that:

- Different potentials lead to different ground states.
- Different ground states give rise to different electron densities.

The Hohenberg-Kohn theorem only proves that the density functional exists. It does not give the form of the true density functional and as such one must derive approximate functionals. Kohn and Sham [9] developed a method as follows; they first imagined a system of non-interacting electrons with the same ground state density, $p(\boldsymbol{r})$, and energy as the system of interest (the system of interest does of course contain interacting electrons). The non-interacting system is accurately represented by a Slater Determinant, the one electron orbitals, $\phi_n(\boldsymbol{r})$, of which satisfy:

$$\begin{aligned} \left(-\frac{\hbar^2}{2m_e}\nabla^2 + V_s(r)\right)\phi_n(\boldsymbol{r}) &= \epsilon_n\phi_n(\boldsymbol{r}) \\ p_v(\boldsymbol{r}) &= \sum_n |\phi_n(\boldsymbol{r})|^2 \end{aligned} \tag{3.12}$$

The Hohenberg-Kohn theorem proves that the potential on the system of non-interacting electrons, V_s, can't be the same as the external potential on the system

of interacting electrons, V, and that the wavefunctions for the non-interacting and interacting systems are not necessarily the same. Applying the variational principle (equation 3.9) the energy of the system of non-interacting electrons is equal to the minimum in the following functional:

$$E_s = \langle \Phi | T_s + V_s | \Phi \rangle \tag{3.13}$$

Where T_s corresponds to the kinetic energy part of equation 3.12 ($-\frac{\hbar^2}{2m_e}\nabla^2$). To solve this functional derivative the minimum is searched for in two stages. In the first the minimum energy Slater determinant is searched for holding the electron density constant, *i.e.* the following functional is minimised:

$$E_s = T_s[p(\boldsymbol{r})] + \int \mathrm{d}\boldsymbol{r} V_s(\boldsymbol{r}) p(\boldsymbol{r}) \tag{3.14}$$

Next a minimisation of the functional with respect to the electron density is performed using a Lagrange multiplier to constrain the number of electrons. This corresponds to solving the following equation:

$$\begin{aligned} \frac{\delta}{\delta p(\boldsymbol{r})}\left[T_s[p(\boldsymbol{r})] \;+\; \int \mathrm{d}\boldsymbol{r} V_s(\boldsymbol{r}) p(\boldsymbol{r}) - E_s \int \mathrm{d}\boldsymbol{r} p(\boldsymbol{r})\right] &= 0 \\ \Rightarrow \frac{\delta T_s[p(\boldsymbol{r})]}{\delta p(\boldsymbol{r})} \;&=\; -V_s(\boldsymbol{r}) + E_s \end{aligned} \tag{3.15}$$

The energy of the system that includes interaction between electrons is given by the following functional:

$$E[p(\boldsymbol{r})] = T_s[p(\boldsymbol{r})] + \frac{1}{2}\int\int \mathrm{d}\boldsymbol{r}\mathrm{d}\boldsymbol{r}' \frac{p(\boldsymbol{r})p(\boldsymbol{r}')}{|\boldsymbol{r}' - \boldsymbol{r}|} + \int \mathrm{d}\boldsymbol{r} V(\boldsymbol{r}) p(\boldsymbol{r}) + E_{xc}[p(\boldsymbol{r})] \tag{3.16}$$

Here $E_{xc}[p(\boldsymbol{r})]$ is a functional that takes into account the difference between the kinetic energy functional for the non-interacting system and the equivalent functional for the interacting system. The minimum in the functional derivative, again

holding the total number of electrons fixed, is:

$$\begin{aligned}\frac{\delta}{\delta p(\boldsymbol{r})}\Bigg[[T_s[p(\boldsymbol{r})] + \frac{1}{2}\int\int \mathrm{d}\boldsymbol{r}\mathrm{d}\boldsymbol{r}'\frac{p(\boldsymbol{r})p(\boldsymbol{r}')}{|\boldsymbol{r}'-\boldsymbol{r}|}] \;&+\; \int \mathrm{d}\boldsymbol{r}V(\boldsymbol{r})p(\boldsymbol{r}) \\ &+\; E_{xc}[p(\boldsymbol{r})] + E\int \mathrm{d}\boldsymbol{r}p(\boldsymbol{r})\Bigg] = 0 \\ \frac{\delta T_s[p]}{\delta p(\boldsymbol{r})} + \int \mathrm{d}\boldsymbol{r}'\frac{p(\boldsymbol{r}')}{|\boldsymbol{r}'-\boldsymbol{r}|} + V(\boldsymbol{r}) \;&+\; \frac{\delta E_{xc}}{\delta p(\boldsymbol{r})} - E = 0 \end{aligned} \tag{3.17}$$

The energy, E_s, in equation 3.15 must be equal to the energy, E, in equation 3.17 because of the Hohenberg-Kohn theorem - these two systems have identical electron densities and thus must have identical ground state energies. From this equality we thus obtain:

$$V_s(\boldsymbol{r}) = V(\boldsymbol{r}) + \int \mathrm{d}\boldsymbol{r}'\frac{p(\boldsymbol{r}')}{|\boldsymbol{r}'-\boldsymbol{r}|} + \frac{\delta E_{xc}}{\delta p(\boldsymbol{r})} \tag{3.18}$$

This combined with equation 3.12 provides a method for self consistently calculating the energy of the system.

The exact form of $E_{xc}[p(\boldsymbol{r})]$ is not known so approximations have to be introduced to calculate this quantity. The simplest approximation for $E_{xc}[p(\boldsymbol{r})]$ is given below:

$$E_{xc}[p(\boldsymbol{r})] = \int d\boldsymbol{r}p(\boldsymbol{r})\epsilon_{xc}(p(\boldsymbol{r})) \tag{3.19}$$

Where $\epsilon_{xc}(p(\boldsymbol{r}))$ is the exchange correlation energy density at point $\boldsymbol{r}$ and is only a function of the density. This approximation is called the Local Density Approximation (LDA) and works surprisingly well, particularly for systems where the electron distribution is approximately homogenous like nearly-free electron metals. It works less well for systems with inhomogeneous electron distributions, like atoms, largely because of the spurious self-interaction term which arises because, unlike in Hartree-Fock theory, exchange is not treated exactly [10].

Another commonly used approximation is the Generalised Gradient Approximation (GGA) which is very similar to LDA except that the exchange correlation density function depends on the density and the local gradient of the density. There

are a variety of GGA functionals [10] which are widely used in chemistry. These are of near equal computational expense to LDA but provide a much improved description of exchange and correlation at short range, albeit with a tendency to slightly underestimate binding energies.

The final class of functionals used in this work include an exact exchange contribution from Hartree-Fock or a mixture of Hartree-Fock and LDA or GGA [11, 12, 13]. These, so called, exact exchange functionals are the most accurate functionals available to DFT because DFT introduces a spurious self-interaction because of its inaccurate treatment of exchange, which is removed by the introduction of Hartree-Fock exchange. What is more, this mixing of methods gives rise to a functional that is more accurate than Hartree-Fock because of the inclusion of local correlation effects. This increase in accuracy comes however with quite a substantial increase in computational cost over the LDA and GGA functionals.

3.1.3 Basis Sets

A difficulty has been neglected - so far the recipes suggested will work well for atoms, for which it is easy to solve the HF / KS equations numerically, but for molecules such numerical solution is not feasible. To resolve this the spatial wavefunctions are expanded in a set of 3D basis functions as below:

$$\psi_i = \sum_{j=1}^{M} c_{ji}\phi_j \tag{3.20}$$

where the c_{ji}s are a set of undetermined coefficients. To obtain the true electronic wavefunction one would require an infinite number of such basis functions but in practice this is computationally impossible, so a finite basis set is employed, which gives rise to an error termed the basis-set truncation error. Use of basis functions converts equations 3.11 and 3.18 into matrix equations which have to be solved for the coefficients c_{ji}. There are many different basis functions that can be used but

this work uses only two varieties that are described below:

3.1.3.1 Gaussian Basis Sets

Gaussian basis sets can be used for clusters or periodic systems; the functions used here are Gaussian functions centred on the atoms in the system. These Gaussians are of the form:

$$\theta_{ijk}(\boldsymbol{r} - \boldsymbol{r_c}) = (x - x_c)^i (y - y_c)^j (z - z_c)^k e^{-\alpha|\boldsymbol{r}-\boldsymbol{r_c}|^2} \tag{3.21}$$

Here (x_c, y_c, z_c) are the Cartesian coordinates of the centre of the gaussian, the i, j and k are non negative integers and α is a positive exponent. If $i = j = k = 0$ the gaussian is an s-type gaussian, while if $i + j + k = 1$ the gaussian is p-type, or for $i + j + k = 2$ the gaussian is d-type and so on. The main advantage of Gaussian basis sets is that any product of two Gaussians at different centres is a single Gaussian function centred at a point between the two centres, which makes all the two electron integrals required for Hartree-Fock and DFT very easy to compute. One big disadvantage of Gaussian basis sets or any localised basis set is the basis set superposition error (BSSE). This results because atoms that interact have overlapping basis functions and thus an atom can "borrow" basis functions from nearby atoms, effectively increasing its basis set. Hence, because of BSSE the description of the basis set on an atom depends on the geometry of the system.

Gaussian basis sets are constructed by performing atomic SCF calculations to optimise the exponents (α) for the basis functions. These basis sets, complete with the optimised exponents, can then be used in calculations on molecules. The simplest basis sets are termed minimal basis sets, these have one linear combination of Gaussian functions to describe each of the occupied orbitals of of the atom of interest. So for a single water molecule one would have a basis set with 2H1s orbitals and one basis function for each of the 1s, 2s, $2p_x$, $2p_y$ and $2p_z$ orbitals of oxygen. Complexity is then added in two ways: one can have double zeta or triple zeta basis

functions, where each orbital is described by 2 or 3 linear combinations of Gaussians respectively, or additional linear combinations of Gaussians which describe orbitals which are unoccupied in the atom can be added so that an accurate description of polarisation in molecules is provided. Adding orbitals in this way is termed adding polarisation functions.

3.1.3.2 Plane Wave Basis Sets

In a periodic system there are an infinite number of electrons but Bloch's theorem states that the wavefunction must be periodic in order to satisfy the symmetry of the lattice:

$$\begin{aligned} \Psi_{j,k}(\boldsymbol{r}) &= u_j(\boldsymbol{r})e^{i\boldsymbol{k}.\boldsymbol{r}} \\ \text{where} \quad u_j(\boldsymbol{r}+\mathbf{1}) &= u_j(\boldsymbol{r}) \end{aligned} \tag{3.22}$$

In this equation $\boldsymbol{k}$ is a wavevector confined to the first Brillouin Zone, the vector $\mathbf{1}$ denotes the addition of some integral number of each of the lattice vectors and hence $u_j(\boldsymbol{r})$ is a function that has the same periodicity as the potential - in this case the periodicity of the lattice. As $u_j(\boldsymbol{r})$ is periodic it can be expanded in a Fourier series [14]:

$$\begin{aligned} u_j(\boldsymbol{r}) &= \sum_G c_{j,\boldsymbol{G}} e^{i\boldsymbol{G}.\boldsymbol{r}} \\ \Rightarrow \Psi_{j,k}(\boldsymbol{r}) &= \sum_G c_{j,\boldsymbol{G}} e^{i\boldsymbol{G}.\boldsymbol{r}} e^{i\boldsymbol{k}.\boldsymbol{r}} \\ \Rightarrow \Psi_{j,k}(\boldsymbol{r}) &= \sum_G c_{j,\boldsymbol{k}+\boldsymbol{G}} e^{i(\boldsymbol{k}+\boldsymbol{G}).\boldsymbol{r}} \end{aligned} \tag{3.23}$$

In this equation the $c_{j,\boldsymbol{k}+\boldsymbol{G}}$ are the expansion coefficients and the wavevectors $\boldsymbol{G}$ are such that the plane waves are commensurate with the lattice. In principle the number of $\boldsymbol{G}$ vectors and $\boldsymbol{k}$ vectors should be infinite but the values of the wavefunction at two points in reciprocal space are identical if those points are sufficiently

close. Thus the wavefunction can be calculated at a finite number of k-points. Furthermore, because the energy of a free electron with a wavevector $(\boldsymbol{k}+\boldsymbol{G})$ has an energy of $E_c = \frac{\hbar^2(\boldsymbol{k}+\boldsymbol{G})^2}{8m\pi^2}$ the size of a plane wave basis set can be specified with one parameter, a cutoff energy. Our basis set then contains all the plane waves whose "energies" are less than this cutoff. This is one advantage of plane waves, as unlike local orbital schemes, if one wishes to increase the size of the basis set it is simply a matter of increasing a single parameter rather than placing a whole new set of functions into the system. Furthermore, for plane waves there is no basis set superposition error.

Problematically, the curvature of the wavefunction is very large near nuclei and it is necessary to use a large number of plane waves to describe the wavefunction in these regions correctly. To sidestep this issue the core region is often treated using a pseudopotential, which replaces the real potential, within a core region of radius r_c with an effective potential. Modern pseudopotentials are constructed from first principles, such that the continuity of the wavefunctions and their first derivatives across the core boundary is preserved and the valence orbital eigenvalues are the same as those in an all electron calculation on the atom [14].

Throughout this thesis plane waves are used in simulations of periodic solids whilst Gaussians are used in simulations of clusters. To perform a cluster calculation using a plane wave code one would have to put the cluster in a simulation box, which would be repeated throughout space. This box would have to be large enough that repeats of the cluster in adjacent boxes would not interact with the cluster in the central box. For plane waves the size of the basis set is dependent on the size of the simulation box and hence cluster simulations with plane wave codes are very computationally expensive.

3.2 Analysing the electronic wavefunction

The discussion above refers only to wavefunctions. The wavefunction does not describe the system in terms of bonds or molecules. This is because in reality these are solely human ideas that make chemistry easier to understand. In the interests of understanding what is going on it would be useful to obtain information from wavefunctions about the electron density on particular molecules. Furthermore, it would be useful if one could break down the QM energy into components describing the amount of exchange, electrostatic force, correlation and short range repulsion. The first issue then is that one must first develop a method of partitioning the charge density between molecules.

3.2.1 Maximally Localised Wannier Functions

Unlike the Kohn-Sham orbitals obtained from DFT calculations using Gaussian basis sets, which can be thought of as atomic or molecular orbitals, the Kohn-Sham orbitals output by plane wave quantum simulations are difficult to interpret in terms of atoms and molecules because it is unclear how to partition the electron density. However, one can perform a Wannier transformation of the wavefunctions using a unitary matrix, U.

$$w_n(r) = \sum_{m=1}^{J} U_{mn}|\phi_m > \tag{3.24}$$

Where the sum from 1 to J runs over all the Kohn-Sham states ϕ_m. There is considerable flexibility in the choice of U, the unitary matrix, used to yield the Wannier function. In this work U is chosen so that the Wannier function spread, as calculated using equation 3.25, is minimised. This minimisation is carried out in an iterative procedure.

$$\Omega = \sum_{n=1}^{J}[< 0n|r^2|0n > - < 0n|r|0n >^2] = \sum_{n=1}^{J}(< r^2 >_n - \overline{\boldsymbol{r}}_n^2) \tag{3.25}$$

This procedure outputs a set of orbitals of low spread, so called maximally lo-

calised Wannier Functions [15], which have centres lying near molecular or atomic centres, which can be interpreted as molecular / atomic orbitals [16].

3.2.2 The electrostatic expansion

Having obtained descriptions of molecular orbitals it would be useful to have simple prescriptions to break down the energy into its constituent components. Calculating the amounts of exchange, short range repulsion and correlation is far from trivial but there are simple recipes for calculating the electrostatic interaction energies between molecules / atoms, which rely on the electrostatic expansion. The Born interpretation of quantum mechanics states that, if the wavefunction is normalised, then the charge density at any point is given by:

$$p(r) = |\Psi(r)|^2 \tag{3.26}$$

Where N is some normalisation constant and Ψ is the electronic wavefunction. The electric field due to a static charge distribution is given by Coulomb's Law:

$$\boldsymbol{E}(\boldsymbol{r}) = \frac{1}{4\pi\epsilon_0}\int \frac{\widehat{\boldsymbol{\imath}}}{\imath^2} p(\boldsymbol{r}')\mathrm{d}\tau' \tag{3.27}$$

Here $\widehat{\boldsymbol{\imath}}$ is a unit vector which points from $\boldsymbol{r}'$ to $\boldsymbol{r}$ and $\imath$ is the distance between $\boldsymbol{r}'$ and $\boldsymbol{r}$. This integral, which is taken over all space, is a vector function and is thus difficult to handle, however if the charges are not moving then it is a vector function whose curl is equal to zero at every point and as such it is equal to the gradient of some scalar. The scalar field whose grad is the electric field is called the potential and for a static charge distribution is given by:

$$V(\boldsymbol{r}) = \frac{1}{4\pi\epsilon_0}\int \frac{1}{\imath} p(\boldsymbol{r}')\mathrm{d}\tau' \tag{3.28}$$

It is possible to calculate $\imath$ using the law of cosines, where θ here is the angle

between the position vectors $\boldsymbol{r}$ and $\boldsymbol{r'}$:

$$\begin{aligned} \imath^2 = r^2 + (r')^2 - 2rr'\cos\theta' &= r^2\left[1 + \left(\frac{r'}{r}\right)^2 - 2\left(\frac{r'}{r}\right)\cos\theta'\right] \\ \Rightarrow \imath &= r(1+\epsilon)^{\frac{1}{2}} \\ \text{where} \quad \epsilon &= \left(\frac{r'}{r}\right)\left(\frac{r'}{r} - 2\cos\theta'\right) \end{aligned} \tag{3.29}$$

If the point of interest is well outside the charge distribution then ϵ is small and one may take a binomial expansion for $\frac{1}{\imath}$ thus:

$$\frac{1}{\imath} = \frac{1}{r}(1+\epsilon)^{-\frac{1}{2}} = \frac{1}{r}\left(1 - \frac{1}{2}\epsilon + \frac{3}{8}\epsilon^2 - \frac{5}{16}\epsilon^3 + ...\right) \tag{3.30}$$

Substituting in for ϵ and collecting together like powers of (r'/r) one obtains:

$$\frac{1}{\imath} = \frac{1}{r}\left[1 + \left(\frac{r'}{r}\right)\cos\theta' + \left(\frac{r'}{r}\right)^2 \frac{3\cos^2\theta' - 1}{2} + \left(\frac{r'}{r}\right)^3 \frac{5\cos^3\theta' - 3\cos\theta'}{2} + ...\right] \tag{3.31}$$

Pleasingly, the coefficients of the powers in the above equation are equal to the Legendre polynomials and thus equation 3.27 for the electrostatic potential can be rewritten:

$$V(\boldsymbol{r}) = \frac{1}{4\pi\epsilon_0}\sum_{n=0}^{\infty}\frac{1}{r^{(n+1)}}\int (r')^n P_n(cos\theta')p(\boldsymbol{r'})\mathrm{d}\tau' \tag{3.32}$$

Here the P_n are the various Legendre Polynomials and the equation is the multipole expansion. The first term is called the monopole (q), the second the dipole (μ), the third the quadrupole (θ), the fourth the octupole (Ω) and the fifth the hexadecapole (ξ). Typically two schemes are used to describe multipoles, the first expresses them in terms of spherical harmonics and the second in terms of Cartesian tensors. The Cartesian tensors for the first 5 terms in the multipole expansion are

given below (the Einstein summation convention is used throughout) [17]:

$$q = \int p(\boldsymbol{r})\mathrm{d}\boldsymbol{r} \tag{3.33}$$

$$\mu_\alpha = \int p(\boldsymbol{r}) r_\alpha \mathrm{d}\boldsymbol{r} \tag{3.34}$$

$$\theta_{\alpha\beta} = \frac{1}{2!}\int p(\boldsymbol{r})[3r_\alpha r_\beta - \boldsymbol{r}^2\delta_{\alpha\beta}]\mathrm{d}\boldsymbol{r} \tag{3.35}$$

$$\Omega_{\alpha\beta\gamma} = \frac{1}{3!}\int p(\boldsymbol{r})[15r_\alpha r_\beta r_\gamma - 3\boldsymbol{r}^2(r_\alpha\delta_{\beta\gamma} + r_\beta\delta_{\alpha\gamma} + r_\gamma\delta_{\alpha\beta})]\mathrm{d}\boldsymbol{r} \tag{3.36}$$

$$\begin{aligned}\xi_{\alpha\beta\gamma\delta} = & \frac{1}{4!}\int p(\boldsymbol{r})[105r_\alpha r_\beta r_\gamma r_\delta + 3\boldsymbol{r}^4(\delta_{\alpha\beta}\delta_{\gamma\delta} + \delta_{\alpha\gamma}\delta_{\beta\delta} + \delta_{\alpha\delta}\delta_{\beta\gamma}) \\ & - 15\boldsymbol{r}^2(r_\alpha r_\beta\delta_{\gamma\delta} + r_\alpha r_\gamma\delta_{\beta\delta} + r_\alpha r_\delta\delta_{\beta\gamma} + r_\beta r_\gamma\delta_{\alpha\delta} + r_\beta r_\delta\delta_{\alpha\gamma} + r_\gamma r_\delta\delta_{\alpha\beta})]\mathrm{d}\boldsymbol{r}\end{aligned} \tag{3.37}$$

These multipoles can be easily obtained from the Wannier functions described in section 3.2.1. Furthermore, electrostatic expansions can be calculated from the wavefunctions obtained from calculations using Gaussian basis sets (this process is described in section 3.2.3).

Two point charges separated by a distance r have a potential energy of $\frac{q_1 q_2}{r}$ atomic units. As equation 3.32 shows this is equal to the potential at $\boldsymbol{r}$ due to the monopole q_1 multiplied by the value of the charge at $\boldsymbol{r}$ (i.e. q_2). A point dipole is charge neutral and thus it follows from the sentiment expressed in the previous sentence that the dipole multiplied by the electric potential at a point will be equal to zero. However, the dipole multiplied by the value of the gradient of the potential is non-zero. From this rather simplistic proof we can assert that a multipole of rank n interacts with the n^{th} derivative of the electric potential. It is thus possible to calculate interaction tensors between a monopole and a rank n multipole by

differentiating $(1/R)$, the first five of these are given below [17]:

$$T = \frac{1}{R} \tag{3.38}$$

$$T^{\alpha} = \nabla_{\alpha} T = \frac{R_{\alpha}}{R^3} \tag{3.39}$$

$$T^{\alpha} = \nabla_{\alpha} T^{\beta}_{ij} = \frac{3R_{\alpha}R_{\beta} - R^2\delta_{\alpha\beta}}{R^5} \tag{3.40}$$

$$T^{\alpha} = \nabla_{\alpha} T^{\beta\gamma} = \frac{1}{R^7}[15R_{\alpha}R_{ij,\beta}R_{\gamma} - 3R^2(R_{\alpha}\delta_{\beta\gamma} + R_{\beta}\delta_{\alpha\gamma} + R_{\gamma}\delta_{\alpha\beta})] \tag{3.41}$$

$$\begin{aligned} T^{\alpha\beta\gamma\delta} &= \nabla_{\alpha} T^{\beta\gamma\delta} = \frac{1}{R^9_{ij}}[105R_{\alpha}R_{\beta}R_{\gamma}R_{\delta} + 3R^4(\delta_{\alpha\beta}\delta_{\gamma\delta} + \delta_{\alpha\gamma}\delta_{\beta\delta} + \delta_{\alpha\delta}\delta_{\beta\gamma})] \\ &- 15R^2(R_{\alpha}R_{\beta}\delta_{\gamma\delta} + R_{\alpha}R_{\gamma}\delta_{\beta\delta} + R_{\alpha}R_{\delta}\delta_{\beta\gamma} + R_{\beta}R_{\gamma}\delta_{\alpha\delta} + R_{\beta}R_{\delta}\delta_{\alpha\gamma} + R_{\gamma}R_{\delta}\delta_{\alpha\beta})] \end{aligned} \tag{3.42}$$

$$\begin{aligned} T^{\alpha\beta\gamma\delta\epsilon} &= \nabla_{\alpha} T^{\beta\gamma\delta\epsilon} = \frac{1}{R^{11}_{ij}}[945R_{\alpha}R_{\beta}R_{\gamma}R_{\delta}R_{\epsilon} + 15R^4(R_{\epsilon}\delta_{\alpha\beta}\delta_{\gamma\delta} + R_{\epsilon}\delta_{\alpha\gamma}\delta_{\beta\delta} \\ &+ R_{\epsilon}\delta_{\alpha\delta}\delta_{\beta\gamma} + R_{\delta}\delta_{\alpha\beta}\delta_{\gamma\epsilon} + R_{\delta}\delta_{\alpha\gamma}\delta_{\beta\epsilon} + R_{\delta}\delta_{\alpha\epsilon}\delta_{\beta\gamma} + R_{\delta}\delta_{\beta\epsilon}\delta_{\gamma\delta} + R_{\alpha}\delta_{\gamma\epsilon}\delta_{\beta\delta} + R_{\alpha}\delta_{\delta\epsilon}\delta_{\beta\gamma} \\ &+ R_{\beta}\delta_{\alpha\epsilon}\delta_{\gamma\delta} + R_{\beta}\delta_{\alpha\gamma}\delta_{\delta\epsilon} + R_{\beta}\delta_{\alpha\delta}\delta_{\gamma\epsilon} + R_{\gamma}\delta_{\alpha\beta}\delta_{\delta\epsilon} + R_{\gamma}\delta_{\alpha\epsilon}\delta_{\beta\delta} + R_{\gamma}\delta_{\alpha\delta}\delta_{\beta\epsilon}) \\ &- 105R^2_{ij}(R_{\alpha}R_{\beta}R_{\gamma}\delta_{\delta\epsilon} + R_{\alpha}R_{\beta}R_{\delta}\delta_{\gamma\epsilon} + R_{\alpha}R_{\beta}R_{\epsilon}\delta_{\gamma\delta} + R_{\alpha}R_{\gamma}R_{\delta}\delta_{\beta\epsilon} + R_{\alpha}R_{\gamma}R_{\epsilon}\delta_{\beta\delta} \\ &+ R_{\alpha}R_{\delta}R_{\epsilon}\delta_{\beta\gamma} + R_{\beta}R_{\gamma}R_{\delta}\delta_{\alpha\epsilon} + R_{\beta}R_{\gamma}R_{\epsilon}\delta_{\alpha\delta} + R_{\beta}R_{\delta}R_{\epsilon}\delta_{\alpha\gamma} + R_{\gamma}R_{\delta}R_{\epsilon}\delta_{\alpha\beta})] \end{aligned} \tag{3.43}$$

Rather conveniently it can be shown that the potential energy of interaction between a rank n multipole and a rank k multipole is simply given by the concatenation of the rank k multipole, the rank n multipole and the rank (n+k) interaction tensor [17].

The multipole expansion also provides a convenient method for describing the distortions of a charge distribution that occur when it is introduced into a crystal. As established above a rank n multipole interacts with the n^{th} derivative of the electric potential, so it can be expressed as a convergent power series in the n^{th} derivative of the electric potential [18] - i.e. for the dipole and quadrupole:

$$\mu_{\alpha} = \mu^0_{\alpha} + \alpha_{\alpha\beta}\nabla_{\beta}V + \frac{1}{2}\beta_{\alpha\beta\gamma}\nabla_{\beta}V\nabla_{\gamma}V + ... \tag{3.44}$$

$$\theta_{\alpha\beta} = \theta^0_{\alpha\beta} + \alpha_{\alpha\beta\gamma\delta}\nabla_{\gamma}\nabla_{\delta}V + \frac{1}{2}\beta_{\alpha\beta\gamma\delta\epsilon\zeta}\nabla_{\gamma}\nabla_{\delta}V\nabla_{\epsilon}\nabla_{\zeta}V + ... \tag{3.45}$$

3.2.3 Distributed Multipole Analysis

The electrostatic expansion for the electric potential converges at all points outside the charge distribution of interest, in other words there is a sphere of convergence outside of which the multipole series converges. One method commonly used to shrink the size of the sphere of convergence is to use distributed multipoles, so rather than having one molecular multipole expansion one has multiple expansions situated at various sites about the molecule (usually the atoms and the centres of bonds). Stone [19] has developed a way of calculating site multipoles directly from the density matrix calculated using a quantum mechanics code which employs Gaussian basis sets. He first notes that the total electron density is given by:

$$p(\boldsymbol{r}) = \sum_{tu} c_t \phi_t(\boldsymbol{r}) c_u \phi_u(\boldsymbol{r}) = \sum_{tu} p_{tu} \phi_t(\boldsymbol{r}) \phi_u(\boldsymbol{r}) \tag{3.46}$$

And that the overlap of two primitive Gaussian functions centred at $\boldsymbol{A}$ and $\boldsymbol{B}$ is a Gaussian centred at $\boldsymbol{P}$, which is given by:

$$\boldsymbol{P} = \frac{\alpha \boldsymbol{A} + \beta \boldsymbol{B}}{\alpha + \beta} \tag{3.47}$$

Thus the charge density can be rewritten as:

$$p(\boldsymbol{r}) = \sum_{tu} -p_{tu} f_t(\boldsymbol{r} - \boldsymbol{A}) f_u(\boldsymbol{r} - \boldsymbol{B}) \exp\left(-\frac{\alpha\beta}{\alpha+\beta}(\boldsymbol{A} - \boldsymbol{B})^2\right) \exp(-(\alpha+\beta)(\boldsymbol{r} - \boldsymbol{P})^2) \tag{3.48}$$

Where $f_t(\boldsymbol{r} - \boldsymbol{A})$ is a homogenous polynomial in the Cartesian components of $(\boldsymbol{r} - \boldsymbol{A})$ as described in section 3.1.3.1. Each term in the above expansion can be expanded as a multipole expansion, with the charge, dipole and quadrupole in them

given by:

$$
\begin{aligned}
q &= -N \int p_{tu} F_{tu}(\boldsymbol{r} - \boldsymbol{P}) \exp(-(\alpha+\beta)(\boldsymbol{r} - \boldsymbol{P})^2) \mathrm{d}\boldsymbol{r} && (3.49)\\
\mu_\alpha &= -N \int p_{tu} r_\alpha F_{tu}(\boldsymbol{r} - \boldsymbol{P}) \exp(-(\alpha+\beta)(\boldsymbol{r} - \boldsymbol{P})^2) \mathrm{d}\boldsymbol{r} && (3.50)\\
\theta_{\alpha\beta} &= -N \int p_{tu} (3 r_\alpha r_\beta - \delta_{\alpha\beta} \boldsymbol{r}^2) F_{tu}(\boldsymbol{r} - \boldsymbol{P}) \times && (3.51)\\
&\qquad\qquad \exp(-(\alpha+\beta)(\boldsymbol{r} - \boldsymbol{P})^2) \mathrm{d}\boldsymbol{r}\\
N &= \exp\left(-\frac{\alpha\beta}{\alpha+\beta}(\boldsymbol{A} - \boldsymbol{B})^2\right)\\
F_{tu}(\boldsymbol{r} - \boldsymbol{P}) &= f_t(\boldsymbol{r} - \boldsymbol{A}) f_u(\boldsymbol{r} - \boldsymbol{B})
\end{aligned}
$$

So the first step in creating the distributed multipole representation is to convert every element in the density matrix from a Gaussian function into a multipole expansion. In and of itself this is not that useful but it is relatively easy to convert a multipole expansion centred at r_j to a multipole expansion centred at the origin (s) using the equations below:

$$
\begin{aligned}
Q_s &= q_j\\
\mu_{s,\alpha} &= q_j r_{j,\alpha} + \mu_{j,\alpha}\\
\theta_{s,\alpha\beta} &= (3 r_{j,\alpha} r_{j,\beta} - \delta_{\alpha\beta} \boldsymbol{r_j}^2) q_j + 3 r_{j,\alpha} \mu_{j,\beta} - \delta_{\alpha\beta} \boldsymbol{\mu_j} \cdot \boldsymbol{r_j} + \theta_{j,\alpha\beta} && (3.52)
\end{aligned}
$$

Where q_j, μ_j and θj are the charge, dipole and quadrupole of the multipole expansion centred at r_j. It is thus easy to see that this equation can be used is to generate molecular multipoles from the "distributed multipole" representation of the density matrix obtained using equations 3.49, 3.50 and 3.52. More useful though is to use this equation to shift the multipoles generated using equations 3.49, 3.50 and 3.52 onto the nearest site of interest on the molecule (usually atoms and bond centres) and thus generate a compact representation of the charge density with a small sphere of convergence.

3.3 Classical Interaction Potentials

So far, other than a digression about obtaining electrostatic information from quantum mechanical calculations, the discussion of calculation of energy for a given structure has focused on techniques based on quantum mechanics. These methods, although accurate, have one major disadvantage - they are computationally expensive and as such they are not feasible if one wishes to probe a large amount of configuration space or if one wishes to study large systems. In these scenarios an alternative classical methodology can be employed. These methods rely on the observation that for any system the potential energy may be divided into terms depending on the coordinates of individual atoms, pairs, triplets, etc [20]:

$$\begin{aligned} V &= \sum_i v_1(\boldsymbol{r}_i) + \sum_i \sum_{j>i} v_2(\boldsymbol{r}_i, \boldsymbol{r}_j) + \sum_i \sum_{j>i} \sum_{k>j>i} v_3(\boldsymbol{r}_i, \boldsymbol{r}_j, \boldsymbol{r}_k) \\ &+ \sum_i \sum_{j>i} \sum_{k>j>i} \sum_{l>k>j>i} v_4(\boldsymbol{r}_i, \boldsymbol{r}_j, \boldsymbol{r}_k, \boldsymbol{r}_l) + \ldots \end{aligned} \tag{3.53}$$

The functions in this expression, that are used to describe the dependence of the potential energy on the various coordinates, contain variable parameters that can be fitted to the results of quantum mechanics calculations or to experimental observables. Furthermore, this series is convergent and so none of the potential models used in this thesis employ anything higher than terms in quadruplets. In fact most potentials incorporate the effects of 3 and higher body terms into the two body interaction and neglect the first term thus providing a description of the dependence of the potential energy on the atomic or molecular coordinates purely in terms of the separation of atoms.

Commonly for water potentials the vibrational degrees of freedom of the water molecules are neglected and only the interaction between water molecules is described. The interaction of two water molecules is described by distributing charge (or multipole) centres about the water molecules to approximately reproduce the charge density of the water molecules. These point charges then interact with the

point charges on a neighbouring water molecule through Coulomb's law. The short range repulsion due to orbital overlap at small separations is typically described using some rapidly decaying function like an exponential or a (A/r^{12}) function and dispersion forces are described using a (B/r^6) function, which mimics the rate of decay of the lowest order dispersive interaction, the dipole induced dipole interaction [20].

3.3.1 The Shell Model

As mentioned above the forces due to the triples and quadruples in equation 3.53 are often incorporated, by the way the potential is fitted, into the two body terms. An alternative more accurate, but more computationally expensive, way of incorporating these higher order terms is to use a shell model. These models still rely only on a sum over all the distinct pairs of particles in the system but incorporate functions that describe the effect that the higher body terms have on the magnitude of the two body interaction by explicitly describing polarisation. Induced multipoles are described by adding extra degrees of freedom to the model - for dipoles these degrees of freedom have a self energy given by $\frac{1}{2}\alpha|\boldsymbol{\mu}|^2$ and the total energy of all the induced dipoles in the system is:

$$E_{\text{dip}} = \frac{1}{2}\alpha|\boldsymbol{\mu}|^2 + \sum_{j=1}^{N}\sum_{k=1}^{N}\left[q_j T_\alpha \mu_{k,\alpha} + \frac{1}{2}\mu_{j,\alpha} T_{\alpha\beta}\mu_{k,\beta}\right] \tag{3.54}$$

As electronic relaxation is much faster than atomic motion one would expect that the dipolar energy will be at a minimum at all times. Hence, one way to perform simulations using this model involves the minimisation of the dipolar energy, either self consistently or using a minimisation algorithm [20], whenever the atoms are moved. In molecular dynamics, an alternative approach is commonly used, the shell is given a fake mass and these equations are incorporated directly into the Hamiltonian [20].

Most commonly only dipoles are described in this way although the method is general and has been extended up to quadrupoles by some workers [21]. Furthermore, if the dipole is represented by two charges connected by a spring, so that the self energy becomes a harmonic term in the length of the spring, a more powerful description of the electronic distortions is provided.

3.3.2 The Ewald Sum

So far the above discussion has applied to simulating small clusters of atoms or molecules. If one wishes to model bulk systems one has to introduce periodic boundary conditions - i.e. periodically repeat the box and all its constituent particles throughout space. Within this supercell, either the minimum image convention is used to calculate the total energy, so each particle interacts with the N-1 (N=number of particles in simulation cell) nearest particles to it in the supercell, or the supercell is generated explicitly [1, 20].

If one has a large enough simulation box, periodic boundary conditions and the minimum image convention would be enough to describe the fully periodic system because the energy of interaction of two molecules decays with distance. For rapidly decaying functions like $(1/r^6)$ this is sufficient. However, for electrostatic interactions, that have a $(1/r)$ dependence on the interatomic separation, the decay is far too gentle and a technique called the Ewald sum [22, 23], which exploits the periodicity of the system, has to be employed. With periodic boundary conditions the potential energy of interacting of point charges can be written as:

$$V = \frac{1}{2}\sum_{\boldsymbol{n}}{}' \left(\sum_{i=1}^{N}\sum_{j=1}^{N} \frac{z_i z_j}{\boldsymbol{r_{ij}} + \boldsymbol{n}} \right) \tag{3.55}$$

Here the sum over all $\boldsymbol{n}$ is over all simple cubic lattice points ($\boldsymbol{n} = (n_x L, n_y L, n_z L)$) and represents the shape of the basic box and the prime indicates that for $\boldsymbol{n} = 0$ the $i = j$ term is omitted. In the Ewald sum a screening distribution with equal

magnitude but opposite sign to the point charge of interest and width κ is added at every point charge. In most implementations this distribution is given by:

$$p_i(\boldsymbol{r}) = \frac{z_i \kappa^3}{\pi^{3/2}} \exp(-\kappa^2 r^2) \tag{3.56}$$

This distribution screens the interaction between neighbouring point charges and as such makes all the interactions short ranged. To reduce the overall potential back to that for the original set of point charges a cancelling distribution is added. This distribution has the same shape but opposite sign to the screening distribution and is summed in reciprocal space - i.e. it is the sum of the Fourier transforms of each cancelling distribution. The resulting sum is then transformed back into real space and added to the part summed in real space. However, because it was summed in reciprocal space, the periodic repeats of the screening distributions are included and the long range parts of the electrostatic interaction are recovered. One important correction must be included, the recipe as described so far includes the interaction of the cancelling distribution centred at $\boldsymbol{r_i}$ with itself, so this self term must be subtracted.

The width of the screening distribution, κ, used in the Ewald sum controls the amount of the material summed in real space. The remainder is then summed in reciprocal space. This parameter is typically chosen so that the contents of the central unit cell are treated in real space and contribution of periodic repeats of the unit cell are treated in the reciprocal space sum. In practice this is done by selecting a value of κ so that the Gaussian is fully decayed within half the shortest box length of the simulation cell.

The Ewald sum can, and has, been generalised so that it can be used with dipoles, quadrupoles and higher order multipoles [24] and there is also a Ewald sum for systems that are only periodic in 2 directions [25]. Furthermore, where one has charges distributed throughout a molecule there is a Ewald sum which performs an intermolecular Coulomb subtract [26].

3.3.3 Quantum Mechanics / Molecular Mechanics

The above discussion about calculating the energy highlights a dilemma in all simulation work: Most systems of interest are too large to be studied using quantum chemical calculations but it is difficult to be certain of the verity of any potential based approach if one is working on a system to which the potential wasn't fitted. QM / MM provides an attractive method of avoiding these issues by allowing one to model certain parts of the system with QM approaches and other parts with a molecular mechanical forcefield. This is particularly useful for systems into which a small localised perturbation has been introduced, as obviously the area near the perturbation can be modelled with QM, whilst surrounding areas, which are largely unaffected by the perturbation, can be treated with a forcefield, fitted to reproduce the properties of the unperturbed system. These sorts of hybrid schemes have been applied with great success to the study to study catalytic processes on surfaces [27] and to study the reactions of proteins [28].

The many ways of implementing QM/MM schemes have been recently reviewed by Lin and Truhler [29] but in this work, the embedding method from QUASI (the Quantum Simulation in Industry project) was used. This works by creating a cluster, which is then divided up into a series of concentric regions each of which is treated using a different level of approximation (see figure 3.1). This is all implemented in ChemShell [27] which allows one to use "GAMESS-UK" to simulate quantum regions [30] and GULP [31] to simulate classical regions.

To generate the cluster one first performs an optimisation of the periodic, unperturbed structure using an accurate molecular mechanics forcefield. The finite cluster is then generated by cutting out a sphere of crystal and distributing point charges around the sphere so that the infinite Madelung potential is reproduced in the active region. The cluster is then divided into regions - the most central region

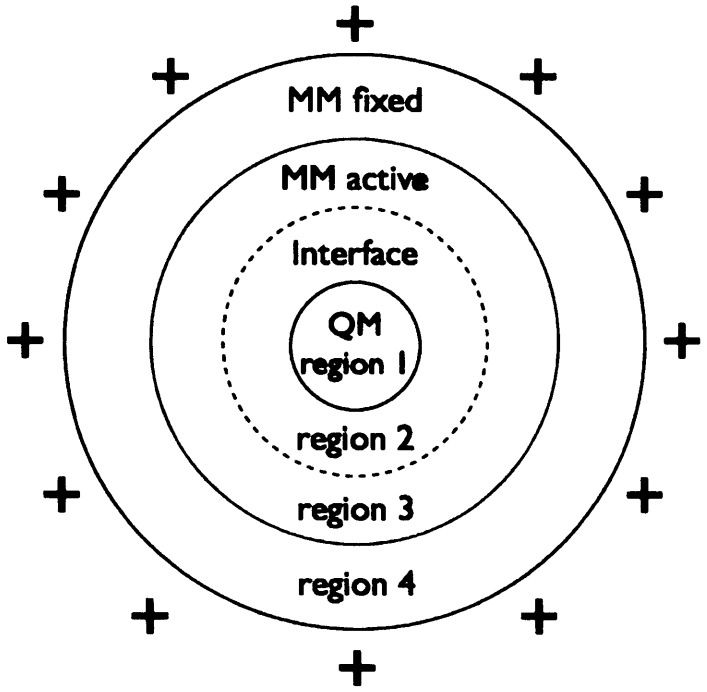

Figure 3.1: Diagram showing the regions of the cluster in QM/MM calculations. Red line indicates the boundary between active region and fixed region and the plus signs indicate the locations of the point charges in region 5.

(region 1) is modelled using quantum mechanics with a Hamiltonian given by:

$$H_{\text{total}} = H_{\text{QM}} + H_{\text{QM/MM,electro}} + H_{\text{QM/MM,non-electro}} \tag{3.57}$$

This equation is the sum of a QM Hamiltonian, which has be dealt with in the sections above on DFT and Hartree-Fock, and some QM/MM Hamiltonian. Finding an explicit form for the QM/MM Hamiltonian is non-trivial, although it is reasonable to divide it into two components:

1. An interaction with the point charges that describe the charge distributions on the MM molecules. This electrostatic interaction can of course distort the electron density causing polarisation which is why it is dealt with separately.

2. A non-electrostatic interaction between the MM molecules and the QM molecules. In QUASI these contributions to the energy are modelled using the same simple distant dependent functions used to model these interactions in the MM forcefield.

Region one is surrounded by region 3 in which the atoms interact through the MM forcefield or by an additional interface region, region 2, which is then surrounded by atoms that interact through the MM forcefield. This interface is used to make the transition from QM to MM description of the interactions less harsh. When optimising all molecules in the active region (regions 1,2 and 3) are free to move but in the surrounding regions (regions 4 and 5) the molecules are held fixed. The "molecules" in these two regions only interact through the electrostatic interaction with the molecules in the active region so only point charges are present in them. The difference is that, whereas in region 4 these point charges are distributed as they would be in a periodic crystal of molecules, in region 5 the point charges are simply distributed on a sphere.

3.4 Moving atoms about

The business of calculating the potential energy has now been covered and we now need a method for selecting reasonable points for calculating the ensemble averages discussed at the start of this chapter. Three of the most commonly used methods are described below:

3.4.1 Lattice Minimisation

The potential energy surface contains many minima of varying depths and at 0K, the static limit, the system will be at a minimum. Furthermore, even at higher temperatures the structure will only be oscillating about a minimum, all of which makes the structures at these minima very important in determining the properties of materials. Thus, one important simulation technique is to minimise the potential energy of the system to establish what the nearest local minimum is for a given starting structure. One crude way to do this is to run molecular dynamics (see section 3.4.2) at a very low temperature. In this approach, however, the system still has some kinetic energy and hence the system is not truly probing the static,

0 K, structure. Therefore, it is often more appropriate to use numerical recipes specifically designed to minimise N dimensional functions to minimise the energy of the system and hence obtain the 0 K structure. These minimisation strategies work by doing a sequence of line-searches for minima until all the gradients of the function are close to zero [20].

3.4.2 Molecular dynamics

Molecular dynamics allows one to produce real trajectories for the atoms in the system and so to replace ensemble averages with time averages. Trajectories are obtained by integrating Newton's second law of motion, which of course assumes that the constituent atoms / molecules can be thought of as classical particles. For many body systems the exact integration of Newton's second law of motion is impossible and so the integration has to be discretized in some way. In this work the Verlet Leapfrog [32] algorithm is used, which calculates new velocities at the half time step from the current acceleration and then updates the positions using these new velocities:

$$\boldsymbol{v}(t+\frac{1}{2}\delta t) = \boldsymbol{v}(t-\frac{1}{2}\delta t) + \delta t\boldsymbol{a}(t) \tag{3.58}$$

$$\text{where} \quad \boldsymbol{a}(t) = \frac{\boldsymbol{F}(t)}{m} \tag{3.59}$$

$$\boldsymbol{r}(t+\delta t) = \boldsymbol{r}(t) + \boldsymbol{v}(t+\frac{1}{2}\delta t)\delta t \tag{3.60}$$

The following flow chart shows how a typical molecular dynamics (eg DL_POLY [33]) code works:

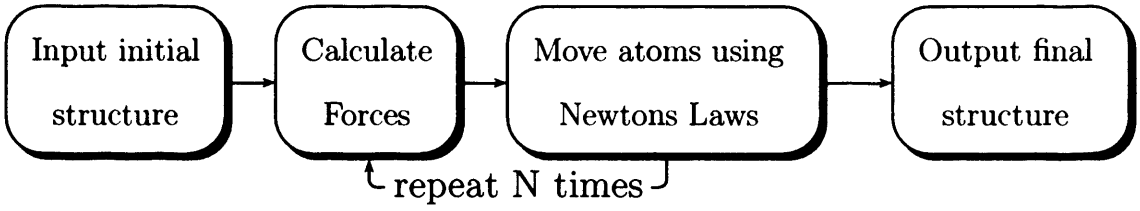

At the start of the simulation the atoms are assigned random velocities according

to the Maxwell-Boltzmann distribution for the temperature of interest.

3.4.2.1 Rigid bonds

As already discussed in section 3.3 a common way to treat intramolecular forces is to assume that they are independent of the surroundings the molecule finds itself in - i.e. to treat molecules as rigid entities. In molecular dynamics this is a useful approximation because intramolecular vibrations are very rapid and thus short time steps are required to get accurate integration of the equations of motion and any purely classical treatment of bond vibration is questionable. Furthermore, it is reasonable as long as the amplitude of vibration is small compared with the molecular dimensions.

For a water molecule fixing the bond lengths and angle results in a reduction in the number of degrees of freedom from 9 to 6. These 6 degrees of freedom can be divided into the 3 translational degrees of freedom of the centre of mass, which can be treated using the maths of the previous section, and 3 rotational degrees of freedom [34], which require a reformulation of Newton's Laws, in which forces are replaced by torques, $\boldsymbol{\tau_i}$ and linear momenta by angular momenta:

$$\boldsymbol{\tau_i} = \sum_a (\boldsymbol{r_{ia}} - \boldsymbol{r_i}) \times \boldsymbol{f_{ia}} = \sum_a \boldsymbol{d_{ia}} \times \boldsymbol{f_{ia}} \tag{3.61}$$

$$\text{and} \quad \boldsymbol{\tau} = \frac{\mathrm{d}\boldsymbol{L}}{\mathrm{dt}} \tag{3.62}$$

$$\text{with} \quad \boldsymbol{L_\alpha} = I_{\alpha\beta}\boldsymbol{\omega_\beta} \tag{3.63}$$

Where $\boldsymbol{d_{ia}}$ is the vector connecting the centre of mass to the site at a, $\boldsymbol{f_{ia}}$ is the force on that site and $I_{\alpha\beta}$ is a rank 2 tensor called the moment of inertia, which is given by [35, 36]:

$$I_{\alpha\beta} = m(\delta_{\alpha\beta}\boldsymbol{r}^2 - r_\alpha r_\beta) \tag{3.64}$$

In recasting Newton's laws of motion as equations describing rotational motion the position vectors are replaced by vectors that give the orientation of the molecule

- *i.e.* the relation between an axis system fixed in space and one fixed with respect to the body. In the case of a water molecule the 3 vectors that provide a body frame are the HOH bisector, the cross product of the two OH vectors and the cross product of these two vectors. Any unit vector $\boldsymbol{e}$ may be expressed in either the body-fixed or space-fixed frames and one may convert from body-fixed vector to the corresponding space-fixed vector using the rotation matrix $\boldsymbol{A}$.

$$\boldsymbol{e}^{\boldsymbol{b}} = \boldsymbol{A}.\boldsymbol{e}^{\boldsymbol{s}} \tag{3.65}$$

The nine components of the rotation matrix, which completely defines the molecular orientation, are the direction cosines of the body-fixed axis vectors in the space-fixed frame. These quantities may be expressed in terms of the three Euler angles ϕ (angle of rotation about the z axis), θ (angle of rotation about the x axis) and ψ (another angle of rotation about the z axis but one that occurs after the first two rotations) [34]:

$$\boldsymbol{A} = \begin{pmatrix} \cos\phi\cos\psi - \sin\phi\cos\theta\sin\psi & \sin\phi\cos\psi + \cos\phi\cos\theta\sin\psi & \sin\theta\sin\psi \\ -\cos\phi\sin\psi - \sin\phi\cos\theta\cos\psi & -\sin\phi\sin\psi + \cos\phi\cos\theta\cos\psi & \sin\theta\cos\psi \\ \sin\phi\sin\theta & -\cos\phi\sin\theta & \cos\theta \end{pmatrix}$$

One can link the values of the time derivatives in the bond-fixed and space-fixed frameworks and thus derive equations of motions in terms of the three Euler angles. But these equations diverge whenever θ approaches 0 or π because the angles ϕ and ψ are then identical. This can be resolved by using quaternion parameters as generalised coordinates [37, 38] - where a quaternion is a set of four scalar quantities (q_0, q_1, q_2, q_3), which satisfy the constraint:

$$q_0^2 + q_1^2 + q_2^2 + q_3^2 = 1 \tag{3.66}$$

There are multiple ways to use these to define the molecular orientation but the

most convenient choice, in the Euler angle convention, is to define [34]:

$$\begin{aligned} q_0 &= \cos\frac{\theta}{2}\cos\frac{\phi+\psi}{2} \\ q_1 &= \sin\frac{\theta}{2}\cos\frac{\phi-\psi}{2} \\ q_2 &= \sin\frac{\theta}{2}\sin\frac{\phi-\psi}{2} \\ q_3 &= \cos\frac{\theta}{2}\sin\frac{\phi+\psi}{2} \end{aligned} \tag{3.67}$$

The rotation matrix then becomes

$$\boldsymbol{A} = \begin{pmatrix} q_0^2+q_1^2-q_2^2-q_3^2 & 2(q_1q_2+q_0q_3) & 2(q_1q_3-q_0q_2) \\ 2(q_1q_2-q_0q_3) & q_0^2-q_1^2+q_2^2-q_3^2 & 2(q_2q_3+q_0q_1) \\ 2(q_1q_3+q_0q_2) & 2(q_2q_3-q_0q_1) & q_0^2-q_1^2-q_2^2+q_3^2 \end{pmatrix}$$

and the equations of motion for the molecules can be written in terms of the quaternions as:

$$\begin{pmatrix} \dot{q}_0 \\ \dot{q}_1 \\ \dot{q}_2 \\ \dot{q}_3 \end{pmatrix} = \frac{1}{2}\begin{pmatrix} q_0 & -q_1 & -q_2 & -q_3 \\ q_1 & q_0 & -q_3 & q_2 \\ q_2 & q_3 & q_0 & -q_1 \\ q_3 & -q_2 & q_1 & q_0 \end{pmatrix}\begin{pmatrix} 0 \\ \omega_x^b \\ \omega_y^b \\ \omega_z^b \end{pmatrix}$$

This set of first order differential equations contain no unpleasant singularities and can be solved using a Verlet Leapfrog algorithm [39]. This algorithm stores the values of $\boldsymbol{L}^s(t-\frac{1}{2}\delta t)$ and $\boldsymbol{Q}(t)$, while the values of the torques, $\boldsymbol{\tau}^s(t)$ are calculated from the instantaneous positions and orientations. These quantities can be used to calculate $\boldsymbol{L}^s(t)$ and then, because the angular velocity in the body-fixed frame can be calculated from the angular momentum, $\boldsymbol{Q}(t+\frac{1}{2}\delta t)$ can be calculated:

$$\boldsymbol{L}^s(t) = \boldsymbol{L}^s(t-\frac{1}{2}\delta t) + \frac{1}{2}\delta t\boldsymbol{\tau}^s(t) \tag{3.68}$$

$$\boldsymbol{Q}(t+\frac{1}{2}\delta t) = \boldsymbol{Q}(t) + \frac{1}{2}\dot{\boldsymbol{Q}}(t)\delta t \tag{3.69}$$

The values from these two equations provide an estimate of $\boldsymbol{Q}(t+\frac{1}{2}\delta t)$, which makes transformations from space-fixed to body-fixed angular momentums and the calculation of $\dot{\boldsymbol{Q}}$ at the half time step possible. This result is used in the second of the main algorithm equations, given below, to calculate $\dot{\boldsymbol{Q}}(t+\frac{1}{2}\delta t)$ from the value of $\boldsymbol{L}^s(t+\frac{1}{2}\delta t)$, which is calculated in the first step:

$$\boldsymbol{L}^s(t+\frac{1}{2}\delta t) = \boldsymbol{L}^s(t-\frac{1}{2}\delta t)+\delta t\boldsymbol{\tau}^s(t) \tag{3.70}$$

$$\boldsymbol{Q}(t+\delta t) = \boldsymbol{Q}(t)+\delta t\dot{\boldsymbol{Q}}(t+\frac{1}{2}\delta t) \tag{3.71}$$

This algorithm is implemented in DL_POLY_2 [33].

3.4.2.2 Selecting an ensemble

The molecular dynamics methods discussed so far would sample trajectories in the NVE ensemble. Ideally though one wishes to do obtain trajectories in which pressure and temperature are kept constant, which would better represent the conditions under which experiments are undertaken. In order to apply these constraints a model is required that exchanges energy / volume between the system and some external "energy bath" / "volume bath" using some type of thermostat / barostat.

Thermostating The instantaneous temperature of a system can be calculated from the momenta of the particles within that system [1]:

$$\mathcal{T} = \frac{2}{3Nk_B}\sum_{i=1}^{N}\frac{p_i^2}{2m_i} \tag{3.72}$$

A simple method to control the temperature of the system is thus to rescale the velocities by a factor of $\sqrt{(T/\mathcal{T})}$, which ensures that they are lying on the Boltzmann distribution of velocities for the temperature T [1]. This rescaling can be applied at every time step or every N time steps, in which case $\mathcal{T}$ is replaced by $<\mathcal{T}>_{\text{last N}}$, and is invaluable for setting T during the equilibration phase [40].

However, the equations solved are not the true equations of motion of the system [41] and during the production run this is a far too brutal method to control the temperature. Berendsen [42] suggested that instead of simply rescaling the velocities in one time step the system be brought back to the appropriate temperature in a time τ, which can be adjusted by the user until any strange behaviour resulting from the velocity rescaling disappears:

$$p_i \rightarrow p_i \times \sqrt{1 + \frac{\delta t}{\tau}\left(\frac{T}{\mathcal{T}} - 1\right)} \tag{3.73}$$

Berendsen *et al.* [42] have shown that this works very well for water when $\tau = 0.4$ps. This method still does not generate true NVT trajectories because the constant temperature constraint is not been incorporated into the Hamiltonian. Nonetheless, this method proves very useful for the purposes of changing state and equilibrating.

Barostating Much like for temperature, instantaneous pressures can be calculated [1]. However, instantaneous pressure rescaling introduces catastrophic errors into the dynamics of the system and as such all pressure rescaling is done in some user defined relaxation time. Pressure is a second order tensor and as such one can implement the cell shape changes in an isotropic or anisotropic manner. In the isotropic case [42]:

$$\begin{aligned}
\mathcal{P} &= \frac{Nk_B\mathcal{T}}{V} - \frac{1}{3V}\sum_i\sum_j r_{ij}F_{ij} \qquad \text{Instantaneous pressure} \qquad (3.74)\\
\chi &= 1 - \beta_T\frac{\delta t}{t_p}(P - \mathcal{P})\\
r &\rightarrow \chi^{1/3}r \qquad V \rightarrow \chi V \qquad \text{Rescale cell lengths and volume}
\end{aligned}$$

While in the anisotropic case, the cell vectors are rescaled so the instantaneous

pressure and scaling factor must both be second order tensors [33]:

$$\mathcal{P}_{\alpha\beta} = \frac{Nk_BT}{V} - \frac{1}{3V}\sum_i\sum_j r_{ij,\alpha}F_{ij,\beta} \tag{3.75}$$

$$\eta_{\alpha\beta} = \delta_{\alpha\beta} - \frac{\beta\Delta t}{\tau_p}(P\delta_{\alpha\beta} - \mathcal{P}_{\alpha\beta}) \tag{3.76}$$

$$H_{\alpha\beta} \rightarrow \eta_{\alpha\beta}H_{\alpha\beta} \tag{3.77}$$

For liquids it is reasonable to use the isotropic scheme. However, for solids, and especially defects in solids, one must use an anisotropic scheme.

3.4.3 Monte Carlo

For any point in the space of our system (x) one can calculate the probability of being at that point $P(x)$, using equation 3.1, and the value of some property $F(x)$. Taking a number of points in phase space and summing the values of $P(x)F(x)$ gives a classical expectation value for the property, F, using a technique known as simple sampling. This does not work very well though because the majority of phase space is taken up by high energy configurations, while the system would be expected to occupy only low energy configurations, which would not necessarily be generated in the sampling procedure. If configurations could be generated with a probability according to the Boltzmann distribution this problem would be resolved but it is impossible to generate random numbers on such a complex probability distribution. Instead, if one could generate a new configuration from the old configuration using some transition function $w(x_n|x_{n+1})$ such that:

- Stationary distribution - $\int w(x_n|x_{n+1})P(x_{n+1}) = P(x_n)$
- and process is ergodic - i.e. the system will visit the whole of phase space during an infinite amount of time regardless of where it starts.

Then if $w(x_n|x_{n+1})$ was sampled for long enough $P(x_n)$, the limiting probability distribution, would be sampled and so accurate ensemble averages would be

calculated.

If the condition known as *detailed balance* (3.78) is required of $w(x_n|x_{n+1})$ then the fact that the distribution $P(x_n)$ is stationary is implied. Furthermore, $w(x_n|x_{n+1})$ can be split up into two components [1] π, which represents the probability that the configuration is generated and A, which represents the probability that the move to the newly generated configuration is accepted. Then detailed balance can be re-expressed in terms of relationships between the ratios of these components:

$$w(x_n|x_{n+1})P(x_{n+1}) = w(x_{n+1}|x_n)P(x_n) \tag{3.78}$$

$$\text{set} \quad w(x_n|x_{n+1}) = \pi(x_n|x_{n+1})A(x_n|x_{n+1}) \tag{3.79}$$

$$\Rightarrow \quad \frac{A(x_{n+1}|x_n)}{A(x_n|x_{n+1})} = \frac{\pi(x_n|x_{n+1})P(x_{n+1})}{\pi(x_{n+1}|x_n)P(x_n)} \tag{3.80}$$

If $\pi(x_n|x_{n+1}) = \pi(x_{n+1}|x_n)$ then the acceptance probability is just the ratio of the Boltzmann probabilities of being in each state. Which leads to the Metropolis Condition [1]:

$$\frac{A(x_{n+1}|x_n)}{A(x_n|x_{n+1})} = \frac{P(x_{n+1})}{P(x_n)} = \frac{e^{-E(x_{n+1})/k_BT}}{Q} \times \frac{Q}{e^{-E(x_n)/k_BT}} = e^{-\Delta E/k_BT} \tag{3.81}$$

$$\Rightarrow A(x_{n+1}|x_n) = e^{-\Delta E/k_BT} \quad \text{if} \quad \Delta E > 0 \tag{3.82}$$

$$\Rightarrow A(x_{n+1}|x_n) = 1 \quad \text{if} \quad \Delta E \leq 0$$

The flow chart below details how this is in incorporated in a typical Monte Carlo code

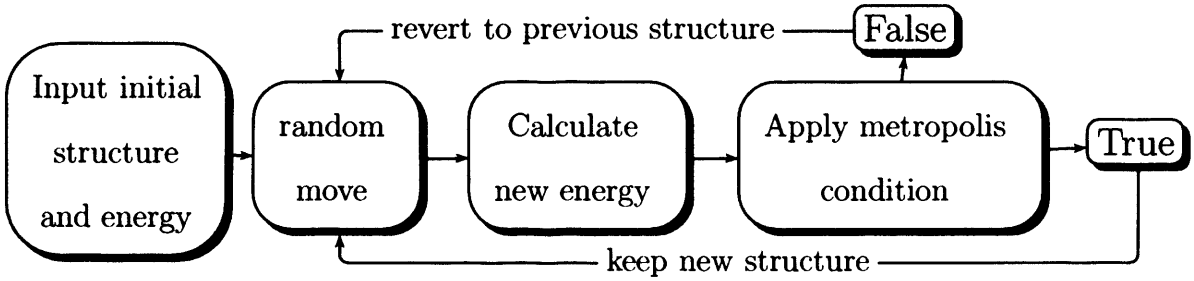

In this work Monte Carlo simulations are used to evaluate averages over differing proton topologies and the random moves are performed using an algorithm first

implemented by Rick [43], which is illustrated in figure 3.2. Monte Carlo calculations are used rather than molecular dynamics as proton topology changing moves are rare events and are, as such, unlikely to be sampled during the timescale of the average molecular dynamics simulations.

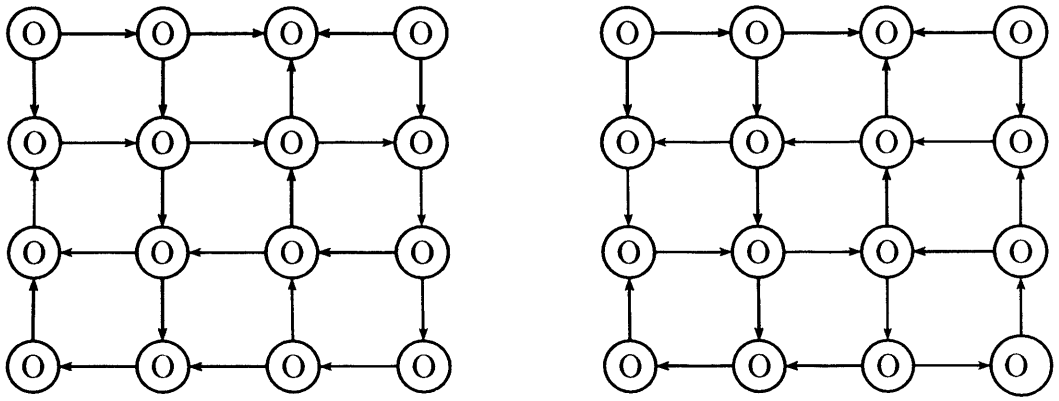

Figure 3.2: Diagram showing the operation of the Rick algorithm. Step one : a closed loop is found in the structure. Step two : all bonds in the loop have their orientation changed.

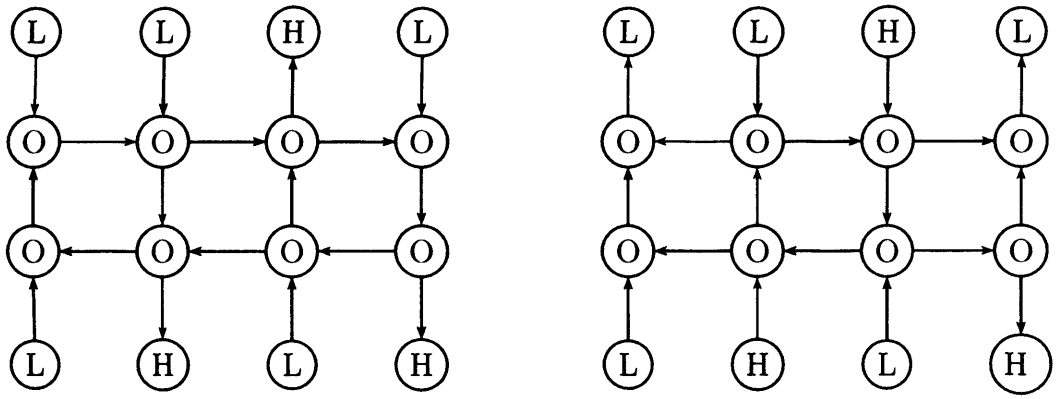

Figure 3.3: Diagram showing the extensions allowed to the Rick algorithm in this work.

The algorithm generates valid hydrogen bonding configurations by first selecting a water (j) at random. One of the four intermolecular hydrogen bonds surrounding it is then selected, which is of course attached to a further water molecule (k). If the hydrogen bond j-k is a donor to k then one picks one of the two hydrogen bond donors projecting out from k, otherwise one picks one of the two acceptors sticking out from k. This process is repeated till the path one has taken through the hydrogen bonding network meets itself; i.e. until a closed loop is found, then

the algorithm changes the orientation of every single bond in the loop.

The algorithm has been extended in this work to work with surfaces - now, as well as loops, any path that starts and ends with bonds dangling from a surface can have the orientations of all bonds in them changed as shown in figure 3.3.

Bibliography

[1] M. P. Allen and D. J. Tildesly. *Computer Simulation of Liquids.* Oxford Science Publications, (1989).

[2] M. Born and J. Oppenheimer. *Ann. Physik*, **84**, 718 (1930).

[3] D. Hartree. *Proc. Cambridge Phil. Soc.*, **24**, 111 (1927).

[4] D. Hartree. *Proc. Cambridge Phil. Soc.*, **24**, 426 (1928).

[5] D. Hartree. *Proc. Cambridge Phil. Soc.*, **25**, 310 (1929).

[6] V. Fock. *Z. Phys.*, **61**, 126 (1930).

[7] C. Roothaan. *Rev. Mod. Phys*, **23**, 69 (1951).

[8] P. Hohenberg and W. Kohn. *Phys. Rev.*, **136**, B864 (1964).

[9] W. Kohn and L. Sham. *Phys. Rev.*, **136** (1965).

[10] R. M. Martin. *Electronic Structure.* Cambridge University Press, (2004).

[11] A. D. Becke. *J. Chem. Phys.*, **98**, 1372 (1993).

[12] A. D. Becke. *J. Chem. Phys.*, **98**, 5648 (1993).

[13] A. D. Becke. *J. Chem. Phys.*, **104**, 1046 (1996).

[14] M. D. Segall, P. L. D. Lindan, M. J. Probert, C. J. Pickard, P. J. Hasnip, S. J. Clark and M. C. Payne. *J. Phys.: Cond. Matt.*, **14**, 2712 (2002).

[15] N. M. nad D. Vanderbilt. *Phys. Rev. B*, **56**, 12847 (1997).

[16] A. Aguado, L. Bernasconi, S. Jahn and P. A. Madden. *Faraday Discuss.*, **124** (2003).

[17] A. J. Stone. *Theory of Intermolecular Forces.* OUP, (2000).

[18] P. Atkins and R. Friedman. *Molecular Quantum Mechanics.* OUP, (1997).

[19] A. J. Stone and M. Alderton. *Molecular Physics*, **50**, 1047 (1985).

[20] A. R. Leach. *Molecular Modelling: Principles and Applications.* Pearson, (2001).

[21] P. A. Madden and M. Wilson. *Chemical Society Reviews*, **25**, 339 (1996).

[22] S. D. Leeuw, J. Perram and E. Smith. *Proc. R. Soc. Lond.*, **A373**, 27 (1980).

[23] D. M. Heyes. *J. Chem. Phys.*, **74**, 1924 (1981).

[24] A. Aguado and P. A. Madden. *J. Chem. Phys.*, **119**, 7471 (2003).

[25] J. Hautman and M. Klein. *Molecular Physics*, **75**, 379 (1992).

[26] D. M. Heyes. *CCP5 Quaterly*, **8**, 29 (1983).

[27] P. Sherwood and et. al. *J. Mol Struc-Theochem*, **632**, 1 (2003).

[28] J. Aqvist and A. Warshel. *Chem. Rev.*, **93**, 2523 (1993).

[29] H. Lin and D. G. Truhler. *Theor. Chem. Acc.*, **117**, 185–199 (2007).

[30] Gamess-uk, (1980). GAMESS-UK is a package of ab initio programs written by M.F. Guest, J.H. van Lenthe, J. Kendrick, and P. Sherwood, with contributions from R.D. Amos, R.J. Buenker, H. van Dam, M. Dupuis, N.C. Handy, I.H. Hillier, P.J. Knowles, V. Bonacic-Koutecky, W. von Niessen, R.J. Harrison, A.P. Rendell, V.R. Saunders, K. Schoffel, A.J. Stone and D. Tozer.

[31] J. D. Gale. *J. Chem. Soc., Faraday Trans.*, **93**, 629 (1997).

[32] W. C. Swope, H. C. Anderson, P. H. Berens and K. R. Wilson. *J. Chem. Phys.*, **76**, 637–649 (1982).

[33] W. Smith and T. Forester. *J. Molec. Graphics*, **14**, 136 (1996).

[34] H. Goldstein. *Classical Mechanics.* Addison-Weasley, (1980).

[35] M. L. Boas. *Mathematical Methods in the physical sciences.* John Wiley and Sons, (1983).

[36] E. G. H. Harbord. Personal communication, (2007).

[37] D. J. Evans. *Mol. Phys.*, **34**, 317–325 (1977).

[38] D. J. Evans and S. Murad. *Mol. Phys.*, **34**, 327–331 (1977).

[39] D. Potter. *Computational Physics.* Wiley, New York, (1972).

[40] L. V. Wookcock and K. Singer. *Trans. Faraday Soc.*, **67**, 257–261 (1971).

[41] H. C. Anderson, M. P. Allen, A. Bellemans, J. Board, J. H. R. Clarke, M. Ferrario, J. M. Haile, S. Nose, J. V. Opheusden and J. P. Ryckaert.

[42] H. J. C. Berendsen, J. P. M. Postma, W. F. V. Gunsteren, A. D. Nola and J. R. Haak. *J CHem. Phys.*, **81**, 3684–3690 (1984).

[43] S. W. Rick. *J. Chem. Phys.*, **122**, 094504 (2005).

Chapter 4

Order-Disorder Phase Transitions

As already discussed in the introduction, although many ice phases are proton disordered at ambient temperatures, they can undergo a phase transition to a proton ordered form at low temperatures. In this chapter an attempt is made to understand the driving force of the proton ordering transitions and then, from the insight obtained, the structures of recently discovered proton ordered ice phases were predicted.

4.1 Ice Ih

As discussed in section 2.5.1.1 the proton ordering transition in ice Ih has been extensively studied using both potentials and *ab initio* approaches. The work here expands on the literature work in two ways:

1. the work of Hirsch and Ojamäe[1] is repeated, with an improved basis set and the RPBE, LDA and PW91 functionals.

2. an analysis of the electrostatic multipoles of the 16 reference hypothetical unit cells using the maximally localised Wannier function scheme developed by Aguado and Madden[2] is reported.

4.1.1 Total energy calculations

As described in section 2.7.1, Hirsch and Ojamäe[1] have reported the total energies of 16 symmetry nonequivalent 8 molecule unit cells calculated using total energy DFT calculations. They reported a slight difficulty in converging the differences in energy between differing proton topologies with basis set size and so their plane wave DFT calculations have been repeated but with an increased plane-wave cutoff and 2 additional functionals. This was done to test whether minima are acutely sensitive to basis set effects and the exchange-correlation terms respectively, with the different functionals providing the insight into how sensitive the energy differences are to the recipe used to calculate the exchange and correlation energies. Furthermore, these calculations were conducted with CASTEP version 3.1 [3], which uses a full BFGS approach to cell (and co-ordinate) optimisation as opposed to older versions, which only used first derivatives to establish minima.

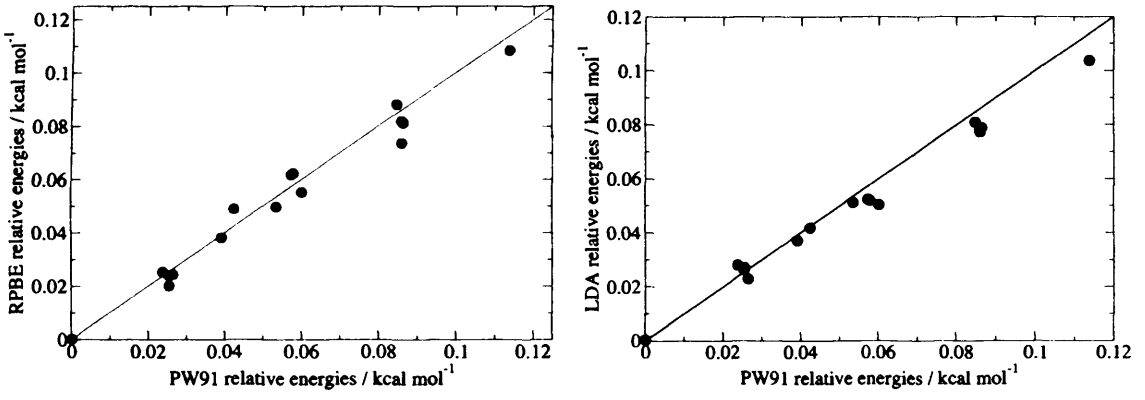

(a) RPBE functional (b) LDA functional

Figure 4.1: Correlation between the relative optimised energies of the 16 different symmetry distinct 8 molecule ice Ih unit cells calculated using the PW91, RPBE and LDA functionals. All energies are given relative to that of ice XI.

The energies of the 16 isomorphs were calculated using the PW91 [4, 5] and RPBE [6] GGA functionals, which use functions of the local density and the gradient of the density to describe exchange and correlation, and with the LDA functional, which uses an exchange correlation function that is a function of only the electron density. A plane-wave cutoff of 550 eV was used and a 6x3x3 Monkhorst-Pack grid of

k-points. This large plane-wave cutoff was employed because of the poor convergence of the energy differences for lower cutoffs. The trend in energy differences is identical to that reported previously [1] and all the functionals predict the correct structure for ice XI in agreement with experiment and previous DFT [1] and Hartree-Fock work [7]. (This is particularly surprising for LDA, which is known to overbind the water dimer because it has an inadequate description of exchange and correlation.) The different functionals have different recipes for estimating the exchange-correlation energy, so the strong correlation between the relative energies, calculated using the various functionals, suggests that, although the way exchange and correlation are parametrised may affect the absolute energies, it does not greatly effect the relative energies of the various ice configurations.

The energy differences calculated for these ice unit cells are all less than 0.15 kcal mol^{-1}, and one might question whether or not DFT can accurately predict such small energy differences. However, the total number and composition of species in each cell is identical, the cell volumes are almost identical and, in this work, the number of plane waves in the basis set is automatically extended when the cell expands to ensure consistent integration conditions. Furthermore, because the separations between water molecules are nearly constant in all the cells the same part of the intermolecular attractive and repulsive potentials are sampled. So, although DFT might not reproduce the absolute energies, it will reproduce relative energies because in the calculations of these quantities any errors, intrinsic in the method, will cancel.

Obviously, in discussing the relative stability of these configurations relative energies is only half the story. To obtain true estimates of the relative stabilities one requires information on the entropies of these systems and as such information on their zero point energies (ZPE). Calculation of reliable zero point energies for these different configurations would be difficult and computationally expensive. However, given that the zero point energy will be dominated by the OH stretching vibration, whose frequency decreases with increasing hydrogen bond length, and the fact that

the hydrogen bond lengths in all these structures are very similar, one might expect that ZPE would have little or no effect on the relative stabilities of different hydrogen bonding topologies.

4.1.2 Electrostatic analysis

As discussed in section 3.1.2, the total energy calculated in DFT is the sum of the kinetic energy of the electrons, electrostatic interactions, exchange interactions and correlation interactions. In the previous section it was shown that the relative energies are independent of the exchange correlation functional employed, which suggests that it is not these terms that are responsible for these energy differences. Furthermore, the kinetic energy of the electrons calculated in DFT assumes that there is no interaction between electrons and so is likely to be only dependent on the number of electrons present. This all suggests that the energy differences are due to differences in the electrostatic energies. As discussed in section 3.2.1 and 3.2.2, it is possible to calculate the electrostatic contribution to the total energy by performing a Wannier transformation on the Kohn-Sham orbitals output by CASTEP and then treating the resulting Wannier functions as atomic orbitals, which can be used to calculate multipoles. This has been implemented in CASTEP by Aguado and Madden [2] for systems composed of ions. With only a small modification this code can be used to calculate the molecular multipoles in ice.

The first step of Aguado and Madden [2] algorithm generates a set of Wannier functions with centres at:

$$\boldsymbol{r}_{\boldsymbol{n}}^{\boldsymbol{\alpha}} = -\sum_{m=1}^{3} \frac{M_{nm}}{b_m} \Im \ln[U^{\dagger} K^{(m)} U]_{mn}, \qquad \alpha = x, y, z \qquad (4.1)$$

$$\text{where} \qquad K_{ij}^{(m)} = < \phi_i | e^{i \boldsymbol{b_m} \cdot \boldsymbol{r}} | \phi_j >$$

In this equation $M_{nm} = \frac{\boldsymbol{b_n} \cdot \boldsymbol{u_m}}{b_n}$ - the normalised projection of the nth reciprocal

lattice (b_n) vector on the mth real space vector (u_m). The $\Im$ indicates that it is the imaginary part of the logarithm that is of interest and the $K_{ij}^{(m)}$ are overlap integrals between the various Kohm-Sham orbitals (ϕ_i).

In the work of Aguado and Madden each Wannier function is assumed to be an atomic orbital of the ion whose nuclei lies closest to its centre. This approach will not work for water because all the electron density about the hydrogens would be transferred to the oxygen leading to a highly unphysical distribution of the charge density. Admittedly it would be possible to solve this problem using a DMA scheme rather than the Wannier function scheme implemented here, however to perform a DMA analysis it is imperative that one uses either a Slater type or Gaussian type basis set, CASTEP meanwhile is a plane wave code though and so DMA analysis is not possible.

To resolve this problem the code was rewritten so that the Wannier functions are assumed to represent the molecular orbitals and thus are assigned to molecules. The locations of molecules are established by first calculating the two hydrogen nuclei nearest to a given oxygen nuclei. These three atoms together make up a water molecule, whose center of mass can be calculated. The Wannier functions are then assigned to the molecule whose centre of mass lies closest to its Wannier function centre.

The second critical difference between this molecular Wannier function approach and the approach favoured by Aguado and Madden is in the calculation of multipoles. In the work of Aguado and Madden the ionic multipoles are calculated using the nuclei as the origin so, because the nucleus lies at $(0, 0, 0)$, it makes no contribution to terms in the multipolar expansion higher than the monopole. Meanwhile, in the molecular version of the code the nuclei don't lie at the origin (the origin in these calculations is the centre of mass) and so the charges on nuclei have to be included when calculating dipoles, quadrupoles, *etc...* Furthermore, because the two 1s electrons are not treated explicitly but are modeled using a pseudopotential, the

charge on the oxygen nucleus is equal to +6. This pseudising of electrons assumes that the core electrons are distributed evenly on a small sphere surrounding the oxygen nucleus and thus at the distance of interest their effect can be reproduced by a multipole expansion containing only monopolar terms.

The Wannier function approach is general but it is costly to calculate the spread functional if one has many k-points and so it would be convenient if these calculations could be done at the Gamma point. The original unit cell has lengths of of 4.380, 7.167, 7.207 Å in a, b, and c cell axes respectively, leading to poor sampling in the a axis direction if Γ point sampling is enforced. This poor sampling leads to substantial deviations in the energy differences from the multi k-point results. However, it was found that the multi k-point results could be reproduced by a gamma point calculation on a supercell with an a-axis double the length of that used in the multi k-point calculations, see figure 4.2.

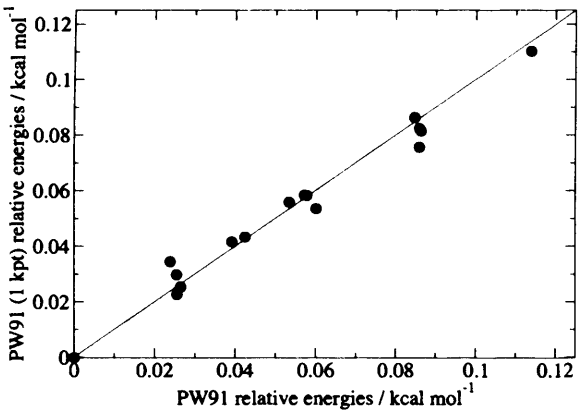

Figure 4.2: Correlation between the PW91 27 k-point energies of the 8 molecule cell and the energies obtained from the 16 molecule (2x1x1) gamma point calculation. All energies are given relative to the energy of the ice XI structure.

The maximum deviation between the energy differences calculated for the 2x1x1 supercell (gamma-point) and the smaller cell with 6x3x3 k-points is 0.011 kcal mol^{-1}. Therefore, because this energy difference is far smaller than the energy differences between different proton topologies, for computational efficiency, these supercells were used in the Wannier function calculations. Figure 4.3 shows an example of the Wannier functions generated using this technique.

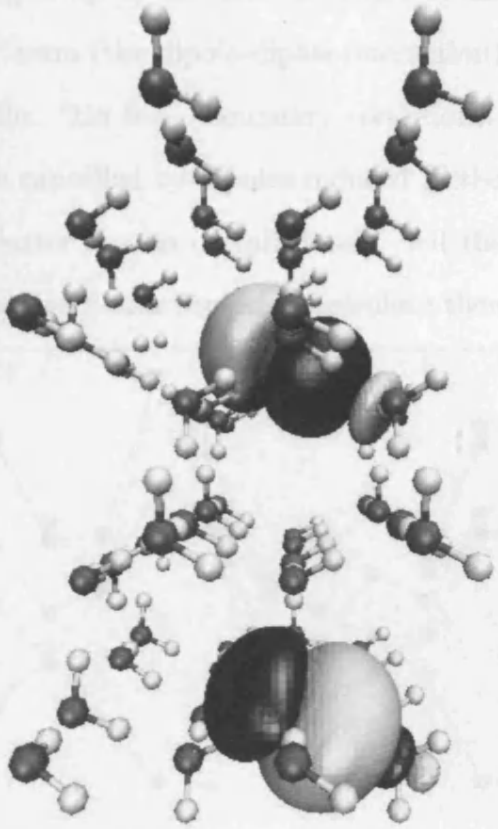

Figure 4.3: Low density isosurfaces of two of the Wannier functions from a calculation on a 64 molecule cell of ice. The light and dark shading indicates the phase of the wavefunction.

Xantheas *et al.* [8, 9] have shown that the electric field around water clusters and in ice Ih is strongly affected by multipoles up to the hexadecapole terms. For this reason multipoles up to the hexadecapole have been calculated and the potential energy has been calculated up to the 6th order in the electrostatic expansion terms using the equation below [10] (see section 3.2.2 for the definitions of the terms used in this equation):

$$\begin{aligned} E &= -T_{\alpha\beta}(\mu^B_\alpha \mu^A_\beta) - \frac{1}{3}T_{\alpha\beta\gamma}(\theta^B_{\alpha\beta}\mu^A_\gamma - \mu^B_\alpha \theta^A_{\beta\gamma}) \\ &- T_{\alpha\beta\gamma\delta}(\frac{1}{15}\Omega^B_{\alpha\beta\gamma}\mu^A_\delta - \frac{1}{9}\theta^B_{\alpha\beta}\theta^A_{\gamma\delta} + \frac{1}{15}\mu^B_\alpha \Omega^A_{\beta\gamma\delta}) \\ &- T_{\alpha\beta\gamma\delta\epsilon}(\frac{1}{105}\xi^B_{\alpha\beta\gamma\delta}\mu^A_\epsilon + \frac{1}{45}\theta^B_{\alpha\beta}\Omega^A_{\gamma\delta\epsilon} - \frac{1}{105}\mu^B_\alpha \xi^A_{\beta\gamma\delta\epsilon} - \frac{1}{45}\Omega^B_{\alpha\beta\gamma}\theta^A_{\delta\epsilon}) \end{aligned} \tag{4.2}$$

The calculated energies up to the various orders in this expression are shown in figure 4.4. The $1/R^3$ term (the dipole-dipole interaction) is calculated using the Ewald Sum with metallic, "tin foil", boundary conditions. This ensures that any macroscopic dipoles are cancelled by dipoles induced in the metal surrounding the cluster of ice, so the cluster has no overall dipole. All the other terms are much shorter ranged and so a direct sum is used to calculate them.

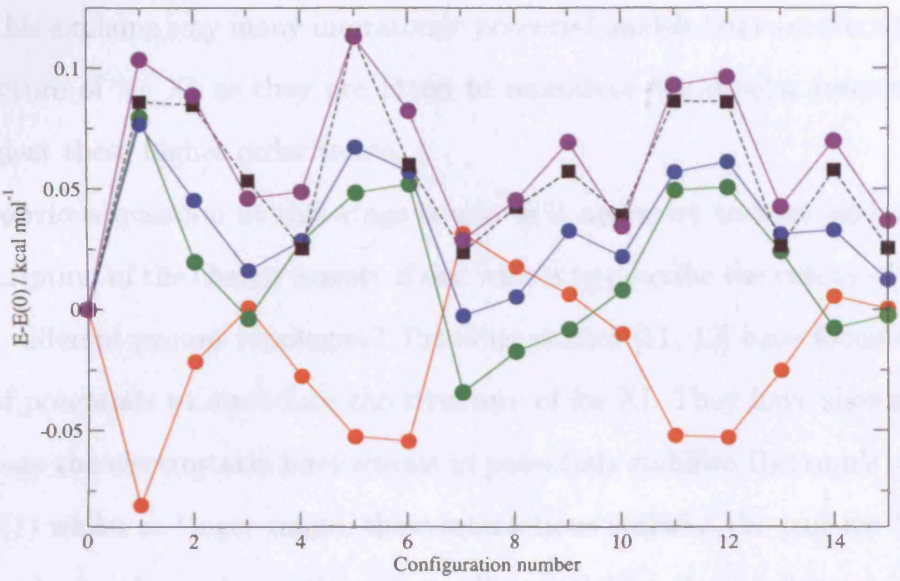

Figure 4.4: Total energies relative to that of ice XI for the 15 symmetrically distinct 8 molecule unit cell configurations of ice Ih. The lines are there only to make the data clearer to visualise. Configuration 0 is the structure of ice XI and configuration 1 is Bjerrum's predicted ice XI structure. The black line represents the PW91 result, red line the electrostatic interaction energy up to terms in $1/R^3$, green line the electrostatic interaction energy up to terms in $1/R^4$, blue line the electrostatic interaction energy up to terms in $1/R^5$ and violet line the electrostatic interaction energy up to terms in $1/R^6$. The multipolar energies have been uniformly scaled to be compatible with the DFT energies.

There is excellent agreement between the purely electrostatic description of energy differences and the full DFT energy differences for ice Ih, but only when terms up to $1/r^6$ in the expansion are considered. However, the value of the potential energy, obtained from the electrostatic potential energy calculation, must be scaled by a factor of 60. Why this scaling is required is unclear - one suggestion is that is due to the absence of the dielectric constant; although the dielectric model is an idea from continuum modeling and so should be unnecessary for molecular scale mod-

els. Another suggestion is that the electrostatic expansion of the potential energy is not fully converged but this does not explain the apparent match in the energies calculated from DFT and electrostatics. This is an subject that requires further investigation.

The $1/r^3$ component of the electrostatic energy (which is that due to dipole-dipole interactions) is strongly inversely-correlated with the true total energy differences. This explains why many interatomic potential models fail to correctly predict the structure of ice XI as they are fitted to reproduce the dipolar properties and they neglect these higher order terms.

The obvious question at this stage is why is it necessary to have such an accurate description of the charge density if one wishes to describe the energy differences between different proton topologies? Previous studies [11, 12] have focused on the failure of potentials to reproduce the structure of ice XI. They have shown that at short range the electrostatic interactions in potentials stabilise Bjerrum's structure [13, 14] (1) whilst at longer ranges these interactions stabilise the true ice XI structure (0). As has been shown though, in all probability, these potentials are only reproducing the terms in $1/r^3$ in the electrostatic expansion and so it was decided to examine the distance dependence of the difference in each term of the electrostatic interaction energy for configurations 0 and 1. This was done by simply changing the value of the cutoff distance and calculating an energy, the results are shown in figure 4.5.

This analysis shows that the dipole-dipole interaction converges very slowly, which agrees with the finding of Buch *et al.* [11] and Rick [12]. Furthermore, at short range it stabilises configuration 1, whilst at longer range it stabilises configuration 0 so that overall the dipole-dipole contribution to the energy difference between structures is rather small. As such higher order multipolar terms, which decay more rapidly than the dipole-dipole interaction, become important. The fact that the majority of the energetic contribution from these steeply distant dependent

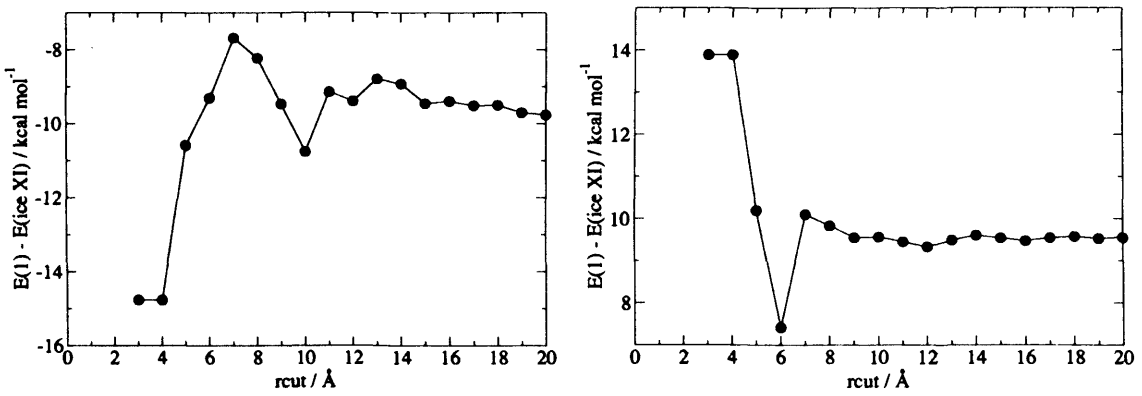

(a) Dipole dipole ($1/r^3$)

(b) Dipole quadrupole ($1/r^4$)

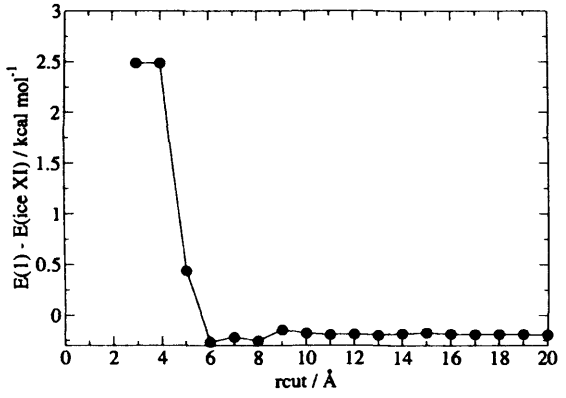

(c) Quadrupole quadrupole + dipole octupole ($1/r^5$)

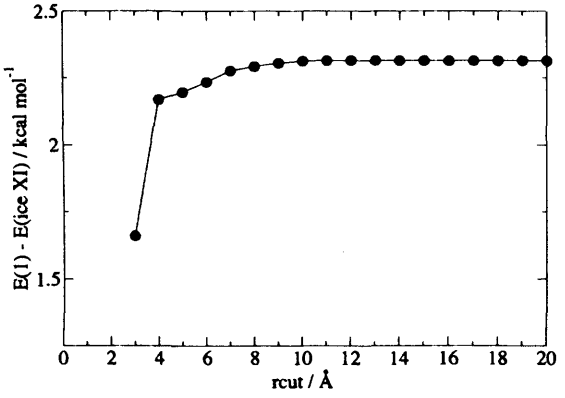

(d) Octupole quadrupole + dipole hexadecapole($1/r^6$)

Figure 4.5: Distance dependence of difference in energy between configurations 0 and 1 as a function of radial cutoff for the various terms in the electrostatic expansion.

terms is from short ranged terms helps explain why the graph invariant approach of Singer *et al.* [15], which fits the energy to very local geometric features, works so well.

It would be interesting to note whether or not molecules surrounded by different proton configurations are polarised differently - in other words whether molecules with different surroundings have different values for their dipole, quadrupole etc... In order to make this comparison however it is necessary to rotate the multipoles from the cell frame, which they are output in, into the body fixed frame whose axes are the bisector of the HOH angle α, the cross product of the two OH vectors β and the cross product of these two vectors $\alpha \times \beta$. Rotation from one frame to the other can then be done using the following equations, which are derived from the definition of a Cartesian tensor [16]:

$$
\begin{aligned}
\mu^b_\alpha &= A_{\alpha\beta}\mu^c_\beta \\
\theta^b_{\alpha\beta} &= A_{\alpha\gamma}A_{\beta\delta}\theta^c_{\gamma\delta} \\
\Omega^b_{\alpha\beta\gamma} &= A_{\alpha\delta}A_{\beta\epsilon}A_{\gamma\zeta}\theta^c_{\delta\epsilon\zeta} \\
\xi^b_{\alpha\beta\gamma\delta} &= A_{\alpha\epsilon}A_{\beta\zeta}A_{\gamma\eta}A_{\delta\theta}\theta^c_{\epsilon\zeta\eta\theta}
\end{aligned} \tag{4.3}
$$

Where in these equations A is the rotation matrix, given below, which is calculated by taking the scalar products of the two sets of basis vectors.

$$
A = \begin{vmatrix}
\boldsymbol{i}^b.\boldsymbol{i}^c & \boldsymbol{j}^b.\boldsymbol{i}^c & \boldsymbol{k}^b.\boldsymbol{i}^c \\
\boldsymbol{i}^b.\boldsymbol{j}^c & \boldsymbol{j}^b.\boldsymbol{j}^c & \boldsymbol{k}^b.\boldsymbol{j}^c \\
\boldsymbol{i}^b.\boldsymbol{k}^c & \boldsymbol{j}^b.\boldsymbol{k}^c & \boldsymbol{k}^b.\boldsymbol{k}^c
\end{vmatrix}
$$

These rotations have been done on all the molecular multipoles in all the unit cells and it has been found that the components of multipoles in different locations within the cell and in differing unit cells are all very similar. This analysis generates a vast amount of data so only the magnitudes of the multipoles are reported here. The average magnitude and the the standard deviation of the molecular multipoles in each of the 16 symmetry distinct unit cells is given in table 4.1. N.B. A multipole can be written as a linear combination of spherical harmonic functions. The magnitude of a multipole is defined, using this scheme, as the square root of the sum of the squares of the coefficients of the spherical harmonics.

Table 4.1 shows that the mean magnitudes of the multipoles in the different unit cells are all very similar. Furthermore, the standard deviations about these means are very small suggesting that all the multipoles at different sites are similar and as such differences in the extent of polarisation on molecules in different sites are not responsible for the energetic differences.

The driving force for proton ordering in ice Ih can thus be understood as a purely electrostatic phenomenon. This is not to say that hydrogen bonding is primarily

	μ / Debye		θ / Debye Å		Ω / Debye Å^2		ξ / Debye Å^3	
	Mean	σ	Mean	σ	Mean	σ	Mean	σ
0	3.604	0.001188	4.587	0.09576	4.225	1.649	4.983	0.008368
1	3.620	0.003133	4.565	0.03336	3.359	0.466	5.324	0.287
2	3.615	0.000077	4.563	0.04135	3.434	0.435	5.268	0.297
3	3.611	0.000707	4.568	0.02911	3.401	0.479	5.118	0.281
4	3.611	0.000841	4.577	0.03104	3.411	0.436	5.149	0.269
5	3.619	0.003642	4.556	0.03382	3.497	0.431	5.322	0.286
6	3.618	0.000214	4.566	0.04111	3.392	0.467	5.266	0.283
7	3.613	0.002494	4.570	0.03666	3.282	0.461	5.116	0.268
8	3.606	0.002494	4.576	0.03666	3.930	1.553	5.057	0.292
9	3.607	0.008858	4.571	0.06625	4.127	1.608	5.107	0.221
10	3.609	0.011840	4.576	0.08107	3.643	1.318	5.136	0.160
11	3.619	0.003754	4.562	0.03617	3.527	0.412	5.295	0.290
12	3.618	0.003092	4.563	0.04063	3.501	0.447	5.299	0.289
13	3.609	0.010720	4.581	0.08071	3.661	1.313	5.136	0.417
14	3.607	0.009449	4.570	0.06694	4.128	1.612	5.108	0.224
15	3.613	0.003793	4.572	0.03559	3.399	0.459	5.115	0.270
Mean	3.612	0.007824	4.570	0.05554	3.620	1.038	5.175	0.274

Table 4.1: Average multipole magnitude and standard deviations of those magnitudes for each of the 16 proton ordered ice Ih unit cells studied in this work. The final line in the table gives the average and standard deviation of all the multipoles in all the phases taken together.

due to electrostatic terms, rather that the differences in energy of structures with identical oxygen sub-lattices but with different hydrogen bonding networks are due to variations in the electrostatic interactions.

4.1.3 Energy and Symmetry

In the previous section it was shown that the forces responsible for the proton ordering in ice Ih are very short ranged in nature. This observation has been exploited by Hirsch and Ojamäe [1] and by Kuo *et al.* [15], who have both fitted the energy to local topological features in the proton topology as discussed in section 2.3.1. This suggests a way of finding ordered forms in other phases because the low energy structures will have the same low energy fragment repeated throughout the cell. In other words the low energy structures will have a small asymmetric unit which is repeated throughout the unit cell using the symmetry operations of its space group to

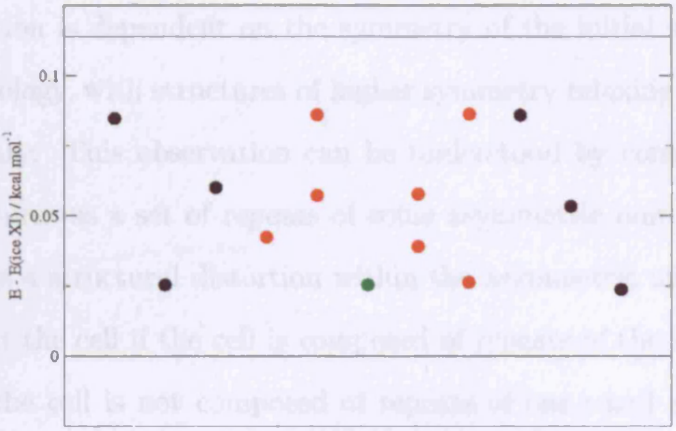

Figure 4.6: Figure showing how the energies of the ice Ih unit cells depend on the symmetry of the structures. The solid black lines represents the highest and lowest energy structures, both of which have two molecules in the asymmetric unit. Each point represents a symmetry distinct proton topology (the position on the x axis is arbitrary). The black dots are the other structures with 2 molecules in their asymmetric unit, the red circles those with 4 molecules in their asymmetric unit and the green dots those with 8 molecules in the asymmetric unit.

generate the remaining water molecules. Obviously the higher the space group symmetry the smaller the asymmetric unit and so one would expect any proton ordered form to have the highest possible space group for which a valid proton topology can be generated. Furthermore, because the highest energy (least favourable) structure will contain the least favourable asymmetric unit repeated throughout the cell, it would also be expected to belong to the highest symmetry space group.

This idea is supported by, and the basis of, Kuo *et al.*'s graph invariants [15] (see section 2.3.1). A graph invariant is a projection operator of a high symmetry space group - given that Kuo *et al.* only ever use totally symmetric projection operators of bond variables to generate their graph invariant functions and that the energy is fitted to the value of the graph invariants suggests low and high energy structures will be those with a high symmetry. To test this assertion figure 4.6 shows the energies of the various structures vs the number of molecules in their asymmetric units. As can be seen the lowest and highest energy structures are amongst the structures that have the smallest asymmetric units.

Kuo and Klein [17] have also noted that the extent to which the lattice relaxes

during optimisation is dependent on the symmetry of the initial structures hydrogen bonding topology, with structures of higher symmetry relaxing more than those of lower symmetry. This observation can be understood by considering the high symmetry structures as a set of repeats of some asymmetric unit. If, during optimisation, there is a structural distortion within the asymmetric unit, then this can occur throughout the cell if the cell is composed of repeats of the asymmetric unit. By contrast, if the cell is not composed of repeats of one small asymmetric unit, in other words if it is of lower symmetry, then any structural distortions may be suppressed because different parts of the structure wish to distort differently. By this argument then one may observe that, for geometry optimisations, the highest energy (least favourable) structure may not have the same symmetry as the lowest energy structure. For single point energy calculations though, one would expect this observation to always be true.

4.2 Ice VII

The observation that electrostatic forces drive the proton ordering of ice Ih begs the question - is this true in other ice phases? Particularly those that order spontaneously without dopants. Ice VII, a very high pressure form of ice, which was discussed in section 2.5.8 has a proton ordering transition to ice VIII, which goes without dopants present. To test whether this transition goes because of electrostatic forces 3 randomly oriented ice VII, 8 molecule unit cell structures were generated. Optimisations of these structures and the structure of ice VIII were then performed in CASTEP using the PW91 functional, a plane-wave cutoff of 550 eV and a 6x6x4 Monkhorst-Pack grid. Then a further single point gamma point calculation, from which Wannier functions were obtained, was performed on a 2x2x1 supercell of each of the structures so that there was comparable sampling along each of the axes. Figure 4.7 shows the electrostatic energy calculated up to the various orders in this multipolar expansion.

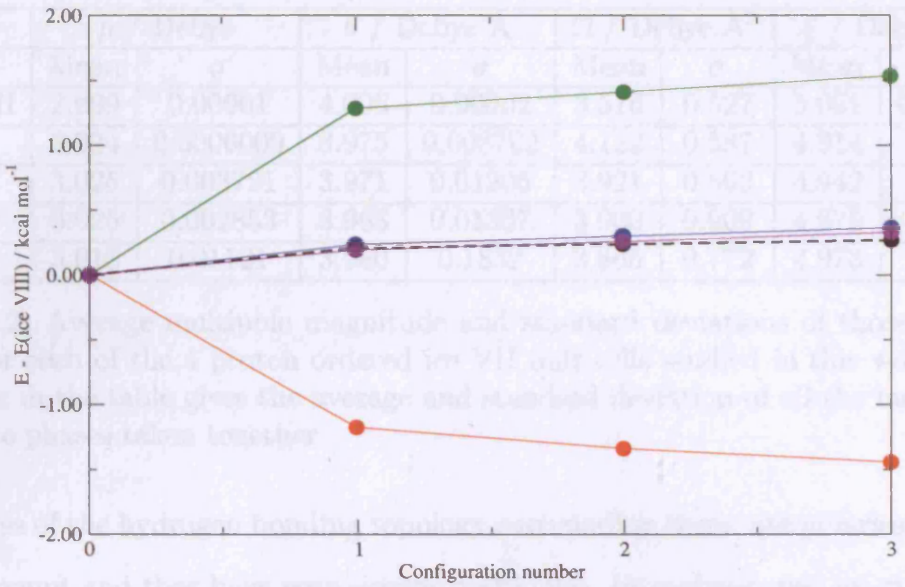

Figure 4.7: Total energies relative to that of ice VIII for the 3 random ice VII cells generated. Again lines are in only to make the figure easier to interpret. Configuration 0 is the structure of ice VIII and the black line represents the PW91 result, red line the electrostatic interaction energy up to terms in $1/R^3$, green line the electrostatic interaction energy up to terms in $1/R^4$, blue line the electrostatic interaction energy up to terms in $1/R^5$ and violet line the electrostatic interaction energy up to terms in $1/R^6$. The multipolar energies have been uniformly scaled to be compatible with the DFT energies.

Again it would seem that the energy differences seem to only depend on the electrostatic component of the potential energy but, whereas for ice Ih the energies only converged on the DFT results when terms up to $1/r^6$ were taken into account, now the energy is converged once terms in $1/r^5$ have been reached. Again though some scaling is required although the scaling factor here is only 6 as opposed to the larger value that was required for the ice Ih energies.

A similar analysis of the multipolar components, akin to that performed on the ice Ih multipoles, has been performed and the results are shown in table 4.2:

Again the multipoles in different locations within the unit cell and in different unit cells are very similar in magnitude. However, the multipoles in ice VII are 26% smaller than those in ice Ih. Thus the arrangement of oxygens in the structure has a strong effect on the amount of polarisation of the water molecules.

In conclusion, in a given ice phase (oxygen network) all the water molecules,

	μ / Debye		θ / Debye Å		Ω / Debye Å^2		ξ / Debye Å^3	
	Mean	σ	Mean	σ	Mean	σ	Mean	σ
Ice VIII	2.999	0.00001	4.006	0.00002	3.516	0.527	5.061	0.00005
1	3.024	0.0006009	3.975	0.008762	4.122	0.587	4.914	0.442
2	3.025	0.003721	3.971	0.01206	3.921	0.863	4.942	0.398
3	3.025	0.002853	3.968	0.01307	3.900	0.909	4.975	0.338
Total	3.018	0.01121	3.980	0.1832	3.865	0.772	4.973	0.347

Table 4.2: Average multipole magnitude and standard deviations of those magnitudes for each of the 4 proton ordered ice VII unit cells studied in this work. The final line in the table gives the average and standard deviation of all the multipoles in all the phases taken together.

regardless of the hydrogen bonding topology surrounding them, are polarised by the same amount and thus have very similar multipoles. In contrast, two ice structures with different oxygen networks have water molecules that are polarised by different amounts. This suggests that in parametrising a potential to reproduce the whole of the water phase diagram one would need to include a large number of polarisation terms.

4.3 Ice XII - determination of ice XIV

Finney and Salzmann [18] have recently carried out work on proton ordering transitions in ice XII and ice V. By doping these ices with HCl and cooling, they managed to extract two new ice phases, ices XIII and XIV. Prior to their publications they issued a challenge to blind predict the structure of these two new ordered phases. The work in section 4.1.3 showed that the ordered form would be expected to be one of the structures of the highest symmetry space group so the problem of predicting ordered forms becomes one of enumerating possible proton topologies for a small unit cell and then calculating their symmetries. Optimisations with density functional theory can then be done to establish which of the structures is the lowest energy and hence the ordered form. Furthermore, because the driving force for proton ordering transitions is primarily electrostatic, as shown in sections 4.1.2 and 4.2, one can have confidence in the verity of any predictions made with DFT.

It was decided to take on the ice XII proton ordering transition first because it is a simpler structure. The enumeration was achieved by borrowing from the work of Kuo *et al.* [15] and realising that any ice structure is a graph and can as such be represented as a set of linked vertices, instead of the full set of coordinates of all the atoms. This list of linked vertices was worked out by first calculating the four nearest neighbours to each oxygen, which gives a list in which every bond in the structure is listed twice so the following code was used to delete all the repeats:

```
! Loop over all oxygens
n=1
do j=1,nmol
! Loop over four neighbours
  do k=1,4
! Establish whether or not bond has already been found
     found=.false.
     do m=1,n-1
       if ((canon(m,1).eq.j).and.(canon(m,2).eq.hydsphere(j,k))) found=.true.
       if ((canon(m,2).eq.j).and.(canon(m,1).eq.hydsphere(j,k))) found=.true.
     end do
! If not found add to canon array.
     if (.not.found) then
       if (n.gt.nmol*2) then
         write(6,*)"Problems in canonical - found too many bonds"
         stop
       end if
       canon(n,1)=j
       canon(n,2)=hydsphere2(j,k)
       n=n+1
     end if
  end do
end do
```

In this code *hydsphere* is an N dimensional array that lists the four nearest oxygen atoms to each oxygen and *canon* is the final list of the 2N pairs of oxygen atoms that make up the hydrogen bonds (N is the number of water molecules). As discussed in section 2.3.1 any hydrogen bonding configuration can be represented by a diagraph of the graph that represents what oxygens are connected - i.e. in a hydrogen bonding topology the hydrogen bonds must be given a direction. This

direction is represented within the program by a further 2N dimensional array called hbonds, whose elements have a value +1 if hydrogen bond j points from canon(j,1) to canon(j,2) or a value of -1 if it points from canon(j,2) to canon(j,1). This hbonds array, if written out in full, is simply a binary string which makes enumeration of all topologies very simple - now one need only convert every number in the range 0 to 2^{2N}-1 to a binary string and test whether the corresponding hydrogen bonding configuration obeys the Bernal-Fowler [19] ice rules, which is done by the code below:

```
nperms=2**(nmol*2)
do j=0,nperms-1
   strucno=j
! Generate binary string from number
   do k=1,nmol
      hbonds(k)=int(strucno/binar(k))
      if (hbonds(k).eq.1) then
        strucno=strucno-binar(k)
      else if (hbonds(k).eq.0) then
        hbonds(k)=-1                                          10
      end if
   end do
! Test if structure obeys Bernal Fowler ice rules
   ncoord(:)=0
 coord=0
  do j=1,nmol*2
    ncoord(canon(j,1))=ncoord(canon(j,1))+hbonds(j)
    ncoord(canon(j,2))=ncoord(canon(j,2))-hbonds(j)
  end do
  ! Each value of ncoord should be zero if valid structure      20
  trial=0
  do j=1,nmol
    trial=trial+abs(ncoord(j))
  end do
  if (trial.eq.0) then
    ! Code to output valid structure
  end if
end do
```

The positions of the hydrogens in the structure are then obtained by using the directions of the two donor hydrogen bonds on each oxygen to generate a body fixed axis system for every molecule.

The process discussed so far is not as sophisticated as that of Kuo *et al.* [15] and as such generates a vast number of structures, because symmetrically equivalent structures are not automatically deleted. However, one symmetry is easily spotted in this representation - namely if the two structures are represented by hbonds arrays that are related by multiplication of all the elements by -1 then they are equivalent. That is to say, if one takes a structure and reverses the directions of all the hydrogen bonds then this second structure is symmetrically equivalent to the first. Thus rather than counting from 0 to $2^N - 1$ (where N is the number of hydrogens) one need only count as far as $2^{N-1} - 1$ as the 2^{N-1} binary strings between 2^{N-1} and $2^N - 1$ can all be generated by taking a binary string in the range 0 to $2^{N-1} - 1$ and multiplying by -1.

Applying the above approach to a 12 molecule ice XII unit cell generates 346 possible structures. The symmetries of all these structures were calculated using FINDSYM [20] and it was found that of the 346 structures 258 have P1 symmetry, 8 have P2 symmetry, 72 have $P2_1$ symmetry and 8 have $P2_12_12_1$ symmetry. $P2_12_12_1$ is the highest symmetry of these space groups and so these 8 structures were optimised in CASTEP using the PW91 functional and 2x2x4 Monkhorst Pack grid of k-points and a plane wave cutoff of 500 eV. When these calculations are performed there are only 4 distinct energies (see table 4.3), which suggests that each structure has been generated twice. The reason each structure is generated twice using this procedure is that the asymmetric unit of the disordered ice XII structure has S_4 point group symmetry and, as such, 4 symmetry operations. All valid hydrogen bonding topologies do not have the same symmetry as the disordered structure, although, if one takes an arbitrary hydrogen bonding topology and applies the symmetry operations of the disordered structure, one generates a hydrogen bonding topology that is symmetrically equivalent.

The energy difference between configuration numbers 3 and 4, whose structures are shown in figure 4.8, is very small. They feature subtly different hydrogen-bond

Configuration number	Energy / kcal mol^{-1}	E - E(ice XIV) / kcal mol^{-1}
1	-10865.948	0.189
2	-10865.987	0.15
3	-10866.094	0.043
4 (ice XIV)	-10866.137	0.0

Table 4.3: Energies of the 4 $P2_12_12_1$ 12 molecule unit cells of ice XII.

networks along [001]. In the lowest energy state (4) the interatomic O-H distance parallel to [001] is 1.750 Å whilst the separation alternates between 1.713 and 1.716 Å in the higher energy structure (3), which suggests that the energy difference between these two networks is due to a reduction in suprafacial intermolecular proton repulsion in configuration 4.

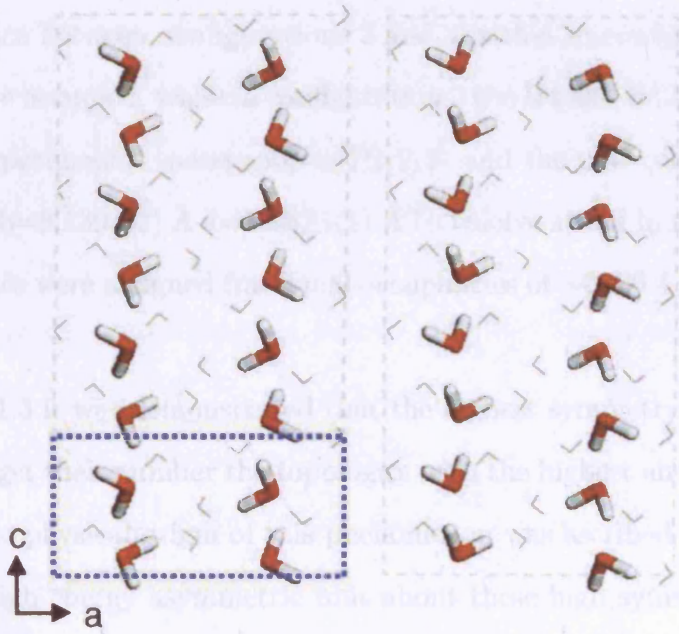

Figure 4.8: Structures of the two low energy $P2_12_12_1$ structures generated. The one on the right is the lowest energy configuration (4), while the one on the left is the is the slightly higher energy configuration (3). The molecules highlighted indicate the differences in the hydrogen bonding topology between the two structures.

A tentative suggestion that configuration 4 corresponds to the experimental ice XIV structure was made [21] but, because of the extremely small energy difference between configurations 3 and 4, it was also suggested that regions of configuration 3 may be present. An apparent mixture of configurations 3 and 4 is precisely what is observed in experiments. Using Salzmann *et al.*'s [18] labeling convention (see table

	x	y	z	occupancy
O1	0.0059(3)	0.2568(5)	0.1304(7)	1.0000
O2	0.6308(3)	0.0078(3)	0.2485(7)	1.0000
O3	0.2525(4)	0.8858(3)	0.0063(6)	1.0000
D4	0.0557(7)	0.3284(7)	0.9845(1)	0.407(3)
D5	0.5275(5)	0.8410(4)	0.4684(1)	0.620(4)
D6	0.0920(2)	0.2056(3)	0.2671(6)	1.0000
D9	0.7895(3)	0.9679(3)	0.8954(7)	1.0000
D11	0.7340(3)	0.4630(3)	0.3225(6)	1.0000
D12	0.4111(4)	0.5790(5)	0.3625(1)	0.593(3)
D13	0.9018(8)	0.1018(7)	0.8552(2)	0.380(4)
D15	0.8472(3)	0.3248(3)	0.4010(6)	1.0000

Table 4.4: Fractional coordinates for ice XIV (80 K and ambient pressure) as determined by Salzmann *et al.* [18]. Numbers in parentheses are statistical errors of the last significant digit.

4.4) the difference between configurations 3 and 4 is that in configuration 4 the H5 and H12 sites are occupied, while in configuration 3 the H4 and H13 site are occupied instead. The experimental spacegroup is $P2_12_12_1$ and the unit cell parameters are: a=8.3499(2) Å b=8.1391(2) Å c=4.0825(1) ÅṪo resolve strain in the fit, the H5:H4 and H12:H13 sites were assigned fractional occupancies of ~0.6:0.4 as shown in table 4.4.

In section 4.1.3 it was demonstrated that the highest symmetry proton topology contained amongst their number the topologies with the highest and lowest energies. Furthermore, the physical origin of this phenomenon was ascribed to the repetition of some low / high energy asymmetric unit about these high symmetry structures. In Ice XII the fact that there are two low energy structures suggests that there are two distinct low energy features - namely those features involving (using the labeling convention of Salzmann discussed above) H4, H5, H12 and H13 and those features involving the remaining part of the hydrogen bonding network. That is to say, permuting the H4, H5, H12 and H13 part of the network has a far smaller effect on the energy than any other sort of permutation. This suggests that there should be a number of lower symmetry structures that consist of a mixture of configurations 3 and 4 with an energy intermediate between those of configurations 3 and 4. In

other words there are 2 symmetrically equivalent hydrogen bonding topologies, one of which has hydrogens on the H4 and H12 sites, while the other has hydrogens on H5 and H13, that should have energies lying between those of configurations 3 and 4. These structures have been generated and found to have a symmetry of $P2_1$ and a relaxed energy, calculated using CASTEP, of -10866.101 kcal mol^{-1} - 0.036 kcal mol^{-1} above configuration 4 and 0.007 kcal mol^{-1} below that of configuration 3.

Experiments [18] have shown that the cooling rate influences the likelihood of the proton ordering transition, which is as expected - if the system is cooled too fast then all kinetic energy is lost before the potential energy barrier to the transition has been overcome. This raises a question though. If one delicately controls the cooling rate could one influence the occupancies of H4, H5, H12 and H13 in ice XIV? These calculations suggest that the system can happily have hydrogens in all these four sites down to ~20 K and at this temperature it seems unlikely that there will be enough kinetic energy to overcome any potential energy barriers. Thus adjusting the cooling rate is unlikely to yield the ability to control hydrogen site occupancies.

To the best of our knowledge the proton ordering transition in ice XII is the first observation of an ordering transition where the ordered form observed consists of a mixture of proton topologies. In ice Ih the ordered form is ferroelectric, so no pure ice XI crystals have been made, but within the domains the crystal consists of a single proton topology. Why exactly ice XII forms this mixed ordered form is unclear but may be that the barrier to this final stage of transition is too large or it may be a geometric consequence of having these 1D chains of water molecules.

4.4 Ice V

As mentioned in the previous section Finney and Salzmann [18] have also found a proton ordered form of ice V. Ice V has a monoclinic unit cell of 28 molecules and here lies the problem with predicting the structure using the techniques used to predict the ordered form of ice XII - according to Pauling's rule [22] there are approximately

85,200 possible structures for a unit cell containing 28 water molecules. Not only is this too many structures to run through FINDSYM, it is too many to store on local computational resources! However, by the logic of section 4.1.3, the ordered form will consist of some small asymmetric unit repeated throughout the cell according to the symmetry operations of some relatively high symmetry group. Thus if one could first find what molecules formed this asymmetric unit one could generate all the high symmetry structures by generating all valid hydrogen bonding topologies of the asymmetric unit using the methods described in the previous section. These asymmetric units could then be repeated about the cell using the operations of the space group and the resulting structures tested to see if they obeyed the Bernal–Fowler ice rules.

To identify the smallest possible asymmetric unit that can be repeated about the cell to produce Bernal-Fowler rule obeying structures the space group of the disordered ice V structure was examined. Ice V has the space group A_{21}/a_1 and an asymmetric unit consisting of 4 oxygens, 14 hydrogens (each hydrogen with an occupancy of 0.5) and 6 hydrogen bonds - 5 of which connect symmetrically non-equivalent oxygen atoms and 1 which connects oxygen number 1 to a symmetric repeat of oxygen 1. It is this last bond that is problematic because there is a mirror plane in the center of it. Obviously, a hydrogen bond can't have a mirror plane in its center as to have one would necessitate having two hydrogens on the bond. If, in this bond, atom *a* donates a hydrogen to atom *b* the symmetry operations of the group will generate a hydrogen bond in which atom *b* donates a hydrogen to atom *a*. The other bonds by contrast are straightforward to deal with as they form part of the asymmetric unit. Thus one can simply generate a list of the oxygen atoms, in the asymmetric unit, that are linked together by hydrogen bonds and then generate all the oxygen positions by repeating the asymmetric unit according to the symmetry operations of the space group. Finally, then one takes the list of oxygens connected by hydrogen bonds obtained in the first step and, if for instance,

the first hydrogen bond connects oxygens 1 and 2 then one takes every instance of a symmetric repeat of an oxygen 1 and connects it to every instance of a symmetric repeat of an oxygen 2. If the bonds are assigned a direction, then one can enumerate over possible asymmetric units using the methods discussed in the previous section. However, this does not deal with the problematic bonds that connect symmetric repeats and generates hydrogen bonding networks that, for ice V, are 8 hydrogen bonds short of the required number. This problem was resolved though, for ice V, by enumerating all possible topologies which have the same orientations of the 5 bonds connecting different oxygen atoms in the asymmetric unit but any orientation for the remaining 8 bonds. This generated 8 structures, the space groups of which, found using FINDSYM [20], were either, $P2_1/c$, or the lower symmetry Pc.

The space group of the ordered form of ice V is thus likely to be $P2_1/c$ for the reasons described in the previous section and it is possible to create an asymmetric unit of ice V within this space group, which contains 6 water molecules and 12 hydrogen bonds none of which connect oxygens to their symmetric repeats. Thus every possible arrangement of hydrogen bonds, with $P2_1/c$ symmetry can be generated by generating every possible arrangement of hydrogen bonds in the asymmetric unit, propagating this asymmetric unit about the lattice using the symmetry operations and testing whether or not the resulting structure obeys the Bernal Fowler rules. Using this scheme for generating hydrogen bonding structures gives 2048 binary strings that correspond to structures which may or may not obey the Bernal Fowler rules. When the Bernal-Fowler ice rules are applied it is found that only 35 of the hydrogen bonding topologies with $P2_1/c$ symmetry obey these rules. In all probability this procedure generates structures that are symmetric repeats but optimisations of all these structures were performed using CASTEP [3] (gamma point, PW91 functional [4, 5], 550 eV cutoff) regardless. The energies obtained are shown in figure 4.9, which shows that there is a clear global minimum and this is the experimentally observed structure ordered form of ice V - ice XIII. Furthermore,

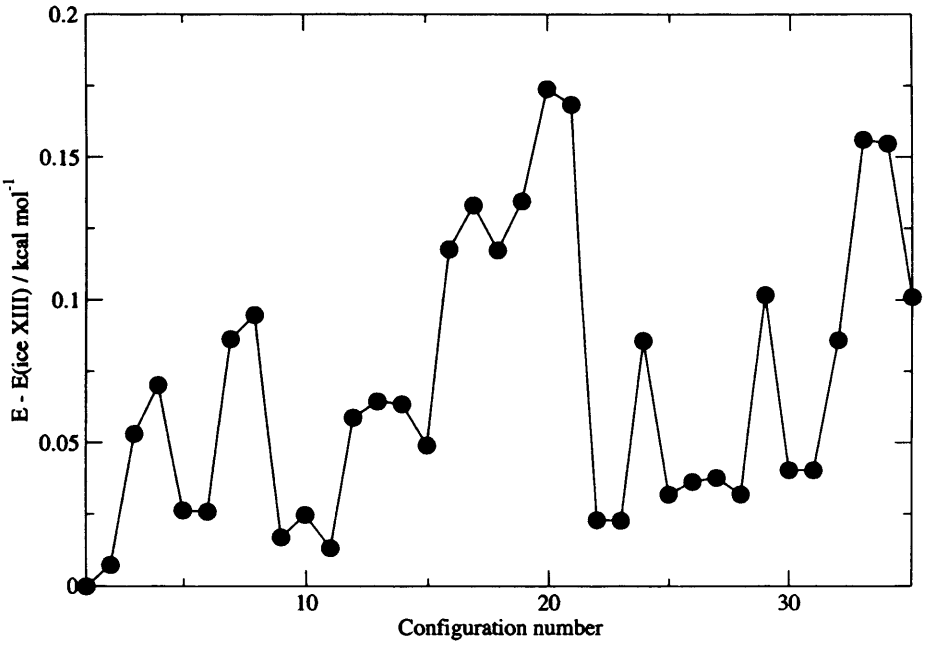

Figure 4.9: Energies, relative to that of ice XIII of all possible $P2_1/c$ hydrogen bonding topologies of ice V.

this figure also shows which structures are likely to be symmetrically identical as there are a number of structures with very similar energies (for example structures 0 and 1).

Figure 4.9 shows that the energy differences between ice XIII and many of the other ice V hydrogen bonding topologies is lower than 0.043 kcal mol^{-1}, which is the energy difference between the lowest energy ice XII topology and the second highest topology. This adds weight to the suggestion that it is something peculiar to the ice XII structure that prevents its full conversion to the lowest energy hydrogen bonding topology as the experimentally observed ice XIII consists of a single hydrogen bonding topology.

4.5 Ice II

Plane wave DFT has proved to be very successful in predicting the structures of ordered forms of ice phases. In this thesis and elsewhere [1, 15, 17, 23] it has been shown that it correctly predicts the ordered forms of ice Ih, ice VII, ice XII, ice V

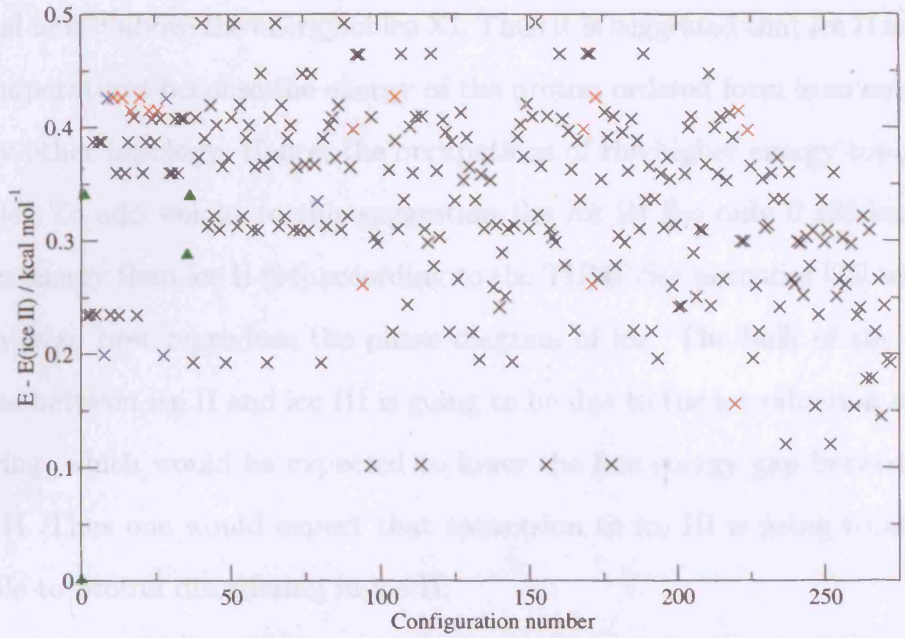

Figure 4.10: Energies, relative to that of ice II of all possible hydrogen bonding topologies of a disordered 12 molecule ice II unit cell. Black crosses are those structures that have P1 symmetry, red P-1 symmetry, blue R-3 symmetry and green triangles are those structures with R3 symmetry.

and ice III. This suggests that it can be used as a useful predictive tool in the study of other ice and hydrate phases.

As discussed in section 2.5.3 ice II is the only known phase of ice that has no proton disordered form - ice II is proton ordered at all temperatures. Why this might be the case can be investigated using plane wave DFT. Furthermore, the feasibility of a new, proton disordered, ice phase, that has the same oxygen network as ice II, can be investigated. This was achieved, in this work, by enumerating all possible proton topologies of ice II using the same technique that was used to enumerate all the possible structures of ice XII. This generates 273 possible structures of which 4 have the same space group as ice II, R-3, 5 have R3 symmetry, 16 have P-1 symmetry and 246 have P1 symmetry. All these configurations were optimised using gamma point calculations in CASTEP [3] (PW91 functional, 500 eV cutoff) the results of which are shown in figure 4.10.

From figure 4.10 the second lowest energy topology lies 0.1 kcal mol^{-1} in energy above that of ice II. By contrast the second highest configuration of ice Ih lies only

0.025 kcal mol^{-1} above the energy of ice XI. Thus it is suggested that ice II is ordered at all temperatures because the energy of the proton ordered form is so much lower than any other topology. Hence, the occupations of the higher energy topologies is negligible. To add weight to this suggestion the ice III lies only 0.106 kcal mol^{-1} higher in energy than ice II [24] according to the TIP4P/ice potential [25] which was fitted so as to best reproduce the phase diagram of ice. The bulk of the entropic difference between ice II and ice III is going to be due to the introduction of proton disordering, which would be expected to lower the free energy gap between ice III and ice II. Thus one would expect that conversion to ice III is going to always be preferable to proton disordering in ice II.

There is one additional thing to note from 4.10 namely that the highest energy (least favourable) structure no longer has the same space group as the lowest energy structure. This is due to the effects of lattice relaxation in the optimisation, which was discussed in section 4.1.3.

4.6 Conclusions

In this chapter it has been shown that DFT predicts the correct structure for all the proton ordered phases for which proton ordering transitions have been observed. This success appears to be due to the fact that all that is necessary to describe these transitions is a highly accurate representation of the electrostatic interaction. In other words changing the proton topology seems to have a negligible effect on the magnitudes of the exchange and correlation interactions.

Another important result is that a recipe has been provided by which the structures of the proton ordered forms of materials, which undergo proton ordering transitions can be predicted. This recipe works by noting that the forces responsible for proton ordering are short ranged and as such the asymmetric units in the proton ordered structures are small so the symmetry of the structure is high. Thus one need only calculate the energies of the highest symmetry proton topologies when

searching for proton ordered forms.

The range of energies different proton topologies topologies seems to be dependent on the particular ice phase of interest, the largest range of energies being in ice II. This range of energies is interesting as its magnitude may affect the magnitude of the configurational entropy, as it may become more difficult to occupy the higher energy levels. Thus one would expect ice V and XII to have lower entropies than ices Ih and VII.

Bibliography

[1] T. K. Hirsch and L. Ojamäe. *J. Phys. Chem. B*, **108**, 15856–15864 (2004).

[2] A. Aguado, L. Bernasconi, S. Jahn and P. A. Madden. *Faraday Discuss.*, **124** (2003).

[3] M. D. Segall, P. L. D. Lindan, M. J. Probert, C. J. Pickard, P. J. Hasnip, S. J. Clark and M. C. Payne. *J. Phys.: Cond. Matt.*, **14**, 2712 (2002).

[4] J. P. Perdew and Y. Wang. *Phys. Rev. B*, **46**, 6671 (1992).

[5] J. A. White and D. M. Bird. *Phys. Rev. B*, **50**, 4954 (1994).

[6] B. Hammer, L. B. Hansen and J. K. Norskov. *Phys. Rev. B*, **59**, 7413 (1999).

[7] S. Casassa, M. Calatayud, K. Doll, C. Minot and C. Pisani. *Chem. Phys. Lett.*, **409**, 110 (2005).

[8] E. R. Batista, S. S. Xantheas and H. Jónson. *J. Chem. Phys.*, **112**, 3285 (2000).

[9] E. R. Batista, S. S. Xantheas and H. Jónson. *J. Chem. Phys.*, **109**, 4546 (1998).

[10] A. J. Stone. *Theory of Intermolecular Forces.* OUP, (2000).

[11] P. S. V. Buch and J. Sadlej. *Phys. Chem. B*, **102**, 8641 (1998).

[12] S. W. Rick. *J. Chem. Phys.*, **122**, 094504 (2005).

[13] N. Bjerrum. *Science*, **115**, 386 (1952).

[14] K. S. Pitzer and J. Polissar. *J. Am. Chem. Soc.*, **60**, 1140 (1956).

[15] S. J. Singer, J.-L. Kuo, T. K. Hirsch, C. Knight, L. Ojamae and M. L. Klein. *Phys. Rev. Lett.*, **94**, 135701 (2005).

[16] M. L. Boas. *Mathematical Methods in the physical sciences.* John Wiley and Sons, (1983).

[17] J.-L. Kuo and M. L. Klein. *J. Phys. Chem. B*, **108**, 19634 (2004).

[18] C. Salzmann, P. Radaelli, A. Hallbrucker, E. Mayer and J. Finney. *Science*, **311**, 1758 (2006).

[19] J. D. Bernal and R. H. Fowler. *J. Chem. Phys.*, **1**, 515 (1933).

[20] H. T. Stokes and D. M. Hatch. Findsym version 3.1, (2004).

[21] G. Tribello, B. Slater and C. Salzmann. *JACS*, **128**, 12594 (2006).

[22] L. Pauling. *J. Amer. Chem. Soc.*, **57**, 2680 (1935).

[23] C. Knight and S. J. Singer. *J. Chem. Phys.*, **125**, 064506 (2006).

[24] C. Vega. Personal communication, (2007).

[25] J. Abascal, E. Sanz, G. G. Fenandez and C. Vega. *J. Chem. Phys.*, **122**, 234511 (2005).

Chapter 5

A new potential for ice Ih

There are many interesting properties of ice that one may wish to simulate that either take place on very long timescales or that require the use of very large unit cells. For instance one may wish to simulate phase transitions, which would take place on very long timescales (milliseconds, seconds or even longer), or one may wish to simulate liquids and as such have need of large supercells to take account of the medium range order. For these applications molecular dynamics approaches based on DFT are impractical and so it is necessary to find some approximate potential that correctly describes the energetics. There are well over 100 water potential models that have been fitted [1]. However, few of these are fitted to reproduce the properties of ice and many of the commonly used water potentials fail to correctly predict the structure of the proton ordered form of ice Ih, ice XI [2, 3]. Most potentials are instead developed for liquid water, for which DFT is impractical because of the large periodic repeat cells required to allow for the medium range structural order. In this chapter an attempt is made to find a potential that correctly reproduces the structure of ice XI and then the resulting potential is used to study the ice Ih (0001) surface.

5.1 Literature Potentials

As described in section 2.7.2, Hirsch and Ojamäe [3] have performed DFT and intermolecular potential calculations on the 16 symmetry distinct 8 molecule ice Ih unit cells [4]. For the DFT calculations they used the local orbital based code DMol^3 (BLYP functional) and the plane-wave based CASTEP [5] (PW91 functional), while for the intermolecular potentials they used the the COMPASS and SPC forcefields. They found that the relative energies calculated using the intermolecular potentials are inversely-correlated with the energies calculated using DFT. To test other potentials, optimisations using GULP [6] (TIP6P, COS/G2 and COS/G3) and *tinker* [7] (AMOEBA) were run of these 16 ice Ih structures using a number of other literature potentials, see figure 5.1:

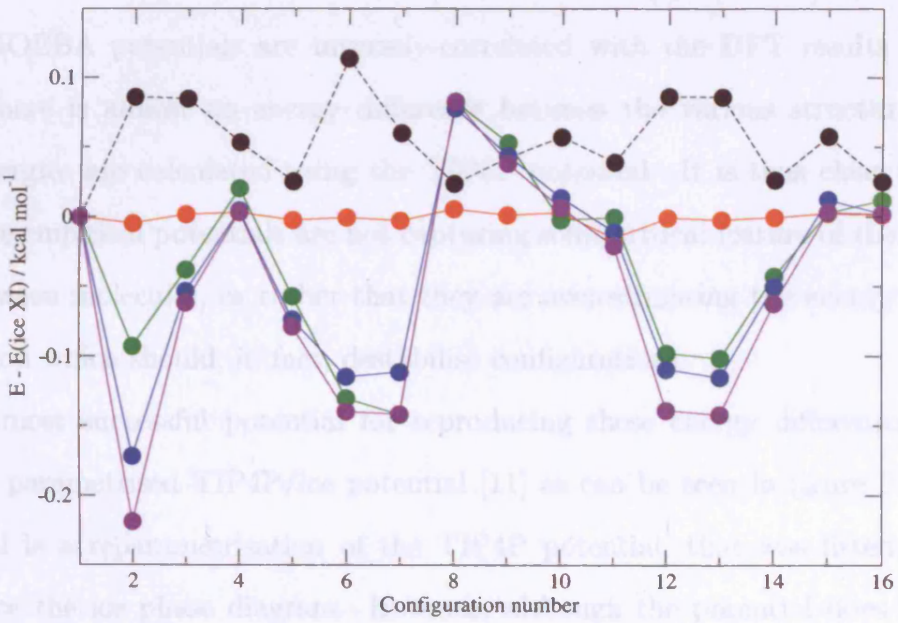

Figure 5.1: Relative energies of the 16 symmetry distinct 8 molecule ice Ih unit cells calculated using a variety of empirical potentials. The black dotted line is the DFT results (PW91, 27 k-point), the red line is TIP6P, the green line is AMOEBA, the blue line is COS/G2 and the purple line is COS/G3.

In this work, the water potentials tested represented a range of the available water potentials which are commonly used. The potential derived by Nada and van der Eerden[8], hereafter referred to as TIP6P, was selected because it was specifically fit-

ted to properties of ice, in particular the melting point. The COS/G2 and COS/G3 [9] potentials are 4 site potentials with a core and shell located on the bisector of the hydrogen bond. They are set up with the geometry of the monomer (COS/G2) and the ideal tetrahedral geometry (COS/G3). Then the position of the site on the bisector, the point charge on the bisector and the point charges on the hydrogen atoms are fitted to the values of the dipole and quadrupole of the water monomer, while the polarizability and van der Waals parameters are fitted so as to best reproduce the density of liquid water at room temperature and pressure and the heat of vaporisation. The AMEOBA [10] potential has point dipoles and quadrupoles on the hydrogen atoms and the oxygen. Dipole polarizability is explicitly treated via mutual induction of dipoles at atomic centres.

Figure 5.1 shows that as for COMPASS and SPC [3] the COS/G2, COS/G3 and AMOEBA potentials are inversely-correlated with the DFT results. Meanwhile, there is almost no energy difference between the various structures when their energies are calculated using the TIP6P potential. It is thus clear that the literature empirical potentials are not capturing some critical feature of the interaction between molecules, or rather that they are overestimating the energy of some interaction which should, in fact, destabilise configurations.

The most successful potential for reproducing these energy differences is the recently parametrised TIP4P/ice potential [11] as can be seen in figure 5.2. This potential is a reparametrisation of the TIP4P potential, that was fitted to best reproduce the ice phase diagram. However, although the potential does find the correct minimum energy hydrogen bonding topology the maximum is not correctly reproduced. Furthermore, the absolute magnitudes of the energy differences are not reproduced.

The fact that conventional literature potentials do not capture the energy differences between different proton ordering topologies is perhaps unsurprising; our own work [12] (see section 4.1.2) has shown that these energy differences depend on terms

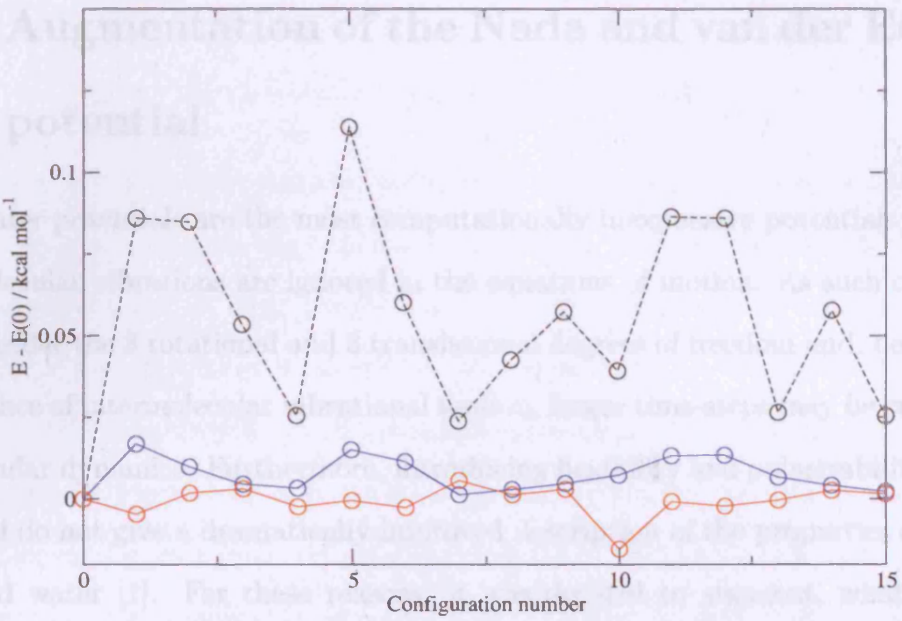

Figure 5.2: Relative energies of the 16 symmetry distinct 8 molecules ice Ih unit cells calculated using the PW91 functional (dotted black line), the TIP6P potential (red line) and the TIP4P/ice potential (blue line).

up to $(1/r^6)$ in the multipole expansion and that different ice phases have different values for the molecular multipoles. As such, to reproduce the energy differences between different proton arrangements found using density functional theory with a plane wave basis set would require a potential that contained terms that described the polarisation of all multipoles up to and including the hexadecapole. No water potential has yet been derived that includes terms that describes polarisation at this level of theory. Although it would be possible to fit such a potential using Drude oscillators [13] or fluctuating charges [14] to describe the multipolar polarizability, the resulting potential would be hugely computationally expensive. An alternative approach is to add some simple empirical term to a well tested potential so that the potential correctly reproduces energy differences between various hydrogen bonding configurations.

5.2 Augmentation of the Nada and van der Eerden potential

Rigid water potentials are the most computationally inexpensive potentials because intramolecular vibrations are ignored in the equations of motion. As such one need only consider the 3 rotational and 3 translational degrees of freedom and, because of the absence of intermolecular vibrational motion, larger time-steps may be employed in molecular dynamics. Furthermore, introducing flexibility and polarizability in the potential do not give a dramatically improved description of the properties of liquid and solid water [1]. For these reasons, it was decided to augment, what was at the time, the most computationally cheap of the potentials tested in the previous section - the TIP6P potential [8]. This potential has the added advantage that it was fitted to reproduce the melting temperature, which is critical if one wishes to get structure/energy/temperature relationships of surfaces correct. TIP6P has 6 point charges distributed as shown in figure 5.3 and Lennard-Jones interaction sites on the oxygen and hydrogen positions.

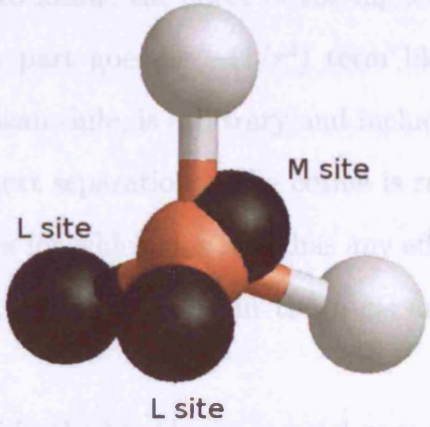

Figure 5.3: The locations of the sites in the TIP6P potential, which are added to better reproduce the charge density about the molecule.

Turning to the modification of the TIP6P potential; Hirsch and Ojamäe[3] showed that the energy (calculated using DFT) of a given proton configuration of ice Ih could be fit to an equation of the form:

$$E(\text{conf}) = E_0 + \alpha n(\text{h-trans}) + \beta n(\text{c-cis}) \tag{5.1}$$

That is to say that hypothetical configurations that contain a large proportion of *h-trans* and *c-cis* arrangements of neighbouring water molecules have higher energies than those that contain large proportions of *h-cis* and *c-trans* arrangements (see figure 2.5). When the energy is calculated using a potential like COS/G2 or COS/G3 though, it is those hydrogen bonding configurations that contain a large proportion of *h-trans* and *c-trans* arrangements of neighbouring water molecules that have low energies, which suggests that potentials incorrectly predict the *h-trans* configuration to be lower energy than the *h-cis* configuration. Based on this observation a term that stabilises the *h-cis* and *c-trans* configurations was developed, which has the form of an intermolecular torsional potential (see equation 5.2) between the $\overrightarrow{\text{OM}}$ vectors on adjacent water molecules and around the $\overrightarrow{\text{OO}}$ vector.

$$E_T = \left[\frac{A}{(\boldsymbol{R}_{\text{O}_k} - \boldsymbol{R}_{\text{O}_j})^8} - \frac{B}{(\boldsymbol{R}_{\text{O}_k} - \boldsymbol{R}_{\text{O}_j})^4}\right] \cos^4 \phi \tag{5.2}$$

This term was chosen to mimic the effect of the higher order multipoles, so the leading distant dependent part goes as $-(1/r^4)$ term like the dipole quadrupole interaction. The $(1/r^8)$, meanwhile, is arbitrary and included simply to ensure that the term is repulsive at short separations. The cosine is raised to the fourth power so that the spread of angles for which this term has any effect is small and maximal for ϕ equals 0° and 180°, as it would be in the *h-cis* and *c-trans* configurations respectively.

The values of A and B in the torsional potential were fitted to first ensure that the distance dependent part is at a minimum when the distance between adjacent water molecules has the bulk ice value. This was achieved by rewriting equation 5.2 in ϵ-σ form (see equation 5.3) and setting the value of σ, the separation at which the potential energy minima will lie, to the average ice O-O separation. ϵ, the depth of the minimum, was then adjusted manually until the best fit to the data from

CASTEP was achieved. The final values of the potential parameters are given in table 5.1.

$$E_T = \epsilon \left[\left(\frac{\sigma}{\boldsymbol{R}_{O_k} - \boldsymbol{R}_{O_j}} \right)^8 - 2 \left(\frac{\sigma}{\boldsymbol{R}_{O_k} - \boldsymbol{R}_{O_j}} \right)^4 \right] \cos^4 \phi \tag{5.3}$$

Lengths and angles			
r_{OH} / Å	0.980	HOH / deg.	108.00
r_{OM} / Å	0.230	LOL / deg.	111.00
r_{OL} / Å	0.8892	MOH / deg.	54.00
Point Charges			
q_H / e	0.477	q_M / e	-0.866
q_L / e	-0.044	q_O /e	0.0
Lennard Jones Parameters			
ϵ_{OO} / k_B K	85.9766	σ_{OO} / Å	3.115
ϵ_{OH} / k_B K	34.5471	σ_{OH} / Å	1.894
ϵ_{HH} / k_B K	13.8817	σ_{HH} / Å	0.673
Torsional Term			
A / eV Å^8		8.530	
B / eV Å^4		0.298	

Table 5.1: The values of the potential parameters for the augmented TIP6P potential.

The initial fitting procedure was done using GULP [6] optimisations, using very stiff harmonic springs ($k \sim 10000$ eV) to represent the rigid bonds and angles. Woodley [15, 16] has shown that this treatment of rigid bonds in optimisation codes does not necessarily work because if, for example, a hydrogen is rotating about an oxygen it should travel along a circular path in order to ensure that the OH bond length remains constant. Within GULP though the moves used in the minimisation algorithm [17, 18] do not move atoms along curved paths but instead move them on straight paths in the direction of the force on the atom of interest. Returning to the hydrogen rotating about the oxygen the force on the hydrogen will act in

a direction tangential to the circular path which the hydrogen should be travelling along. If GULP attempts to move the atom along this tangential path the OH bond will stretch which will, because of the gigantic force constant, drastically increases the energy of the system. The large spring constants on the rigid units can thus prevent the motion of the hydrogen atoms completely and thus prevent the system from finding the minimum in the potential energy. For optimising ice structures this approximation can be justified as it is believed that the structure input is relatively close to the minimum energy structure and thus only a small amount of rotation is needed to get the structure to the potential energy minimum (this has been shown in the literature [3] and is also evident from our own CASTEP calculations). To ensure that treating the rigid units as harmonic springs has not affected the

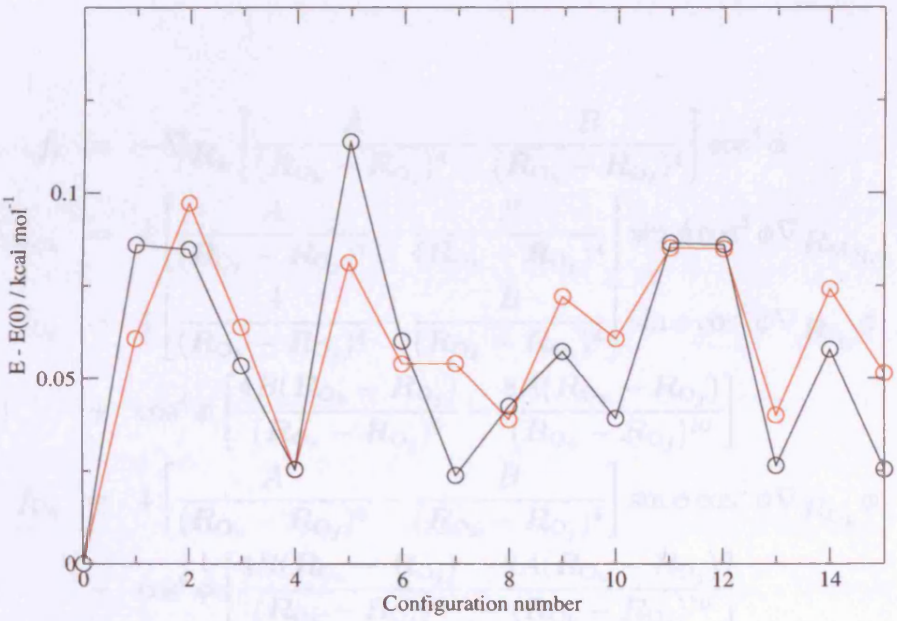

Figure 5.4: Relative energies for the 16 symmetry distinct 8 molecule ice Ih unit cells calculated using the PW91 functional (black line) and the augmented TIP6P (red line). All energies are given relative to the energy of ice XI.

optimised structure too greatly an "optimisation" using the newly fitted potential with DL_POLY_2 [19], a true rigid body code, was carried out. DL_POLY_2 though is incapable of doing potential energy optimisation using an advanced minimisation algorithm like BFGS or RFO as it is a molecular dynamics code, so instead molecular

dynamics at very low temperature, and thus small kinetic energy, was carried out until the value of the potential energy was constant. The potential now predicts the correct structure for ice XI and a reasonable fit to the DFT energies can be obtained as shown in figure 5.4.

5.2.1 Encoding the torsional potential

The new torsional term was not included in the database of potential types available to either GULP [6] or DL_POLY_2 [19] and as such both codes needed to be modified to support this new potential function. Calculating the contribution torsion makes to the potential energy is straightforward and is just a matter of encoding equation 5.2. The forces on each site due this torsional potential are then given by:

$$f_s = -\nabla_{\boldsymbol{R}_s}\left[\frac{A}{(\boldsymbol{R}_{O_k}-\boldsymbol{R}_{O_j})^8}-\frac{B}{(\boldsymbol{R}_{O_k}-\boldsymbol{R}_{O_j})^4}\right]\cos^4\phi \tag{5.4}$$

$$f_{Mo_{j/k}} = 4\left[\frac{A}{(\boldsymbol{R}_{O_k}-\boldsymbol{R}_{O_j})^8}-\frac{B}{(\boldsymbol{R}_{O_k}-\boldsymbol{R}_{O_j})^4}\right]\sin\phi\cos^3\phi\nabla_{\boldsymbol{R}_{Mo_{j/k}}}\phi \tag{5.5}$$

$$\begin{aligned} f_{O_j} &= 4\left[\frac{A}{(\boldsymbol{R}_{O_k}-\boldsymbol{R}_{O_j})^8}-\frac{B}{(\boldsymbol{R}_{O_k}-\boldsymbol{R}_{O_j})^4}\right]\sin\phi\cos^3\phi\nabla_{\boldsymbol{R}_{O_j}}\phi \\ &+ \cos^4\phi\left[\frac{4B(\boldsymbol{R}_{O_k}-\boldsymbol{R}_{O_j})}{(\boldsymbol{R}_{O_k}-\boldsymbol{R}_{O_j})^6}-\frac{8A(\boldsymbol{R}_{O_k}-\boldsymbol{R}_{O_j})}{(\boldsymbol{R}_{O_k}-\boldsymbol{R}_{O_j})^{10}}\right] \end{aligned} \tag{5.6}$$

$$\begin{aligned} f_{O_k} &= 4\left[\frac{A}{(\boldsymbol{R}_{O_k}-\boldsymbol{R}_{O_j})^8}-\frac{B}{(\boldsymbol{R}_{O_k}-\boldsymbol{R}_{O_j})^4}\right]\sin\phi\cos^3\phi\nabla_{\boldsymbol{R}_{O_k}}\phi \\ &- \cos^4\phi\left[\frac{4B(\boldsymbol{R}_{O_k}-\boldsymbol{R}_{O_j})}{(\boldsymbol{R}_{O_k}-\boldsymbol{R}_{O_j})^6}-\frac{8A(\boldsymbol{R}_{O_k}-\boldsymbol{R}_{O_j})}{(\boldsymbol{R}_{O_k}-\boldsymbol{R}_{O_j})^{10}}\right] \end{aligned} \tag{5.7}$$

The cosine of ϕ can be calculated using [20]:

$$\cos\phi = \frac{\boldsymbol{A}.\boldsymbol{B}}{|\boldsymbol{A}||\boldsymbol{B}|} \tag{5.8}$$

where $\boldsymbol{A} = \boldsymbol{F}\times\boldsymbol{G}$ and $\boldsymbol{B} = \boldsymbol{H}\times\boldsymbol{G}$

with $\boldsymbol{F} = \boldsymbol{R}_{Mo_j} - \boldsymbol{R}_{O_j}$ $\boldsymbol{G} = \boldsymbol{R}_{O_j}\times\boldsymbol{R}_{O_j}$ $\boldsymbol{H} = \boldsymbol{R}_{O_k} - \boldsymbol{R}_{Mo_k}$

and similarly the sine may be calculated using [21]:

$$\sin\phi = \frac{\boldsymbol{B}\times\boldsymbol{A}.\boldsymbol{G}}{|\boldsymbol{A}||\boldsymbol{B}||\boldsymbol{G}|} \tag{5.9}$$

The only thing remaining that needs to be calculated are the derivatives of ϕ with respect to each of the atomic coordinates, which are given by [21]:

$$\nabla_{\boldsymbol{R}_{\mathrm{Mo}_j}}\phi = -\frac{|\boldsymbol{G}|}{\boldsymbol{A}^2}\boldsymbol{A} \tag{5.10}$$

$$\nabla_{\boldsymbol{R}_{\mathrm{O}_j}}\phi = = \frac{|\boldsymbol{G}|}{\boldsymbol{A}^2}\boldsymbol{A} + \frac{\boldsymbol{F}.\boldsymbol{G}}{\boldsymbol{A}^2|\boldsymbol{G}|}\boldsymbol{A} - \frac{\boldsymbol{H}.\boldsymbol{G}}{\boldsymbol{B}^2|\boldsymbol{G}|}\boldsymbol{B} \tag{5.11}$$

$$\nabla_{\boldsymbol{R}_{\mathrm{O}_k}}\phi = \frac{\boldsymbol{H}.\boldsymbol{G}}{\boldsymbol{B}^2|\boldsymbol{G}|}\boldsymbol{B} - \frac{\boldsymbol{F}.\boldsymbol{G}}{\boldsymbol{A}^2|\boldsymbol{G}|}\boldsymbol{A} - \frac{|\boldsymbol{G}|}{\boldsymbol{B}^2}\boldsymbol{B} \tag{5.12}$$

$$\nabla_{\boldsymbol{R}_{\mathrm{Mo}_k}}\phi = \frac{|\boldsymbol{G}|}{\boldsymbol{B}^2}\boldsymbol{B} \tag{5.13}$$

Although the torsional term is notionally four-bodied, it acts between two rigid bodies and thus it is only necessary to do a double loop to evaluate forces. Furthermore, because it is short ranged in this work a cutoff of 3.5 Å is used because the maximum torsional energy at this separation is -0.00161 eV and as such any discontinuity in the potential energy is extremely small in comparison to the total energy fluctuations and is not expected to affect structural accuracy. The short ranged nature of this interaction is again believed to mirror the short rangedness of the higher order terms in the electrostatic expansion, which arises because of their steep distance dependence.

5.3 Monte Carlo of Bulk Ice

The objective of this work was to derive a potential that is capable of predicting the lattice energy of ice with reasonable precision, which previously was not possible because, as discussed earlier, potentials were unable to reproduce the structure of ice XI and the energy differences between different hydrogen arrangements in ice

Ih. As such there has been no attempt to ensure that simulations of proton disordered ice Ih have been started with hydrogen arrangements that are energetically reasonable. Instead, Hayward and Reimers [22] derived an energy independent protocol of generating bulk configurations which works by maximising disorder, whilst minimising net polarity within the cell. This seems a sensible approach as surface energy will not converge if the bulk underneath it has a dipole and one wouldn't want to describe a structure that is known to be proton disordered using a highly ordered arrangement of hydrogens. However, it is not known whether or not the requirement of small multipole moments has a large energetic cost or if the Hayward and Reimers simulation cells are even thermally accessible hydrogen bonding topologies for any given temperature. Given that a potential has been fitted which is capable of reproducing the subtle energy differences between differing hydrogen bonding topologies it follows that one ought now to be able to easily answer these questions.

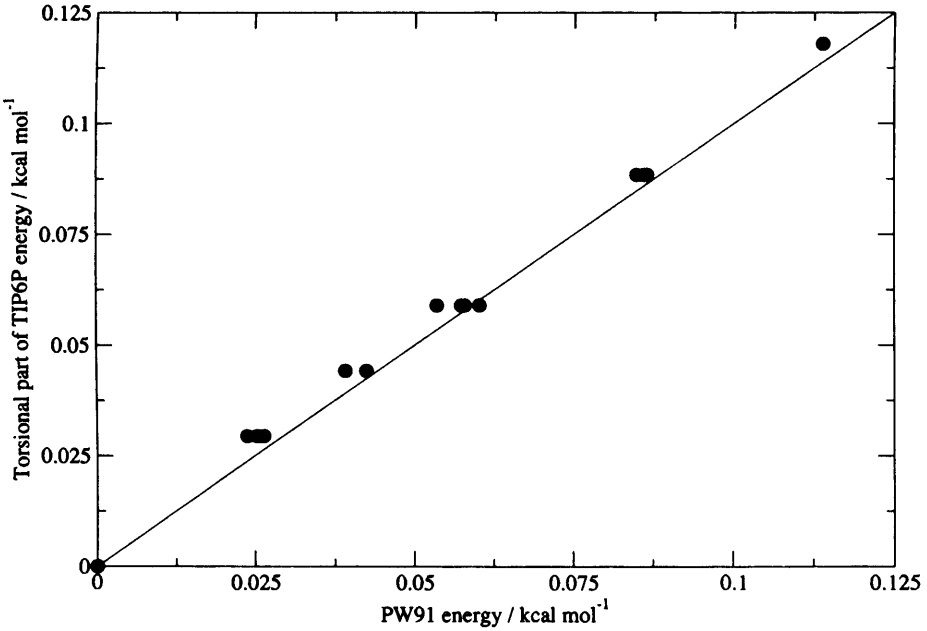

Figure 5.5: Correlation between relative energies calculated using the PW91 functional and only the torsional part of the augmented TIP6P potential. All energies are given relative to the energy of the structure of ice XI.

Proton topology change is a very long time scale process and thus not one that is sampled in conventional MD. If one wished therefore to carry out molecular dy-

namics simulations on bulk ice one must input a starting structure which is an energetically reasonable proton topology. As discussed in section 3.4.3, in Monte Carlo simulations one may use any random move prior to applying the Metropolis condition. So one may move the system using the Rick [23] algorithm, which was discussed in section 3.4.3, and as such change the proton topology. One may also impose conditions of zero dipole by rejecting any move that results in a net dipole, using criterion C2 of Hayward and Reimers [22], which works by noting that there are 24 possible orientations a water molecule can adopt in ice. As such, if the total number of each of the orientations is the same, there will be no net dipole in the cell. In calculating the potential energy it is useful to note that, for the newly modified TIP6P, it is the sum of the pure TIP6P energy and the additional torsional term. As shown in figure 5.1 the energy differences, calculated using the pure TIP6P potential, between the various 8 molecule ice Ih unit cells are less than 0.01 kcal mol^{-1} and thus one can neglect the pure TIP6P parts of the potential energy and use just the difference in the torsional energy when applying the Metropolis Condition. This makes the Monte Carlo calculations computationally very inexpensive. Figure 5.5 shows the strong correlation between the energy differences calculated using the PW91 functional and the differences between total torsional energy for the various configurations.

One initial, quick test that can be carried out to ensure whether or not the Hayward and Reimers [22] cells have reasonable energies is to calculate their total torsional energies and compare it with the values of a similarly sized cell composed of ice XI and one composed of the maximum energy structure (configuration 6). Obviously if the structure lies too close to the maximum energy structure then it throws suspicion on its energetic accessibility. This has been done for Hayward and Reimers' [22] 360 molecule unit cell (22.53531 Å x 23.41938 Å x 22.08000 Å) which, has a total "torsional" energy of -0.7311 eV. Meanwhile a 360 molecule unit cell, of the same dimensions composed of configuration 1 has an energy of -

1.8720 eV and a supercell based upon configuration 6 has an energy of -0.1141 eV. The Hayward and Reimers cell thus has an energy that is just under half of the maximal energy, implying that maximal disorder biases the configurational search to produce structures that have an energy equitable with the mean energy of the 16 hypothetical structures. This is unsurprising as the Hayward and Reimers cell, with its maximal disorder, would be expected to be of space group P1 and, as was discussed in section 4.1.3, P1 structures usually have an equal mixture of high and low energy structural features and as such have energies that lie equidistant from the energies maximum and minimum energy proton topologies.

Monte Carlo (MC) calculations at 0.001 K were run starting from the Hayward and Reimers [22] cell with and without the C2 constraint. Without the C2 constraint an MC run of 500000 steps was performed, and the system evolved to a configuration with energy -1.87168 eV, which is very close to the energy of the system consisting of only the true, ferroelectric ice XI structure suggesting that at low temperatures, without the C2 constraint the simulation is finding the true global minimum energy hydrogen bonding topology. Meanwhile, with the constraint a simulation was performed in which 10^8 configurations were generated of which 914302 had zero net dipole and the final energy reached was -0.96265 eV. The discrepancy between the final energies in the two simulations shows that at these low temperatures requiring the cell to have zero dipole prevents the structure from moving from the high energy structure to lower, more energetically reasonable structures.

Similar MC simulations were done at 100K and it was found that without any constraints the lowest energy reached during the run was -0.8773522 eV, whilst with the constraint the lowest energy reached was -0.8578554 eV. It can thus be concluded that constraining the system to have zero dipole is a valid approximation at higher temperatures.

The observation that at high temperatures imposing a constraint of zero dipole gives energetically reasonable structures suggests that low temperature MC in which

the constraint of zero dipole is applied can be used to generate reasonable, proton disordered, unit cells for use in molecular dynamics simulations. At low temperatures however, the simulations show that assuming the system has no overall dipole can no longer provide a reasonable description of the structure. This is perhaps unsurprising though given that the ordered form of ice Ih is ferroelectric. One question remains which is, at what temperature is it reasonable to start using the Hayward and Reimers' unit cells to perform simulations? As already discussed the difference in energy between the Hayward and Reimers' cell and a cell of pure ice XI is 3.169 x 10^{-3} eV per molecule, which corresponds to a temperature of $\sim$ 37K. By contrast the energy difference between the cell of all ice XI and the cell of all configuration 6 (the global maxima) corresponds a temperature of 57 K, while the energy difference between a cell of all ice XI and the lowest energy zero dipole structure found in this work corresponds to a temperature of 29 K.

A unit cell of 2880 water molecules has been generated using this technique, which was initially constructed by replicating the low energy 360 molecule cell, output from the 0.001 K zero dipole MC run, in a 2x2x2 supercell. 10^8 configurations were generated, of which 111313 had zero net dipole and the final structure had an energy of -7.7085 eV, -0.007 eV lower than the starting structure. This miniscule energy difference suggests that energetically reasonable unit cells can be generated by forming a supercell of a highly proton disordered structure. That is to say that requiring the system to have translational symmetry on the order of 20 Å within its hydrogen bonding network does not impose a disastrous energetic constraint on the system.

5.4 Ice surfaces

As mentioned in section 2.7.2 there has been no systematic study of whether or not the proton topology at an ice surface affects its surface energy. This seems especially pertinent given that Wake's [24] recent work, discussed in section 2.7.2, shows that

there is little or no surface disorder on the (0001) surface unless one is close to the melting temperature.

It is known from experiment that the (0001) surface is one of the most morphologically important surfaces in ice. This plane contains the bilayers of water molecules and as such can be cleaved in one of two ways - either a bilayer is cleaved or one can cleave between bilayers. Cleaving between bilayers is preferable because only (N/2) hydrogen bonds are broken as opposed to the (3N/2) hydrogen bonds which must be broken if a bilayer is cleaved through (here N is the number of water molecules in a bilayer). CASTEP [5] calculations (PW91 functional 550 eV cutoff, 6x3x1 MP grid) on a slab of ice XI 2 bilayers thick backs this conclusion, as cleaving between bilayers gives rise to a surface energy of 0.618 J m^{-2}, while cleaving through a bilayer gives rise to a surface energy of 1.282 J m^{-2}. N.B. These are not converged surface energies as the substrate contains a dipole perpendicular to the surface and so the surface energy depends on the thickness of the slab.

5.4.1 Validating the modified TIP6P potential for surfaces

Although it is possible to study surfaces using density functional theory, it reduces the length and time scales over which simulations can be performed. Ideally then one would wish to study surface structure, and how proton topology affects surface energy, using the newly modified TIP6P potential. However, there is no guarantee that this potential will correctly describe how the surface energy depends on the arrangement of hydrogens at the surface. To test its ability to describe surfaces, test calculations were carried out using CASTEP [5] (PW91 functional 550 eV cutoff, 6x3x1 MP grid) and using the modified TIP6P (low temperature molecular dynamics in DL_POLY_2 [19] using Hautman-Klein Ewald sum). These calculations were carried out on a slab of ice, formed by taking a single unit cell of ice Ih and removing its periodicity in the (0001) direction / introducing a large vacuum gap between adjacent slabs. Slabs with different topologies were formed by taking the 16 unit

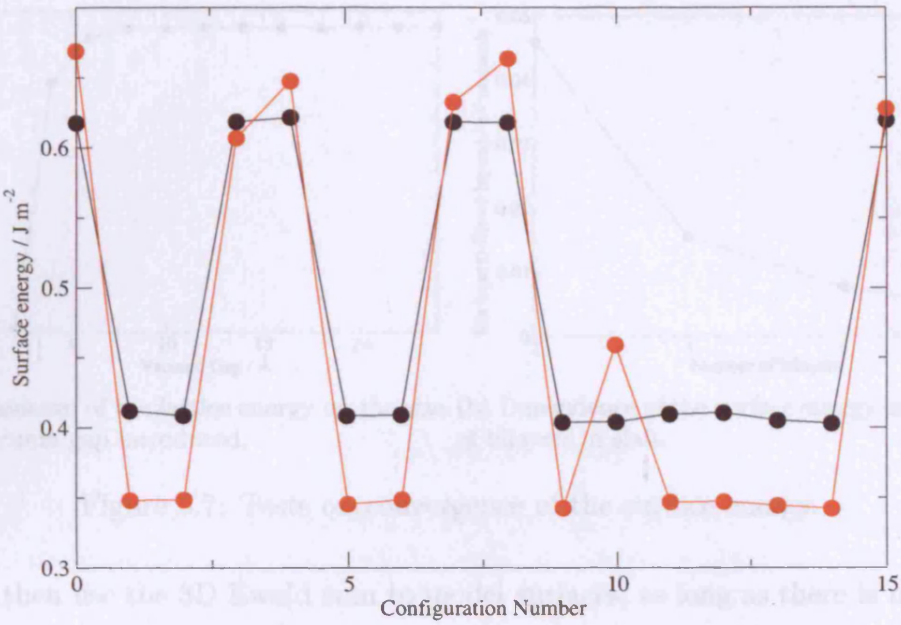

Figure 5.6: The surface energy of a bilayer of each of the 8 molecule symmetry distinct ice Ih unit cells calculated using CASTEP (black line) and using the modified TIP6P potential.

cells defined in the Hirsch and Ojamäe paper [3] and making one slab for each of these topologies. The surface energies of these various structures were then calculated by taking the energy of the slab and subtracting the energy of the bulk material. The results of these calculations are shown in figure 5.6 (N.B. Again the energies in figure 5.6 are not true surface energies as they will not all converge with slab thickness because of dipoles perpendicular to the surface.)

The surface energies in figure 5.6 fall into two narrow energy bands, either ~0.6 J m^{-2} or ~0.4 J m^{-2} and where DFT predicts the lower of these two energies the potential calculations are in agreement. Although the potential slightly overestimates this energy difference and does not exactly reproduce all the fine details of the distribution it still does an acceptable job of describing the bilayer energies.

Performing MD simulations with the Hautmann Klein 2D Ewald sum is considerably slower than doing the same calculations with the normal 3D Ewald sum. If one simply expands the lattice parameter in the direction perpendicular to the surface of interest, thereby introducing a large vacuum gap into the simulation cell,

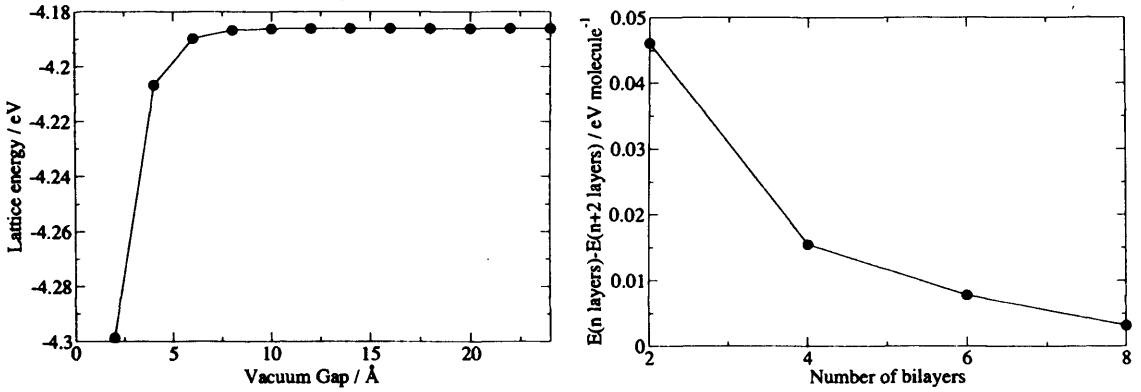

(a) Dependence of the lattice energy on the size of the vacuum gap introduced.

(b) Dependence of the surface energy on number of bilayers in slab.

Figure 5.7: Tests on convergence of the surface energy.

one can then use the 3D Ewald sum to model surfaces, as long as there is no dipole perpendicular to the surface. To ensure that enough vacuum was introduced into the cell single point energies were calculated as a function of size of vacuum gap, for the 2^{nd} of the 16 symmetrically distinct 8 molecule unit cells, which has zero net dipole. The results of these calculations are shown in figure 5.7(a) and show that a vacuum gap of at least 10 Å is required to converge the surface energy.

A further consideration when performing surface calculations is to ensure that the two surfaces of the slab are not interacting and hence the surface energy is converged with slab thickness. To test that the surface energy is converged with respect to slab thickness optimisations (MD at 0.01 K using DL_POLY_2 and a 1 fs timestep) have been carried out on slabs of configuration 2 with 72 water molecules per bilayer. To test whether the surface energy is well converged the difference, in eV per molecule, between the system consisting of n bilayers and the system consisting fo n+2 energy bilayers is calculated as shown in figure 5.7(b), which shows this quantity, and hence the surface energy, is well converged once the system is 4 bilayers thick.

5.4.2 The effect of proton topology on surface energy

Section 5.4.1 showed that the surface energy does indeed appear to depend on the hydrogen bonding topology at the surface, although only two surface terminations

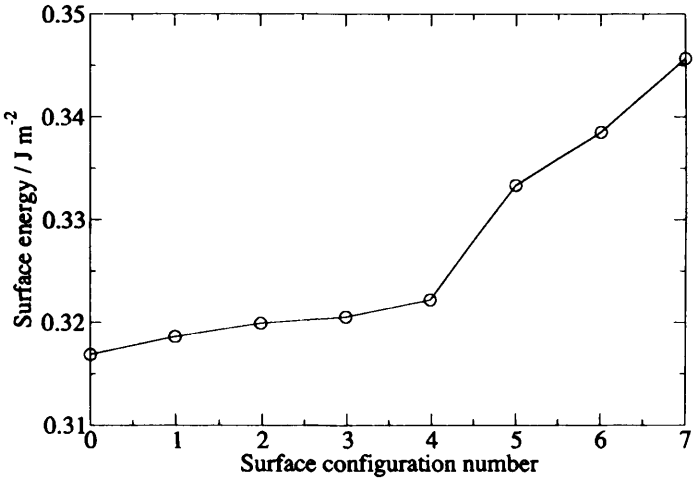

Figure 5.8: Surface energies of the 8 surfaces generated by cutting the 768 molecule Hayward and Reimers unit cell, given in order of increasing energy.

were compared and hence the findings are by no means definite as a more exhaustive investigation may prove this result not to be general. In a real crystal of ice Ih two adjacent bilayers will be linked by hydrogen bonds which will have one of $(N^2/4)$ possible hydrogen bonding configurations (where N is the number of molecules in the bilayer). This structural diversity will be sampled in the Hayward and Reimers cells because there are multiple bilayers and as such multiple bilayer linkages. Thus one way to generate surfaces with different hydrogen bonding topologies is to cut a Hayward and Reimers cell between the first and second bilayer and calculate the surface energy, then to cut it between the second and third and so on... However, one disadvantage with this scheme is that the surface energy obtained is an average over two distinct surfaces because there is no mirror plane between bilayers and as such the top surface of the crystal will have a different hydrogen bonding topology to the bottom face. Thus one could theoretically have one very high energy surface and one very low energy surface and end up with an intermediate value for the average surface energy. Nevertheless, an analysis of the surface energies of the 8 different possible surface terminations in the Hayward and Reimers [22] 768 molecule cell has been carried out using MD at 0.01 K with a 1 fs timestep in DL_POLY_2 [19]. Figure 5.8 shows the surface energies calculated.

These calculations show that, although there is a variation in surface energy for the various different possible surface topologies it is not as large as the variation in surface energy observed amongst the bilayers (see figure 5.6). The difference in energy between the highest and lowest energy slabs investigated here is approximately equal to the energy of 5 hydrogen bonds, which is a substantial energy difference.

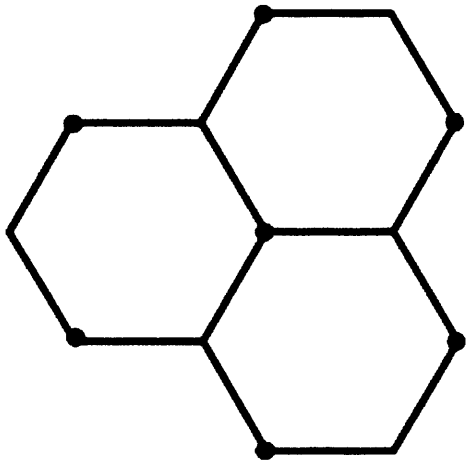

Figure 5.9: Schematic diagram of the (0001) surface of ice, which shows that around every site (red dot) there is a dangling proton there are a further 6 sites (blue dots) which may also have a dangling proton.

As discussed in section 5.2, Hirsch and Ojamäe [3] have shown that the energy, calculated for a cell of bulk ice, can be fitted to a linear combination of the number of *h-cis* and *c-trans* conformers of neighbouring waters, which raises the question - is there a similar way to fit the surface energy to features of the hydrogen bonding topology at the surface? The energetic cost of forming a (0001) surface will be dominated by the breaking of the $(N/2)$ hydrogen bonds that link the two previously connected bilayers. This bond breaking is going to result in the formation of hydrogens that stick out of the surface, so called dangling hydrogens. The number of dangling hydrogens formed during any surface forming event is going to be constant but one might imagine that the surface energy would depend on the arrangement of these dangling hydrogens on the surface. If the dangling hydrogens are clustered the energy will be high because of repulsive forces between dangling atoms. On the (0001) surface of ice, each site at which a dangling hydrogen may sit is surrounded

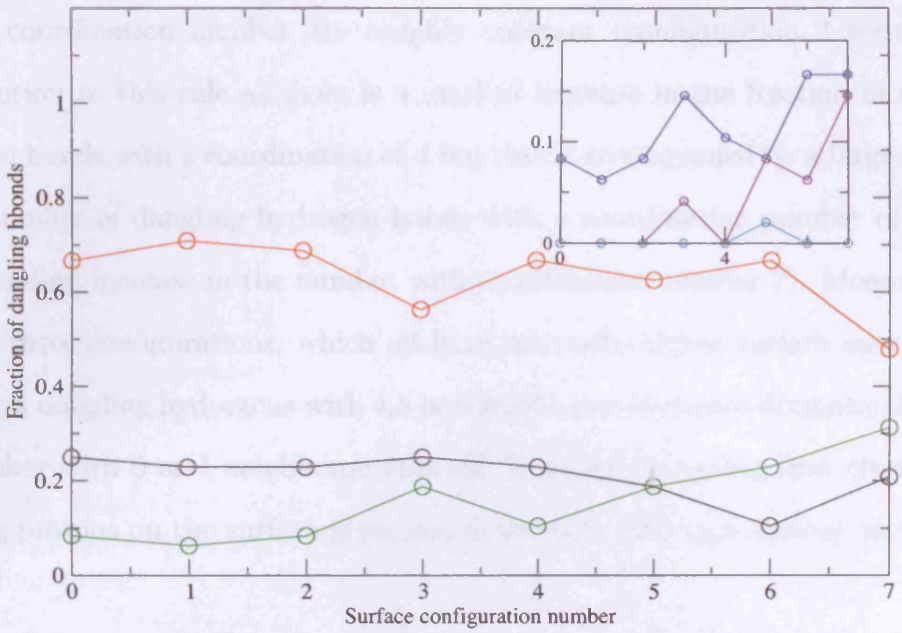

Figure 5.10: Fraction of dangling hydrogens with each coordination number on each of the surfaces generated from the Hayward and Reimers unit cell. In the main graph the black line gives the total fraction with 0 or 1 neighbours, the red line gives the fraction with 2 or 3 neighbours and the green line gives the fraction with 4,5 or 6 neighbours. In the inset the blue line gives the fraction with 4 neighbours, the purple line the fraction with 5 and the pink line the fraction with 6.

by 6 similar sites, see figure 5.9. Thus one may take a particular dangling hydrogen and count how many of the six surrounding hydrogen sites are occupied and obtain a dangling hydrogen coordination number. If this is done for all the hydrogen sites on a surface one can obtain a convenient measure of the extent to which the hydrogens are clustered on the surface. There is evidence from the bilayer calculations (section 5.4.1) that surfaces where the hydrogens are clustered will be high in energy, as for the high energy bilayers each dangling hydrogen is surrounded by six hydrogen atoms, whilst the low energy bilayers have all their dangling hydrogen surrounded by only two hydrogens. An analysis of the extent clustering has been carried out on the Hayward and Reimers surfaces cell and the results are shown in figure 5.10.

Figure 5.10 shows that, in all the surface topologies investigated, the majority of dangling hydrogen bonds are surrounded by 2 or 3 neighbours and that for the first 5 configurations, which all have very similar surface energies, the proportions

of each coordination number are roughly constant (configuration 3 seems to be an exception to this rule as there is a marked increase in the fraction of dangling hydrogen bonds with a coordination of 4 but this is accompanied by a large decrease in the number of dangling hydrogen bonds with a coordination number of 3 and a corresponding increase in the number with coordination number 2). Meanwhile for the last three configurations, which all have markedly higher surface energies, the fraction of dangling hydrogens with 4,5 or 6 neighbours increases dramatically, while the number with 0 or 1 neighbours falls off. It would thus seem that clustering of dangling protons on the surface gives rise to surfaces with high surface energies.

5.4.3 Monte Carlo on surfaces

Using the Rick algorithm [23], with the extensions to the allowed moves described in section 3.4.3, it is possible to perform Monte Carlo over the allowed surface hydrogen bonding topologies. If this is done at low temperature hydrogen bonding topologies that give rise to low energy surfaces can be generated. An 110000 step Monte Carlo simulation has been carried out at 0.01 K. The energy as a function of simulation "time" in this simulation is shown in figure 5.11(a), along with the fraction of dangling bonds with each coordination number 5.11(b).

Figure 5.11 shows that there some correlation between the changes in the total energy and the changes in the structure of the surface. It would appear that over the course of the simulation the number of dangling hydrogens with 1 neighbour decreases while the fraction with 2 increases. However, the energy change over the course of the simulation is very small which suggests that the simulation was started with a highly favourable proton topology at the surface. This seems reasonable given that in the previous section it was shown that it is the larger clusters (4, 5 or 6 neighbours) which make noticeable differences to the surface energy.

The lowering in energy observed in figure 5.11(a), which is not correlated with the surface structure change, is probably due to energy lowering effects in the bulk,

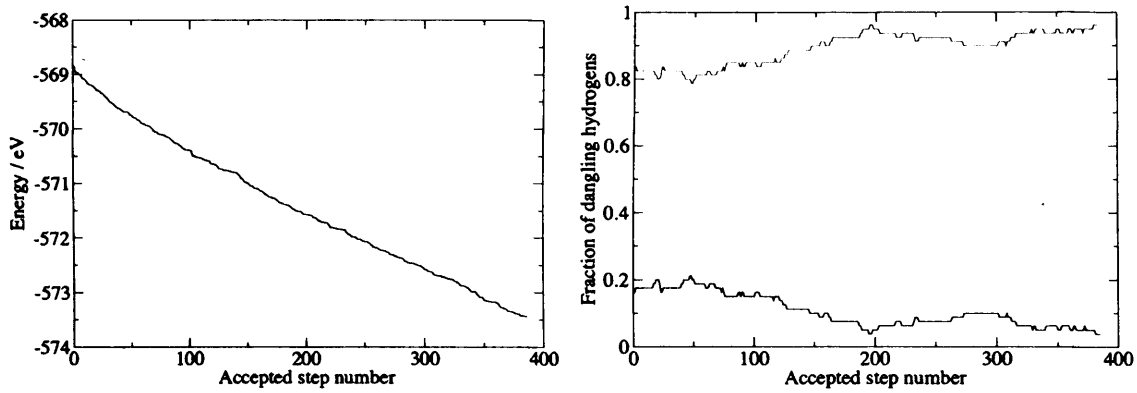

(a) Change in the total energy over the course of simulation

(b) Change in the surface structure over the course of simulation

Figure 5.11: Results for Monte Carlo simulation at 0.01 K. In the right pane the change in the surface structure is shown; in this figure the black line is the fraction of dangling hydrogen with one neighbour and the red line is fraction of dangling hydrogens with 2 neighbours.

that is to say those effects that make the structure more like ice XI, the lowest energy proton topology for bulk ice. This is confirmed by examining the torsional energy over the course of the simulation - the reduction of which is responsible for roughly half the drop in energy.

Figure 5.11(a) shows, rather worryingly, that the energy of the system is not converged with respect to simulation time. It seems as if the simulation is stuck, which is evidenced by the frequency of acceptance of 3.5 x 10^{-2}. This acceptance frequency was found to fall over the course of the simulation and by the end is equal to 4.983 x 10^{-4}. At 0K the most favorable bulk ice Ih topology is the ice XI structure. However, the ice XI structure has a very high energy (0001) surface (see section 5.3) because all the dangling hydrogen bonds are clustered on one of the two surfaces of the crystal. As such one might expect there will be a competition between the formation of ordered ice XI in the bulk and some lower energy proton topology at the surface or that during the transition to ice XI the morphology of the crystal changes such that the (0001) surface is not present. This is the subject of further investigations that are ongoing.

The uneven distribution of dangling hydrogen atoms at the surface suggests that the distribution of charge over the surface is not going to be even. In particular one

would expect that in regions where there are dangling hydrogen atoms the surface will be positively charged. As such the water molecules with dangling hydrogens in these regions may be more acidic, because it becomes more favourable to loose the dangling hydrogen atoms because of the repulsions they experience from their near neighbours. Also, because of the charge in the areas where dangling hydrogen bonds are clustered, these regions might be expected to provide interesting sites for binding and heterogenous catalysis. As such it would be interesting to see whether or not at higher temperatures a greater fraction of high coordination number dangling hydrogen bonds are observed. To this end Monte Carlo calculations at the range of temperatures ice is found in the atmosphere (190 K - 270 K) have been carried out. 50000 steps of Monte Carlo were performed at 190 K, 210 K, 230 K, 250 K and 270 K and it was found that as the temperature was increased so the acceptance ratio was increased. However, even at the highest temperature the acceptance ratio was only 0.316, suggesting that there a large number of possible surface configurations that are energetically inaccessible and also justifying the use of Monte Carlo to select a sensible starting proton configuration for any surface simulation. To establish the extent to which the temperature affects the extent of clustering of hydrogens on the surface the locations of each dangling bonds and the number of the six possible hydrogen sites surrounding the central dangling bond has been calculated for each proton topology visited during the MC simulation. This quantity has then been averaged over the entire simulation run, as can be seen in figure 5.12.

Figure 5.12, shows that as one increases the temperatures the fraction of dangling hydrogens with the higher "coordination numbers" increases, while the fraction of dangling hydrogens with 2 or 3 neighbours decreases. It would seem from the data on the dangling hydrogens with 0 or 1 neighbours that these low "coordination number" hydrogens can only exist in structures where there are also hydrogens with high coordination number (i.e 4, 5 or 6 neighbours). At lower temperatures the system compensates for the introduction of the high energy dangling hydrogens (i.e.

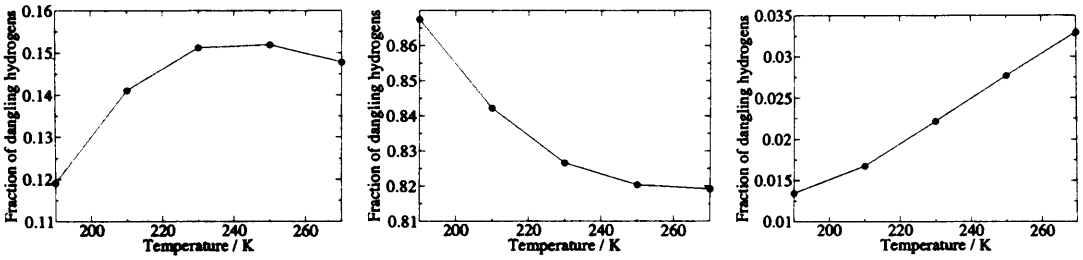

(a) Fraction of dangling hydrogens with 0 or 1 neighbours.

(b) Fraction of dangling hydrogens with 2 or 3 neighbours.

(c) Fraction of dangling hydrogens with 4,5 or 6 neighbours.

Figure 5.12: Fraction of dangling hydrogens with the various different numbers of neighbors as a function of temperature.

those with 4, 5 or 6 neighbours) by introducing large numbers of these low energy dangling hydrogens (those with 0 or 1 neighbours), while at the highest temperatures this is not necessary.

5.5 Molecular dynamics

The next step in this work would be to use the reasonable surface topologies, obtained from the Monte Carlo, as start points for molecular dynamics simulations, which would allow one to model the effects that temperature has on the surface structure and to explore the correlated events. Faraday [25] proposed that the surface of ice was liquid-like, and simulations of this sort would allow one to establish whether or not this is true. The original TIP6P potential is particularly suited to the study of surface pre-melting because, unlike the TIP4P or SPC potential, it reproduces the correct melting point of ice. Prior to using the modified TIP6P potential to model surfaces though it is necessary to test whether or not introduction of the torsional term has introduced any problems into the potentials description of the dynamical structure of ice and water.

5.5.1 Liquid Water

To assess whether the additional torsional term added to the potential causes any deviation in the dynamical water structure a molecular dynamics simulations was carried out with the modified TIP6P was performed on a water box containing 768 water molecules. A timestep of 1 fs was used to integrate the equations of motion with the velocity Verlet algorithm. The cells were first equilibrated in the NPT ensemble for 5 ps using temperature rescaling at every step, before being run on for a further 380 ps in the NPT ensemble at 300 K using the Berendsen algorithms to control the pressure and temperature. The total energy as a function of simulation time is shown in figure 5.13

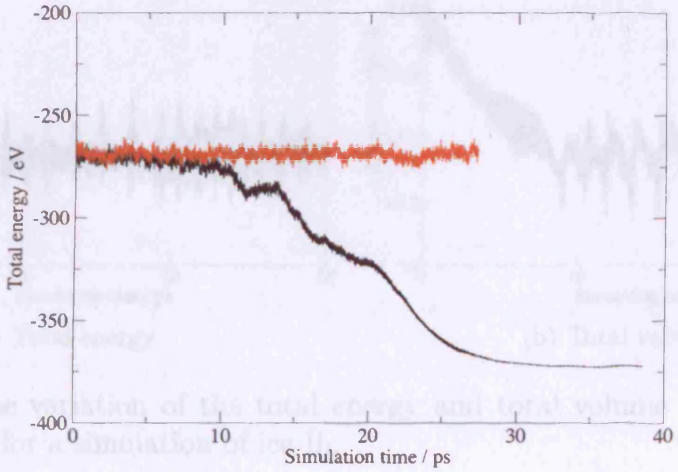

Figure 5.13: The black line gives the total energy as a function of simulation time for a molecular dynamics simulation of 768 water molecules interacting through the modified TIP6P potential. The red line gives the results of a similar simulation which used the unmodified TIP6P

The simulation was started off from a configuration output from an equilibrated unmodified TIP6P calculation. Clearly the potential introduces some dramatic perturbation to the structure, which from the radial distribution function appears to be a drastic over-structuring of water.

5.5.2 Ice Ih

It was hoped that by performing a molecular dynamics simulation of ice Ih some insight into what causes the dramatic deviations observed in the water simulations. Thus a 300 ps molecular dynamics simulations of ice Ih starting from the 432 molecule Hayward and Reimers [22] ice Ih configuration was carried out. In this simulation the system was equilibrated for 0.5 ps before being run on at 200 K using the Berendsen algorithm to control the temperature and the Berendsen anisotropic barostat to control the pressure. Figure 5.14(a) shows the variation of the total energy as a function of time in these simulations.

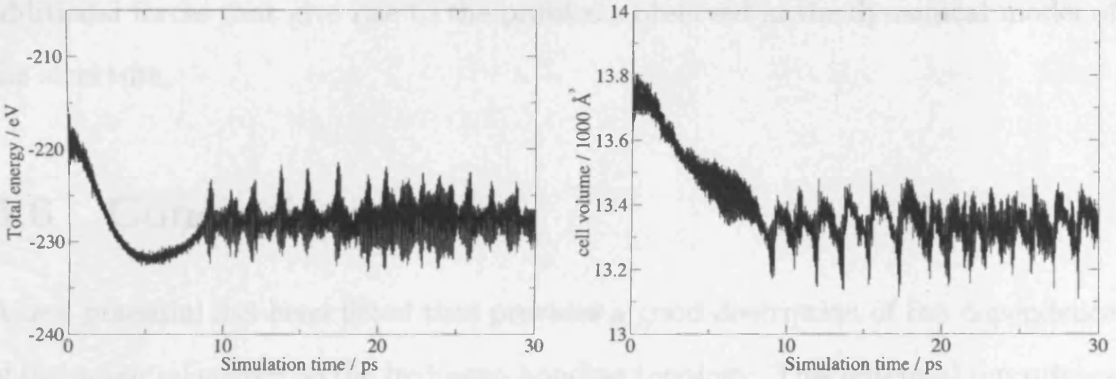

(a) Total energy (b) Total volume

Figure 5.14: The variation of the total energy and total volume as a function of simulation time for a simulation of ice Ih.

Figure 5.14(a) shows that there is first a drop in the energy and this then settles down into what appears to be a periodic fluctuation in the total energy. Similar behavior has been observed for the cell volume in this simulation 5.14(b) but this is not the source of the energy fluctuations as there are similar fluctuations in total energy during similar constant volume simulations. A reasonable explanation for this fluctuation is that there is a relatively low energy vibrational mode that is active in ice at these temperatures that causes neighbouring water molecules to rotate relative to each other as shown in the figure 5.15.

With the torsional term present the restoring force on this phonon will not just act to return molecules to the equilibrium torsional angle, but will also cause the

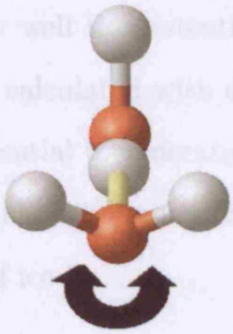

Figure 5.15: A visual illustration of the phonon which the potential describes very poorly. This is believed to cause the problems encountered in the molecular dynamics simulations.

two oxygen atoms to move together or move apart. In all probability it is these additional forces that give rise to the problems observed in the dynamical model of the structure.

5.6 Conclusions

A new potential has been fitted that provides a good description of the dependence of the potential energy on the hydrogen bonding topology. This potential reproduces the energy differences between topologies that are observed in DFT. The work carried out with this potential has highlighted the importance of taking in to account the proton topologies when one performs simulations of bulk ice Ih at low temperatures and, more interestingly, the subtle effect that surface proton topology has on the surface energy. With regard to the surface it has been shown that clustering of dangling hydrogen atoms at the surface leads to high energy surface terminations. Monte Carlo simulations have shown that the concentration of these high energy, clustered, dangling hydrogen bonds on the surface is very low and that as such it is important to consider the surface proton topology when performing simulations of the surface of ice.

The failure of the potential to describe derivatives though means that one can not use the potential to investigate the dynamics of the low energy surface proton

topologies generated. Given how well the potential reproduces the dependence of the energy of the surface energy calculated with density functional theory though, it may be possible to use the potential to generate a viable surface proton topology that could then be run on using *ab initio* molecular dynamics methods to obtain a good description of the surface of ice Ih.

Bibliography

[1] B. Guillot. *Journal of Molecular Liquids*, **101**, 219 (2002).

[2] P. S. V. Buch and J. Sadlej. *Phys. Chem. B*, **102**, 8641 (1998).

[3] T. K. Hirsch and L. Ojamäe. *J. Phys. Chem. B*, **108**, 15856–15864 (2004).

[4] S. J. Singer, J.-L. Kuo, T. K. Hirsch, C. Knight, L. Ojamae and M. L. Klein. *Phys. Rev. Lett.*, **94**, 135701 (2005).

[5] M. D. Segall, P. L. D. Lindan, M. J. Probert, C. J. Pickard, P. J. Hasnip, S. J. Clark and M. C. Payne. *J. Phys.: Cond. Matt.*, **14**, 2712 (2002).

[6] J. D. Gale. *J. Chem. Soc., Faraday Trans.*, **93**, 629 (1997).

[7] P. Ren and J. W. Ponder. *J. Comput. Chem.*, **23**, 1497 (2002).

[8] H. Nada and J. P. J. M. van der Eerden. *J. Chem. Phys.*, **118**, 7401–7413 (2003).

[9] H. Yu and W. F. van Gunsteren. *J. Chem. Phys.*, **121**, 9529–9563 (2004).

[10] P. Ren and J. W. Ponder. *J. Phys. Chem.*, **107**, 5933 (2003).

[11] J. Abascal, E. Sanz, G. G. Fenandez and C. Vega. *J. Chem. Phys.*, **122**, 234511 (2005).

[12] G. Tribello and B. Slater. *Chem. Phys. Lett.*, **425**, 246 (2006).

[13] P. A. Madden and M. Wilson. *Chemical Society Reviews*, **25**, 339 (1996).

[14] J. Jeon, A. E. Lefohn and G. A. Voth. *J. Chem. Phys.*, **118**, 7504 (2003).

[15] S. M. Woodley, P. D. Battle, J. D. Gale and C. R. A. Catlow. *Chem. Mater*, **15**, 1669 (2003).

[16] S. Woodley. Personal communication, (2006).

[17] D. F. Shanno. *Math. Comput.*, **24**(647) (1970).

[18] A. Banerjee, N. Adams, J. Simons and R. Shepard. *J. Phys. Chem.*, **89**, 52 (1985).

[19] W. Smith and T. Forester. *J. Molec. Graphics*, **14**, 136 (1996).

[20] M. P. Allen and D. J. Tildesly. *Computer Simulation of Liquids.* Oxford Science Publications, (1989).

[21] A. Blondel and M. Karplus. *J. Comp. Chem.*, **17**, 1132 (1995).

[22] J. A. Hayward and J. R. Reimers. *J. Chem. Phys.*, **106**, 1518 (1996).

[23] S. W. Rick. *J. Chem. Phys.*, **122**, 094504 (2005).

[24] C. L. Wake, G. Tribello and B. Slater. *In Preparation*, (2007).

[25] M. Faraday. *Quant. J. Sci. Lit. Arts*, **15**, 71 (1823).

Chapter 6

Structural analogies between ice, carbon, silica and zeolites

That there are structural analogies between dense ice phases, siliceous materials, water clathrates and zeolites is well known [1] - all are composed of tetrahedral units that share vertices and thus form infinite 4-connected nets. These tetrahedra can pack in a wide variety of ways to give numerous different nets and a wide variety of solid phases - there are 15 known phases of ice [2], 7 dense silica phases [3] and a staggering 170 known zeolite topologies [4]. However, even this large number is only a tiny fraction of the set of mathematically possible infinite 4-connected nets which can be obtained from tiling theory [5, 6, 7].

Clearly the variety of nets possible which a particular combination of chemical elements can crystallise into provides insight into the nature of the interatomic / intermolecular interactions in these substances, as it is these which will control the position of the local minimum on the potential energy surface, at which each possible net will find itself. These minima can correspond to structures which are stable or metastable and can as such provide an upper bound on the energy of metastable structures and hence provide a compass for exploring the rest of 4-connected net space for potential new structures in the synthesisable territory for the particular element combination of interest.

There have been numerous attempts to understand the synthesisable territory for silica and pure silica zeolites. Early studies [8] showed that there was good agreement between the energies obtained from simple interatomic potential calculations and those obtained from calorimetry and hence provided the compass for an exploration of 4-connected net space. This was then followed by work which used these potentials to pick out potential new zeolite structures from the vast databases of possible 4-connected nets and work [9] which has attempted to establish what the low and high energy structural features in any given net are and use this insight to search the vast number of hypothetical structures. However, there seem to be far fewer studies in the literature on the synthesisable region for ice and clathrate materials - i.e. what structures is it possible to synthesise from H_2O building blocks. In this chapter this is attempted by taking known zeolite structures deleting the oxygen atom and replacing the silicon atoms by water molecules in a sort of isomorphic transformation. Comparisons are then made between SiO_2 and water's synthesisable landscapes using data mining, which shows that the size of these territories can be explained using simple intuitive models for the differences in the intermolecular and intramolecular interactions of SiO_2 and water. These models are then used to guide experimental efforts to synthesise new materials and also used to make predictions about the boundaries of the synthesisable zone for other materials which form 4-connected nets.

Density functional theory has been used throughout this chapter to study the relative energies of the various possible ice and clathrate phases as investigations of the effect proton arrangement has on the energy of the system have been carried out and, as shown in section 5.1, interatomic potential calculations are not sufficient to capture the sensitive energetics of proton ordering.

6.1 Diamond and Lonsdaleite - a comparison with Carbon

Perhaps the most well known 4-connected net is the diamond net, which is the same net that forms the framework in the dense silica phase cristobalite and the metastable ice phase, ice Ic. Closely related to this net is the lonsdaleite net, which is the backbone of a rare allotrope of carbon, the rare dense silica phase tridymite and the lowest pressure form of ice, ice Ih. These two structures are shown in figure 6.1.

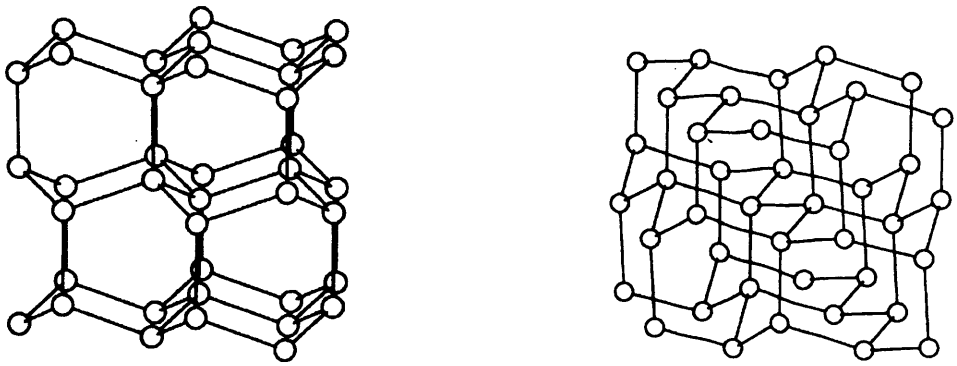

(a) Lonsdaleite Net (b) Diamond Net

Figure 6.1: The diamond and lonsdaleite nets.

It is interesting to note that, whereas for carbon the structure composed of the diamond net is the more common form, for ice it is the structure based on the lonsdaleite net that is more commonly observed. The implication is that diamond is a lower energy net for structures composed of carbon, whereas for ice the lonsdaleite net is preferred. The reason why this should be the case is not at all clear and makes one question whether this is a true thermodynamic effect. However, the calculations, reported in table 6.1, show that this is clearly the case but also that the energy differences between these two phases are small for carbon, ice and silica, which is also to be expected given the similarity of the two nets. In table 6.1 the carbon energies are calculated using the PBE functional implemented in CASTEP 3.0 [10] with a 450 eV cutoff (at this value the energy difference is converged to $1x10^{-2}$ kJ mol^{-1})

and a k-point spacing of 0.05 $Å^{-1}$ (for which the energy difference is converged to 0.002 kJ mol^{-1}). The ice energies have the lowest energy proton topology for the net of interest and are calculated using the PW91 functional implemented in CASTEP [10] with grids of 6x6x3 k-points and 6x3x3 k-points for ice Ic and Ih respectively and a 500 eV cutoff. For completeness the energies of the silica phases were also calculated using the Sanders Leslie Catlow [11] interatomic potential with GULP [12]. This potential was used rather than DFT because simulations [8, 13] have shown that it reproduces the available experimental thermochemical data [14] as well as more computationally expensive DFT calculations.

	Diamond Net		Lonsdaleite Net	
	Name	Energy / kJ mol^{-1}	Name	Energy / kJ mol^{-1}
Carbon	Diamond	0.0	Lonsdaleite	2.4522
Ice	Ice Ic	0.1709	Ice Ih	0.0
Silica	Cristobalite	0.0	Tridymite	0.2418

Table 6.1: The energies, relative to the net of lower energy, for the structures of carbon, ice and silica that have the diamond and lonsdaleite nets as the backbones of their structures.

The relative stability of these two phases are reversed when one isomorphically transforms from ice to carbon is far from obvious, although one difference between ice and carbon is that ice is a molecular solid whereas all the atoms in carbon are joined by strong covalent bonds. However, this discussion of chemical bonding is somewhat heretical given that within the framework of quantum mechanics there is no distinction between covalent and ionic bonding, let alone inter and intramolecular interactions. As section 4.1.2 showed, a discussion of the interaction between water molecules often provides useful insight into the nature of the structure directing effects in ice phases. Section 4.1.2 also showed that the representation of water molecules as overall charge neutral molecular multipole expansions is reasonable, which suggests that the leading term in the interaction of water molecules is going to be the, orientation dependent, dipole-dipole ($1/r^3$) interaction. By contrast, carbon consists of spherical, charge neutral carbon atoms, whose only interaction

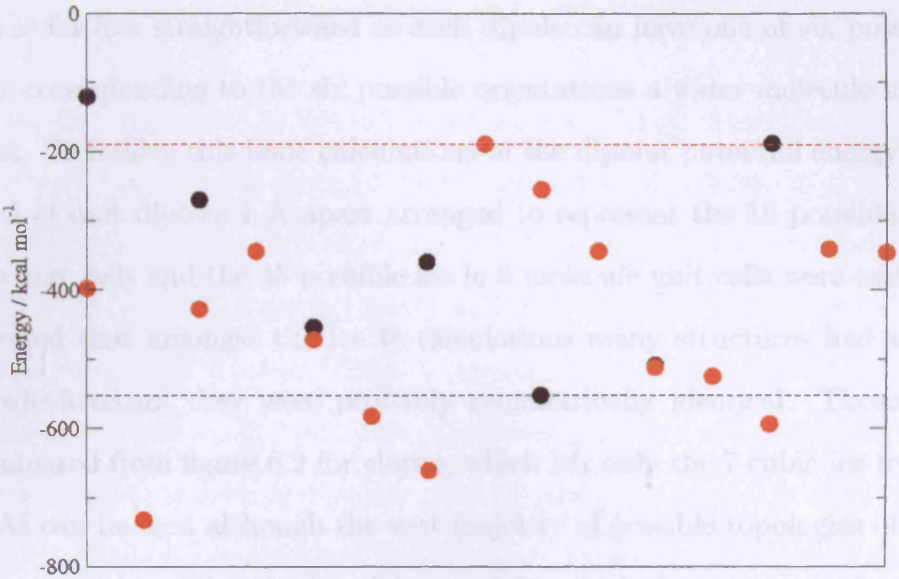

Figure 6.2: The dipolar interaction energies of diamond and lonsdaleite nets with dipoles arranged as they would be in a number of symmetrically distinct hydrogen bonding topologies. Each point represents a symmetry distinct proton topology (the position on the x axis is arbitrary). Red dots mark the energies of dipoles arranged on the vertices of the lonsdaleite net while black dots are dipoles arranged on the diamond net. The black and red lines indicate the lowest energy topology of diamond and the highest energy topology of lonsdaleite respectively.

will be through the distant dependent short range repulsive interaction and, at longer ranges, dispersive forces. One might suspect therefore that any simple distant dependent function would stabilise the diamond net over the lonsdaleite one, whereas the introduction of orientational dependence in the interatomic forces will stabilise lonsdaleite.

To test this assertion diamond and lonsdaleite nets were set up so that all the bond lengths were equal to 1 Å and the "energy" of this net was then calculated using a fictitious lennard-jones function, which had σ, the distance to the potential minimum, set as 1 Å and a value for ϵ of 0.1 eV. The energy of the hypothetical diamond net, calculated using this potential, was found to equal -0.3110 eV molecule^{-1} whereas the energy of the lonsdaleite net was -0.3098 eV molecule^{-1}. This agrees with what was expected for simple distant dependent functions.

Performing a comparison of the dipolar electrostatic potential energies for these

two nets is far less straightforward as each dipole can have one of six possible orientations corresponding to the six possible orientations a water molecule may have in the net. To resolve this issue calculations of the dipolar potential energy for nets composed of unit dipoles 1 Å apart arranged to represent the 16 possible ice Ih 8 molecule unit cells and the 45 possible ice Ic 8 molecule unit cells were carried out. It was found that amongst the ice Ic calculations many structures had the same energy, which meant they were probably symmetrically identical. These repeats were eliminated from figure 6.2 for clarity, which left only the 7 cubic ice topologies shown. As can be seen although the vast majority of possible topologies of the two nets have similar energies the lonsdaleite net has a number of topologies that are lower energy than the diamond ones and the highest energy topology is one based on the diamond net.

Table 6.1 also showed that the cristobalite is lower energy than tridymite and thus that the situation for silica seems to be much like that for carbon - namely Si-Si distant dependent interactions stabilise the diamond net over the lonsdaleite net. This is problematic however given the phase diagram in figure 6.3 which shows that the tridymite structure forms at lower temperatures than the cristobalite structure. This model though has neglected the effect the oxygens have on the relative stability of these two phases. In both cristobalite and tridymite there are temperature driven phase transitions, which result in a change in the symmetry of the system. These transitions do not affect the positions of the silicon atoms and have been shown to occur due to the freezing out of normal modes as temperature is lowered [15]. Thus to understand the relative stability of cristobalite and tridymite one is likely to need a model that includes the effects that the oxygen atom motions have on the entropy of the system.

6.2 Dense silica and ice phases

As already discussed silica is another material that forms structures based on 4-connected nets and, what is more, the synthesisable territory for silica is far larger than that for carbon. Currently there are about 50 possible nets that can be made using only silica but only 6 are not metastable and so appear on the phase diagram shown in figure 6.3 [3]. Amongst these 6 phases there are four distinct 4-connected nets, cristobalite (diamond), tridymite (lonsdaleite), coesite and α-quartz. Furthermore, there is also a known metastable silica phase called moganite which is a twin of two quartz lattices, the structural details of which, along with those of the coesite and quartz structures are given in table 6.2.

α-Quartz	
Trigonal $P3_121$ a = 4.913 Å b = 5.405 Å	
Vertices at 3 a	(0.5299,0.0,0.3333)
Schläfli symbol	6 6 6_2 6_2 8_7 8_7
Coordination sequence	4 12 30 52 80 116 156 204 258 318 384 458 536
Coesite	
Monoclinic C2/c a = 7.173 Å b = 12.328 Å c = 7.175 Å β = 120.0°	
Vertices at 8 f	(0.359,0.3916,0.4274)
Schläfli symbol	4 6 4 6 8 9_2
Coordination sequence	4 10 22 47 83 125 171 215 288 349 415 518 591
Vertices at 8 f'	(0.4934,0.1577,0.4596)
Schläfli symbol	4 8 4 9_7 6 8
Coordination sequence	4 10 23 47 83 127 174 221 276 356 428 494 603
Moganite	
Monoclinic C2/c a = 13.518 Å b = 4.670 Å c = 8.385Å β = 129.041°	
Vertices at 4 e	(0.0,0.94606,0.75)
Schläfli symbol	4 4 6_2 6_2 8_2 8_2
Coordination sequence	4 10 24 40 64 90 120 160 200 244 300 354 412
Vertices at 8 f	(0.16410,0.27726,0.14526)
Schläfli symbol	4 8_6 6 6 6 6
Coordination sequence	4 11 24 41 62 90 122 157 200 247 296 354 416

Table 6.2: The structural details of the dense silica phases α-quartz, coesite and moganite.

The phase diagram for silica is far less complex than that of water (figure 2.2) as silica phases are stable over much broader temperature and pressure ranges than

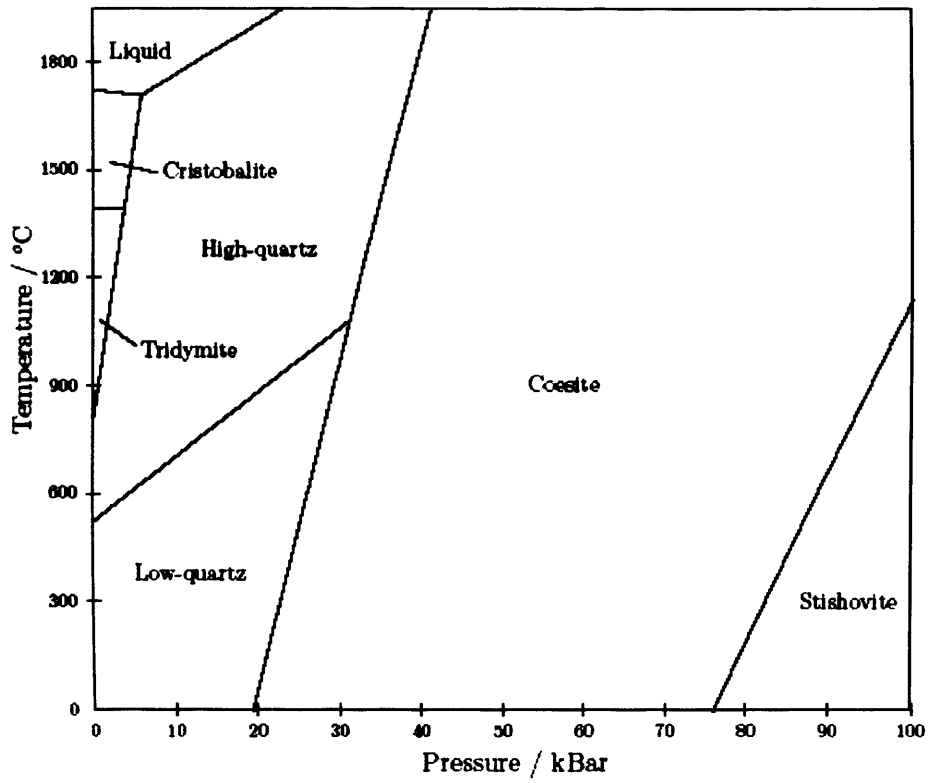

Figure 6.3: The phase diagram of silica.

water phases. This is probably because the bonds between silicas are strong covalent Si-O bonds and as such the barrier to any phase transition, which will involve bond breaking, is higher than the transition barriers between ice phases, which are held together by weaker hydrogens bonds.

To investigate the differences between the ice and silica synthesisable territories the energies of all silica phases, ice phases and phases of ice and silica but composed of silica and ice respectively were calculated (N.B. some of the ice phases are isostructural with silica phases - in particular ice III to keatite [1] and ice VI to stishovite). All the ice calculations were done using the PW91 functional, implemented in CASTEP [10], at the gamma point with a 500 eV cutoff. The silica calculations were done using GULP [12] and the Sanders-Leslie-Catlow interatomic potential [11]. The results of these calculations are shown in figure 6.4 - in this figure the energies are plotted against the framework density, which is defined as the number of H_2O / SiO_2 "molecules" in the unit cell divided by the unit cell volume,

in Angstroms, and multiplied by 1000.

To generate ice structures that obeyed the Bernal Fowler rules from a knowledge of the oxygen positions a computer program was written. In essence this program worked much like those used in section 4.3 to generate all allowed topologies of a given hydrogen bonding phase. Again an array that gave the directions of all hydrogen bonds was used to represent the structure but now for each structure generated the difference between the number of hydrogen bond donors and acceptors on each oxygen was calculated and the magnitudes of these quantities summed. In an ideal structure this number should be equal to zero so this quantity was used as the "energy" in a Monte Carlo routine that only allowed downhill moves.

The first point of note about figure 6.4 is that the range of energies the structures have is very similar in both structures, which is contrary to what one might have expected given that ice is held together by hydrogen bonds whilst silica is held together by covalent bonds. Also the densities of the ice structures are considerably higher than their silica counterparts - this is unsurprising though given that SiO_2 units are considerably larger than water molecules. Turning to the ice map, the energies of the structures increases in line with what one would expect from the phase diagram. The exception to this is ice II, which has a higher energy than one would expect but then again this structure is proton ordered and would as such be expected to have a lower entropy than the other, disordered, structures.

In ice all the phase transitions which change the oxygen network are pressure driven, which helps explain the correlation between energy and density for these phases. The density can be increased by contracting the lattice and shortening all the hydrogen bonds. This contraction has an energetic cost however that increases with the amount of contraction, which becomes problematic when there is a large amount of contraction and this cost is very high. These high costs can be circumvented however by changing the lattice so that the equilibrium hydrogen bonds lengths can be maintained but in a denser structure. Turning to figure 6.4(a) one can see that

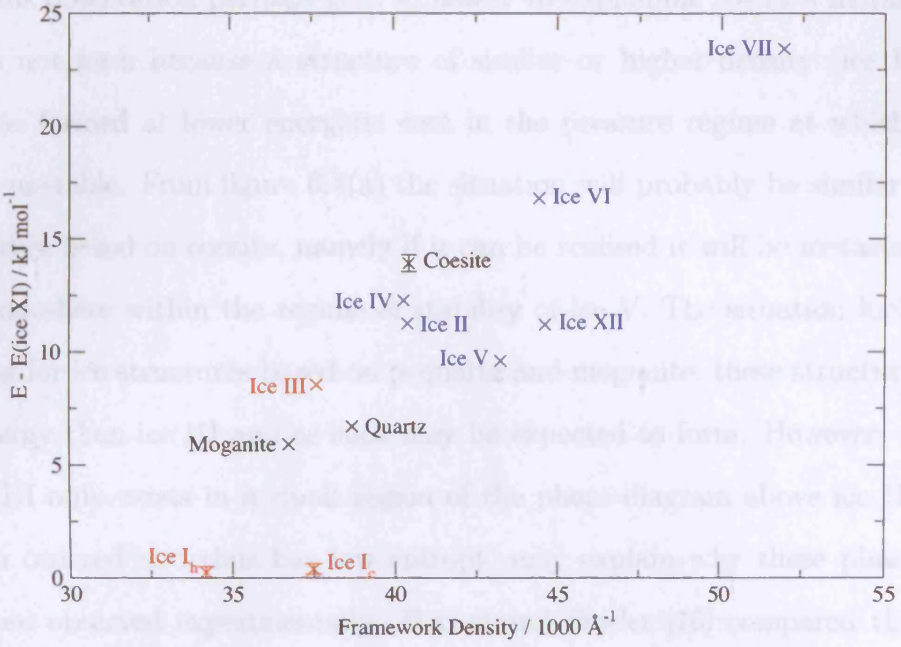

(a) Ice energies

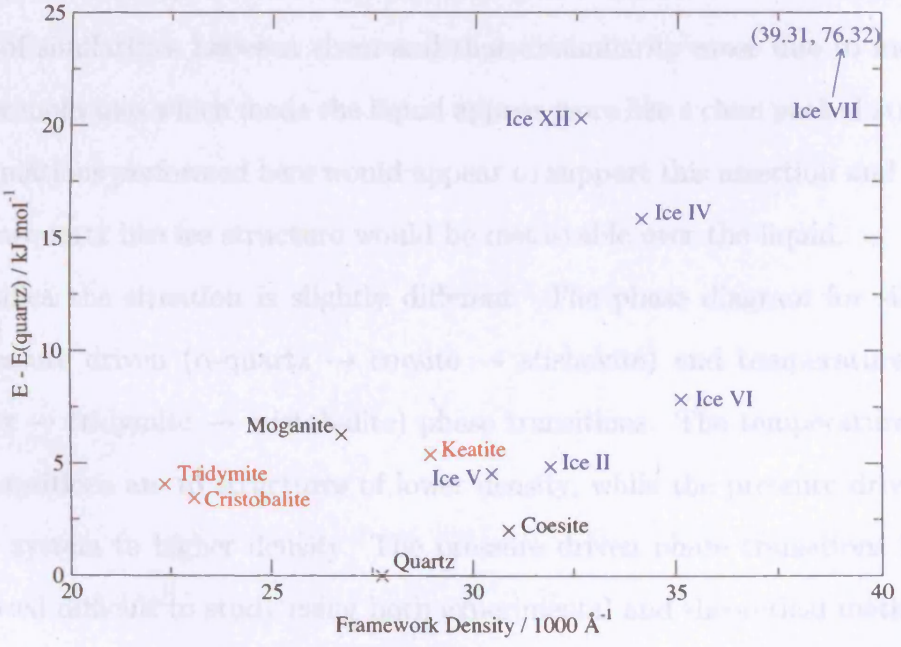

(b) Silica energy

Figure 6.4: The energies of all the nets of the known ice and silica phases. Blue crosses are those phases which are known for ice, black that are known for silica only and red those structures observed in both materials. Error bars in the ice figure, if shown, show the range of energies different hydrogen bonding topologies found by sampling of multiple configurations.

the metastable phase ice IV has a similar density but higher energy than ice II and ice V. This observation perhaps goes someway to explaining ice IV's metastability - it does not form because a structure of similar or higher density (ice II or ice V) can be formed at lower energetic cost in the pressure regime at which ice III becomes unstable. From figure 6.4(a) the situation will probably be similar for any ice structure based on coesite, namely if it can be realised it will be metastable and occur somewhere within the regime of stability of ice V. The situation looks more promising for ice structures based on α-quartz and moganite, these structures lie at lower energy than ice III and as such may be expected to form. However, the fact that ice III only exists in a small region of the phase diagram above ice II, which is proton ordered and thus has low entropy, may explain why these phases have never been observed experimentally. Bernal and Fowler [16] compared the X-ray scattering curve of liquid water and that of α-quartz and showed that there were a number of similarities between them and that dissimilarity arose due to motion of the water molecules which made the liquid appear more like a close packed structure. The calculations performed here would appear to support this assertion and suggest that an α-quartz like ice structure would be metastable over the liquid.

For silica the situation is slightly different. The phase diagram for silica has both pressure driven (α-quartz $\rightarrow$ coesite $\rightarrow$ stishovite) and temperature driven (α-quartz $\rightarrow$ tridymite $\rightarrow$ cristobalite) phase transitions. The temperature driven phase transitions are to structures of lower density, while the pressure driven ones take the system to higher density. The pressure driven phase transitions in silica have proved difficult to study using both experimental and theoretical methods because of the large number of metastable phases that silica exhibits and its propensity to amorphise when placed under pressure. Recent theoretical work [17], which used metadynamics to study the α-quartz-stishovite phase transition, has shown that during the transitions the system goes through 3 distinct structural phase transitions. Furthermore, this work also shows that on application of pressure coesite can

be transformed to an as yet unknown phase of silica and that the investigation of the quartz-coesite and coesite-stishovite phase transitions is very difficult. As such, silica analogues of the ice structures could possibly be intermediates in these phase transitions or metastable phases that form when the crystallisation conditions are unusual.

From figure 6.4(b) the silica phases appear to be clustered in four density ranges, in the first of these are the high temperature structures, tridymite and cristobalite. The second contains α-quartz and moganite, the third coesite, ice V, ice II, ice XII and keatite and finally the fourth contains stishovite and ice IV. In the second of these regions quartz is the lowest energy structure and so it comes as no surprise that it is the most stable phase at low pressures. In the third region coesite is the lowest energy structure and again this tallies with what one might expect from the phase diagram. Although, given that keatite is a rare metastable form of silica, one might expect that silica structures based on the ice V and ice II structure, which, according to this work, have lower energies than keatite might also exist as metastable phases. By contrast it seems unlikely that it would be possible to synthesise silica structures with the same framework as ice IV and ice XII as these lie at such high energy relative to the most stable phase with a similar density.

6.3 Clathrates

As discussed in section 2.6 ice forms inclusion compounds with small gas molecules that are isostructural with certain known zeolite structures [1]. There are far fewer known clathrate structures than there are known zeolite frameworks because it is not currently possible to use templates with structure directing effects to synthesise exotic cages in clathrates. In this section and the next an attempt is made to understand the structure driving effects in clathrates and thus from the zeolite structural database [4] to predict the structures of, as yet unknown, clathrates.

The energies of the known clathrates were calculated using CASTEP [10] with

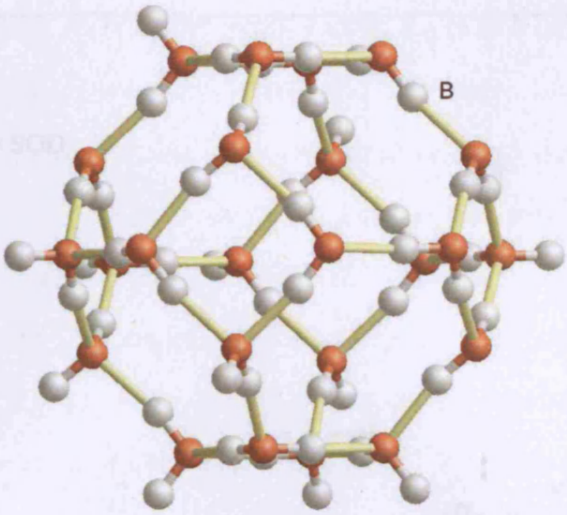

Figure 6.5: Fragment of the optimised structure of the hydrate framework of HPF_6. Despite the absence of the guest molecule the structure of the cages is preserved. Examination, by eye, of the bond highlighted B shows that there are bent hydrogen bonds in this structure.

the PW91 functional at the gamma point and using a 500 eV cutoff. In these calculations the cages are unfilled but none the less the structure finds a minimum in the potential energy in which the structures of the cages are conserved, see figure 6.5. The energies of the empty structures obtained are shown in figure 6.6 against the framework topology.

The range of energies the clathrate structures have is very small as is their range of densities. Furthermore, unlike the dense phases, where all the pressure induced phase transitions took the system to a structure of higher framework density, here the pressure induced phase transition from the sII structure to the sH structure, which is observed for clathrates, would take one to a system of lower framework density. Based on these two observations the guest-guest and framework-guest interactions clearly have a huge effect on the structure.

The framework-guest interaction has been modelled by van der Waals and Platteeuw [18], who attempted to predict gas hydrate equilibrium pressures. Their model was based on the equality between the chemical potentials of the hydrate phase, H, and a coexisting water phase, π, which could be ice, liquid water or a mixture of both.

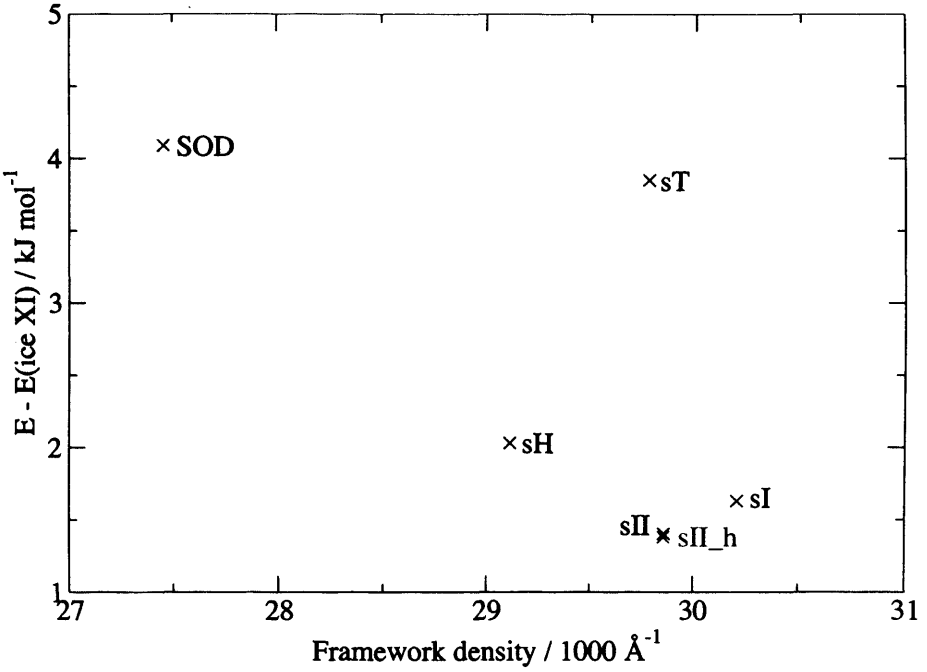

Figure 6.6: The energies of the known clathrate structures calculated using density functional theory. The energies given are for a random hydrogen bonding topology and empty cages. The red structure is the hypothetical hexagonal packing of the sII clathrate, discussed by Jeffrey in Inclusion Compounds volume 1.

$$\Delta\mu_w^H = \mu_w^\beta - \mu_w^H = \mu_w^\beta - \mu_w^\pi = \Delta\mu_w^\pi \tag{6.1}$$

In this equation μ_w^β is the chemical potential of the metastable empty hydrate lattice. Using statistical mechanics it is then possible to show that the difference between the chemical potential of the empty and filled hydrate lattices is given by:

$$\Delta\mu_w^H(T,P) = -RT\sum_m v_m \ln(1 - \sum_j \Theta_{mj}) \tag{6.2}$$

Where v_m is the number of cages of type m per water molecule in the hydrate lattice and Θ_{mj} is the fraction of the cages of type m that are occupied by guest j. If one assumes that there is one guest molecule per cage then Θ_{mj} is given by a Langmuir adsorption relation.

$$\Theta_{mj}(T,P) = \frac{C_{ml}(T)f_l(T,P)}{1 + \sum_j C_{mj}(T)f_j(T,P)} \tag{6.3}$$

where $f_l(T, P)$ is the fugacity of guest l and C_{ml} is the Langmuir constant. To calculate the value of C_{ml}, van der Waals and Platteeuw assumed that the cage was spherical, which made the calculation of the interaction between guest and cage more straightforward. Subsequent work has shown that for large guest molecules this approximation breaks down and it becomes important to use the explicit positions of water molecules [19], include the interaction with the guest with its second coordination sphere [20], the guest-guest interaction [20] and the fact that the guest present will affect the sizes of the cages present [21]. A refinement of this model [22] includes all these factors and also include terms that allow the cages to distort to accommodate different sized guest molecules. This refined model has been used to study the phase behaviour of multiple and single component clathrate hydrates but can also be used to make qualitative assertions about these interactions as is done throughout the following two sections.

6.3.1 The guest-guest interaction

Simulations on the formation of type I methane hydrate [23] have shown that these materials do not nucleate via a labile cluster mechanism, in which the guest causes the formation of an cage-like structure in it hydration sphere, but instead the clathrate cages grow as order develops in the arrangement of the guests. Clearly then during the initial nucleation the guest-guest interaction has a huge effect on the structure that is formed. However, these simulations also show that methane hydrate initially nucleates in a structure that resembles the type II structure, so clearly at some later point the structure changes to minimise the energy of the structure and it is this minimisation that controls the final structure adopted. At this stage one would expect that the guest-guest interaction would give the smallest contribution to the energy of the system and as such have the smallest effect on the final structure adopted. None the less for the sII and sII_h structure this interaction almost certainly has a strong structure directing effect. The second of these structures is

a hypothetical structure suggested by Jeffrey [24, 25] as a likely candidate for new clathrate materials. It consists of an alternative packing of the cages present in the sII structure and, as figure 2.13 shows, has an energy that is almost identical to that of the sII structure. Furthermore, because the two structures have an identical set of cages one would expect the framework-guest interaction to be almost the same in both.

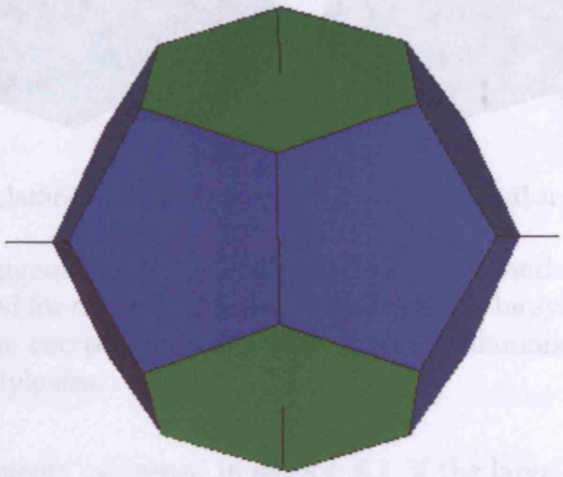

Figure 6.7: The $5^{12}6^4$ cage which is present in both the sI and sII_h structures. On this figure the locations of the 4 C_3 axis have been marked to indicate that this polyhedron has the same symmetry as a regular tetrahedron.

In examining the positions of the centres in the cages a realisation was had about these two structures - both structures are composed of 5^{12} and $5^{12}6^4$ cages but can be better understood by just examining the way the larger cages pack together. The $5^{12}6^4$ cage has the same symmetry as a regular tetrahedron, as shown in figure 6.7. As such in the sII and sII_h nets the centres of these cages lie on the positions at which one finds the vertices in the diamond and lonsdaleite nets respectively, see figure 6.8.

The sII structure always has the small guest molecules in the 5^{12} cages and larger guests in the $5^{12}6^4$ cage [24]. The guest-guest interactions will be dominated by the interactions between the large guest molecules because the strength of intermolecular interactions is dependent on the molecular size. From the arguments expressed in section 6.1 one would thus expect the sII structure to be observed. However,

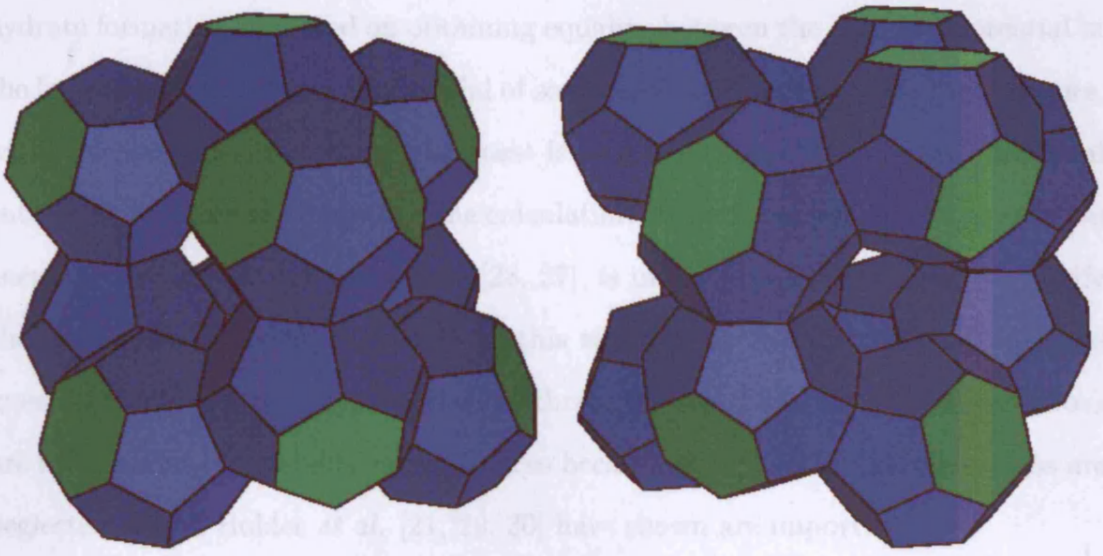

(a) sII clathrate (b) sII_h clathrate

Figure 6.8: The arrangements of the $5^{12}6^4$ polyhedra in sII and sII_h (the 5^{12} polyhedra have been omitted for clarity). These polyhedra have the symmetries of a regular tetrahedron and these two packings thus correspond to diamond and lonsdaleite like packings of these polyhedra.

again from the arguments expressed in section 6.1, if the large guest molecule has a large dipole one might expect orientation dependent interaction between dipoles will stabilise the sII_h structure. Nobody has managed to isolate this structure as a single phase, although it has been observed as a stacking defect in samples of a hydrate of tetrahydrofuran (THF) [26, 25]. This molecule has a substantial dipole, which from the analysis provided in section 6.1, would provide a favourable interaction between the molecules in the $5^{12}6^4$ cages of the sII_h structure.

6.3.2 The framework-guest interaction

The framework-guest interaction clearly makes a difference to the structure because the cell parameters are dependent on the particular guest [24, 27]. Furthermore, given that the empty cage structures do not form, the guest is clearly involved in the formation of the cages, the particular cages formed and thus the structure which condenses for a given guest [23]. In section,6.3 where the van der Waals Platteeuw theory was discussed, it was shown that current theories on the thermodynamics of

hydrate formation are based on obtaining equality between the chemical potential in the hydrate and the chemical potential of some coexistent water phase. Furthermore, within these models the role of the guest is simply to provide some configurational entropy to stabilise the hydrate. The calculation of the framework guest interaction energies, as has been studied before [28, 27], is undertaken here in order to justify the use of the methods, developed in this section, for the discovery of potential guest molecules for new hypothetical clathrate phases. Only qualitative assertions are made about the stability of the lattices because the role of lattice distortions are neglected, which Holder *et al.* [21, 29, 30] have shown are important.

The cages observed in the different structures, their point group symmetries and the ratios of the lengths of their rotation axis are shown in figure 6.9. As this figure shows all of the observed cages have a very high symmetry and, excluding the oblate $5^{12}6^2$ cage, have the roughly same extents in the three dimensions of space. The simplest model for the host guest interaction is to assume that guest molecules are hard spheres and that the cage swells such that the water molecules which form the cage lie on the surfaces of these "guest spheres." This model goes some way towards explaining the high symmetry and roughly equal extent in all directions - one would expect the water molecules to arrange themselves around the central sphere such as to minimise the amount of empty cage. Thus, if one expands the size of the guest molecule, the cage must swell in order to fit in the guest. This swelling clearly has an energetic cost which is, in all probability, is related to the lengths of the hydrogen bonds. As such one expects it will be more energetically costly to fit large guest molecules into small cages and this cost will put an upper bound on the size of guest that can fit into a given cage. Experimentally, in only the sI structure, and only for the smallest guests, can there be occupation of all the cages by the same species - in all other clathrate structures different cages are occupied by a different sized guests. To better understand why this is the case the cages were all set up so that their hydrogen bonds all had unit lengths. Then the distance between the centre of

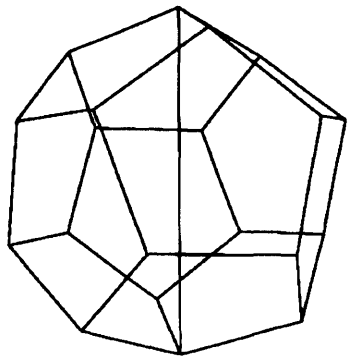

(a) 5^{12} cage - I_d (sI, sII and sH)

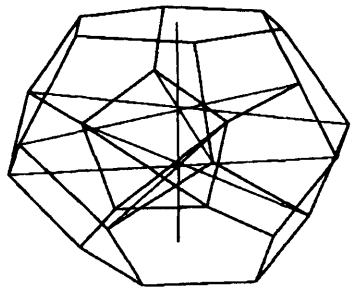

(b) $5^{12}6^2$ cage - D_{6d} (sI)

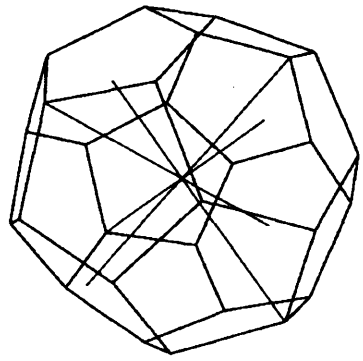

(c) $5^{12}6^4$ cage - T_d (sII)

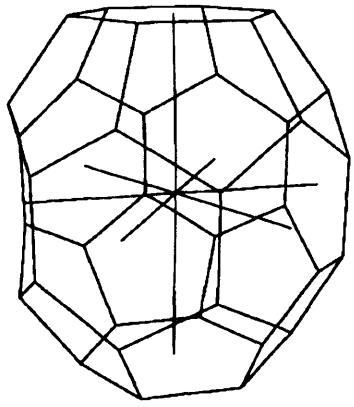

(d) $5^{12}6^8$ cage - D_{6h} (sH)

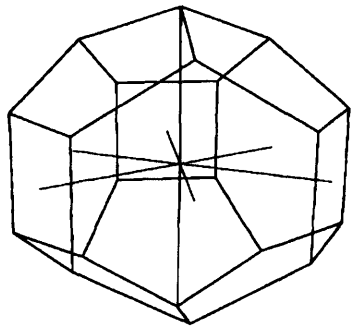

(e) $4^35^66^3$ cage - D_{3h} (sH)

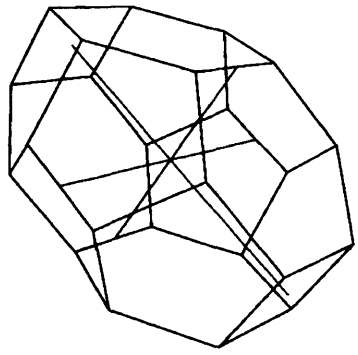

(f) $4^25^86^4$ cage - D_{2h} (sT)

$5^{12}6^2$ cage		
red : 1.0	green : 0.692	
$5^{12}6^8$ cage		
red : 1.0	green : 0.830	
$4^35^66^3$ cage		
red : 0.864	green : 1.0	
$4^25^86^4$ cage		
red : 1.0	green : 0.845	blue : 0.706

Figure 6.9: Figure showing the shapes, symmetries and spatial extents of the cages observed in the known clathrate structures. Lines of the same colour indicate distances that must be equal by symmetry. The table gives the ratios of the non-equivalent lengths to each other.

Cage symbol	Guest radius	5^{12} ratio
5^{12}	1.363	1.0
$5^{12}6^2$	1.441	1.057
$5^{12}6^4$	1.654	1.213
$5^{12}6^8$	1.790	1.313
$4^3 5^6 6^3$	1.300	0.954
$4^2 5^8 6^4$	1.285	0.942

Table 6.3: The largest guest molecule that can fit into a cage if all the hydrogen bonds that make it up have unit length.

the cage and the closest of the surrounding water molecules was used to calculate the ratios between the sizes of guests that can fit in the various cages. This analysis is presented in table 6.3.

If guests really do behave like hard spheres then the ideal structure for a clathrate with only one type of guest would be one in which all the cages are spherical and of the same size. This structure is impossible to form though but as table 6.3 shows one can form a structure, sI clathrate, in which all the cages have very similar sizes. Furthermore, this is the structure Weaire and Phelan have shown has the smallest surface area for a space-filling arrangement of cells of equal volume [31, 32] and as such is the most stable structure for a monodisperse dry foam. One would expect that a clathrate would attempt to minimise the amount of surface area and so this adds weight to this explanation as to why it is only this structure which forms clathrates in which all the cages are occupied. Table 6.3 also suggests that to form the sII and sH structures requires two guests, a small one to fit in the 5^{12} and $4^3 5^6 6^3$ cages, which both have similar sizes, and a large one to fit in the $5^{12}6^4$ or $5^{12}6^8$ cage. The particular structure adopted will depend on the size of the larger guest with big guest molecules favouring sH over sII.

The structure directing effects of templates on zeolites have been studied computationally by Lewis *et al.* [33]. In the course of their work they have written a piece of software, called ZEBEDDE, which can be used to calculate the interaction between silica framework structures and templates lying with in them. ZEBEDDE, in the mode in which it has been used in this work, works by randomly translating,

rotating and distorting template molecules in the cages to anneal the total energy of the system. This energy is the sum of the intramolecular energy, which is the repulsion dispersion interaction between the guest molecule and the framework, and the intermolecular energy of the template. At the heart of the energy calculating routines of ZEBEDDE is the pcff forcefield [34] which contains terms for the interaction of water molecules with anything - as such this code can be easily used to investigate the framework-guest interaction in clathrates. This is precisely what has been done in this work - the optimised structures from CASTEP for the sI, sII and sH clathrates have been loaded into ZEBEDDE, a guest molecule has been placed into one of the cages and the interaction between guest and framework has been calculated by allowing the structure to anneal at 0 K. The results for loading of the 5^{12} cage in sI, sII and sH are shown in figure 6.10.

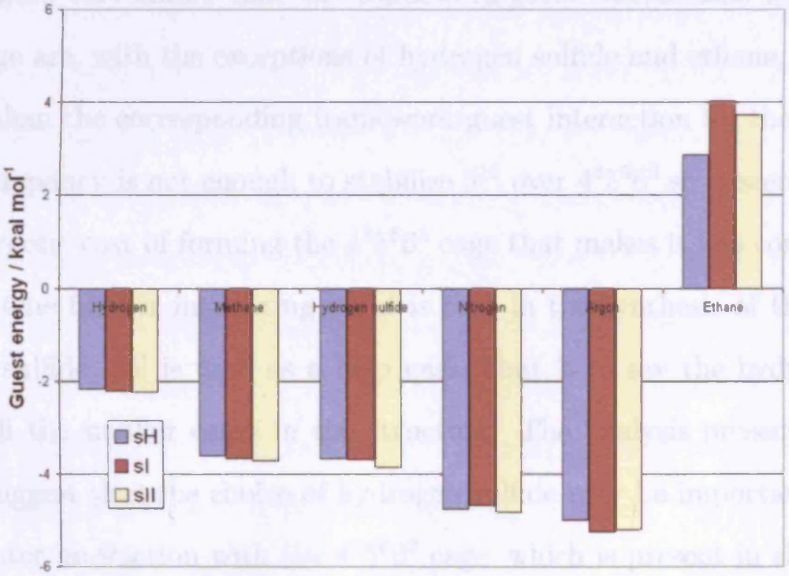

Figure 6.10: The framework-guest interactions for various guest molecules in the 5^{12} cages of the sI, sII and sH clathrate structures.

Figure 6.10 shows there is a minimum in the framework-guest energy when the guest is argon and this is the case for all three clathrate structures. This minimaum corresponds to the point when the water molecules are sat at a distance from the guest which is as close to the minimum in the repulsion dispersion potential of the

guest as possible. For guests which have this minimum in their potential at a shorter distance the dispersive interaction between guest and framework is reduced, while for guests which have this minima at greater distances the repulsive interaction between guest and framework is increased. Figure 6.10 also shows that the discrepancies between the framework-guest energies in these three different structures are small, which suggests that the 5^{12} cage has a similar size in all these structures and that it is the interaction of the guest with its first hydration sphere that is the dominant factor in determining the framework-guest energy of the system.

Table 6.3 showed that the 5^{12} and $4^3 5^6 6^3$ cages have very similar sizes. One may ask therefore - why is it that the 5^{12} cage is so much more common amongst the known clathrates? Is it that the framework-guest interaction is larger for 5^{12} cages because they are more symmetric or just that the $4^3 5^6 6^3$ is a more unstable cage? Figure 6.11 shows that the framework-guest interactions for guests in the $4^3 5^6 6^3$ cage are, with the exceptions of hydrogen sulfide and ethane, all slightly less negative than the corresponding framework-guest interaction for the 5^{12} cage. This slight discrepancy is not enough to stabilise 5^{12} over $4^3 5^6 6^3$ so it seems likely that it is the energetic cost of forming the $4^3 5^6 6^3$ cage that makes it less common than the 5^{12} cage. One further interesting point is that in the synthesis of the sH clathrate hydrogen sulfide [35] is used as a help gas. That is to say the hydrogen sulfide is used to fill the smaller cages in the structure. The analysis presented here would seem to suggest that the choice of hydrogen sulfide may be important as this guest has a greater interaction with the $4^3 5^6 6^3$ cage, which is present in sH, than the 5^{12} cage.

The analysis presented in table 6.3 and what is known about the synthesis of clathrate structures suggests that the particular structure the system adopts is dependent on the size of the largest guest molecule present. The largest guest molecule will of course sit in the largest cage in the structure so one can understand how different guest molecules affect the structure adopted by calculating the framework-

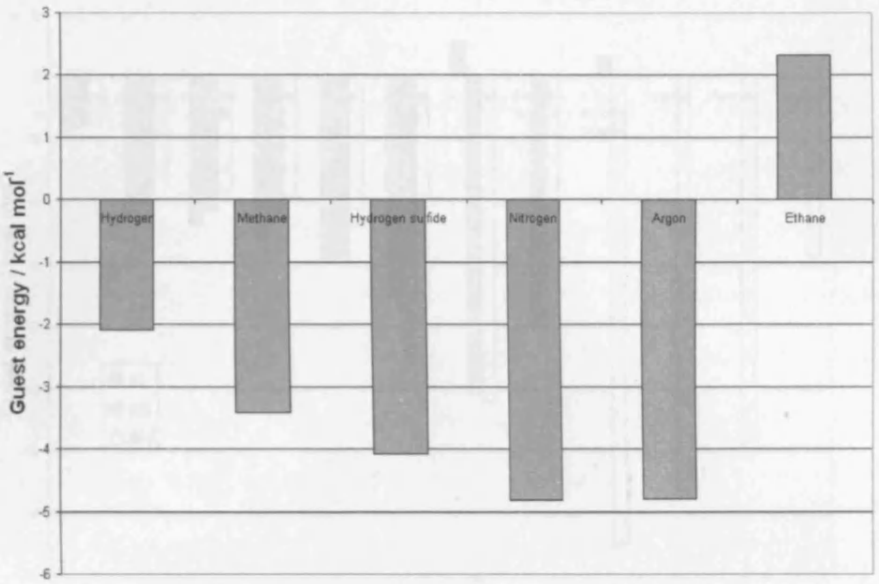

Figure 6.11: The framework-guest interactions for various guest molecules in the $4^3 5^6 6^3$ cage of the sH clathrate structure.

guest interaction of various guests placed in the largest cages of the sI ($5^{12}6^2$), sII ($5^{12}6^4$)and sH ($5^{12}6^8$) structures. This analysis is presented in figure 6.12.

Figure 6.12 shows, perhaps unsurprisingly, that for the smallest guests the $5^{12}6^2$ cage of the sI structure has the most favourable framework-guest interaction. This situation changes for intermediate sized guests when the $5^{12}6^4$ cage of sII becomes most stable and then changes again for the largest guests for which the $5^{12}6^8$ cage of sH is most stable. Remarkably, given the simplicity of the model, the minimum in the framework-guest interaction energy for the sH cage falls on one of the molecules that has been used to synthesise this cage [35]. However, the crossovers between different structural regimes are not quite in the right places, suggesting that a more sophisticated model is required if this is to be reproduced.

Klauda and Sandler [22] have developed a model that allows one to investigate how the clathrate structure that is formed from water and a mixture of methane and ethane depends on the mole fraction of ethane present. They find that for low mole fractions of ethane the sII structure is the stable phase. This can be understood qualitatively from by examining the framework-guest interaction energies for

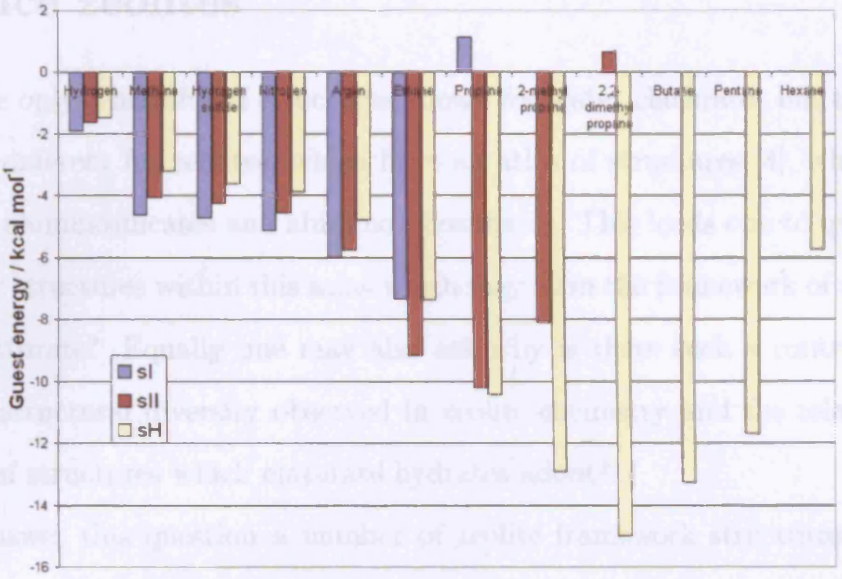

Figure 6.12: The framework-guest interactions for various guest molecules in the largest cages of the sI, sII and sH structures.

methane and ethane in the 5^{12}, $5^{12}6^2$ and $5^{12}6^4$ cages calculated in figures 6.10 and 6.12. The sII structure consists of a 2:1 mixture of 5^{12} and $5^{12}6^4$ cages, while sI consists of a 3:1 mixture of $5^{12}6^2$ and 5^{12} cages. From figure 6.10 ethane does not fit well into the sI cages, thus for high fractions of ethane one would expect sI to form in preference to sII because the number of 5^{12} cages is smaller and so there are more sites into which the ethane molecules can fit. For low mole fractions of ethane though, the sII structure can be adopted with the ethane molecules in the large $5^{12}6^4$ cages and methane molecules in the 5^{12} cages, which they fit into comfortably.

The analysis presented in this section proves that ZEBEDDE can provide a useful tool for finding suggested guest molecules which could be used to synthesise novel new clathrate hydrates. Furthermore, it suggests that one under utilised method for discovering new clathrates may be to use a combination of smaller guest molecules to stabilise small cages and large guest molecules to stabilise large cages and thereby increase the ratio between the different sized cages in the structures.

6.4 Ice zeolites

There are only a handful of structures known for water clathrates but the situation is vastly different for zeolites, which have an atlas of structures [4], which includes silicates, aluminosilicates and alumino-phosphates. This leads one to question - are there any structures within this atlas which may form the framework of a new stable water clathrate? Equally one may also ask why is there such a contrast between the vast structural diversity observed in zeolite chemistry and the relatively small number of structures which clathrate hydrates adopt?

To answer this question a number of zeolite framework structures were taken from the atlas of zeolite framework types [4] and, using the program discussed in section 6.2, valid hydrogen bonding topologies were generated for each of these nets. Each structure thus generated was optimised, at the gamma point, in CASTEP [10], with full anisotropic cell relaxation allowed and a plane wave cutoff of 500 eV. The energies of each topology plotted against the final framework density is shown in figure 6.13. The largest of these structures has 136 water molecules and a unit cell lengths of 16.5 Å . As such it was necessary to run such calculations on the national super computer resource, HPCx, on up to 128 processors. For the very large unit cells it is no longer feasible to optimise in P1, so for these structures the generator program was used in tandem with findsym [36]. A script was written that ran the generator program and then ran findsym on the output. This process was repeated a few thousand times and the highest symmetry structure generated was optimised with CASTEP, using its symmetry to lower the computational cost of the calculation.

Figure 6.13 shows that the majority of the zeolite framework types selected make poor clathrates because their ice forms have high energies. It also shows that the energy of the system appears to be related to the dimensionality of the channel system present in the structure, which is almost certainly a consequence of the more general tendency for the energy to increase with decreasing framework density

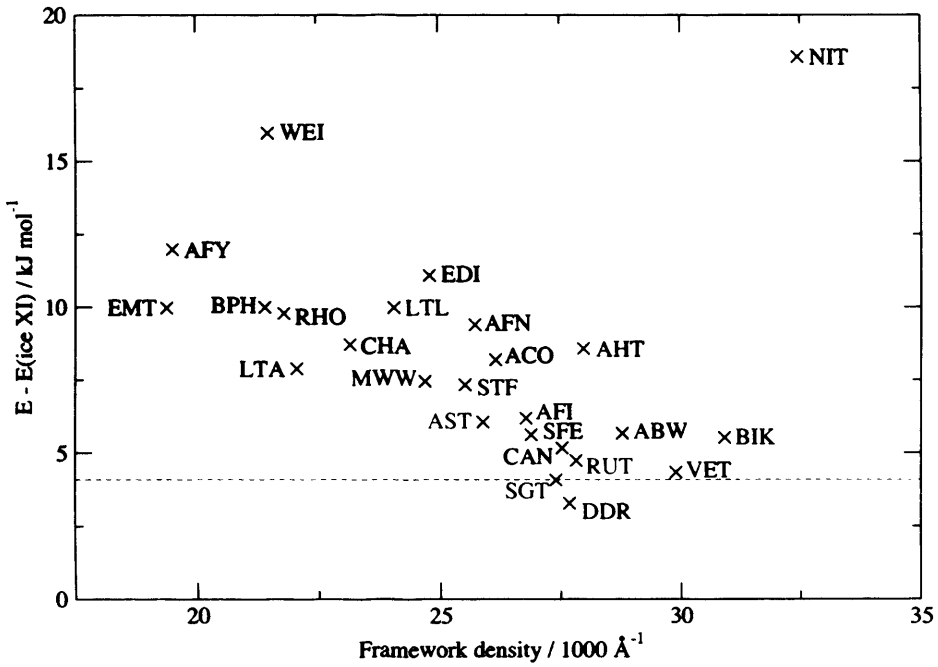

Figure 6.13: Energies, relative to that of ice XI, of the hypothetical clathrate structures based on zeolite topologies vs their framework topologies. The red line is the energy of the clathrate structure based on sodalite, which forms the backbone of the hydrate of HPF_6 and is the highest energy structure that we are aware forms. The colours indicate the dimensionality of the channel system, red are 0D, blue are 1D, green are 2D and black are 3D.

as it does for siliceous materials. Figure 6.13 shows that there are a number of potentially synthesisable new clathrate hydrates that lie either lower in energy than HPF_6 hydrate or just slightly higher, which all contain either 0D, 1D or 2D channel systems. The systems with channel systems that have dimensionalities greater than O, like VET see figure 6.14, are of particular interest because there are currently no known clathrates which have channel systems like these. A potential problem in forming channels in hydrate systems is that, unlike in silica, the guest molecule plays a key role in increasing the activation barriers to framework collapse. In other words the guest molecules have to be large enough to fill the pores in the structure. In channel systems there must be parts of the channel in which the guest is not present as bringing guests too close together in the channels would cause hugely unfavourable repulsive interactions between guest molecules. In zeolites the framework is maintained in these regions by the strong Si-O-Si bonds but in ice it

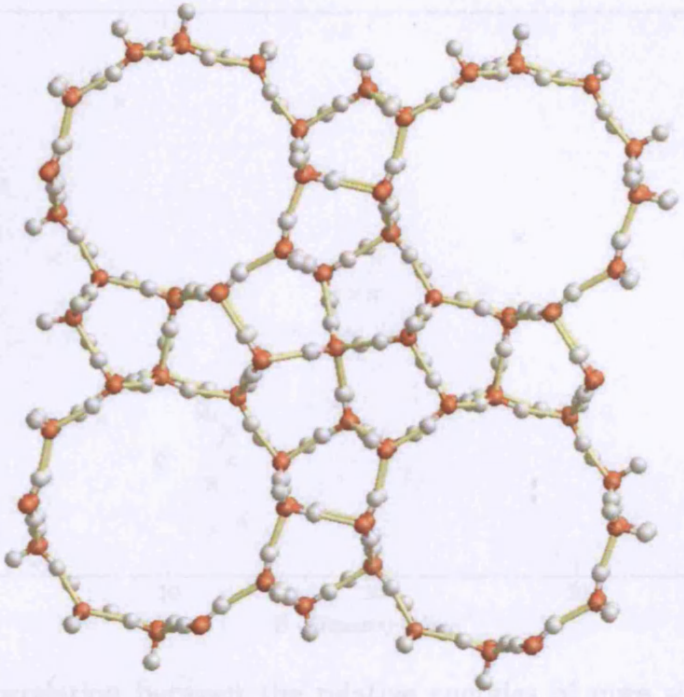

Figure 6.14: The arrangement of the water molecules in the hydrate framework based on VET. Observe the 12-ring channels that run through the structure.

is questionable whether the hydrogen bonds would be strong enough to hold the channels open in these regions and prevent collapse of the structure.

Figure 6.13 shows that the DDR and SGT frameworks have lower energies than the SOD framework, which is currently highest energy framework for which there is a hydrate structure known. As such these structures are of particular interest and are discussed at greater length in section 6.4.1.

Calculations of the energies of all the known zeolite topologies, with all the T sites occupied by silicon atoms, have been performed by Zwijnenburg [9] using the Sanders-Leslie-Catlow potential [11]. They observe a energy map that is very similar to that observed for clathrates structures, which begs the question: are the energies for the pure silica zeolites and the hypothetical water clathrates correlated? Figure 6.15 seems to suggest that for most structures they are with a number of marked exceptions, namely the majority of the dense ice and silica phases and the known clathrate structures.

Zwijnenburg [9] has shown that the energy of pure silica zeolites, with frameworks

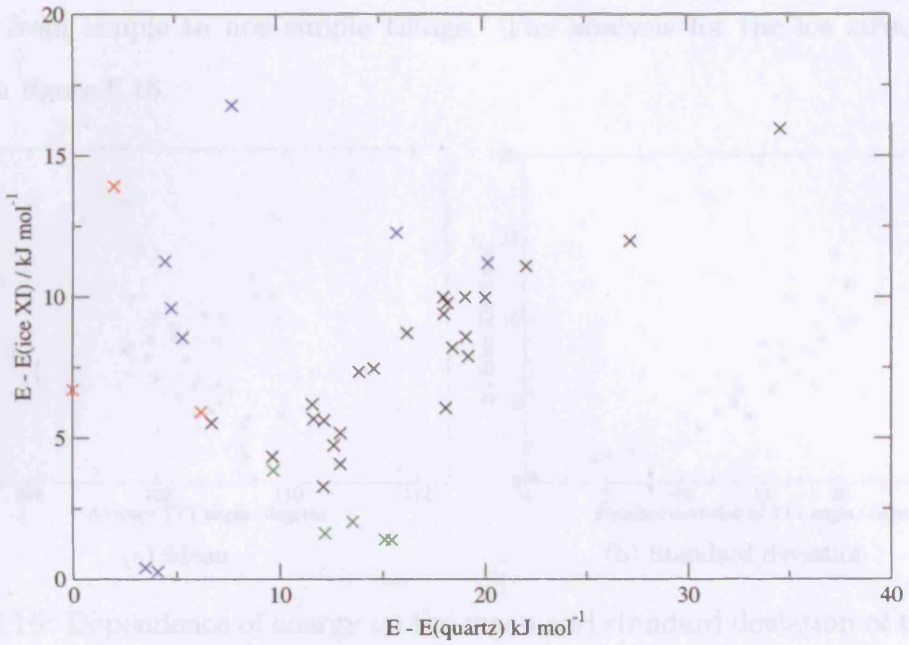

Figure 6.15: Correlation between the relative energies of pure silica and ice like structures. Black crosses are hypothetical zeolite structures, red crosses are dense silica phases, green crosses known clathrate phases and blue crosses are the dense ice phases. The energies are shows relative to the lowest energy phases at 0 K.

that are simple tilings (see section 2.4.1), is correlated with the average face size in the structure and the standard deviation of the face size distribution. Given the correlation between the pure silica zeolite energies and hypothetical clathrates one would expect a similar findings for zeolite like structures composed of water molecules. However, many of the zeolite structures and dense structures investigated in this work are not simple tilings and thus the calculation of face size distributions is not possible. The TTT angle, where T is the position of the vertices (O in ice and Si in pure silica zeolites) in the net, is correlated with the face size as all the faces in a simple tiling are regular polygons, thus small faces will have small TTT angles while larger faces will have larger TTT angles. Thus one might expect that the energy of a simple tiling will be correlated with the mean and standard deviation of the distribution of TTT angles in the structure. The advantage of these quantities is that, unlike the face size distributions, it is possible to calculate these quantities for simple tilings and non-simple tilings and thus see if the rule Zwijnenburg suggested

extends from simple to non-simple tilings. The analysis for the ice structures is shown in figure 6.16.

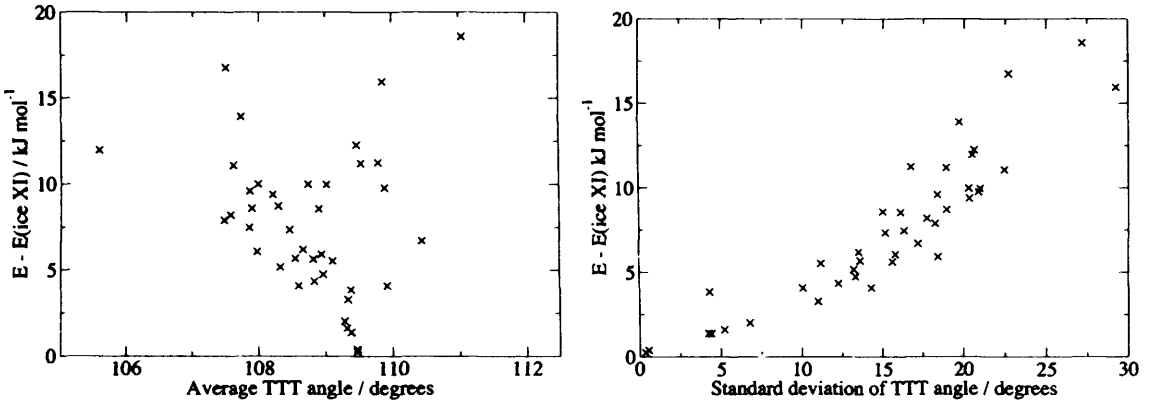

(a) Mean (b) Standard deviation

Figure 6.16: Dependence of energy on the mean and standard deviation of the TTT angle.

As can be seen from figure 6.16 there is a clear minimum for the energy versus average TTT angle, which corresponds to ice XI, and the energy rises steeply if one moves away from that minimum. Meanwhile, the energy is clearly correlated with the standard deviation of the TTT angle much as was expected. This explains the correlation between the silica and ice energies - clearly for both these systems there is an energetic cost for distorting the TTT angle.

In silica, the Si-O-Si bonds are bent whereas the hydrogen bonds in ice like structures are straight, as such α-quartz is the lowest energy structure for silica, whilst ice XI (lonsdaleite) is the lowest energy structure for ice. When ice is compressed it forms ice phases in which the hydrogen bonds are not straight, leading to the question - can the differences in the energetics observed for ice and silica be put down the fact that the energetic cost of bending hydrogen bonds is greater than that required to bend Si-O-Si bonds?

Figure 6.17 shows the energy is inversely-correlated with the average OHO angle, which adds weight to the suggestion that the hydrogen bond in ice like structures is less flexible that the Si-O-Si bond.

An analysis of the HOH angle reveals that in these structures this angle never

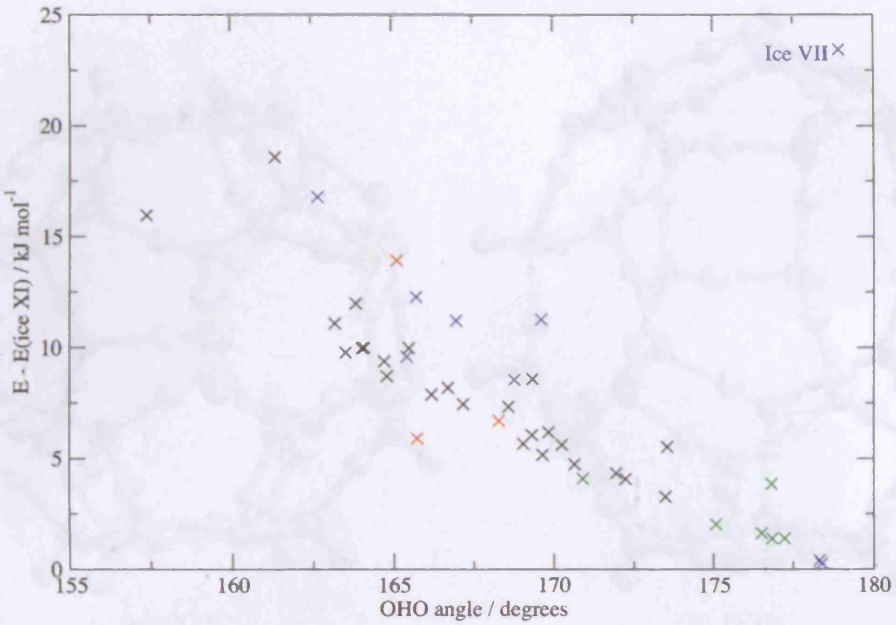

Figure 6.17: The energy vs the average OHO angle for all of the phases of ice studied in this work. The black crosses are the hypothetical phases, blue crosses are dense ice phases, red crosses are dense silica phases and green crosses are the known water clathrates.

distorts by more than 10° from the gas phase HOH angle and thus one can obtain a very good estimate for how bent the hydrogen bonds will be in the optimised structure by simply setting up a structure in which all the water molecules with their gas phase geometries. This combined with the fact that in ice one is attempting to minimise the standard deviation for the TTT angles could provide an inexpensive way of searching hypothetical zeolite framework databases for potential new clathrate or hydrate structures.

6.4.1 DDR and SGT

Earlier in the above section it was noticed that amongst the low energy and hence possibly synthesisable hypothetical clathrate hydrate structures the DDR and SGT frameworks had the lowest energies. As such these structures merit some further investigation.

Figure 6.19 shows that both SGT and DDR are simple tilings with more complex structures than the currently known water clathrates. Furthermore, they appear to

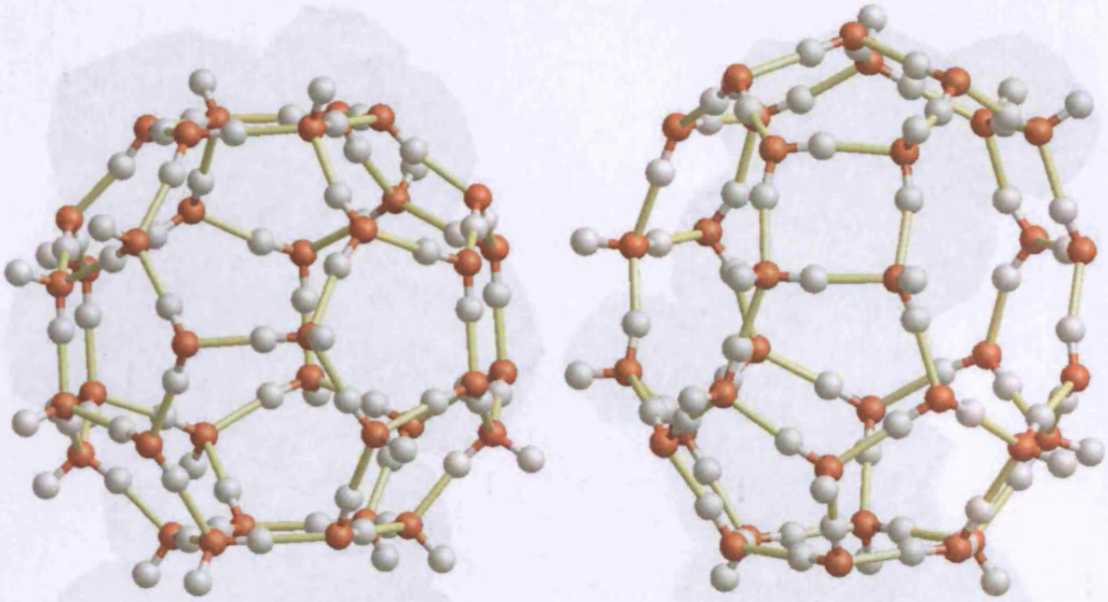

(a) SGT (b) DDR

Figure 6.18: The arrangements of the water molecules in the large cages of the DDR and SGT structures.

be composed of cages that are considerably more asymmetric and contain a greater proportion of energetically unfavourable four rings. Most importantly though, these two structures have larger cages than any of the currently known clathrate hydrate structures and so have the potential to store large gas molecules. The arrangement of water molecules in the large cages of these structures are shown in figure 6.18.

SGT is composed of $4^3 5^6$ cages and $5^{12}6^8$ (NB this cage has a different symmetry to the $5^{12}6^8$ cage in sH), while DDR is composed of alternating layers of 5^{12} cages and $4^3 5^6 6^1$ and $4^3 5^{12} 6^1 8^3$ cages. The shapes of these cages, their point group symmetries and the ratios of their principal dimensions are shown in figure 6.20.

Figure 6.20 shows that, much like was the case for the known clathrate structures, the cages in SGT are pseudospherical - in fact the $5^{12}6^8$ cage in SGT is more spherical than the $5^{12}6^8$ cage in the sH structure. However, for DDR the situation is different as both the $4^3 5^{12} 6^1 8^3$ cage and the $4^3 5^6 6^1$ cage are highly non-spherical.

It is possible to make pure silica versions of both the DDR and SGT structures using a template molecule. One might hope therefore that it would be possible to use a similar sort of templating to form clathrate hydrate structures based on these

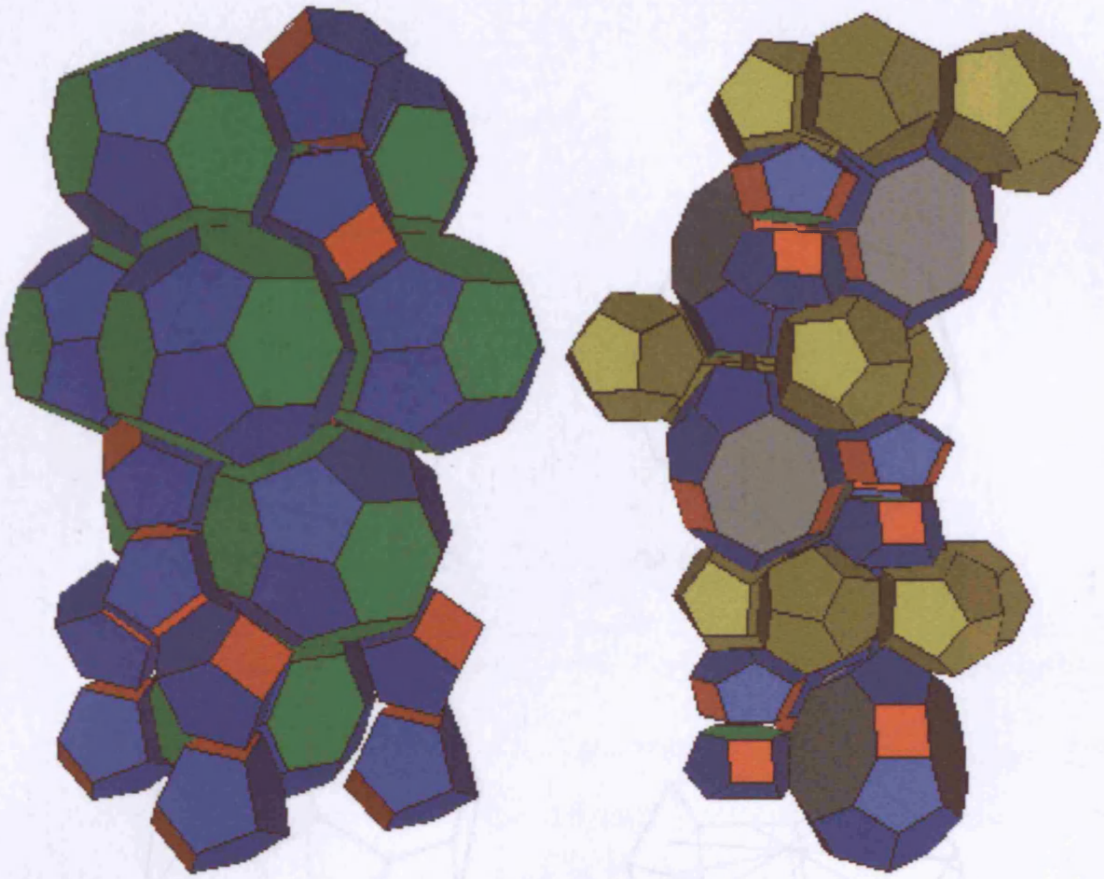

(a) SGT (b) DDR

Figure 6.19: The way polyhedra pack in the SGT and DDR structures. For clarity all 4 sided faces are shown in red, 5 sided faces in blue, 6 sided faces in green, 8 sided faces in grey and all 5^{12} polyhedra are shown in yellow.

two frameworks. One must be careful in selecting templates for clathrates however that they do not form hydrogen bonds because, whereas for silica hydrogen bonding from guest to framework and subsequent incorporation of the guest molecule into the framework is far less favourable than the formation of strong covalent bonds, for ice guest-framework hydrogen bonds will be equally, and in some cases more, favourable to hydrogen bond formation in the framework itself. In practice this means avoiding suggesting amines and alcohols as guest molecules.

To begin the process of template design an analysis of the cages present in these two structures and the ratios of their sizes to the 5^{12} cage was carried out. The results of this analysis are given in table 6.4 along with a reminder of the sizes of the cages present in the known clathrates.

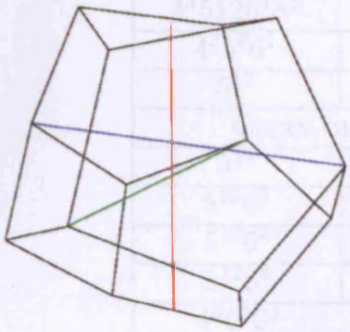

(a) 4^35^6 cage - C_{2v} (SGT)

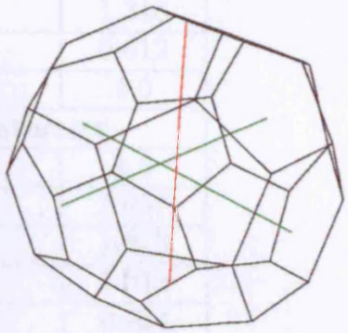

(b) $5^{12}6^8$ cage - C_{2v} (SGT)

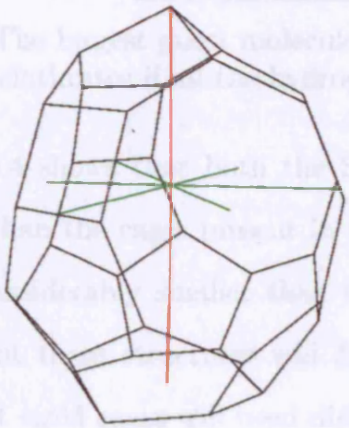

(c) $4^35126^18^3$ cage - C_{3v} (DDR)

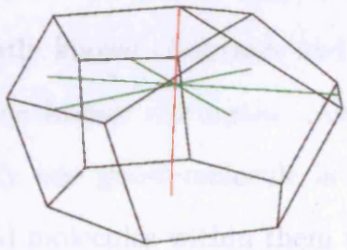

(d) $4^35^66^1$ cage - C_{3v} (DDR)

4^35^6 cage		
red : 0.857	green : 0.995	blue : 1.0
$5^{12}6^8$ cage		
red : 1.0	green : 0.946	
$4^35126^18^3$ cage		
red : 1.0	green : 0.746	
$4^35^66^1$ cage		
red : 0.665	green : 1.0	

Figure 6.20: Figure showing the shapes, symmetries and spatial extents of the cages in the SGT and DDR structures. Lines of the same colour indicate distances that must be equal by symmetry. The table gives the ratios of the non-equivalent lengths to each other.

Cage symbol	Guest radius	5^{12} ratio
Cages in SGT		
$4^3 5^6$	1.111	0.815
$5^{12}6^8$	1.820	1.335
Cages in DDR		
$4^3 5126^1 8^3$	1.796	1.318
$4^3 5^6 6^1$	0.834	0.612
5^{12}	1.363	1.0
Cages in known clathrates		
5^{12}	1.363	1.0
$5^{12}6^2$	1.441	1.057
$5^{12}6^4$	1.654	1.213
$5^{12}6^8$	1.790	1.313
$4^3 5^6 6^3$	1.300	0.954
$4^2 5^8 6^4$	1.285	0.942

Table 6.4: The largest guest molecule that can fit into the cages of DDR, SGT and the known clathrates if all the hydrogen bonds that make it up have unit length.

Table 6.4 shows that both the SGT and DDR structures contain cages that are larger than the cages present in the currently known clathrates and also cages that are considerably smaller than those in the known clathrates. As such it is unlikely that these structures will form if only one guest molecule is present as the different sized cages will need different sized molecules within them to stabilise them. ZEBEDDE [33] can be used to investigate what guests fit into the various cages in these structures. First and foremost the small cages (SGT: $4^3 5^6$ and DDR: $4^3 5^6 6^1$) because the size of molecules available only has a lower bound, namely hydrogen. Figure 6.21 shows the framework-guest interactions for various different guest molecules in these cages.

Figure 6.21 suggests that only hydrogen will fit in the smallest cage of SGT, but that there are perhaps a few more options for the small cage of DDR. The framework-guest interactions for all the molecules in these cages though are considerably less negative than if they were placed in the larger 5^{12} cage (see figure 6.10). This presents a potential problem, although this may be resolved if the framework-guest energy of whatever is placed in the larger cages is very favourable.

The DDR structure is of particular interest because it has both the properties

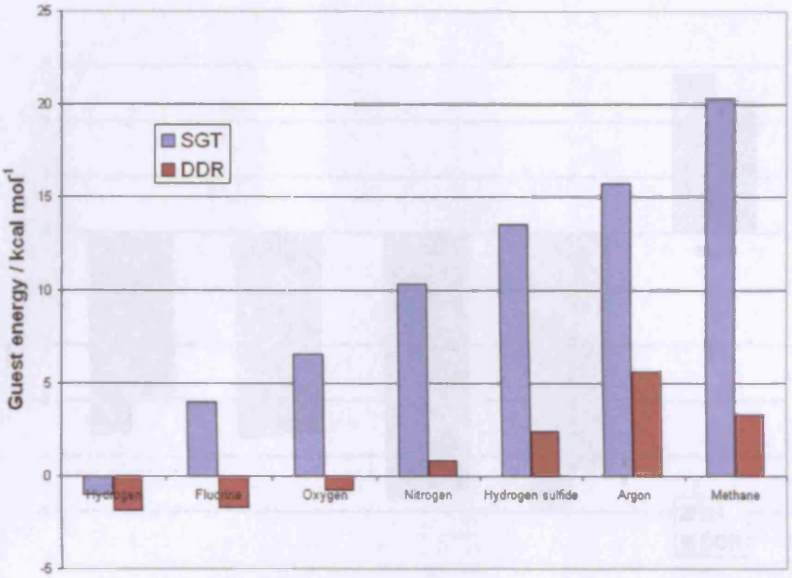

Figure 6.21: The framework-guest interactions for various guest molecules in the $4^3 5^6$ cage of SGT and the $4^3 5^6 6^1$ cage of DDR.

of a clathrate and the properties of a zeolites with an extended channel system [37]. Furthermore, figure 6.21 has already shown that the smallest cages in the structure are going to form more easily than those in SGT. As well as the small cage this structure contains two further types of cage, 5^{12} cages and $4^3 5^1 2^6 1^8 3^3$ cages. The guest molecules that fit in the 5^{12} cages in other clathrate structures were discussed in figure 6.10 and as figure 6.22 shows the guests that fit well in this cage in the DDR structure are almost identical to those that fit in this cage in other structures. However, the guests have lower binding energies in the 5^{12} cage of DDR than they do in the 5^{12} cages of other structures, which suggests that in the DDR structure the 5^{12} is larger than it would be in the known clathrates or slightly distorted.

Having established what guests fit in the small cages in these structures leaves only the guests in the large cages to investigate. As table 6.4 shows the large $4^3 5^{12} 6^1 8^3$ cage of DDR and the $5^{12} 6^8$ cages of sH and SGT can fit similarly sized largest guest molecules. This assertion is backed up by the analysis presented in figure 6.23 which shows that the butane is the straight chain alkane that fits most comfortably in the large cages in sH and DDR. For SGT the situation is more com-

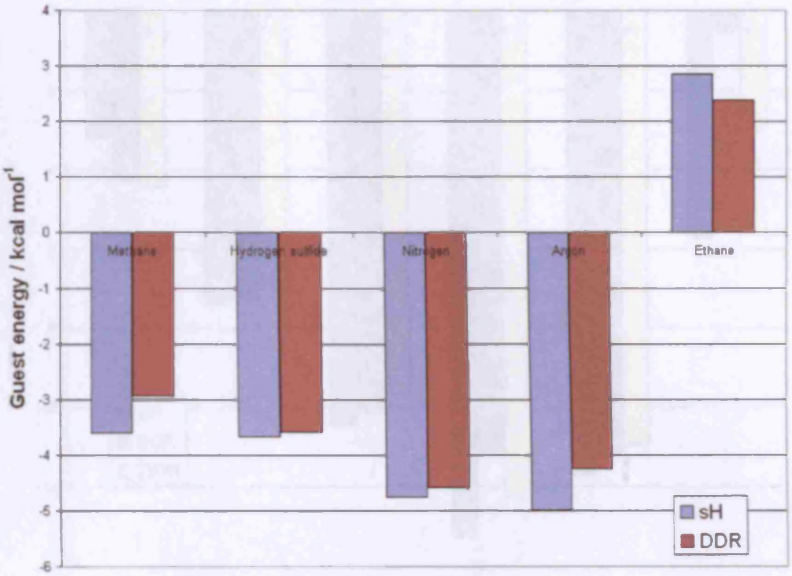

Figure 6.22: The framework-guest interactions for various guest molecules in the 5^{12} cages of the DDR structure.

plex as pentane and butane have very similar framework-guest energies, probably because there is more space for pentane to distort and thereby reduce its length in this cage.

Figures 6.20 and 6.9 show that the large cages in sH, SGT and DDR all have different symmetries - in particular SGT and sH both contain $5^{12}6^8$ cages that differ only in the arrangement of the faces and hence their symmetry. It was wondered whether the symmetry of the guest molecule would direct the structure of the cage that formed around it - namely whether or not structures in which the cage and guest had the same symmetry would have favourable guest framework interaction energies. Figure 6.24 shows the results of a test of this assertion in which different *n*-substituted butanes were placed in the large cages of sH, DDR and SGT.

Figure 6.24 shows that rather than the higher symmetry structures stabilising the $5^{12}6^8$ cage of sH over that of SGT, as one would expect if the symmetry of the guest controlled the symmetry of the cage, the opposite is the case. The reason for this is obvious if one examines the shapes of the cages, which are given in figures 6.20 and 6.9. It is simply that the $5^{12}6^8$ cage in SGT has a greater extent in the

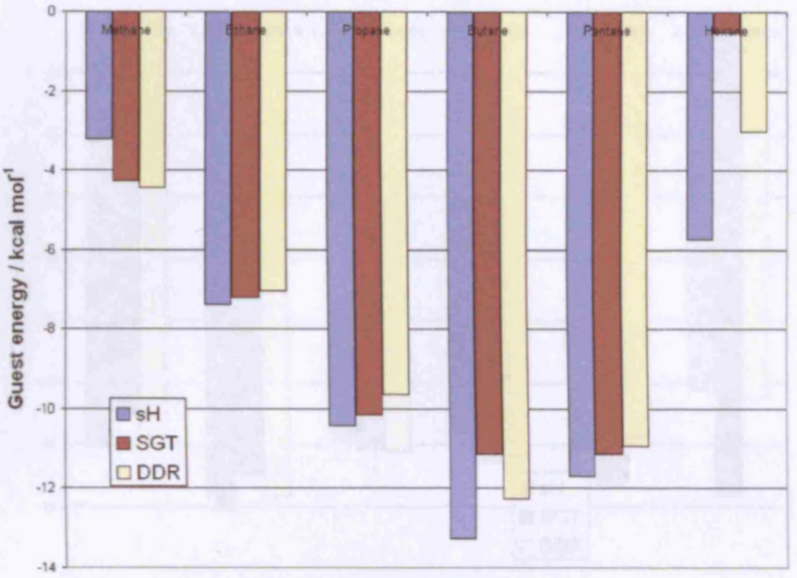

Figure 6.23: The framework-guest interactions for various straight chain alkane guest molecules in the $5^{12}6^8$ cages of sH and SGT and in the $4^3 5^{12} 6^1 8^3$ cage of DDR.

directions perpendicular to the principal axis of this cage, it is "fatter", than the $5^{12}6^8$ cage in sH. As such the more substituted "fatter" butane molecules fit better in the SGT cage than they do in the sH cage, as figure 6.20 shows. Adamantane is a "fat" molecule and as such would be expected to have a high guest framework interaction with the large cage of SGT and smaller interactions with the large cages of DDR and sH. Figure 6.25 confirms that this to be the case and in fact proves that adamantane is the most promising candidate for the formation of the SGT framework.

Figure 6.24 shows that DDR, although never the most stable cage for any given molecule, prefers to contain molecules that are "fat" at one end and "thinner" at the other, like 2,2-dimethyl butane. This again makes sense when one examines the shape of the cage, which is tapered having a large extent perpendicular to its C_3 axis at its base and a smaller extent at its top, as shown in figure 6.20. Numerous attempts have been made to find an appropriately shaped guest molecule to fit into this cage but this has proved highly problematic. From the ZEBEDDE calculations carried out it appears that the large cage in DDR has a width that is intermediate

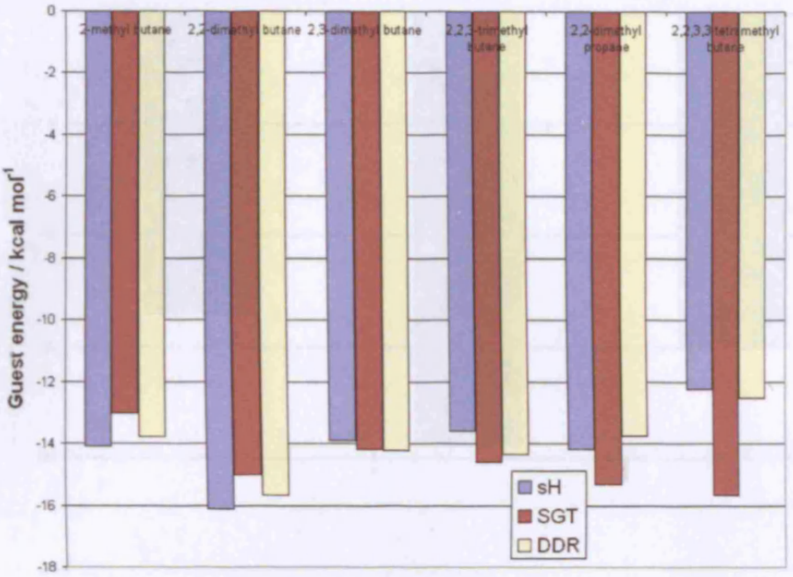

Figure 6.24: The framework-guest interactions for various n-substituted butanes in the $4^3 5^{12} 6^1 8^3$ cage of DDR and $5^{12} 6^8$ cages of the sH and SGT clathrate hydrate structures.

between those of the sH and SGT structures. Figure 6.24 shows that 2,2-dimethyl butane is guest molecule that best fits in the $5^{12} 6^8$ cage of sH. Therefore one might expect that if one could increase the sizes of the methyl substituents attached to the second carbon of this chain one would find that these new larger guests would fit most favourably into the large cage of DDR, while increasing the size of the methyl substituents further would create molecules which fit best in the large cage of SGT. Two ways of increasing the size of the methyl groups were attempted:

1. The carbon at the two position was replaced by a silica and one of the methyls attached to it was replaced by fluorine, which lengthened the Si-C bonds thereby making the base of the molecule larger.

2. Some or all of the hydrogens were replaced by larger fluorine atoms

All the molecules attempted were found to have more favourable framework-guest interactions with the large SGT cage than the large DDR cage, which suggests that the window of molecular sizes for which the $4^3 5^{12} 6^1 8^3$ cage of DDR is the most stable cage that will form about is very small. Furthermore, even if a suitable molecule

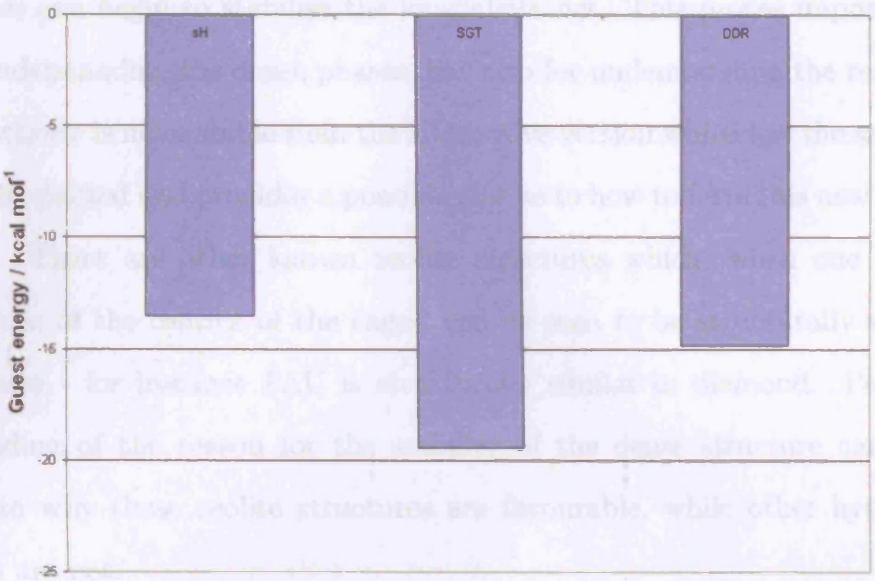

Figure 6.25: The framework-guest interaction for adamantane in the $4^3 5126^1 8^3$ cage of DDR and $5^{12}6^8$ cages of the sH and SGT clathrate hydrates structures.

were to found to fit in the large cage the stabilisation afforded to the structure from this interactions may not be enough to counter act the destabilising effect of having molecules in the smaller cages in this structure rather than the small cages in other structures, with which they interact more strongly (see figures 6.22 and 6.21). By contrast it seems more likely that the large difference between the binding energy of adamantane in the $5^{12}6^8$ cage of SGT with the binding energy energy of this molecule $5^{12}6^8$ cage in DOH will be enough to counter act the effect of having hydrogen molecules in the small $4^3 5^6$ cages.

6.5 Conclusions

This chapter has shown that comparing the chemistry of different species which form four connected nets can provide insights into the inter-atomic interactions in these different structures and can provide a method for predicting new structures. In particular it has been shown that the diamond net is stabilised by isotropic repulsive forces between atoms, but the introduction of a dipole on the species at

the vertices can begin to stabilise the lonsdaleite net. This proves important, not just for understanding the dense phases, but also for understanding the reason that the sII clathrate is more stable than the alternative version which has the same cages hexagonally packed and provides a possible clue as to how to form this new clathrate structure. There are other known zeolite structures which, when one examines the positions of the centres of the cages, can be seen to be structurally similar to dense phases - for instance FAU is structurally similar to diamond. Perhaps an understanding of the reason for the stability of the dense structure can provide insight into why these zeolite structures are favourable, while other hypothetical structures are not.

Through comparison of the energies of similar nets composed of SiO_2 and water it has been shown that the energetic landscapes for these two materials are very similar and that any difference is due to the fact that hydrogen bonds are considerably less flexible than Si-O-Si bonds. Furthermore, it seems likely, from the comparison of the relative energies of different possible 4-connected nets for water and silica, that the reason ice forms fewer structures than silica is not that the local minima corresponding to more exotic four connected nets are inaccessibly high in energy for ice but rather the energetic barriers to collapse of these nets are higher for the silica based structures.

Finally, on the clathrates the work presented here seems to suggest that the empty cage structures do correspond to local minima in the potential energy surface. Experimental work [24] shows that the lattice parameters for the clathrate structures typically only vary by only about 2 Å on changing the guest present in the cages, which suggests each of these structures only has a limited number of cage sizes for which the structure is stable. What is more, the DFT values for the lattice parameters for each of these structures is close to what one observes for the experimental lattice parameters. This observation suggests a way new clathrate structures may be designed - one first examines the available hypothetical zeolite

structural databases for simple tilings which contain mostly five and six rings. One then optimises these structures in CASTEP and measures the size of the various cages within them - one can then use ZEBEDDE to calculate what are appropriate guest molecules for the new structure.

Bibliography

[1] M. O'Keeffe and B. G. Hyde. *Crystal structures I. Patterns and Symmetry.* Mineralogical Society of America, (1996).

[2] V. F. Petrenko and R. W. Whitworth. *Physics of ice.* OUP, (1999).

[3] R. Devine, J.-P. Duraud and E. Dooryhee. *Structure and imperfections in amorphous and crystalline silicon dioxide.* Wiley, (2000).

[4] C. B. ad W. M. Meier and D. H. Olson. *Atlas of Zeolite Framework Types.* Elsevier, (2001).

[5] A. Wells and R. Sharpe. *Acta. Cryst.*, **16**, 857 (1963).

[6] J. Smith. *Chem. Rev.*, **88**, 149 (1988).

[7] O. Delgado-Friedrichs, M. Foster, M. O'Keeffe, D. Proserpio, M. Treacy and O. Yaghi. *J. Solid State Chem.*, **178**, 2533 (2005).

[8] N. J. Henson, A. K. Cheetham and J. D. Gale. *Chemistry of Materials*, **6**, 1647 (1994).

[9] M. Zwijnenburg, S. Bromley, M. Foster, R. Bell, O. Delgado-Friedrichs, J. Jansen and T. Maschmeyer. *Chemistry of materials*, **16**, 3809 (2004).

[10] M. D. Segall, P. L. D. Lindan, M. J. Probert, C. J. Pickard, P. J. Hasnip, S. J. Clark and M. C. Payne. *J. Phys.: Cond. Matt.*, **14**, 2712 (2002).

[11] M. J. Sanders, M. Leslie and C. R. A. Catlow. *Chem. Comm.*, **19**, 1271 (1984).

[12] J. D. Gale. *J. Chem. Soc., Faraday Trans.*, **93**, 629 (1997).

[13] M. Zwijnenburg, F. Cora and R. Bell. *J. Phys. Chem. B.*, **111**, 6156 (2007).

[14] P. Piccione, C. Laberty, S. Yang, M. Camblor, A. Navrotsky and M. Davis. *J. Phys. Chem.*, **104**, 10001 (2000).

[15] A. Pryde and M. Dove. *Phys. Chem. Minerals*, **26**, 171 (1998).

[16] J. D. Bernal and R. H. Fowler. *J. Chem. Phys.*, **1**, 515 (1933).

[17] R. Martonak, D. Donadio, A. Oganov and M. Parrinello. *Nature Materials*, **5**, 623 (2006).

[18] J. van der Waals and J. Platteeuw. *Advances in Chemical Physics*, **2**, 1 (1959).

[19] K. Sparks, J. Tester, Z. Cao and B. Trout. *J. Phys. Chem. B*, **103**, 6308 (1999).

[20] J. Klauda and S. Sandler. *J. Phys. Chem. B*, **106**, 5722 (2002).

[21] S. R. Zele, S. Y. Lee and G. D. Holder. *J. Phys. Chem. B*, **103**, 10250 (1999).

[22] J. Klauda and S. Sandler. *Chemical Engineering Science*, **58**, 27 (2003).

[23] C. Moon, P. Taylor and P. Rodger. *JACS*, **125**, 4706 (2003).

[24] G. A. Jeffrey. *Inclustion Compounds volume 1*, chapter Hydrate Inclusion Compounds. Academic Press, (1984).

[25] E. Smelik and H. K. Jr. *Zeitschrift fur Kristallographie*, **211**, 84 (1996).

[26] J. Ripmeester. Personal communication, (2007).

[27] E. D. Sloan. *Clathrate Hydrates of Natural Gasses.* Marcel Dekker Inc., (1990).

[28] R. M. Barrer and D. J. Ruzicka. *Trans. Faraday Soc.*, **58**, 2253 (1962).

[29] S. Y. Lee and G. D. Holder. *AICHE Journal*, **48**, 161 (2002).

[30] S. Y. Lee and G. D. Holder. *Annals of the New York Academy of Sciences*, **912**, 614 (2000).

[31] D. Weaire and R. Phelan. *Phil. May. Lett.*, **69**, 107 (1994).

[32] R. Phelan, D. Weaire and K. Brakke. *Experimental Mathematics*, **4**, 181 (1995).

[33] D. W. Lewis, D. J. Willock, C. R. A. Catlow, J. M. Thomas and G. J. Hutchings. *Nature*, **382**, 604 (1996).

[34] H. Sun, S. Mumby, J. R. Maple and A. T. Hagler. *J. Am. Chem. Soc.*, **116**, 2978 (1994).

[35] J. Ripmeester, J. Tse, C. Ratcliffe and B. Powell. *Nature*, **325**, 135 (1987).

[36] H. T. Stokes and D. M. Hatch. Findsym version 3.1, (2004).

[37] H. van Koningsveld and H. Gies. *Z. Kristallogr.*, **219**, 637 (2004).

Chapter 7

Conclusions and future work

Although there have been individual conclusions for each of the results chapters in this thesis, here they are brought together in order that general themes and any future direction for the work may be reflected on. Three broad areas have been addressed:

1. Studies on proton ordering phase transitions in disordered ice phases.
2. A study on how proton topology affects surface and bulk energy in ice Ih.
3. A comparison of known and hypothetical ice and silica structures.

In the studies of proton ordering phase transitions plane wave DFT calculations and subsequent Wannier transformations have shown that the energy differences between different proton topologies are largely due to electrostatic effects. Furthermore, the proton ordering in ices V and XII have been investigated using DFT, which has correctly predicted the structures of the ordered forms of ices V and XII (ices XII and XIV respectively). Finally, the energy difference between ordered ice II and its proton disordered analogues have been calculated. These energy differences are larger than they are in any of the other investigated ice phases, which suggests that ice II has no proton disordered analogue because the energy required to "excite" the proton topology is too large.

At first glance, there seems to be little else that can be done to investigate proton ordering transitions - between this work and the work of Kuo *et. al.* [1, 2, 3, 4, 5] all the known phases of ice, except ice IV, have been studied and the structures of their ordered forms predicted. However, there are also proton ordering transitions in clathrate materials [6] and given the size of the unit cells for some of the known clathrate structures these present a gigantic problem for theory. From this work one one way to attempt to solve this problem would be to use plane wave DFT calculations and subsequent Wannier transformations to obtain molecular multipoles for the water molecules present in these structures and then to use these multipoles and the electrostatic expansion to search through the vast number of possible hydrogen bonding topologies for the lowest energy topology. It would be interesting to find out, using these calculations, whether the ordered form for a clathrate is dependent on the guest molecule present or if the proton ordering forces the guest to adopt a particular orientation in the cage. The methods used for finding low energy proton topologies may also prove useful in predicting ground states in systems which have frustrated magnetism.

In predicting the ordered forms of proton disordered structures the thermodynamic driving force for proton ordering have been investigated. In order to better understand the transitions one should also investigate the kinetic boundaries to the transitions, which may provide clues as to why dopants, such as HCl or KCl, must be present for the transitions in ices Ih, V and XII to occur, while in ices III and VII dopants are surplus to requirements.

Proton ordering transitions involve a change in the proton topology within the structure, which as discussed in earlier parts of this thesis, is also the rate limiting step in electrical conduction in these materials. Furthermore, when a line defect moves through crystal of ice the surrounding proton topology must change so that no additional defects are introduced. As a result the rate of proton topology change can also affect the rates of line defect motion and hence the rates of slip and glide

in ice crystals. Proton topology change occurs through the motion of point defects like Bjerrum defects, OH^- ions, H_3O^+ ions, vacancies and interstitials. An in depth study of the structure and dynamics of these defects, in each of the known ice phases, would provide great insight into the behaviour of ice.

In chapter 5 a new potential was fitted, which allowed an investigation of the dependence of the potential energy on the hydrogen bonding topology to be carried out. This investigation has shown that, in simulations of bulk ice at very low temperatures, one must take account of these effects but that at most temperatures relevant to the atmosphere one can neglect the bulk proton topology. The most important conclusions from this chapter is that changing the proton topology at the surface can have a substantial effect on the surface energy, with surfaces which contain more clustering of dangling hydrogen bonds having greater energies. As such if one wishes to have a good description of the surface of ice Ih one must ensure that an energetically sensible hydrogen bonding topology for the surface is selected. This result has implications for any simulation of the surface of ice, be it a study of what are the most favourable morphologies for ice crystals or a study of surface reactivity.

The work presented in this thesis is limited by the potential used, which does not correctly reproduce the dynamic structure. It is important that new potentials for ice should correctly reproduce both the dynamics of the liquid and solid and the dependence of the energy on the proton topology. Given that the energy differences between different bulk proton topologies is small, ensuring that the bulk proton topology is a low energy one is probably not important at temperatures relevant to the Earth's atmosphere. As such one, somewhat unsatisfactory, solution to this lack of a potential may be to use either the TIP6P [7] potential or TIP4P/ice [8] potential to simulate surfaces and hope that, although these potentials do not reproduce the DFT energy differences between different bulk proton topologies, they will reproduce the energy differences between surfaces with different proton topologies. Another

is to use density functional theory to find a low energy structure - although this is much more computationally expensive than using a potential. However, this cost may be avoidable if one used the graph invariant software developed by Kuo *et. al.* [3] to fit the surface energy, calculated using DFT, to local structural features in the hydrogen bonding topology. Even so once a low energy hydrogen bonding topology for the surface has been found further studies are limited because DFT must be used - so only processes that occur on relatively short time and length scales can be investigated.

Another thing the work with potentials has highlighted is the need for better potentials to describe ice. Amongst the many water potentials in the literature there are comparatively few that have been fitted with the properties of ice in mind - the exceptions to this seeming to be the TIP4P/ice and TIP6P potentials. New ice potentials would allow one to perform free energy calculations which would give more insight into the probability of forming the new ice phases predicted in chapter 6, provide a computationally inexpensive way of studying the defects and allow one to study the surface of ice.

In the final major theme of this work the phases that can be made using ice and silica have been compared. This work has suggested the possibility of new dense ice phases, which would be expected to be observed in the centre of water's phase diagram where there is the greatest potential for the discovery of new phases, and also a number of potential new silica or zeolite structures. Investigations of zeolite structures, but made out of water, has shown that most of the energies of these structures are correlated with the energies of the analogous pure silica zeolites, with any differences being a result of the difference in flexibility between the OHO angle and the O-Si-O angle. Finally, potential new clathrate phases, which have larger cages and can thus hold larger guest molecules than any of the currently known clathrates, have been identified and Zebedde has been used to investigate potential guest molecules for these structures.

To extend this work an investigation of the free energies of these new ice, silica and clathrate phases must be carried out. Recent work on ice [8] and silica [9] has used potentials to calculate phase diagrams for these two systems and it would be hoped that, similar free energy calculations could be used to provide clues as to what temperature and pressure regimes these new structures will be found in.

Clathrates are hugely interesting materials that present a real challenge to theoretical understanding. Interesting work could be carried out using molecular dynamics to establish how the guest molecules move about in the cage and extend the current understanding of how clathrate materials form. Certainly the work with Zebedde could be extended and the stability of different guest molecules in different cages could be established. Ideally, if one could also find a way of describing how the energy of the framework varied as the cages swell to incorporate larger guest molecules or contracted as a response to external pressure one could obtain, not only an understanding of why particular guest molecules and combinations of guest molecules form different clathrates, but also of the pressure driven phase transitions that are observed in gas clathrates.

Bibliography

[1] J.-L. Kuo and S. J. Singer. *Physcial Review E*, **67**, 016114 (2003).

[2] J.-L. Kuo, J. V. Coe, S. J. Singer, Y. B. Band and L. Ojamae. *J. Chem. Phys.*, **114**, 2527–2540 (2001).

[3] S. J. Singer, J.-L. Kuo, T. K. Hirsch, C. Knight, L. Ojamae and M. L. Klein. *PRL*, **94**, 135701 (2005).

[4] C. Knight and S. J. Singer. *J. Chem. Phys.*, **125**, 064506 (2006).

[5] J.-L. Kuo and M. L. Klein. *J. Phys. Chem. B*, **108**, 19634 (2004).

[6] V. F. Petrenko and R. W. Whitworth. *Physics of ice.* OUP, (1999).

[7] H. Nada and J. P. J. M. van der Eerden. *J. Chem. Phys.*, **118**, 7401–7413 (2003).

[8] J. Abascal, E. Sanz, G. G. Fenandez and C. Vega. *J. Chem. Phys.*, **122**, 234511 (2005).

[9] M. Ford, S. Auerbach and P. Monson. *J. Chem. Phys.*, **121**, 8415 (2004).

Appendix A

A QM-MM method for ice

In order to undergo the phase transitions discussed in chapter 4 there must be a change in the proton topology of the system. Furthermore, processes like line defect movement and electrical conductivity require proton topology changes to occur [1]. These changes are believed to occur through the motion of point defects about the lattice, which makes the study of point defects in ice an important area of research. Experimental studies of defects are very difficult as the concentration of defects in bulk materials is very small. Theoretical studies, by contrast, are straightforward as defects can be introduced by simply moving atoms in the input file. However, in all calculations on defective systems large numbers of atoms must be used and so pure quantum mechanical approaches become unfeasible. Potentials meanwhile are generally fitted to reproduce the bulk system and assume that water molecules can be treated as rigid unpolarisable entities. As such potentials will not necessarily correctly reproduce the structure around a defect. These twin problems can been effectively side stepped by adopting the hybrid quantum mechanical-molecular mechanical approach described in section 3.3.3 [2] and describing the area near the defect using quantum mechanics and the bulk like surroundings using a potential. It was hoped that in this project the QUASI model could be used to study defects in ice using QM-MM approaches. However, this work has proved highly problematic, hence its relegation to an appendix in this thesis, not least because QUASI was

	Vacancy energy / kcal mol^{-1}	
Molecules in QM region	Config 1	Ice XI
5	29.56	28.39
18	33.23	30.30
27	33.91	28.05

Table A.1: Vacancy energies for different hydrogen bonding topologies and different QM region sizes, calculated using the TIP6P potential to describe the MM molecules.

initially designed with the simulations of metallic and ionic solids in mind rather than molecular systems.

The first modification made to the method was to adjust the construct routine so that the interfaces between regions did not cut through covalent bonds, so the interaction between molecules in the MM regions could be described using the TIP6P potential. In the quantum region an augmented TZVPP basis set [3, 4] was used with the B3LYP functional [5], which reproduces the dipole of an isolated water molecule well. A calculation of the vacancy energy for two distinct proton bonding topologies (ice XI and Hirsch and Ojamäe configuration number 1) was attempted using this model and gave the results in table A.1. For reasons which will be become clear later the numbers quoted in this table are for single point energies of the defective and undefective structures. One reason for this however is that within ChemShell optimisation of the full active region is not possible because there is no rigid body optimisation software.

As table A.1 shows the energy difference between the two proton topologies shows a strong dependence on the size of the QM region, which is clearly an unphysical effect. This was believed to be occurring because of a mismatch in the dipoles in the the QM and MM regions. It is easy to adjust the value of the dipole on the MM molecules by adjusting the values of the point charges on the sites of the potential. This has been done, the results are shown in figure A.1, to ascertain what effect making these changes has on the energy difference between the two proton topologies for a five molecule QM region. Changing the values of the point charges obviously changes the balance between attractive and repulsive forces in the

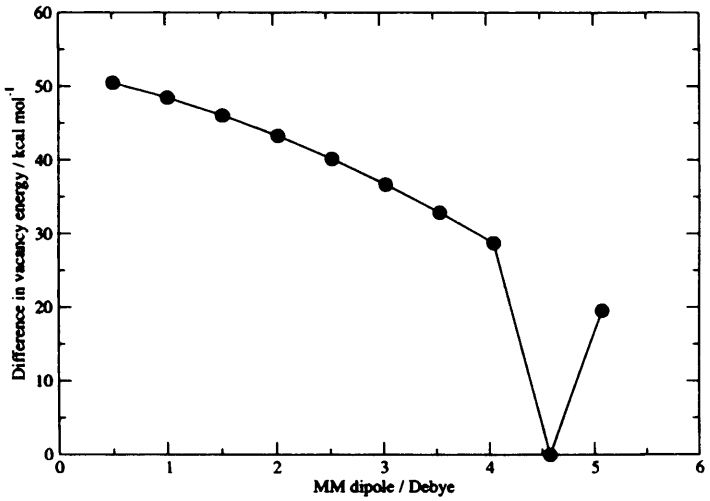

Figure A.1: The effect the value of the MM dipole has on the energy difference between the vacancy energies calculated for two different proton topologies. The minima in this curve corresponds to the point where the QM and MM dipoles are matched.

potential so the potential is no longer physically accurate and thus any forces arising from it are questionable so optimisation is not possible. What the potential does provide however is a description of the electrostatics, which will act to polarise the electron distribution in the QM region.

Figure A.1 seems to suggest that if the MM dipole has the correct value this discrepancy will disappear and that one option for fitting the electrostatic terms in the potential would be to minimise this energy difference. To do this however, would require a lot of calculations, so an alternative solution to this problem was sought. GAMESS-UK [6], the program Chemshell uses to do the QM part of the calculation, has implemented within it the DMA scheme described in section 3.2.3 [7]. This suggests that one approach to matching the electrostatics in the MM and QM region would be to use the output from DMA analysis on the molecules in the QM region to fit the potential in the MM region. That is to say that one could perform a calculation with some initial MM potential and obtain multipoles using DMA. The multipoles so obtained, could then be used to refit the MM potential and this process could be repeated until self convergence was achieved. Software to do exactly this was developed, with the average charge and dipole on the oxygen

	Vacancy energy / kcal mol^{-1}	
Molecules in QM region	Config 1	Ice XI
5	29.75	30.51
18	31.93	31.51
27	32.80	30.12

Table A.2: Vacancy energies for different hydrogen bonding topologies and different QM region sizes, calculated using an electrostatic potential that has been fitted on the fly to the QM electrostatics.

and hydrogen positions of the molecules of the QM region being used to fit the charges on a pair of closely separated point charges at each atomic position. After this fitting process was undertaken a vacancy energy was calculated for each of the two topologies of interest - the results of these calculations are given in table A.2.

As table A.2 shows the size of the QM region still has an effect on the difference in vacancy energy between the two topologies. However, the increase in this energy difference as a function of QM region size is far smaller than it was when the TIP6P potential was used to describe the MM region. This suggests that this approach is a sensible one although there is still much that must be done before a detailed study of defects in ice can be undertaken.

Bibliography

[1] V. F. Petrenko and R. W. Whitworth. *Physics of ice.* OUP, (1999).

[2] P. S. et. al. *J. Mol Struc-Theochem*, **632**, 1 (2003).

[3] A. Schafer, C. Huber and R. Ahlrichs. *J. Chem. Phys.*, **100**, 5829 (1994).

[4] A. Sokol. Personal communication, (2006).

[5] P. Stephens, F. Devlin, C. Chabalowski and M. Frisch. *J.Phys.Chem.*, **98**, 11623 (1994).

[6] Gamess-uk, (1980). GAMESS-UK is a package of ab initio programs written by M.F. Guest, J.H. van Lenthe, J. Kendrick, and P. Sherwood, with contributions from R.D. Amos, R.J. Buenker, H. van Dam, M. Dupuis, N.C. Handy, I.H. Hillier, P.J. Knowles, V. Bonacic-Koutecky, W. von Niessen, R.J. Harrison, A.P. Rendell, V.R. Saunders, K. Schoffel, A.J. Stone and D. Tozer.

[7] A. Stone and M. Alderton. *Molecular Physics*, **50**, 1047 (1985).

Appendix B

Outline of new programs

During the course of this PhD a number of new computer programs have been created. All these programs have been written in Fortran 90 and a brief outline of each of them and their purposes are given below:

B.1 Electrostatic Energy

A program called *electro* has been written to calculate the potential energy of interaction of the multipoles output from the Wannier function analysis performed in CASTEP. These multipoles are output in the cell frame so the potential energy can be calculated directly from them. The program creates a supercell, the size of which is specified by the user, of the multipoles input and calculates the potential energy up to order $(1/r^6)$ in the electrostatic expansion. As a large supercell is used and the system need only do one iteration a direct sum is used to calculate the potential energy of interaction of all the terms in the multipolar expansion of higher order than the dipole-dipole interaction. The dipole-dipole interaction meanwhile is calculated using a Ewald sum.

B.2 Multipole Rotation

A program called multipole_rotate has been written to rotate the multipoles output from CASTEP from the cell frame into the body fixed frame so that the values of multipoles on different molecules can be compared. The body fixed frame used in this code has as its axis the HOH bisector, the cross product of the two OH vectors and the cross product of these two vectors. An additional add on code has been written to take the multipoles output, in the body fixed frame, and calculate their average magnitude and the standard deviation of their magnitude.

B.3 Generate

This program takes in the positions of the vertices of an infinite 4 connected net and generates a hydrogen bonding topology that obeys the Bernal-Fowler rules. It requires an input file called coordinates.dat, which gives the value of the cell constants, $a, b, c, \alpha, \beta, \gamma$ on the first line and has an empty second line followed by the positions of all the vertices in the unit cell in fractional coordinates. This program is run by issuing the command:

./generate.x

Once this command has been issued it asks the user for the number of vertices in the unit cell, whether the user wishes to generate all possible hydrogen bonding topologies for the net given (although this feature only works for nets with small number of vertices) and for a random number. If the user chooses not to enumerate all structures the final structure is output to the file coordinates.gin, whereas if all topologies are output a large number of fort files, containing all the structures, are output.

B.4 Monte Carlo with hydrogen bonding topology changing moves

Two versions of this software have been written, the first was designed for bulk systems and the later is for surfaces. There are two principal differences between these two codes:

1. The surface version uses the full modified TIP6P potential in the calculation of the energy, whereas the bulk version only uses the torsional part of the modified TIP6P.

2. The surface version of the code allows the additional topology changing described in section 3.4.3.

A slight limitation of both these codes is that only orthorhombic simulation cells can be used. Both codes require two input files, monte.inpt and coordinates.dat, the first of which contains the simulation parameters and the second the cell lengths and coordinates.

Within both these codes two representations of the structure are used - the first is a representation of the coordinates of all the atoms, while the second tells which oxygens are connected and the directions of the connections. The first of these representations is used in the energy evaluation routines, while the second is used for the parts of the program that deal with the topology changing moves and also to store the configuration at each time step.

In the surfaces code it is necessary to constrain the system so that there is zero dipole perpendicular to the surface. This constraint is applied by giving each and every molecule a unit dipole parallel to its HOH bisector and summing the dipoles on all the molecules - if there is a net dipole perpendicular to the surface the move is then rejected out right. Finally, the Ewald sum in the surfaces code is a 3D Ewald sum and a vacuum gap between surfaces of 20 Å is used to ensure that there is no interaction between adjacent slabs.

B.5 Programs for use in QM-MM

As discussed in appendix A the hybrid QM-MM method developed during the course of this work relies on using the DMA method to fit the charges on the MM atoms. A code called dma_avmults has been developed to obtain multipole from the GAMESS-UK output and change the potential parameters in the input files for chemshell. This code first reads in the site dipoles from the .pun file output by GAMESS-UK, rotates them from the cell frame to the body frame and calculates averages. It was found early on that all dipoles had a negligible component out of the plane, the oxygen dipole lay along the HOH bisector, the charges on the two hydrogens were equal and that the dipole on the second hydrogen was given equal to the dipole on the first hydrogen reflected in the plane parallel to the HOH bisector. As such constraints of zero dipole in certain directions and the symmetries described above were applied to the average values of the dipoles obtained from GAMESS-UK.

The second step in the fitting process was to use the obtained values of the dipoles to refit the the model. The model represents each dipole as a pair of closely separated point charges so that overall there were six point charges in the model. The first three of these point charge lie on the elemental site and have components due to the monopole due to it being the positive end of the dipole. The second charge lies a distance d away along the dipole vector and has a charge of $-q$, where q is given by:

$$q = \frac{\mu}{d} \tag{B.1}$$

Once this fitting procedure has been completed the input file for Chemshell is rewritten and the charges and all site positions are updated.

Appendix C

Details on Methods

C.1 DFT calculations - CASTEP

All the DFT calculations were performed in CASTEP. Details of kpoint sampling, exchange correlation functional choice and the plane wave cutoff in these calculations has been detailed in the text. A sample input is provided below, as can be seen in all these calcalations the SCF tolerance was set at 0.0000005 eV and the optimisation tolerances were set as the input shows. Ultra soft pseudo-potentials were used throughout.

task : GeometryOptimization
xc_functional : PW91
spin_polarized : false
opt_strategy : Speed
page_wvfns : 0
cut_off_energy : 550.0000000000
grid_scale : 1.7500000000
finite_basis_corr : 2
elec_energy_tol : 0.0000005000
max_scf_cycles : 100
fix_occupancy : false
metals_method : dm
mixing_scheme : Pulay
mix_charge_amp : 0.5000000000
mix_charge_gmax : 1.5000000000
mix_history_length : 20
nextra_bands : 4

smearing_width : 0.1000000000
geom_energy_tol : 0.0000050000
geom_force_tol : 0.0100000000
geom_stress_tol : 0.0200000000
geom_disp_tol : 0.0005000000
geom_max_iter : 100
geom_method : BFGS
fixed_npw : false
calculate_stress : true
popn_calculate : true
popn_bond_cutoff : 3.0000000000
pdos_calculate_weights : false
num_dump_cycles : 0

An input for one of the Wannier function calculations which was performed in CASTEP is given below:

task : WannierFunctions
continuation default
grid_scale 1.75
calculate_stress false
wannier_spread_type Resta
wannier_min_algor sd
wannier_print_cube 3
wannier_sd_step 0.05
wannier_max_sd_steps 100000
wannier_ion_moments .true.
wannier_ion_rmax 1.00

C.2 Molecular dynamics - DLPOLY

Molecular dynamics calculations were performed using DLPOLY and a sample CONTROL file is given below.

temp 0.01
pressure 0.001013
steps 20000
equilibrium 2000
scale every 1 steps
timestep 0.001
print 10
ensemble nst berendsen 0.005 0.05
cutoff 10
delr 0.5
ewald precision 1.0000E-5

```
job time 14400000
close time 14000000
traj 0 500 0
finish
```

All the programs created during the course of this work and the inputs and outputs for computational chemistry codes are available from the author in a zipped tar file.